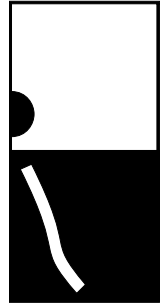


# Vehicle Dynamics

HOCHSCHULE  
REGENSBURG  
UNIVERSITY  
OF APPLIED  
SCIENCES



LECTURE NOTES  
Prof. Dr. Georg Rill  
© March 2009



# Contents

<b>Contents</b>	<b>I</b>
<b>1 Introduction</b>	<b>1</b>
1.1 Terminology . . . . .	1
1.1.1 Vehicle Dynamics . . . . .	1
1.1.2 Driver . . . . .	1
1.1.3 Vehicle . . . . .	2
1.1.4 Load . . . . .	3
1.1.5 Environment . . . . .	3
1.2 Driver Model . . . . .	3
1.3 Reference frames . . . . .	4
<b>2 Road</b>	<b>6</b>
2.1 Modeling Aspects . . . . .	6
2.2 Deterministic Profiles . . . . .	7
2.2.1 Bumps and Potholes . . . . .	7
2.2.2 Sine Waves . . . . .	8
2.3 Random Profiles . . . . .	9
2.3.1 Statistical Properties . . . . .	9
2.3.2 Classification of Random Road Profiles . . . . .	11
2.3.3 Realizations . . . . .	12
2.3.3.1 Sinusoidal Approximation . . . . .	12
2.3.3.2 Shaping Filter . . . . .	14
2.3.3.3 Two-Dimensional Model . . . . .	14
<b>3 Tire</b>	<b>16</b>
3.1 Introduction . . . . .	16
3.1.1 Tire Development . . . . .	16
3.1.2 Tire Composites . . . . .	17
3.1.3 Tire Forces and Torques . . . . .	17
3.1.4 Measuring Tire Forces and Torques . . . . .	18
3.1.5 Modeling Aspects . . . . .	19
3.1.6 Typical Tire Characteristics . . . . .	22
3.2 Contact Geometry . . . . .	24
3.2.1 Basic Approach . . . . .	24

## Contents

3.2.2	Local Track Plane . . . . .	26
3.2.3	Tire Deflection . . . . .	28
3.2.4	Static Contact Point . . . . .	30
3.2.5	Length of Contact Patch . . . . .	31
3.2.6	Contact Point Velocity . . . . .	33
3.2.7	Dynamic Rolling Radius . . . . .	34
3.3	Steady State Forces and Torques . . . . .	36
3.3.1	Wheel Load . . . . .	36
3.3.2	Tipping Torque . . . . .	37
3.3.3	Rolling Resistance . . . . .	38
3.3.4	Longitudinal Force and Longitudinal Slip . . . . .	39
3.3.5	Lateral Slip, Lateral Force and Self Aligning Torque . . . . .	42
3.3.6	Bore Torque . . . . .	45
3.3.6.1	Modeling Aspects . . . . .	45
3.3.6.2	Maximum Torque . . . . .	45
3.3.6.3	Bore Slip . . . . .	46
3.3.6.4	Model Realisation . . . . .	47
3.3.7	Different Influences . . . . .	48
3.3.7.1	Wheel Load . . . . .	48
3.3.7.2	Friction . . . . .	50
3.3.7.3	Camber . . . . .	51
3.3.8	Combined Forces . . . . .	54
3.3.8.1	Generalized Slip . . . . .	54
3.3.8.2	Suitable Approximation . . . . .	56
3.3.8.3	Results . . . . .	58
3.4	First Order Tire Dynamics . . . . .	59
3.4.1	Simple Dynamic Extension . . . . .	59
3.4.2	Enhanced Force Dynamics . . . . .	60
3.4.2.1	Compliance Model . . . . .	60
3.4.2.2	Relaxation Lengths . . . . .	62
3.4.3	Enhanced Torque Dynamics . . . . .	63
3.4.3.1	Self Aligning Torque . . . . .	63
3.4.3.2	Bore Torque . . . . .	63
3.4.3.3	Parking Torque . . . . .	65
<b>4</b>	<b>Drive Train</b>	<b>68</b>
4.1	Components . . . . .	68
4.2	Wheel and Tire . . . . .	69
4.2.1	Eigen-Dynamics . . . . .	69
4.2.2	Performance at Stand Still . . . . .	72
4.2.3	Driving and Braking Torques . . . . .	73

4.3	Drive Shafts, Half Shafts and Differentials . . . . .	74
4.3.1	Structure . . . . .	74
4.3.2	Active Differentials . . . . .	75
4.4	Transmission . . . . .	76
4.5	Clutch . . . . .	77
4.6	Engine . . . . .	78
4.6.1	Combustion engine . . . . .	78
4.6.2	Hybrid drive . . . . .	79
<b>5</b>	<b>Suspension System</b>	<b>80</b>
5.1	Purpose and Components . . . . .	80
5.2	Some Examples . . . . .	81
5.2.1	Multi Purpose Systems . . . . .	81
5.2.2	Specific Systems . . . . .	82
5.2.3	Toe-in, Toe-out . . . . .	82
5.2.4	Wheel Camber . . . . .	83
5.2.5	Design Position of Wheel Rotation Axis . . . . .	84
5.2.6	Steering Geometry . . . . .	85
5.3	Steering Systems . . . . .	87
5.3.1	Components and Requirements . . . . .	87
5.3.2	Rack and Pinion Steering . . . . .	87
5.3.3	Lever Arm Steering System . . . . .	88
5.3.4	Toe Bar Steering System . . . . .	88
5.3.5	Bus Steer System . . . . .	89
<b>6</b>	<b>Force Elements</b>	<b>91</b>
6.1	Standard Force Elements . . . . .	91
6.1.1	Springs . . . . .	91
6.1.2	Anti-Roll Bar . . . . .	92
6.1.3	Damper . . . . .	94
6.1.4	Rubber Elements . . . . .	95
6.2	Dynamic Force Elements . . . . .	96
6.2.1	Testing and Evaluating Procedures . . . . .	96
6.2.2	Simple Spring Damper Combination . . . . .	100
6.2.3	General Dynamic Force Model . . . . .	101
6.2.3.1	Hydro-Mount . . . . .	103
<b>7</b>	<b>Vertical Dynamics</b>	<b>106</b>
7.1	Goals . . . . .	106
7.2	Basic Tuning . . . . .	106
7.2.1	From complex to simple models . . . . .	106
7.2.2	Natural Frequency and Damping Rate . . . . .	110

## Contents

7.2.3	Spring Rates . . . . .	112
7.2.3.1	Minimum Spring Rates . . . . .	112
7.2.3.2	Nonlinear Springs . . . . .	113
7.2.4	Influence of Damping . . . . .	115
7.2.5	Optimal Damping . . . . .	115
7.2.5.1	Avoiding Overshoots . . . . .	115
7.2.5.2	Disturbance Reaction Problem . . . . .	117
7.3	Sky Hook Damper . . . . .	121
7.3.1	Modeling Aspects . . . . .	121
7.3.2	Eigenfrequencies and Damping Ratios . . . . .	123
7.3.3	Technical Realization . . . . .	124
7.4	Nonlinear Force Elements . . . . .	125
7.4.1	Quarter Car Model . . . . .	125
7.4.2	Results . . . . .	127
<b>8</b>	<b>Longitudinal Dynamics</b>	<b>129</b>
8.1	Dynamic Wheel Loads . . . . .	129
8.1.1	Simple Vehicle Model . . . . .	129
8.1.2	Influence of Grade . . . . .	130
8.1.3	Aerodynamic Forces . . . . .	131
8.2	Maximum Acceleration . . . . .	132
8.2.1	Tilting Limits . . . . .	132
8.2.2	Friction Limits . . . . .	132
8.3	Driving and Braking . . . . .	133
8.3.1	Single Axle Drive . . . . .	133
8.3.2	Braking at Single Axle . . . . .	134
8.3.3	Braking Stability . . . . .	135
8.3.4	Optimal Distribution of Drive and Brake Forces . . . . .	136
8.3.5	Different Distributions of Brake Forces . . . . .	138
8.3.6	Anti-Lock-System . . . . .	138
8.3.7	Braking on $\mu$ -Split . . . . .	139
8.4	Drive and Brake Pitch . . . . .	140
8.4.1	Vehicle Model . . . . .	140
8.4.2	Equations of Motion . . . . .	143
8.4.3	Equilibrium . . . . .	143
8.4.4	Driving and Braking . . . . .	144
8.4.5	Anti Dive and Anti Squat . . . . .	145
<b>9</b>	<b>Lateral Dynamics</b>	<b>146</b>
9.1	Kinematic Approach . . . . .	146
9.1.1	Kinematic Tire Model . . . . .	146
9.1.2	Ackermann Geometry . . . . .	146

9.1.3	Space Requirement . . . . .	147
9.1.4	Vehicle Model with Trailer . . . . .	149
9.1.4.1	Kinematics . . . . .	149
9.1.4.2	Vehicle Motion . . . . .	150
9.1.4.3	Entering a Curve . . . . .	152
9.1.4.4	Trailer Motions . . . . .	152
9.1.4.5	Course Calculations . . . . .	154
9.2	Steady State Cornering . . . . .	154
9.2.1	Cornering Resistance . . . . .	154
9.2.2	Overturning Limit . . . . .	156
9.2.3	Roll Support and Camber Compensation . . . . .	159
9.2.4	Roll Center and Roll Axis . . . . .	162
9.2.5	Wheel Loads . . . . .	162
9.3	Simple Handling Model . . . . .	163
9.3.1	Modeling Concept . . . . .	163
9.3.2	Kinematics . . . . .	163
9.3.3	Tire Forces . . . . .	164
9.3.4	Lateral Slips . . . . .	165
9.3.5	Equations of Motion . . . . .	165
9.3.6	Stability . . . . .	167
9.3.6.1	Eigenvalues . . . . .	167
9.3.6.2	Low Speed Approximation . . . . .	167
9.3.6.3	High Speed Approximation . . . . .	167
9.3.6.4	Critical Speed . . . . .	168
9.3.7	Steady State Solution . . . . .	169
9.3.7.1	Steering Tendency . . . . .	169
9.3.7.2	Side Slip Angle . . . . .	171
9.3.7.3	Slip Angles . . . . .	173
9.3.8	Influence of Wheel Load on Cornering Stiffness . . . . .	173
9.4	Mechatronic Systems . . . . .	175
9.4.1	Electronic Stability Control (ESC) . . . . .	175
9.4.2	Steer-by-Wire . . . . .	176
<b>10</b>	<b>Driving Behavior of Single Vehicles</b>	<b>177</b>
10.1	Standard Driving Maneuvers . . . . .	177
10.1.1	Steady State Cornering . . . . .	177
10.1.2	Step Steer Input . . . . .	178
10.1.3	Driving Straight Ahead . . . . .	179
10.1.3.1	Random Road Profile . . . . .	179
10.1.3.2	Steering Activity . . . . .	181
10.2	Coach with different Loading Conditions . . . . .	182
10.2.1	Data . . . . .	182

*Contents*

10.2.2 Roll Steering . . . . .	182
10.2.3 Steady State Cornering . . . . .	183
10.2.4 Step Steer Input . . . . .	184
10.3 Different Rear Axle Concepts for a Passenger Car . . . . .	184

# 1 Introduction

## 1.1 Terminology

### 1.1.1 Vehicle Dynamics

Vehicle dynamics is a part of engineering primarily based on classical mechanics but it may also involve physics, electrical engineering, chemistry, communications, psychology etc. Here, the focus will be laid on ground vehicles supported by wheels and tires. Vehicle dynamics encompasses the interaction of:

- driver
- vehicle
- load
- environment

Vehicle dynamics mainly deals with:

- the improvement of active safety and driving comfort
- the reduction of road destruction

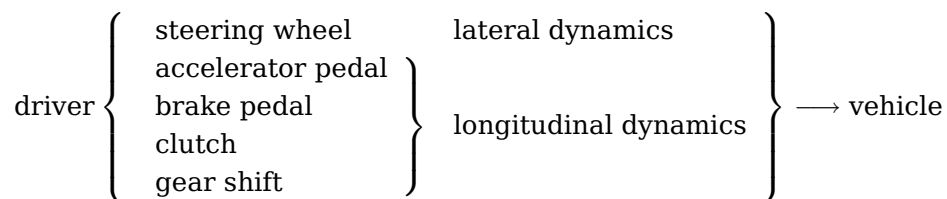
In vehicle dynamics are employed:

- computer calculations
- test rig measurements
- field tests

In the following the interactions between the single systems and the problems with computer calculations and/or measurements shall be discussed.

### 1.1.2 Driver

By various means the driver can interfere with the vehicle:



## 1 Introduction

The vehicle provides the driver with these information:

$$\text{vehicle} \left\{ \begin{array}{l} \text{vibrations:} \quad \text{longitudinal, lateral, vertical} \\ \text{sounds:} \quad \text{motor, aerodynamics, tires} \\ \text{instruments:} \quad \text{velocity, external temperature, ...} \end{array} \right\} \longrightarrow \text{driver}$$

The environment also influences the driver:

$$\text{environment} \left\{ \begin{array}{l} \text{climate} \\ \text{traffic density} \\ \text{track} \end{array} \right\} \longrightarrow \text{driver}$$

The driver's reaction is very complex. To achieve objective results, an 'ideal' driver is used in computer simulations, and in driving experiments automated drivers (e.g. steering machines) are employed. Transferring results to normal drivers is often difficult, if field tests are made with test drivers. Field tests with normal drivers have to be evaluated statistically. Of course, the driver's security must have absolute priority in all tests. Driving simulators provide an excellent means of analyzing the behavior of drivers even in limit situations without danger. It has been tried to analyze the interaction between driver and vehicle with complex driver models for some years.

### 1.1.3 Vehicle

The following vehicles are listed in the ISO 3833 directive:

- motorcycles
- passenger cars
- busses
- trucks
- agricultural tractors
- passenger cars with trailer
- truck trailer / semitrailer
- road trains

For computer calculations these vehicles have to be depicted in mathematically describable substitute systems. The generation of the equations of motion, the numeric solution, as well as the acquisition of data require great expenses. In times of PCs and workstations computing costs hardly matter anymore. At an early stage of development, often only prototypes are available for field and/or laboratory tests. Results can be falsified by safety devices, e.g. jockey wheels on trucks.

### 1.1.4 Load

Trucks are conceived for taking up load. Thus, their driving behavior changes.

$$\text{Load} \left\{ \begin{array}{l} \text{mass, inertia, center of gravity} \\ \text{dynamic behaviour (liquid load)} \end{array} \right\} \longrightarrow \text{vehicle}$$

In computer calculations problems occur at the determination of the inertias and the modeling of liquid loads. Even the loading and unloading process of experimental vehicles takes some effort. When carrying out experiments with tank trucks, flammable liquids have to be substituted with water. Thus, the results achieved cannot be simply transferred to real loads.

### 1.1.5 Environment

The environment influences primarily the vehicle:

$$\text{Environment} \left\{ \begin{array}{l} \text{road: irregularities, coefficient of friction} \\ \text{air: resistance, cross wind} \end{array} \right\} \longrightarrow \text{vehicle}$$

but also affects the driver:

$$\text{environment} \left\{ \begin{array}{l} \text{climate} \\ \text{visibility} \end{array} \right\} \longrightarrow \text{driver}$$

Through the interactions between vehicle and road, roads can quickly be destroyed. The greatest difficulty with field tests and laboratory experiments is the virtual impossibility of reproducing environmental influences. The main problems with computer simulation are the description of random road irregularities and the interaction of tires and road as well as the calculation of aerodynamic forces and torques.

## 1.2 Driver Model

Many driving maneuvers require inputs of the driver at the steering wheel and the gas pedal which depend on the actual state of the vehicle. A real driver takes a lot of information provided by the vehicle and the environment into account. He acts anticipatory and adapts his reactions to the dynamics of the particular vehicle. The modeling of human actions and reactions is a challenging task. That is why driving simulators operate with real drivers instead of driver models. However, offline simulations will require a suitable driver model.

Usually, driver models are based on simple mostly linear vehicle models where the motion of the vehicle is reduced to horizontal movements and the wheels on each axle are lumped together [33]. Standard driver models consist of two levels: anticipatory feed forward (open loop) and compensatory (closed loop) control Fig. 1.1.

## 1 Introduction

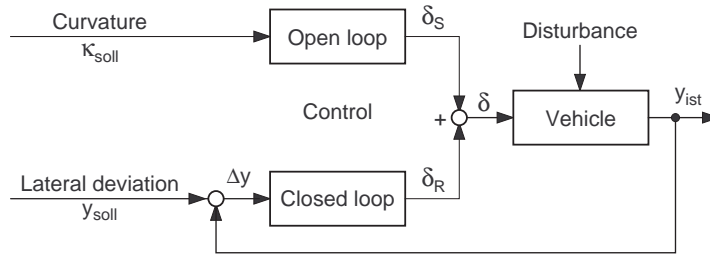


Figure 1.1: Two-level control driver model [16]

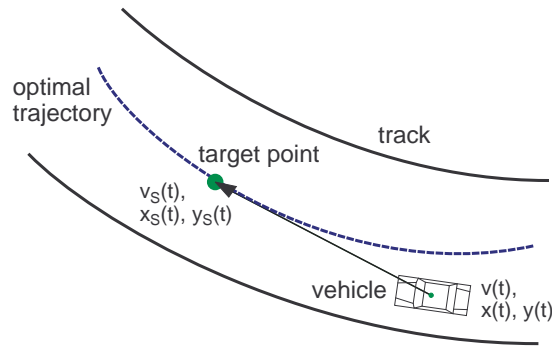


Figure 1.2: Enhanced driver model

The properties of the vehicle model and the capability of the driver are used to design appropriate transfer functions for the open and closed loop control. The model includes a path prediction and takes the reaction time of the driver into account.

Different from technical controllers, a human driver normally does not simply follow a given trajectory, but sets the target course within given constraints (i.e. road width or lane width), Fig. 1.2. On the anticipation level the optimal trajectory for the vehicle is predicted by repeatedly solving optimal control problems for a non-linear bicycle model whereas on the stabilization level a position control algorithm precisely guides the vehicle along the optimal trajectory [32]. The result is a virtual driver who is able to guide the virtual vehicle on a virtual road at high speeds as well as in limit situations where skidding and sliding effects take place. A broad variety of drivers spanning from unskilled to skilled or aggressive to non-aggressive can be described by this driver model [10].

### 1.3 Reference frames

A reference frame fixed to the vehicle and a ground-fixed reference frame are used to describe the overall motions of the vehicle, Figure 1.3.

### 1.3 Reference frames

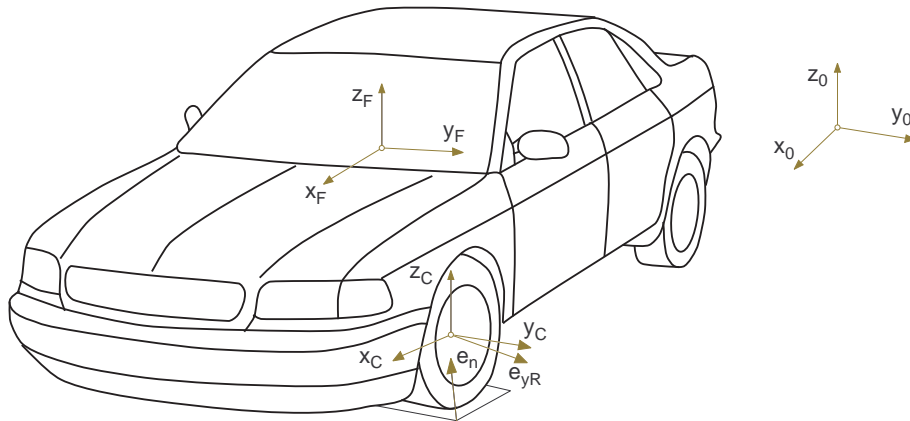


Figure 1.3: Frames used in vehicle dynamics

The ground-fixed reference frame with the axis  $x_0, y_0, z_0$  serves as an inertial reference frame. Within the vehicle-fixed reference frame the  $x_F$ -axis points forward, the  $y_F$ -axis to the left, and the  $z_F$ -axis upward. The wheel rotates around an axis which is fixed to the wheel carrier. The reference frame  $C$  is fixed to the wheel carrier. In design position its axes  $x_C, y_C$  and  $z_C$  are parallel to the corresponding axis of vehicle-fixed reference frame  $F$ . The momentary position of the wheel is fixed by the wheel center and the orientation of the wheel rim center plane which is defined by the unit vector  $e_{yR}$  into the direction of the wheel rotation axis. Finally, the normal vector  $e_n$  describes the inclination of the local track plane.

## 2 Road

### 2.1 Modeling Aspects

Sophisticated road models provide the road height  $z_R$  and the local friction coefficient  $\mu_L$  at each point  $x, y$ , Fig. 2.1.

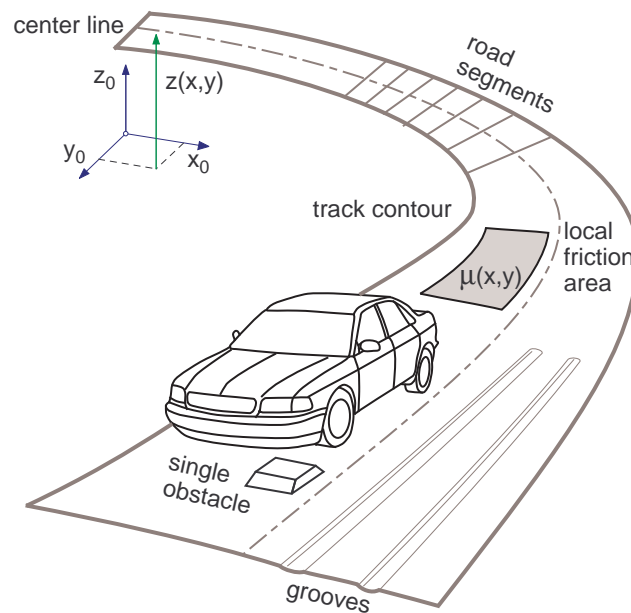


Figure 2.1: Sophisticated road model

The tire model is then responsible to calculate the local road inclination. By separating the horizontal course description from the vertical layout and the surface properties of the roadway almost arbitrary road layouts are possible, [3].

Besides single obstacles or track grooves the irregularities of a road are of stochastic nature. A vehicle driving over a random road profile mainly performs hub, pitch and roll motions. The local inclination of the road profile also induces longitudinal and lateral motions as well as yaw motions. On normal roads the latter motions have less influence on ride comfort and ride safety. To limit the effort of the stochastic description usually simpler road models are used.

If the vehicle drives along a given path its momentary position can be described by the path variable  $s = s(t)$ . Hence, a fully two-dimensional road model can be reduced to a parallel track model, Fig. 2.2.

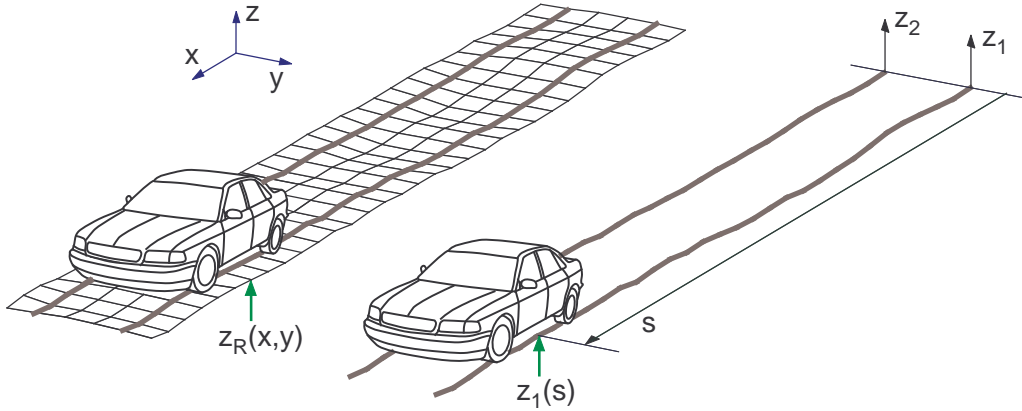


Figure 2.2: Parallel track road model

Now, the road heights on the left and right track are provided by two one-dimensional functions  $z_1 = z_1(s)$  and  $z_2 = z_2(s)$ . Within the parallel track model no information about the local lateral road inclination is available. If this information is not provided by additional functions the impact of a local lateral road inclination to vehicle motions is not taken into account.

For basic studies the irregularities at the left and the right track can be considered to be approximately the same,  $z_1(s) \approx z_2(s)$ . Then, a single track road model with  $z_R(s) = z_1(s) = z_2(s)$  can be used. Now, the roll excitation of the vehicle is neglected too.

## 2.2 Deterministic Profiles

### 2.2.1 Bumps and Potholes

Bumps and Potholes on the road are single obstacles of nearly arbitrary shape. Already with simple rectangular cleats the dynamic reaction of a vehicle or a single tire to a sudden impact can be investigated. If the shape of the obstacle is approximated by a smooth function, like a cosine wave, then, discontinuities will be avoided. Usually the obstacles are described in local reference frames, Fig. 2.3.

Then, the rectangular cleat is simply defined by

$$z(x, y) = \begin{cases} H & \text{if } 0 < x < L \text{ and } -\frac{1}{2}B < y < \frac{1}{2}B \\ 0 & \text{else} \end{cases} \quad (2.1)$$

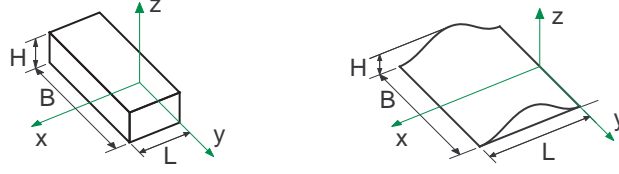


Figure 2.3: Rectangular cleat and cosine-shaped bump

and the cosine-shaped bump is given by

$$z(x, y) = \begin{cases} \frac{1}{2} H \left( 1 - \cos \left( 2\pi \frac{x}{L} \right) \right) & \text{if } 0 < x < L \text{ and } -\frac{1}{2}B < y < \frac{1}{2}B \\ 0 & \text{else} \end{cases} \quad (2.2)$$

where  $H$ ,  $B$  and  $L$  denote height, width and length of the obstacle. Potholes are obtained if negative values for the height ( $H < 0$ ) are used.

In a similar way track grooves can be modeled too, [34]. By appropriate coordinate transformations the obstacles can then be integrated into the global road description.

### 2.2.2 Sine Waves

Using the parallel track road model, a periodic excitation can be realized by

$$z_1(s) = A \sin(\Omega s), \quad z_2(s) = A \sin(\Omega s - \Psi), \quad (2.3)$$

where  $s$  is the path variable,  $A$  denotes the amplitude,  $\Omega$  the wave number, and the angle  $\Psi$  describes a phase lag between the left and the right track. The special cases  $\Psi = 0$  and  $\Psi = \pi$  represent the in-phase excitation with  $z_1 = z_2$  and the out of phase excitation with  $z_1 = -z_2$ .

If the vehicle runs with constant velocity  $ds/dt = v_0$ , the momentary position of the vehicle is given by  $s = v_0 t$ , where the initial position  $s = 0$  at  $t = 0$  was assumed. By introducing the wavelength

$$L = \frac{2\pi}{\Omega} \quad (2.4)$$

the term  $\Omega s$  can be written as

$$\Omega s = \frac{2\pi}{L} s = \frac{2\pi}{L} v_0 t = 2\pi \frac{v_0}{L} t = \omega t. \quad (2.5)$$

Hence, in the time domain the excitation frequency is given by  $f = \omega/(2\pi) = v_0/L$ .

For most of the vehicles the rigid body vibrations are in between  $0.5 Hz$  to  $15 Hz$ . This range is covered by waves which satisfy the conditions  $v_0/L \geq 0.5 Hz$  and  $v_0/L \leq 15 Hz$ .

For a given wavelength, lets say  $L = 4 m$ , the rigid body vibration of a vehicle are excited if the velocity of the vehicle will be varied from  $v_0^{min} = 0.5 Hz * 4 m = 2 m/s = 7.2 km/h$  to  $v_0^{max} = 15 Hz * 4 m = 60 m/s = 216 km/h$ . Hence, to achieve an excitation in the whole frequency range with moderate vehicle velocities profiles with different varying wavelengths are needed.

## 2.3 Random Profiles

### 2.3.1 Statistical Properties

Road profiles fit the category of stationary Gaussian random processes, [4]. Hence, the irregularities of a road can be described either by the profile itself  $z_R = z_R(s)$  or by its statistical properties, Fig. 2.4.

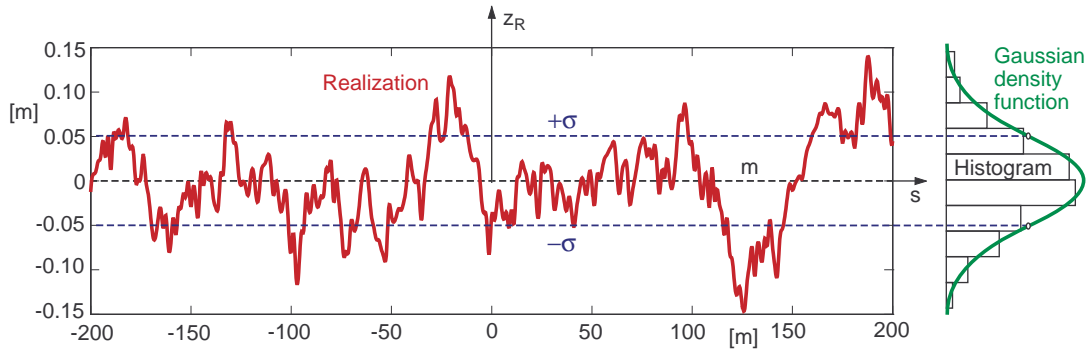


Figure 2.4: Road profile and statistical properties

By choosing an appropriate reference frame, a vanishing mean value

$$m = E \{z_R(s)\} = \lim_{X \rightarrow \infty} \frac{1}{X} \int_{-X/2}^{X/2} z_R(s) ds = 0 \quad (2.6)$$

can be achieved, where  $E \{ \}$  denotes the expectation operator. Then, the Gaussian density function which corresponds with the histogram is given by

$$p(z_R) = \frac{1}{\sigma \sqrt{2\pi}} e^{-\frac{z_R^2}{2\sigma^2}}, \quad (2.7)$$

where the deviation or the effective value  $\sigma$  is obtained from the variance of the process  $z_R = z_R(s)$

$$\sigma^2 = E \{z_R^2(s)\} = \lim_{X \rightarrow \infty} \frac{1}{X} \int_{-X/2}^{X/2} z_R(s)^2 ds. \quad (2.8)$$

## 2 Road

Alteration of  $\sigma$  effects the shape of the density function. In particular, the points of inflexion occur at  $\pm\sigma$ . The probability of a value  $|z| < \zeta$  is given by

$$P(\pm\zeta) = \frac{1}{\sigma\sqrt{2\pi}} \int_{-\zeta}^{+\zeta} e^{-\frac{z^2}{2\sigma^2}} dz. \quad (2.9)$$

In particular, one gets the values:  $P(\pm\sigma)=0.683$ ,  $P(\pm2\sigma)=0.955$ , and  $P(\pm3\sigma)=0.997$ . Hence, the probability of a value  $|z| \geq 3\sigma$  is 0.3%.

In extension to the variance of a random process the auto-correlation function is defined by

$$R(\xi) = E\{z_R(s)z_R(s+\xi)\} = \lim_{X \rightarrow \infty} \frac{1}{X} \int_{-X/2}^{X/2} z_R(s)z_R(s+\xi) ds. \quad (2.10)$$

The auto-correlation function is symmetric,  $R(\xi) = R(-\xi)$ , and it plays an important part in the stochastic analysis. In any normal random process, as  $\xi$  increases the link between  $z_R(s)$  and  $z_R(s+\xi)$  diminishes. For large values of  $\xi$  the two values are practically unrelated. Hence,  $R(\xi \rightarrow \infty)$  will tend to 0. In fact,  $R(\xi)$  is always less  $R(0)$ , which coincides with the variance  $\sigma^2$  of the process. If a periodic term is present in the process it will show up in  $R(\xi)$ .

Usually, road profiles are characterized in the frequency domain. Here, the auto-correlation function  $R(\xi)$  is replaced by the power spectral density (psd)  $S(\Omega)$ . In general,  $R(\xi)$  and  $S(\Omega)$  are related to each other by the Fourier transformation

$$S(\Omega) = \frac{1}{2\pi} \int_{-\infty}^{\infty} R(\xi) e^{-i\Omega\xi} d\xi \quad \text{and} \quad R(\xi) = \int_{-\infty}^{\infty} S(\Omega) e^{i\Omega\xi} d\Omega, \quad (2.11)$$

where  $i$  is the imaginary unit, and  $\Omega$  in  $rad/m$  denotes the wave number. To avoid negative wave numbers, usually a one-sided psd is defined. With

$$\Phi(\Omega) = 2S(\Omega), \quad \text{if } \Omega \geq 0 \quad \text{and} \quad \Phi(\Omega) = 0, \quad \text{if } \Omega < 0, \quad (2.12)$$

the relationship  $e^{\pm i\Omega\xi} = \cos(\Omega\xi) \pm i \sin(\Omega\xi)$ , and the symmetry property  $R(\xi) = R(-\xi)$  Eq. (2.11) results in

$$\Phi(\Omega) = \frac{2}{\pi} \int_0^{\infty} R(\xi) \cos(\Omega\xi) d\xi \quad \text{and} \quad R(\xi) = \int_0^{\infty} \Phi(\Omega) \cos(\Omega\xi) d\Omega. \quad (2.13)$$

Now, the variance is obtained from

$$\sigma^2 = R(\xi=0) = \int_0^{\infty} \Phi(\Omega) d\Omega. \quad (2.14)$$

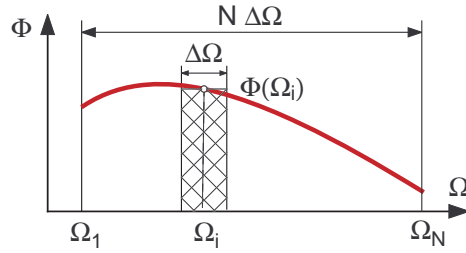


Figure 2.5: Power spectral density in a finite interval

In reality the psd  $\Phi(\Omega)$  will be given in a finite interval  $\Omega_1 \leq \Omega \leq \Omega_N$ , Fig. 2.5. Then, Eq. (2.14) can be approximated by a sum, which for  $N$  equal intervals will result in

$$\sigma^2 \approx \sum_{i=1}^N \Phi(\Omega_i) \Delta\Omega \quad \text{with} \quad \Delta\Omega = \frac{\Omega_N - \Omega_1}{N}. \quad (2.15)$$

### 2.3.2 Classification of Random Road Profiles

Road elevation profiles can be measured point by point or by high-speed profilometers. The power spectral densities of roads show a characteristic drop in magnitude with the wave number, Fig. 2.6a. This simply reflects the fact that the irregularities

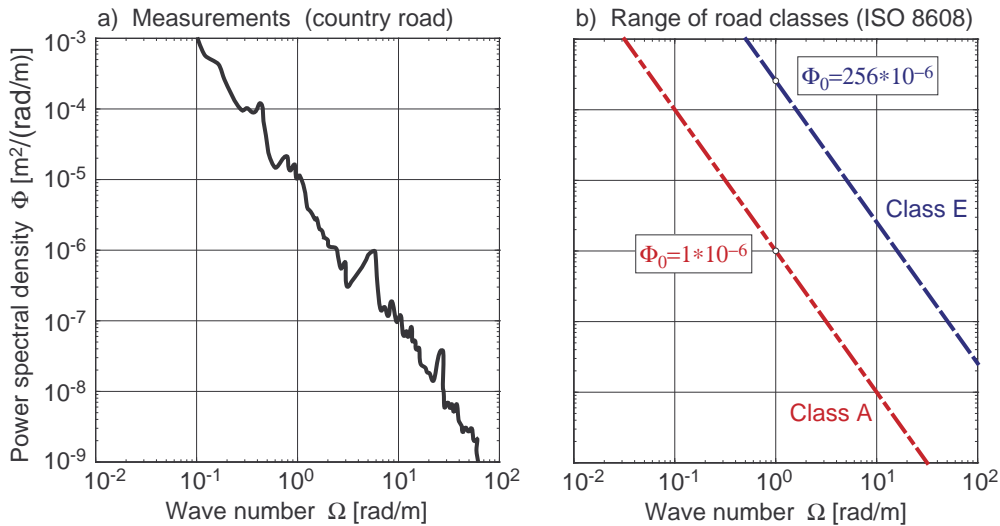


Figure 2.6: Road power spectral densities: a) Measurements [2], b) Classification

of the road may amount to several meters over the length of hundreds of meters, whereas those measured over the length of one meter are normally only some centimeter in amplitude.

## 2 Road

Random road profiles can be approximated by a psd in the form of

$$\Phi(\Omega) = \Phi(\Omega_0) \left( \frac{\Omega}{\Omega_0} \right)^{-w}, \quad (2.16)$$

where,  $\Omega = 2\pi/L$  in  $rad/m$  denotes the wave number and  $\Phi_0 = \Phi(\Omega_0)$  in  $m^2/(rad/m)$  describes the value of the psd at a the reference wave number  $\Omega_0 = 1 rad/m$ . The drop in magnitude is modeled by the waviness  $w$ .

According to the international directive ISO 8608, [11] typical road profiles can be grouped into classes from A to E. By setting the waviness to  $w = 2$  each class is simply defined by its reference value  $\Phi_0$ . Class A with  $\Phi_0 = 1 * 10^{-6} m^2/(rad/m)$  characterizes very smooth highways, whereas Class E with  $\Phi_0 = 256 * 10^{-6} m^2/(rad/m)$  represents rather rough roads, Fig. 2.6b.

### 2.3.3 Realizations

#### 2.3.3.1 Sinusoidal Approximation

A random profile of a single track can be approximated by a superposition of  $N \rightarrow \infty$  sine waves

$$z_R(s) = \sum_{i=1}^N A_i \sin(\Omega_i s - \Psi_i), \quad (2.17)$$

where each sine wave is determined by its amplitude  $A_i$  and its wave number  $\Omega_i$ . By different sets of uniformly distributed phase angles  $\Psi_i$ ,  $i = 1(1)N$  in the range between 0 and  $2\pi$  different profiles can be generated which are similar in the general appearance but different in details.

The variance of the sinusoidal representation is then given by

$$\sigma^2 = \lim_{X \rightarrow \infty} \frac{1}{X} \int_{-X/2}^{X/2} \left( \sum_{i=1}^N A_i \sin(\Omega_i s - \Psi_i) \right) \left( \sum_{j=1}^N A_j \sin(\Omega_j s - \Psi_j) \right) ds. \quad (2.18)$$

For  $i = j$  and for  $i \neq j$  different types of integrals are obtained. The ones for  $i = j$  can be solved immediately

$$J_{ii} = \int A_i^2 \sin^2(\Omega_i s - \Psi_i) ds = \frac{A_i^2}{2\Omega_i} \left[ \Omega_i s - \Psi_i - \frac{1}{2} \sin(2(\Omega_i s - \Psi_i)) \right]. \quad (2.19)$$

Using the trigonometric relationship

$$\sin x \sin y = \frac{1}{2} \cos(x-y) - \frac{1}{2} \cos(x+y) \quad (2.20)$$

the integrals for  $i \neq j$  can be solved too

$$\begin{aligned}
 J_{ij} &= \int A_i \sin(\Omega_i s - \Psi_i) A_j \sin(\Omega_j s - \Psi_j) ds \\
 &= \frac{1}{2} A_i A_j \int \cos(\Omega_{i-j} s - \Psi_{i-j}) ds - \frac{1}{2} A_i A_j \int \cos(\Omega_{i+j} s - \Psi_{i+j}) ds \quad (2.21) \\
 &= -\frac{1}{2} \frac{A_i A_j}{\Omega_{i-j}} \sin(\Omega_{i-j} s - \Psi_{i-j}) + \frac{1}{2} \frac{A_i A_j}{\Omega_{i+j}} \sin(\Omega_{i+j} s - \Psi_{i+j})
 \end{aligned}$$

where the abbreviations  $\Omega_{i\pm j} = \Omega_i \pm \Omega_j$  and  $\Psi_{i\pm j} = \Psi_i \pm \Psi_j$  were used. The sine and cosine terms in Eqs. (2.19) and (2.21) are limited to values of  $\pm 1$ . Hence, Eq. (2.18) simply results in

$$\sigma^2 = \underbrace{\lim_{X \rightarrow \infty} \frac{1}{X} \sum_{i=1}^N [J_{ii}]_{-X/2}^{X/2}}_{\sum_{i=1}^N \frac{A_i^2}{2\Omega_i} \Omega_i} + \underbrace{\lim_{X \rightarrow \infty} \frac{1}{X} \sum_{i,j=1}^N [J_{ij}]_{-X/2}^{X/2}}_0 = \frac{1}{2} \sum_{i=1}^N A_i^2. \quad (2.22)$$

On the other hand, the variance of a sinusoidal approximation to a random road profile is given by Eq. (2.15). So, a road profile  $z_R = z_R(s)$  described by Eq. (2.17) will have a given psd  $\Phi(\Omega)$  if the amplitudes are generated according to

$$A_i = \sqrt{2\Phi(\Omega_i)\Delta\Omega}, \quad i = 1(1)N, \quad (2.23)$$

and the wave numbers  $\Omega_i$  are chosen to lie at  $N$  equal intervals  $\Delta\Omega$ .

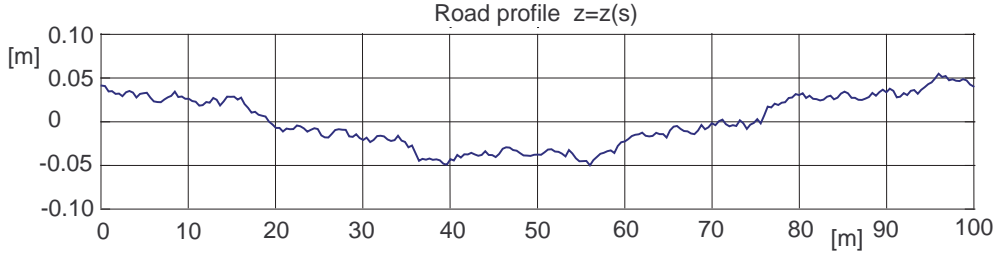


Figure 2.7: Realization of a country road

A realization of the country road with a psd of  $\Phi_0 = 10 * 10^{-6} m^2/(rad/m)$  is shown in Fig. 2.7. According to Eq. (2.17) the profile  $z = z(s)$  was generated by  $N = 200$  sine waves in the frequency range from  $\Omega_1 = 0.0628 rad/m$  to  $\Omega_N = 62.83 rad/m$ . The amplitudes  $A_i$ ,  $i = 1(1)N$  were calculated by Eq. (2.23) and the MATLAB<sup>®</sup> function rand was used to produce uniformly distributed random phase angles in the range between 0 and  $2\pi$ . More sophisticated approximations will divide the range of wave numbers in intervals where the bandwidth  $b_i = (\Omega_i + \Delta\Omega_i) / \Omega_i$  is kept constant.

### 2.3.3.2 Shaping Filter

The white noise process produced by random number generators has a uniform spectral density, and is therefore not suitable to describe real road profiles. But, if the white noise process is used as input to a shaping filter more appropriate spectral densities will be obtained, [21]. A simple first order shaping filter for the road profile  $z_R$  reads as

$$\frac{d}{ds} z_R(s) = -\gamma z_R(s) + w(s), \quad (2.24)$$

where  $\gamma$  is a constant, and  $w(s)$  is a white noise process with the spectral density  $\Phi_w$ . Then, the spectral density of the road profile is obtained from

$$\Phi_R = H(\Omega) \Phi_W H^T(-\Omega) = \frac{1}{\gamma + i\Omega} \Phi_W \frac{1}{\gamma - i\Omega} = \frac{\Phi_W}{\gamma^2 + \Omega^2}, \quad (2.25)$$

where  $\Omega$  is the wave number, and  $H(\Omega)$  is the frequency response function of the shaping filter.

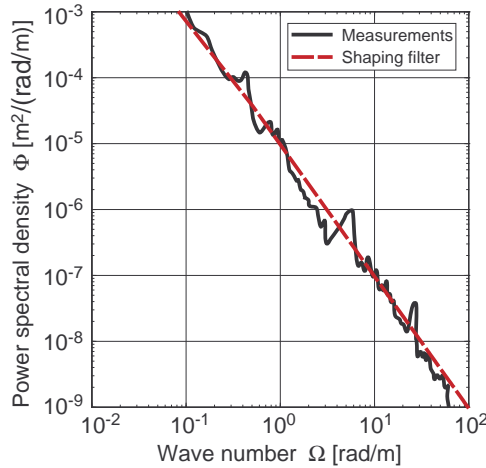


Figure 2.8: Shaping filter as approximation to measured psd

By setting  $\Phi_W = 10 * 10^{-6} m^2/(rad/m)$  and  $\gamma = 0.01 rad/m$  the measured psd of a typical country road can be approximated very well, Fig. 2.8.

The shape filter approach is also suitable for modeling parallel tracks, [23]. Here, the cross-correlation between the irregularities of the left and right track have to be taken into account too.

### 2.3.3.3 Two-Dimensional Model

The generation of fully two-dimensional road profiles  $z_R = z_R(x, y)$  via a sinusoidal approximation is very laborious. Because a shaping filter is a dynamic system,

### 2.3 Random Profiles

the resulting road profile realizations are not reproducible. By adding band-limited white noise processes and taking the momentary position  $x, y$  as seed for the random number generator a reproducible road profile can be generated, [24].

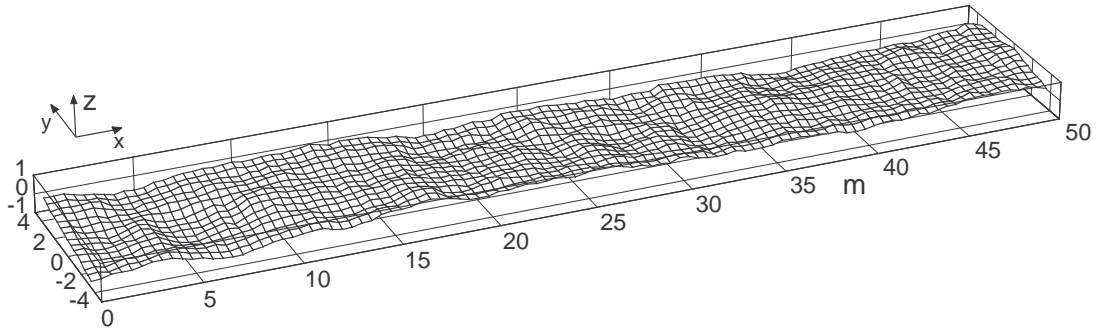


Figure 2.9: Two-dimensional road profile

By assuming the same statistical properties in longitudinal and lateral direction two-dimensional profiles, like the one in Fig. 2.9, can be obtained.

# 3 Tire

## 3.1 Introduction

### 3.1.1 Tire Development

Some important mile stones in the development of pneumatic tires are shown in Table 3.1.

Table 3.1: Milestones in tire development

1839	Charles Goodyear: vulcanization
1845	Robert William Thompson: first pneumatic tire (several thin inflated tubes inside a leather cover)
1888	John Boyd Dunlop: patent for bicycle (pneumatic) tires
1893	The Dunlop Pneumatic and Tyre Co. GmbH, Hanau, Germany
1895	André and Edouard Michelin: pneumatic tires for Peugeot Paris-Bordeaux-Paris (720 Miles): 50 tire deflations, 22 complete inner tube changes
1899	Continental: "long-lived" tires (approx. 500 Kilometer)
1904	Carbon added: black tires.
1908	Frank Seiberling: grooved tires with improved road traction
1922	Dunlop: steel cord thread in the tire bead
1942	Synthetic rubber becomes extremely important during WWII
1943	Continental: patent for tubeless tires
1946	Radial Tire
1952	High quality nylon tire
	⋮

Of course the tire development did not stop in 1952, but modern tires are still based on this achievements. Today, run-flat tires are under investigation. A run-flat tire enables the vehicle to continue to be driven at reduced speeds (i.e. 80 km/h or 50 mph) and for limited distances (80 km or 50 mi). The introduction of run-flat tires makes it mandatory for car manufacturers to fit a system where the drivers are made aware the run-flat has been damaged.

### 3.1.2 Tire Composites

Tires are very complex. They combine dozens of components that must be formed, assembled and cured together. And their ultimate success depends on their ability to blend all of the separate components into a cohesive product that satisfies the driver's needs. A modern tire is a mixture of steel, fabric, and rubber. The main composites of a passenger car tire with an overall mass of  $8.5 \text{ kg}$  are listed in Table 3.2.

Table 3.2: Tire composites: 195/65 R 15 ContiEcoContact, data from [www.felge.de](http://www.felge.de)

Reinforcements: steel, rayon, nylon	16%
Rubber: natural/synthetic	38%
Compounds: carbon, silica, chalk, ...	30%
Softener: oil, resin	10%
Vulcanization: sulfur, zinc oxide, ...	4%
Miscellaneous	2%

### 3.1.3 Tire Forces and Torques

In any point of contact between the tire and the road surface normal and friction forces are transmitted. According to the tire's profile design the contact patch forms a not necessarily coherent area, Fig. 3.1.

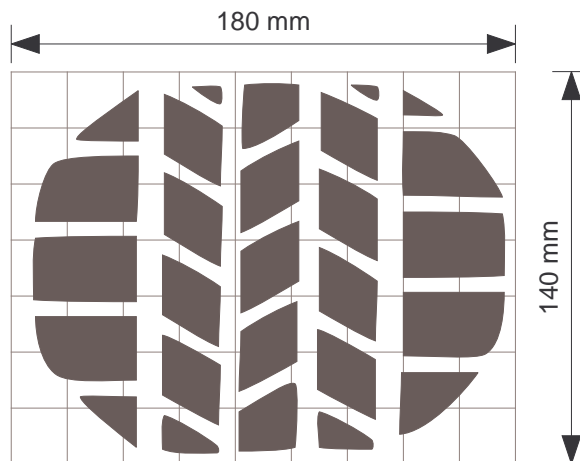


Figure 3.1: Footprint of a test tire of size 205/55 R16 at  $F_z = 4700 \text{ N}$  and  $p = 2.5 \text{ bar}$

The effect of the contact forces can be fully described by a resulting force vector applied at a specific point of the contact patch and a torque vector. The vectors are

### 3 Tire

described in a track-fixed reference frame. The  $z$ -axis is normal to the track, the  $x$ -axis is perpendicular to the  $z$ -axis and perpendicular to the wheel rotation axis  $e_{yR}$ . Then, the demand for a right-handed reference frame also fixes the  $y$ -axis.

$F_x$	longitudinal force
$F_y$	lateral force
$F_z$	vertical force or wheel load
$T_x$	tilting torque
$T_y$	rolling resistance torque
$T_z$	self aligning and bore torque

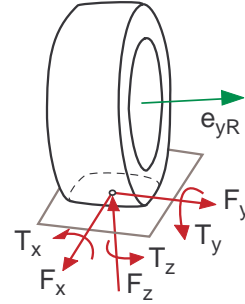


Figure 3.2: Contact forces and torques

The components of the contact force vector are named according to the direction of the axes, Fig. 3.2. A non symmetric distribution of the forces in the contact patch causes torques around the  $x$  and  $y$  axes. A cambered tire generates a tilting torque  $T_x$ . The torque  $T_y$  includes the rolling resistance of the tire. In particular, the torque around the  $z$ -axis is important in vehicle dynamics. It consists of two parts,

$$T_z = T_B + T_S . \quad (3.1)$$

The rotation of the tire around the  $z$ -axis causes the bore torque  $T_B$ . The self aligning torque  $T_S$  takes into account that, in general, the resulting lateral force is not acting in the center of the contact patch.

#### 3.1.4 Measuring Tire Forces and Torques

To measure tire forces and torques on the road a special test trailer is needed, Fig. 3.4. Here, the measurements are performed under real operating conditions. Arbitrary surfaces like asphalt or concrete and different environmental conditions like dry, wet or icy are possible. Measurements with test trailers are quite cumbersome and in general they are restricted to passenger car tires.

Indoor measurements of tire forces and torques can be performed on drums or on a flat bed, Fig. 3.4.

On drum test rigs the tire is placed either inside or outside of the drum. In both cases the shape of the contact area between tire and drum is not correct. That is why, one can not rely on the measured self aligning torque. Due its simple and robust design, wide applications including measurements of truck tires are possible.

The flat bed tire test rig is more sophisticated. Here, the contact patch is as flat as on the road. But, the safety walk coating which is attached to the steel bed does not generate the same friction conditions as on a real road surface.

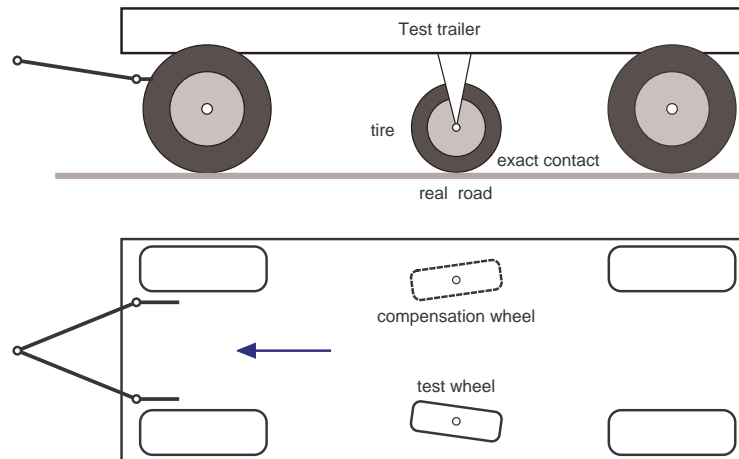


Figure 3.3: Layout of a tire test trailer

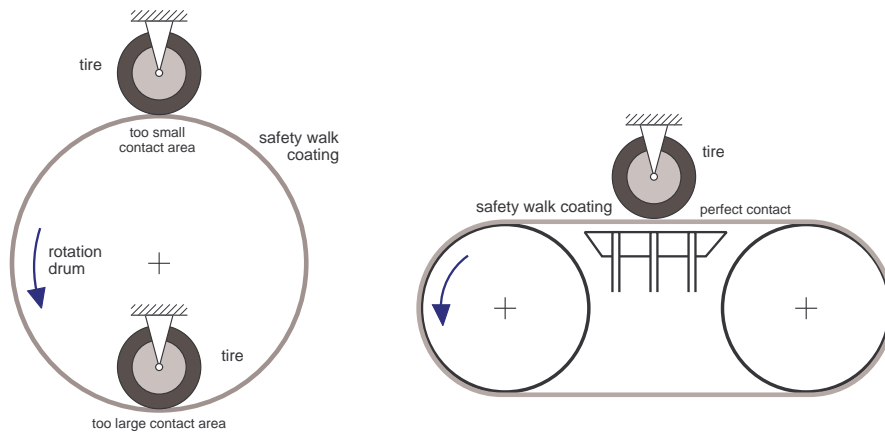


Figure 3.4: Drum and flat bed tire test rig

Tire forces and torques are measured in quasi-static operating conditions. Hence, the measurements for increasing and decreasing the sliding conditions usually result in different graphs, Fig. 3.5. In general, the mean values are taken as steady state results.

### 3.1.5 Modeling Aspects

For the dynamic simulation of on-road vehicles, the model-element “tire/road” is of special importance, according to its influence on the achievable results. It can be said that the sufficient description of the interactions between tire and road is one of the most important tasks of vehicle modeling, because all the other components of the chassis influence the vehicle dynamic properties via the tire contact forces

### 3 Tire

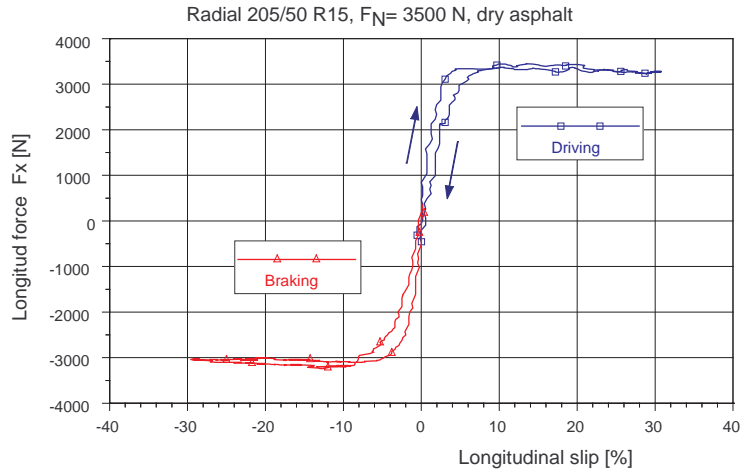


Figure 3.5: Typical results of tire measurements

and torques. Therefore, in the interest of balanced modeling, the precision of the complete vehicle model should stand in reasonable relation to the performance of the applied tire model. At present, two groups of models can be identified, handling models and structural or high frequency models, [15].

Structural tire models are very complex. Within RMOD-K [19] the tire is modeled by four circular rings with mass points that are also coupled in lateral direction. Multi-track contact and the pressure distribution across the belt width are taken into account. The tire model FTire [7] consists of an extensible and flexible ring which is mounted to the rim by distributed stiffnesses in radial, tangential and lateral direction. The ring is approximated by a finite number of belt elements to which a number of mass-less tread blocks are assigned, Fig. 3.6.

Complex tire models are computer time consuming and they need a lot a data. Usually, they are used for stochastic vehicle vibrations occurring during rough road rides and causing strength-relevant component loads, [22].

Comparatively lean tire models are suitable for vehicle dynamics simulations, while, with the exception of some elastic partial structures such as twist-beam axles in cars or the vehicle frame in trucks, the elements of the vehicle structure can be seen as rigid. On the tire's side, "semi-physical" tire models prevail, where the description of forces and torques relies, in contrast to purely physical tire models, also on measured and observed force-slip characteristics. This class of tire models is characterized by an useful compromise between user-friendliness, model-complexity and efficiency in computation time on the one hand, and precision in representation on the other hand.

In vehicle dynamic practice often there exists the problem of data provision for a special type of tire for the examined vehicle. Considerable amounts of experimental

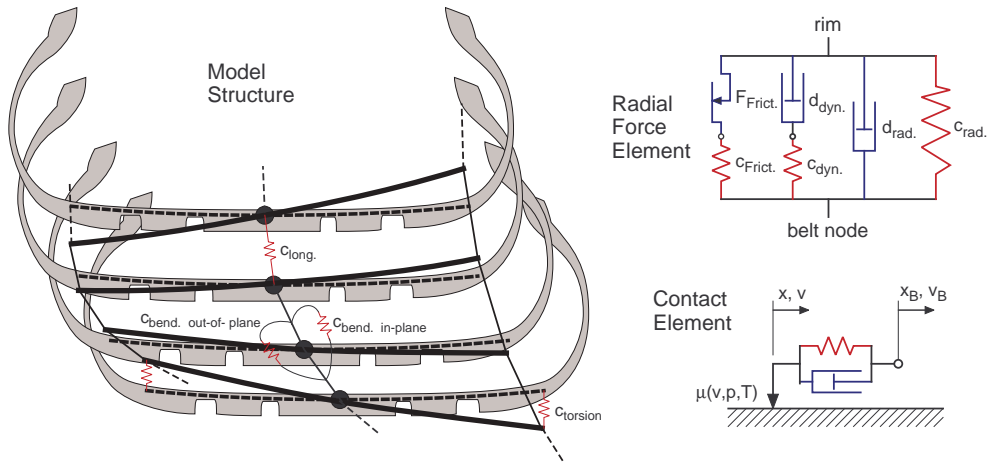


Figure 3.6: Complex tire model (FTire)

data for car tires has been published or can be obtained from the tire manufacturers. If one cannot find data for a special tire, its characteristics can be guessed at least by an engineer's interpolation of similar tire types, Fig. 3.7. In the field of truck tires there is still a considerable backlog in data provision. These circumstances must be respected in conceiving a user-friendly tire model.

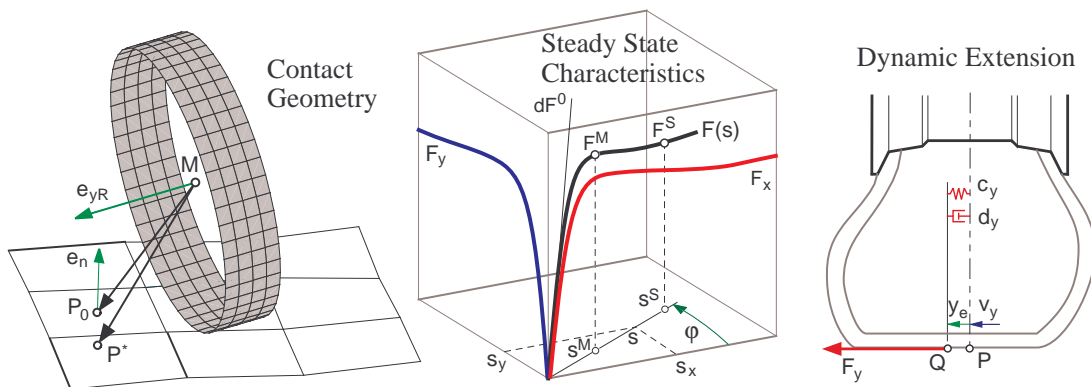


Figure 3.7: Handling tire model: TMeasy [8]

For a special type of tire, usually the following sets of experimental data are provided:

- longitudinal force versus longitudinal slip (mostly just brake-force),
- lateral force versus slip angle,
- aligning torque versus slip angle,

### 3 Tire

- radial and axial compliance characteristics,

whereas additional measurement data under camber and low road adhesion are favorable special cases.

Any other correlations, especially the combined forces and torques, effective under operating conditions, often have to be generated by appropriate assumptions with the model itself, due to the lack of appropriate measurements. Another problem is the evaluation of measurement data from different sources (i.e. measuring techniques) for a special tire, [9]. It is a known fact that different measuring techniques result in widely spread results. Here the experience of the user is needed to assemble a “probably best” set of data as a basis for the tire model from these sets of data, and to verify it eventually with own experimental results.

#### 3.1.6 Typical Tire Characteristics

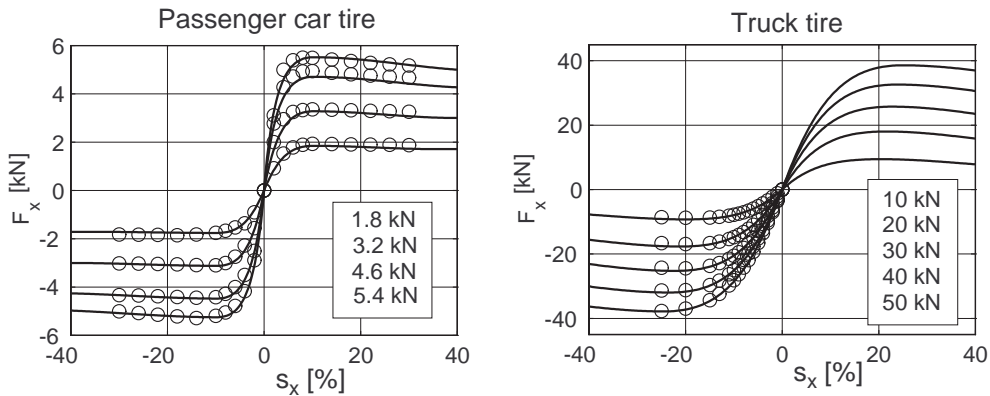


Figure 3.8: Longitudinal force:  $\circ$  Meas.,  $-$  TMeasy

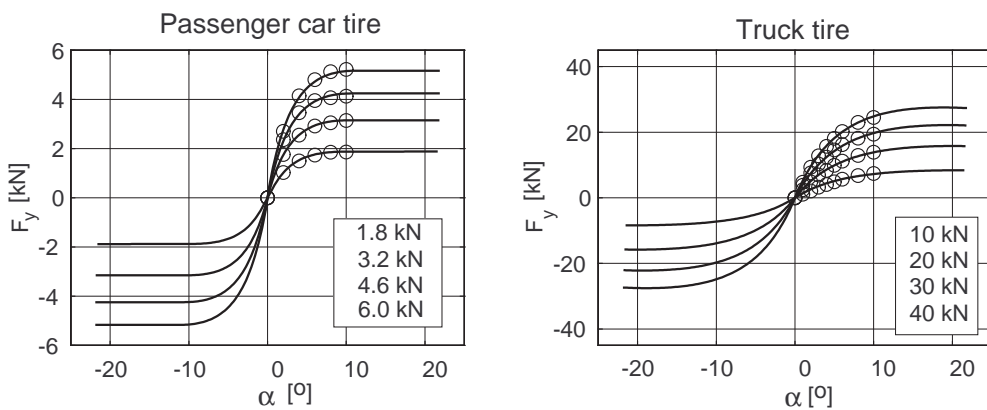


Figure 3.9: Lateral force:  $\circ$  Meas.,  $-$  TMeasy

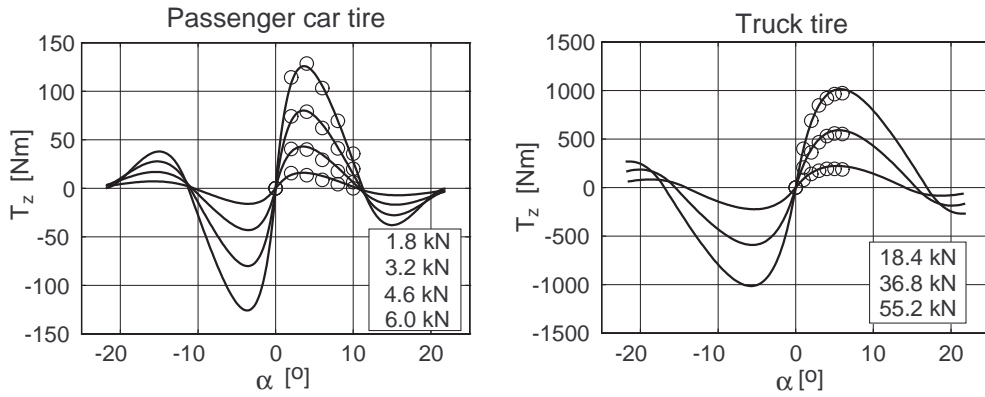


Figure 3.10: Self-aligning torque:  $\circ$  Meas.,  $-$  TMeasy

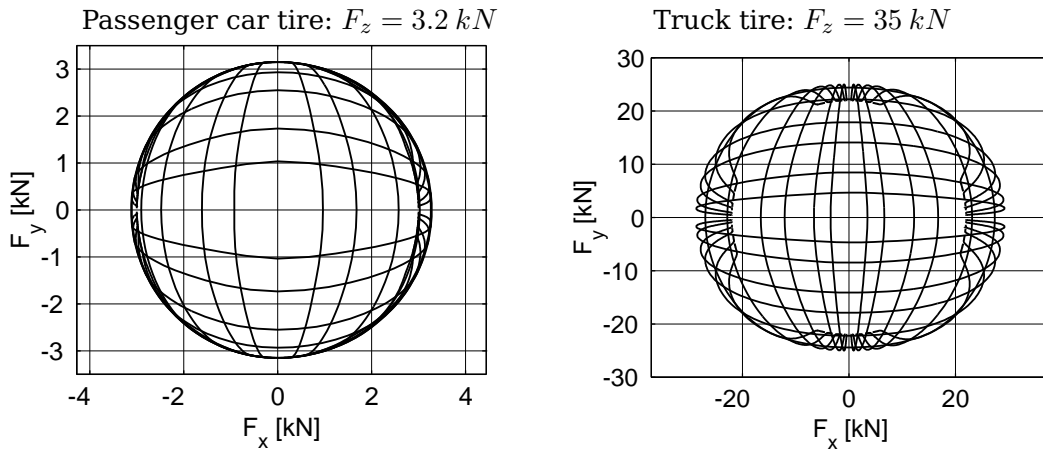


Figure 3.11: Two-dimensional characteristics:  $|s_x| = 1, 2, 4, 6, 10, 15\%$ ;  $|\alpha| = 1, 2, 4, 6, 10, 14^\circ$

Standard measurements provide the longitudinal force  $F_x$  as a function from the longitudinal slip  $s_x$  and the lateral force  $F_y$  and the self-aligning torque  $M_z$  as a function of the slip angle  $\alpha$  for different wheel loads  $F_z$ . Although similar in general the characteristics of a typical passenger car tire and a typical truck tire differ quite a lot in some details, Figs. 3.8 and 3.10. Usually, truck tires are designed for durability and not for generating large lateral forces. The characteristic curves  $F_x = F_x(s_x)$ ,  $F_y = F_y(\alpha)$  and  $M_z = M_z(\alpha)$  for the passenger car and truck tire can be approximated quite well by the tire handling model TMeasy [8]. Within the TMeasy model approach one-dimensional characteristics are automatically converted to two-dimensional combined-slip characteristics, Fig. 3.11.

## 3.2 Contact Geometry

### 3.2.1 Basic Approach

The current position of a wheel in relation to the fixed  $x_0$ -  $y_0$ -  $z_0$ -system is given by the wheel center  $M$  and the unit vector  $e_{yR}$  in the direction of the wheel rotation axis, Fig. 3.12. The irregularities of the track can be described by an arbitrary

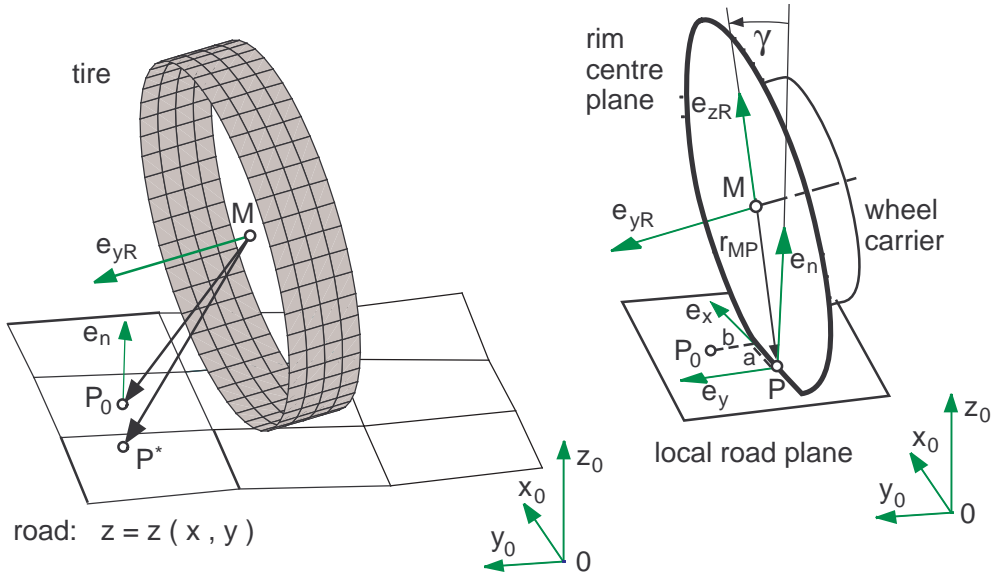


Figure 3.12: Contact geometry

function of two spatial coordinates

$$z = z(x, y). \quad (3.2)$$

At an uneven track the contact point  $P$  can not be calculated directly. At first, one can get an estimated value with the vector

$$r_{MP^*} = -r_0 e_{zB}, \quad (3.3)$$

where  $r_0$  is the undeformed tire radius, and  $e_{zB}$  is the unit vector in the  $z$ -direction of the body fixed reference frame.

The position of this first guess  $P^*$  with respect to the earth fixed reference frame  $x_0, y_0, z_0$  is determined by

$$r_{0P^*,0} = r_{0M,0} + r_{MP^*,0} = \begin{bmatrix} x^* \\ y^* \\ z^* \end{bmatrix}, \quad (3.4)$$

where the vector  $r_{0M}$  describes the position of the rim center  $M$ . Usually, the point  $P^*$  does not lie on the track. The corresponding track point  $P_0$  follows from

$$r_{0P_0,0} = \begin{bmatrix} x^* \\ y^* \\ z(x^*, y^*) \end{bmatrix}, \quad (3.5)$$

where Eq. (3.2) was used to calculate the appropriate road height. In the point  $P_0$  the track normal  $e_n$  is calculated, now. Then the unit vectors in the tire's circumferential direction and lateral direction can be determined. One gets

$$e_x = \frac{e_{yR} \times e_n}{|e_{yR} \times e_n|} \quad \text{and} \quad e_y = e_n \times e_x, \quad (3.6)$$

where  $e_{yR}$  denotes the unit vector into the direction of the wheel rotation axis. Calculating  $e_x$  demands a normalization, as  $e_{yR}$  not always being perpendicular to the track. The tire camber angle

$$\gamma = \arcsin(e_{yR}^T e_n) \quad (3.7)$$

describes the inclination of the wheel rotation axis against the track normal.

The vector from the rim center  $M$  to the track point  $P_0$  is split into three parts now

$$r_{MP_0} = -r_S e_{zR} + a e_x + b e_y, \quad (3.8)$$

where  $r_S$  denotes the loaded or static tire radius,  $a$ ,  $b$  are distances measured in circumferential and lateral direction, and the radial direction is given by the unit vector

$$e_{zR} = e_x \times e_{yR} \quad (3.9)$$

which is perpendicular to  $e_x$  and  $e_{yR}$ . A scalar multiplication of Eq. (3.8) with  $e_n$  results in

$$e_n^T r_{MP_0} = -r_S e_n^T e_{zR} + a e_n^T e_x + b e_n^T e_y. \quad (3.10)$$

As the unit vectors  $e_x$  and  $e_y$  are perpendicular to  $e_n$  Eq. (3.10) simplifies to

$$e_n^T r_{MP_0} = -r_S e_n^T e_{zR}. \quad (3.11)$$

Hence, the static tire radius is given by

$$r_S = -\frac{e_n^T r_{MP_0}}{e_n^T e_{zR}}. \quad (3.12)$$

The contact point  $P$  given by the vector

$$r_{MP} = -r_S e_{zR} \quad (3.13)$$

### 3 Tire

lies within the rim center plane. The transition from the point  $P_0$  to the contact point  $P$  takes place according to Eq. (3.8) by the terms  $a e_x$  and  $b e_y$  perpendicular to the track normal  $e_n$ . The track normal, however, was calculated in the point  $P_0$ . With an uneven track the point  $P$  no longer lies on the track and can therefore no longer be considered as contact point.

With the newly estimated value  $P^* = P$  now the Eqs. (3.5) to (3.13) can be repeated until the difference between  $P$  and  $P_0$  is sufficiently small.

Tire models which can be simulated within acceptable time assume that the contact patch is sufficiently flat. At an ordinary passenger car tire, the contact patch has approximately the size of  $15 \times 20 \text{ cm}$  at normal load. So, it makes no sense to calculate a fictitious contact point to fractions of millimeters, when later on the real track will be approximated by a plane in the range of centimeters. If the track in the contact patch is replaced by a local plane, no further iterative improvements will be necessary for the contact point calculation.

#### 3.2.2 Local Track Plane

Any three points which by chance do not coincide or form a straight line will define a plane. In order to get a good approximation to the local track inclination in longitudinal and lateral direction four points will be used to determine the local track normal. Using the initial guess in Eq. (3.3) and the unit vector  $e_{yr}$  pointing into the direction of the wheel rotation axis the longitudinal or circumferential direction can be estimated by the unit vector

$$e_x^* = \frac{e_{yR} \times e_{zB}}{|e_{yR} \times e_{zB}|}. \quad (3.14)$$

Now, points can be placed on the track in the front, in the rear, to the left, and to the right of the wheel center

$$\begin{aligned} r_{MQ_1^*} &= \Delta x e_{x^*} && - r_0 e_{zB} \quad , \\ r_{MQ_2^*} &= -\Delta x e_{x^*} && - r_0 e_{zB} \quad , \\ r_{MQ_3^*} &= && \Delta y e_{yR} - r_0 e_{zB} \quad , \\ r_{MQ_4^*} &= && -\Delta y e_{yR} - r_0 e_{zB} \end{aligned} \quad (3.15)$$

In order to sample the contact patch as good as possible the distances  $\Delta x$  and  $\Delta y$  will be adjusted to the unloaded tire radius  $r_0$  and to the tire width  $b$ . By setting  $\Delta x = 0.1 r_0$  and  $\Delta y = 0.3 b$  a realistic behavior even on track grooves could be achieved, [34].

Similar to Eq. (3.5) the corresponding points on the road can be found from

$$r_{0Q_{i,0}} = \begin{bmatrix} x_i^* \\ y_i^* \\ z(x_i^*, y_i^*) \end{bmatrix}, \quad i = 1(1)4, \quad (3.16)$$

### 3.2 Contact Geometry

where  $x_i^*$  and  $y_i^*$  are the  $x$ - and  $y$ -components of the vectors

$$r_{0Q_i^*,0} = r_{0M,0} + r_{MQ_i^*,0} = \begin{bmatrix} x_i^* \\ y_i^* \\ z_i^* \end{bmatrix}, \quad i = 1(1)4. \quad (3.17)$$

The lines fixed by the points  $Q_1$  and  $Q_2$  or  $Q_3$  and  $Q_4$  respectively define the inclination of the local track plane in longitudinal and lateral direction, Fig. 3.13.

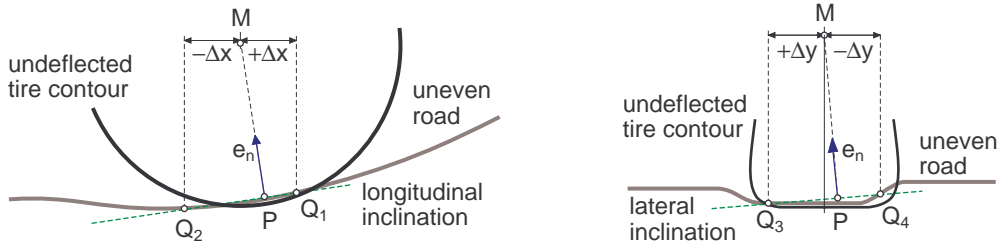


Figure 3.13: Inclination of local track plane in longitudinal and lateral direction

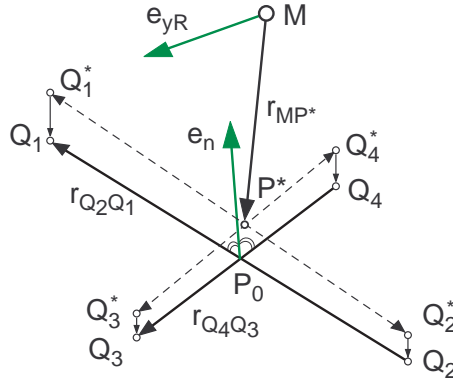


Figure 3.14: Local track normal

Hence, the vectors  $r_{Q_2Q_1} = r_{0Q_1} - r_{0Q_2}$  and  $r_{Q_4Q_3} = r_{0Q_3} - r_{0Q_4}$  can be used to calculate the local track normal, Fig. 3.14. One gets

$$e_n = \frac{r_{Q_2Q_1} \times r_{Q_4Q_3}}{|r_{Q_2Q_1} \times r_{Q_4Q_3}|}. \quad (3.18)$$

The unit vectors  $e_x$ ,  $e_y$  in longitudinal and lateral direction are calculated from Eq. (3.6). The mean value of the track points

$$r_{0P_0,0} = \frac{1}{4} (r_{0Q_1,0} + r_{0Q_2,0} + r_{0Q_3,0} + r_{0Q_4,0}) \quad (3.19)$$

### 3 Tire

serves as first improvement of the contact point,  $P^* \rightarrow P_0$ . Finally, the corresponding point  $P$  in the rim center plane is obtained by Eqs. (3.12) and (3.13).

On rough roads the point  $P$  not always is located on the track. But, together with the local track normal it represents the local track unevenness very well. As in reality, sharp bends and discontinuities, which will occur at step- or ramp-sized obstacles, are smoothed by this approach.

#### 3.2.3 Tire Deflection

For a vanishing camber angle  $\gamma = 0$  the deflected zone has a rectangular shape, Fig. 3.15. Its area is given by

$$A_0 = \Delta z b, \quad (3.20)$$

where  $b$  is the width of the tire, and the tire deflection is obtained by

$$\Delta z = r_0 - r_s. \quad (3.21)$$

Here, the width of the tire simply equals the width of the contact patch,  $w_C = b$ .

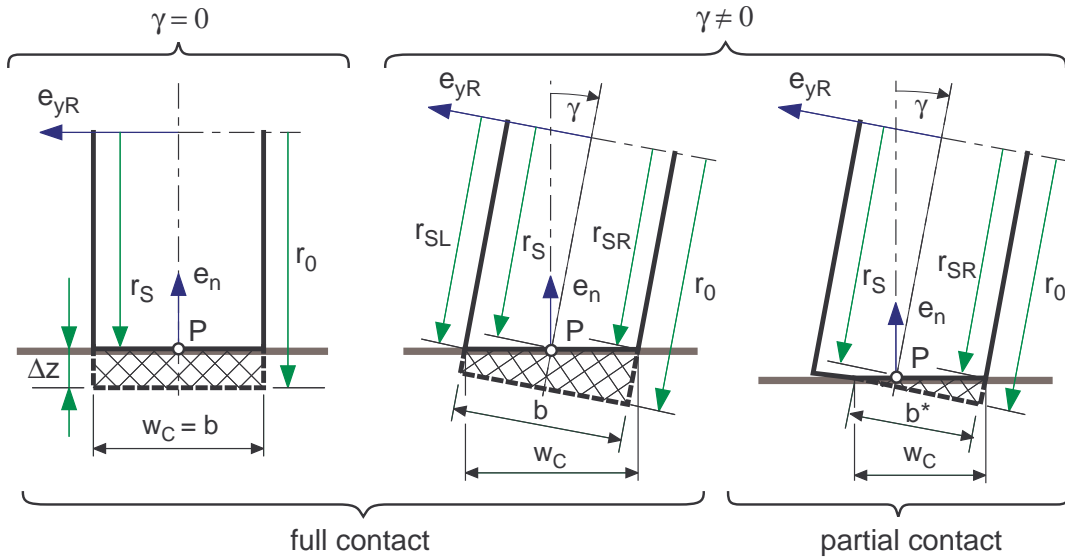


Figure 3.15: Tire deflection

On a cambered tire the deflected zone of the tire cross section depends on the contact situation. The magnitude of the tire flank radii

$$r_{SL} = r_s + \frac{b}{2} \tan \gamma \quad \text{and} \quad r_{SR} = r_s - \frac{b}{2} \tan \gamma \quad (3.22)$$

determines the shape of the deflected zone.

### 3.2 Contact Geometry

The tire will be in full contact to the road if  $r_{SL} \leq r_0$  and  $r_{SR} \leq r_0$  hold. Then, the deflected zone has a trapezoidal shape with an area of

$$A_\gamma = \frac{1}{2}(r_0 - r_{SR} + r_0 - r_{SL}) b = (r_0 - r_S) b. \quad (3.23)$$

Equalizing the cross sections  $A_0 = A_\gamma$  results in

$$\Delta z = r_0 - r_S. \quad (3.24)$$

Hence, at full contact the tire camber angle  $\gamma$  has no influence on the vertical tire force. But, due to

$$w_C = \frac{b}{\cos \gamma} \quad (3.25)$$

the width of the contact patch increases with the tire camber angle.

The deflected zone will change to a triangular shape if one of the flank radii exceeds the undeflected tire radius. Assuming  $r_{SL} > r_0$  and  $r_{SR} < r_0$  the area of the deflected zone is obtained by

$$A_\gamma = \frac{1}{2}(r_0 - r_{SR}) b^*, \quad (3.26)$$

where the width of the deflected zone follows from

$$b^* = \frac{r_0 - r_{SR}}{\tan \gamma}. \quad (3.27)$$

Now, Eq. (3.26) reads as

$$A_\gamma = \frac{1}{2} \frac{(r_0 - r_{SR})^2}{\tan \gamma}. \quad (3.28)$$

Equalizing the cross sections  $A_0 = A_\gamma$  results in

$$\Delta z = \frac{1}{2} \frac{(r_0 - r_S + \frac{b}{2} \tan \gamma)^2}{b \tan \gamma}. \quad (3.29)$$

where Eq. (3.22) was used to express the flank radius  $r_{SR}$  by the static tire radius  $r_S$ , the tire width  $b$  and the camber angle  $\gamma$ . Now, the width of the contact patch is given by

$$w_C = \frac{b^*}{\cos \gamma} = \frac{r_0 - r_{SR}}{\tan \gamma \cos \gamma} = \frac{r_0 - r_S + \frac{b}{2} \tan \gamma}{\sin \gamma}, \quad (3.30)$$

where the Eqs. (3.27) and (3.22) were used to simplify the expression. If  $\tan \gamma$  and  $\sin \gamma$  are replaced by  $|\tan \gamma|$  and  $|\sin \gamma|$  then, the Eqs. (3.29) and (3.30) will hold for positive and negative camber angles.

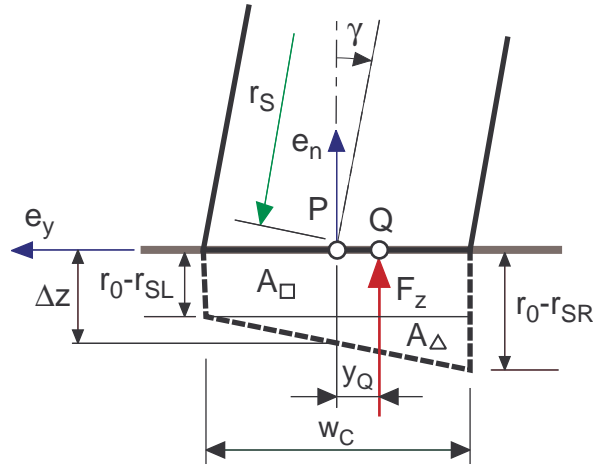


Figure 3.16: Lateral deviation of contact point at full contact

### 3.2.4 Static Contact Point

Assuming that the pressure distribution on a cambered tire with full road contact corresponds with the trapezoidal shape of the deflected tire area, the acting point of the resulting vertical tire force  $F_z$  will be shifted from the geometric contact point  $P$  to the static contact point  $Q$ , Fig. 3.16.

The center of the trapezoidal area determines the lateral deviation  $y_Q$ . By splitting the area into a rectangular and a triangular section we will obtain

$$y_Q = - \frac{y_{\square} A_{\square} + y_{\Delta} A_{\Delta}}{A} . \quad (3.31)$$

The minus sign takes into account that for positive camber angles the acting point will move to the right whereas the unit vector  $e_y$  defining the lateral direction points to the left. The area of the whole cross section results from

$$A = \frac{1}{2} (r_0 - r_{SL} + r_0 - r_{SR}) w_C , \quad (3.32)$$

where the width of the contact patch  $w_C$  is given by Eq. (3.25). Using the Eqs. (3.22) and (3.24) the expression can be simplified to

$$A = \Delta z w_C . \quad (3.33)$$

As the center of the rectangular section is located on the center line which runs through the geometric contact point,  $y_{\square} = 0$  will hold. The distance from the center of the triangular section to the center line is given by

$$y_{\Delta} = \frac{1}{2} w_C - \frac{1}{3} w_C = \frac{1}{6} w_C . \quad (3.34)$$

Finally, the area of the triangular section is defined by

$$A_{\Delta} = \frac{1}{2} (r_0 - r_{SR} - (r_0 - r_{SL})) w_C = \frac{1}{2} (r_{SL} - r_{SR}) w_C = \frac{1}{2} (b \tan \gamma) w_C, \quad (3.35)$$

where Eq. (3.22) was used to simplify the expression. Now, Eq. (3.31) can be written as

$$y_Q = -\frac{\frac{1}{6} w_C \frac{1}{2} b \tan \gamma w_C}{\Delta z w_C} = -\frac{b \tan \gamma}{12 \Delta z} w_C = -\frac{b^2}{12 \Delta z} \frac{\tan \gamma}{\cos \gamma}. \quad (3.36)$$

If the cambered tire has only a partial contact to the road then, according to the deflection area a triangular pressure distribution will be assumed, Fig. 3.17.

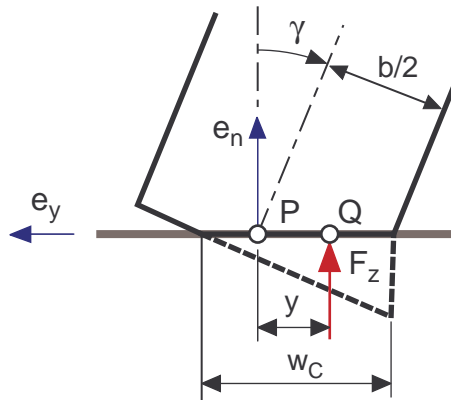


Figure 3.17: Lateral deviation of contact point at partial contact

Now, the location of the static contact point  $Q$  is given by

$$y_Q = \pm \left( \frac{1}{3} w_C - \frac{b}{2 \cos \gamma} \right), \quad (3.37)$$

where the width of the contact patch  $w_C$  is determined by Eq. (3.30) and the term  $b/(2 \cos \gamma)$  describes the distance from the geometric contact point  $P$  to the outer corner of the contact patch. The plus sign holds for positive and the minus sign for negative camber angles.

The static contact point  $Q$  described by the vector

$$r_{0Q} = r_{0P} + y_Q e_y \quad (3.38)$$

represents the contact patch much better than the geometric contact point  $P$ .

### 3.2.5 Length of Contact Patch

To approximate the length of the contact patch the tire deformation is split into two parts, Fig. 3.18. By  $\Delta z_F$  and  $\Delta z_B$  the average tire flank and the belt deformation

### 3 Tire

are measured. Hence, for a tire with full contact to the road

$$\Delta z = \Delta z_F + \Delta z_B = r_0 - r_S \quad (3.39)$$

will hold.

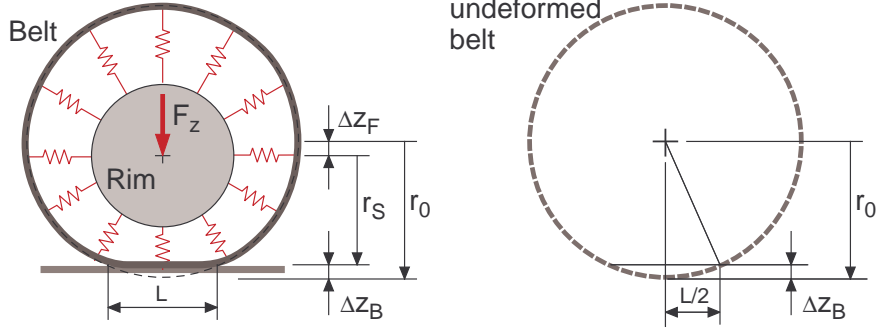


Figure 3.18: Length of contact patch

Assuming both deflections being approximately equal will lead to

$$\Delta z_F \approx \Delta z_B \approx \frac{1}{2} \Delta z. \quad (3.40)$$

Approximating the belt deflection by truncating a circle with the radius of the undeformed tire results in

$$\left(\frac{L}{2}\right)^2 + (r_0 - \Delta z_B)^2 = r_0^2. \quad (3.41)$$

In normal driving situations the belt deflections are small,  $\Delta z_B \ll r_0$ . Hence, Eq. (3.41) can be simplified and will result in

$$\frac{L^2}{4} = 2r_0 \Delta z_B \quad \text{or} \quad L = \sqrt{8r_0 \Delta z_B} = \sqrt{8r_0 \frac{1}{2} \Delta z} = 2\sqrt{r_0 \Delta z}, \quad (3.42)$$

where Eq. (3.40) was used to approximate the belt deflection  $\Delta z_B$  by the overall tire deformation  $\Delta z$ .

Inspecting the passenger car tire footprint in Fig. 3.1 leads to a contact patch length of  $L \approx 140 \text{ mm}$ . For this tire the radial stiffness and the inflated radius are specified with  $c_R = 265\,000 \text{ N/m}$  and  $r_0 = 316.9 \text{ mm}$ . The overall tire deflection can be estimated by  $\Delta z = F_z/c_R$ . At the load of  $F_z = 4700 \text{ N}$  the deflection amounts to  $\Delta z = 4700 \text{ N} / 265\,000 \text{ N/m} = 0.0177 \text{ m}$ . Then, Eq. (3.42) produces a contact patch length of  $L = 2\sqrt{0.3169 \text{ m} * 0.0177 \text{ m}} = 0.1498 \text{ m} \approx 150 \text{ mm}$  which corresponds quite well with the length of the tire footprint.

### 3.2.6 Contact Point Velocity

To calculate the tire forces and torques which are generated by friction the contact point velocity will be needed. The static contact point  $Q$  given by Eq. (3.38) can be expressed as follows

$$r_{0Q} = r_{0M} + r_{MQ}, \quad (3.43)$$

where  $M$  denotes the wheel center and hence, the vector  $r_{MQ}$  describes the position of static contact point  $Q$  relative to the wheel center  $M$ . The absolute velocity of the contact point will be obtained from

$$v_{0Q,0} = \dot{r}_{0Q,0} = \dot{r}_{0M,0} + \dot{r}_{MQ,0}, \quad (3.44)$$

where  $\dot{r}_{0M,0} = v_{0M,0}$  denotes the absolute velocity of the wheel center. The vector  $r_{MQ}$  contains the tire deflection  $\Delta z$  normal to the road and it takes part on all those motions of the wheel carrier which do not contain elements of the wheel rotation. Hence, its time derivative can be calculated from

$$\dot{r}_{MQ,0} = \omega_{0R,0}^* \times r_{MQ,0} + \Delta \dot{z} e_{n,0}, \quad (3.45)$$

where  $\omega_{0R}^*$  is the angular velocity of the wheel rim without any component in the direction of the wheel rotation axis,  $\Delta \dot{z}$  denotes the change of the tire deflection, and  $e_n$  describes the road normal. Now, Eq. (3.44) reads as

$$v_{0Q,0} = v_{0M,0} + \omega_{0R,0}^* \times r_{MQ,0} + \Delta \dot{z} e_{n,0}. \quad (3.46)$$

As the point  $Q$  lies on the track,  $v_{0Q,0}$  must not contain any component normal to the track

$$e_{n,0}^T v_{0Q,0} = 0 \quad \text{or} \quad e_{n,0}^T (v_{0M,0} + \omega_{0R,0}^* \times r_{MQ,0}) + \Delta \dot{z} e_{n,0}^T e_{n,0} = 0. \quad (3.47)$$

As  $e_{n,0}$  is a unit vector,  $e_{n,0}^T e_{n,0} = 1$  will hold, and then, the time derivative of the tire deformation is simply given by

$$\Delta \dot{z} = -e_{n,0}^T (v_{0M,0} + \omega_{0R,0}^* \times r_{MQ,0}). \quad (3.48)$$

Finally, the components of the contact point velocity in longitudinal and lateral direction are obtained from

$$v_x = e_{x,0}^T v_{0Q,0} = e_{x,0}^T (v_{0M,0} + \omega_{0R,0}^* \times r_{MQ,0}) \quad (3.49)$$

and

$$v_y = e_{y,0}^T v_{0Q,0} = e_{y,0}^T (v_{0M,0} + \omega_{0R,0}^* \times r_{MQ,0}), \quad (3.50)$$

where the relationships  $e_{x,0}^T e_{n,0} = 0$  and  $e_{y,0}^T e_{n,0} = 0$  were used to simplify the expressions.

### 3.2.7 Dynamic Rolling Radius

At an angular rotation of  $\Delta\varphi$ , assuming the tread particles stick to the track, the deflected tire moves on a distance of  $x$ , Fig. 3.19. With  $r_0$  as unloaded and  $r_S = r_0 - \Delta r$  as loaded or static tire radius

$$r_0 \sin \Delta\varphi = x \quad \text{and} \quad r_0 \cos \Delta\varphi = r_S \quad (3.51)$$

hold. If the motion of a tire is compared to the rolling of a rigid wheel, then, its

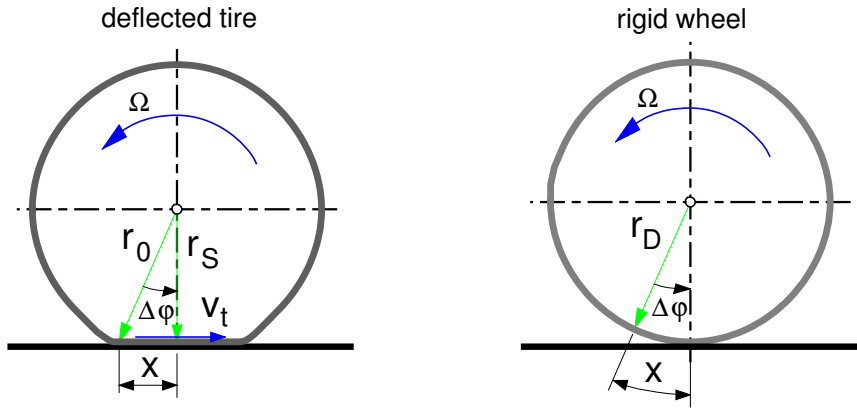


Figure 3.19: Dynamic rolling radius

radius  $r_D$  will have to be chosen so that at an angular rotation of  $\Delta\varphi$  the tire moves the distance

$$r_0 \sin \Delta\varphi = x = r_D \Delta\varphi. \quad (3.52)$$

Hence, the dynamic tire radius is given by

$$r_D = \frac{r_0 \sin \Delta\varphi}{\Delta\varphi}. \quad (3.53)$$

For  $\Delta\varphi \rightarrow 0$  one obtains the trivial solution  $r_D = r_0$ . At small, yet finite angular rotations the sine-function can be approximated by the first terms of its Taylor-Expansion. Then, Eq. (3.53) reads as

$$r_D = r_0 \frac{\Delta\varphi - \frac{1}{6}\Delta\varphi^3}{\Delta\varphi} = r_0 \left(1 - \frac{1}{6}\Delta\varphi^2\right). \quad (3.54)$$

With the according approximation for the cosine-function

$$\frac{r_S}{r_0} = \cos \Delta\varphi = 1 - \frac{1}{2}\Delta\varphi^2 \quad \text{or} \quad \Delta\varphi^2 = 2 \left(1 - \frac{r_S}{r_0}\right) \quad (3.55)$$

one finally gets

$$r_D = r_0 \left(1 - \frac{1}{3} \left(1 - \frac{r_S}{r_0}\right)\right) = \frac{2}{3}r_0 + \frac{1}{3}r_S. \quad (3.56)$$

### 3.2 Contact Geometry

Due to  $r_S = r_S(F_z)$  the fictive radius  $r_D$  depends on the wheel load  $F_z$ . Therefore, it is called dynamic tire radius. If the tire rotates with the angular velocity  $\Omega$ , then

$$v_t = r_D \Omega \quad (3.57)$$

will denote the average velocity at which the tread particles are transported through the contact patch.

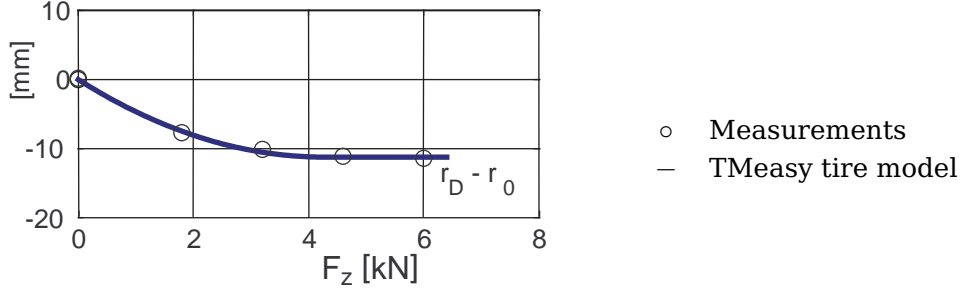


Figure 3.20: Dynamic tire radius

In extension to Eq.(3.56), the dynamic tire radius is approximated in the tire model TMeasy by

$$r_D = \lambda r_0 + (1 - \lambda) \underbrace{\left( r_0 - \frac{F_z^S}{c_z} \right)}_{\approx r_S} \quad (3.58)$$

where the static tire radius  $r_S = r_0 - \Delta r$  has been approximated by using the linearized tire deformation  $\Delta r = F_z^S/c_z$ . The parameter  $\lambda$  is modeled as a function of the wheel load  $F_z$

$$\lambda = \lambda_N + (\lambda_{2N} - \lambda_N) \left( \frac{F_z}{F_z^N} - 1 \right), \quad (3.59)$$

where  $\lambda_N$  and  $\lambda_{2N}$  denote the values for the pay load  $F_z = F_z^N$  and the doubled pay load  $F_z = 2F_z^N$ .

Table 3.3: TMeasy model data for the dynamic rolling radius

$c_z^N = 190$ [kN/m]	vertical tire stiffness at payload, $F_z = F_z^N$
$c_z^{2N} = 206$ [kN/m]	vertical tire stiffness at double payload, $F_z = 2F_z^N$
$\lambda_N = 0.375$ [-]	coefficient for dynamic tire radius at payload, $F_z = F_z^N$
$\lambda_N = 0.750$ [-]	coefficient for dynamic tire radius at payload, $F_z = 2F_z^N$

### 3 Tire

The corresponding TMeasy tire model data for a typical passenger car tire are printed in Table 3.3. This simple but effective model approach fits very well to measurements, Fig. 3.20.

## 3.3 Steady State Forces and Torques

### 3.3.1 Wheel Load

The vertical tire force  $F_z$  can be calculated as a function of the normal tire deflection  $\Delta z$  and the deflection velocity  $\Delta \dot{z}$

$$F_z = F_z(\Delta z, \Delta \dot{z}). \quad (3.60)$$

Because the tire can only apply pressure forces to the road the normal force is restricted to  $F_z \geq 0$ . In a first approximation  $F_z$  is separated into a static and a dynamic part

$$F_z = F_z^S + F_z^D. \quad (3.61)$$

The static part is described as a nonlinear function of the normal tire deflection

$$F_z^S = a_1 \Delta z + a_2 (\Delta z)^2. \quad (3.62)$$

The constants  $a_1$  and  $a_2$  may be calculated from the radial stiffness at nominal and double payload

$$c_N = \left. \frac{d F_z^S}{d \Delta z} \right|_{F_z^S = F_z^N} \quad \text{and} \quad c_{2N} = \left. \frac{d F_z^S}{d \Delta z} \right|_{F_z^S = 2F_z^N}. \quad (3.63)$$

The derivative of Eq. (3.62) results in

$$\frac{d F_z^S}{d \Delta z} = a_1 + 2 a_2 \Delta z. \quad (3.64)$$

From Eq. (3.62) one gets

$$\Delta z = \frac{-a_1 \pm \sqrt{a_1^2 + 4a_2 F_z^S}}{2a_2}. \quad (3.65)$$

Because the tire deflection is always positive, the minus sign in front of the square root has no physical meaning, and can be omitted therefore. Hence, Eq. (3.64) can be written as

$$\frac{d F_z^S}{d \Delta z} = a_1 + 2 a_2 \left( \frac{-a_1 + \sqrt{a_1^2 + 4a_2 F_z^S}}{2a_2} \right) = \sqrt{a_1^2 + 4a_2 F_z^S}. \quad (3.66)$$

### 3.3 Steady State Forces and Torques

Combining Eqs. (3.63) and (3.66) results in

$$\begin{aligned} c_N &= \sqrt{a_1^2 + 4a_2 F_z^N} & \text{or} & & c_N^2 &= a_1^2 + 4a_2 F_z^N, \\ c_{2N} &= \sqrt{a_1^2 + 4a_2 2F_z^N} & \text{or} & & c_{2N}^2 &= a_1^2 + 8a_2 F_z^N \end{aligned} \quad (3.67)$$

finally leading to

$$a_1 = \sqrt{2c_{2N}^2 - c_N^2} \quad \text{and} \quad a_2 = \frac{c_{2N}^2 - c_N^2}{4F_z^N}. \quad (3.68)$$

Results for a passenger car and a truck tire are shown in Fig. 3.21. The parabolic approximation in Eq. (3.62) fits very well to the measurements. The radial tire stiffness of the passenger car tire at the payload of  $F_z = 3\,200\text{ N}$  can be specified with  $c_z = 190\,000\text{ N/m}$ . The payload  $F_z = 35\,000\text{ N}$  and the stiffness  $c_z = 1\,250\,000\text{ N/m}$  of a truck tire are significantly larger.

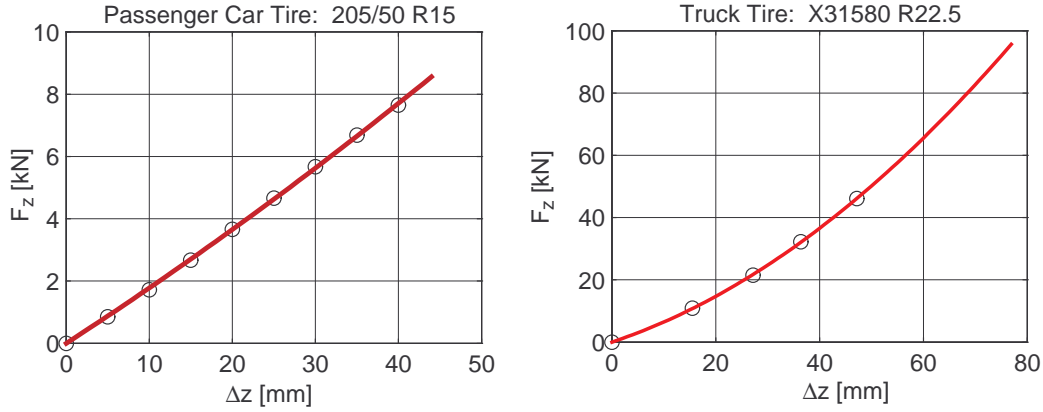


Figure 3.21: Tire radial stiffness:  $\circ$  Measurements, — Approximation

The dynamic part is roughly approximated by

$$F_z^D = d_R \Delta \dot{z}, \quad (3.69)$$

where  $d_R$  is a constant describing the radial tire damping, and the derivative of the tire deformation  $\Delta \dot{z}$  is given by Eq. (3.48).

#### 3.3.2 Tipping Torque

The lateral shift of the vertical tire force  $F_z$  from the geometric contact point  $P$  to the static contact point  $Q$  is equivalent to a force applied in  $P$  and the tipping torque

$$M_x = F_z y \quad (3.70)$$

### 3 Tire

acting around a longitudinal axis in  $P$ . Fig. 3.22 shows a negative tipping torque. Because a positive camber angle moves the contact point into the negative  $y$ -direction and hence, will generate a negative tipping torque.

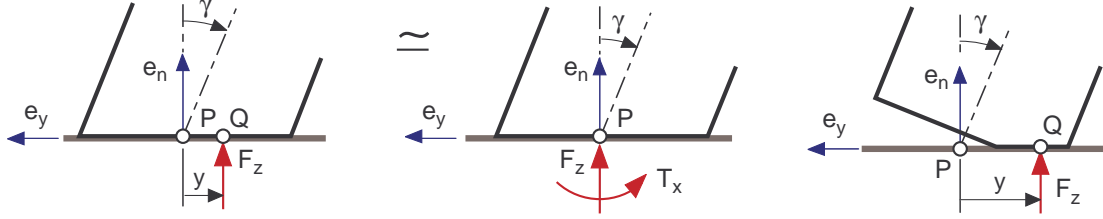


Figure 3.22: Tipping torque at full and partial contact

As long as the cambered tire has full contact to the road the lateral displacement  $y$  is given by Eq. (3.36). Then, Eq. (3.70) reads as

$$M_x = -F_z \frac{b^2}{12 \Delta z} \frac{\tan \gamma}{\cos \gamma}. \quad (3.71)$$

If the wheel load is approximated by its linearized static part  $F_z \approx c_N \Delta z$  and small camber angles  $|\gamma| \ll 1$  are assumed, then, Eq. (3.71) simplifies to

$$M_x = -c_N \Delta z \frac{b^2}{12 \Delta z} \gamma = -\frac{1}{12} c_N b^2 \gamma, \quad (3.72)$$

where the term  $\frac{1}{12} c_N b^2$  can be regarded as the tipping stiffness of the tire.

The use of the tipping torque instead of shifting the geometric contact point  $P$  to the static contact point  $Q$  is limited to those cases where the tire has full or nearly full contact to the road. If the cambered tire has only partly contact to the road, the geometric contact point  $P$  may even be located outside the contact area whereas the static contact point  $Q$  is still a real contact point.

#### 3.3.3 Rolling Resistance

If a non-rotating tire has contact to a flat ground the pressure distribution in the contact patch will be symmetric from the front to the rear, Fig. 3.23. The resulting vertical force  $F_z$  is applied in the center  $C$  of the contact patch and hence, will not generate a torque around the  $y$ -axis.

If the tire rotates tread particles will be stuffed into the front of the contact patch which causes a slight pressure increase, Fig. 3.23. Now, the resulting vertical force is applied in front of the contact point and generates the rolling resistance torque

$$T_y = -F_z x_R \text{sign}(\Omega), \quad (3.73)$$

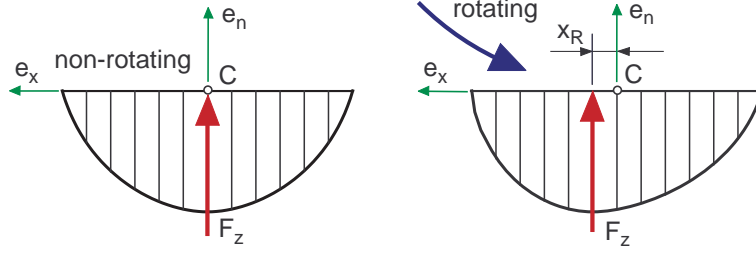


Figure 3.23: Pressure distribution at a non-rotation and rotation tire

where  $\text{sign}(\Omega)$  assures that  $T_y$  always acts against the wheel angular velocity  $\Omega$ . The simple approximation of the sign function

$$\text{sign}(\Omega) \approx d\Omega \quad \text{with} \quad |d\Omega| \leq 1 \quad (3.74)$$

will avoid discontinuities. However, the parameter  $d < 0$  have to be chosen appropriately.

The distance  $x_R$  from the center  $C$  of the contact patch to the working point of  $F_z$  usually is related to the unloaded tire radius  $r_0$

$$f_R = \frac{x_R}{r_0}. \quad (3.75)$$

According to [16] the dimensionless rolling resistance coefficient slightly increases with the traveling velocity  $v$  of the vehicle

$$f_R = f_R(v). \quad (3.76)$$

Under normal operating conditions,  $20 \text{ km/h} < v < 200 \text{ km/h}$ , the rolling resistance coefficient for typical passenger car tires is in the range of  $0.01 < f_R < 0.02$ . The rolling resistance hardly influences the handling properties of a vehicle. But it plays a major part in fuel consumption.

### 3.3.4 Longitudinal Force and Longitudinal Slip

To get a certain insight into the mechanism generating tire forces in longitudinal direction, we consider a tire on a flat bed test rig. The rim rotates with the angular velocity  $\Omega$  and the flat bed runs with the velocity  $v_x$ . The distance between the rim center and the flat bed is controlled to the loaded tire radius corresponding to the wheel load  $F_z$ , Fig. 3.24.

A tread particle enters at the time  $t = 0$  the contact patch. If we assume adhesion between the particle and the track, then the top of the particle will run with the bed velocity  $v_x$  and the bottom with the average transport velocity  $v_t = r_D \Omega$ .

### 3 Tire

Depending on the velocity difference  $\Delta v = r_D \Omega - v_x$  the tread particle is deflected in longitudinal direction

$$u = (r_D \Omega - v_x) t. \quad (3.77)$$

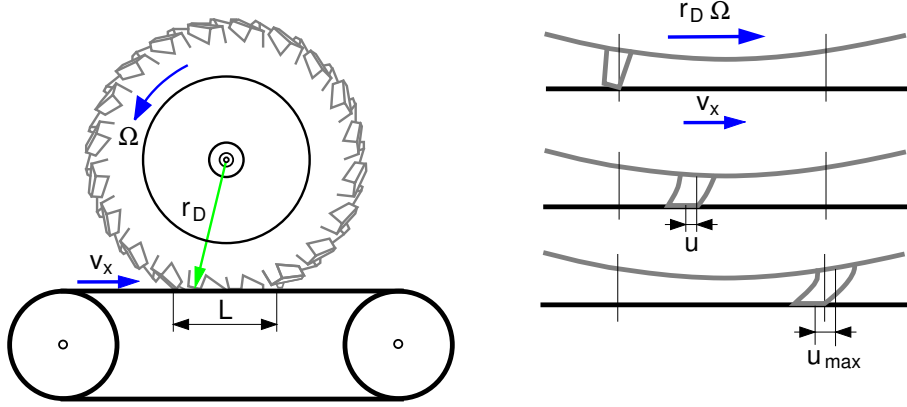


Figure 3.24: Tire on flat bed test rig

The time a particle spends in the contact patch can be calculated by

$$T = \frac{L}{r_D |\Omega|}, \quad (3.78)$$

where  $L$  denotes the contact length, and  $T > 0$  is assured by  $|\Omega|$ . The maximum deflection occurs when the tread particle leaves the contact patch at the time  $t = T$

$$u_{max} = (r_D \Omega - v_x) T = (r_D \Omega - v_x) \frac{L}{r_D |\Omega|}. \quad (3.79)$$

The deflected tread particle applies a force to the tire. In a first approximation we get

$$F_x^t = c_x^t u, \quad (3.80)$$

where  $c_x^t$  represents the stiffness of one tread particle in longitudinal direction. On normal wheel loads more than one tread particle is in contact with the track, Fig. 3.25a. The number  $p$  of the tread particles can be estimated by

$$p = \frac{L}{s + a}, \quad (3.81)$$

where  $s$  is the length of one particle and  $a$  denotes the distance between the particles.

Particles entering the contact patch are undeformed, whereas the ones leaving have the maximum deflection. According to Eq. (3.80), this results in a linear force

### 3.3 Steady State Forces and Torques

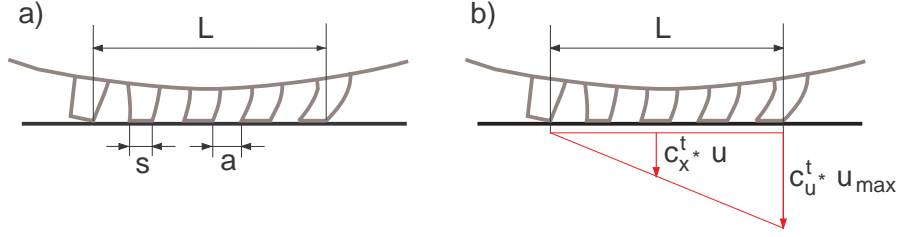


Figure 3.25: a) Particles, b) Force distribution,

distribution versus the contact length, Fig. 3.25b. The resulting force in longitudinal direction for  $p$  particles is given by

$$F_x = \frac{1}{2} p c_x^t u_{max}. \quad (3.82)$$

Using the Eqs. (3.81) and (3.79) this results in

$$F_x = \frac{1}{2} \frac{L}{s+a} c_x^t (r_D \Omega - v_x) \frac{L}{r_D |\Omega|}. \quad (3.83)$$

A first approximation of the contact length  $L$  was calculated in Eq. (3.42). Approximating the belt deformation by  $\Delta z_B \approx \frac{1}{2} F_z / c_R$  results in

$$L^2 \approx 4 r_0 \frac{F_z}{c_R}, \quad (3.84)$$

where  $c_R$  denotes the radial tire stiffness, and nonlinearities and dynamic parts in the tire deformation were neglected. Now, Eq. (3.82) can be written as

$$F_x = 2 \frac{r_0}{s+a} \frac{c_x^t}{c_R} F_z \frac{r_D \Omega - v_x}{r_D |\Omega|}. \quad (3.85)$$

The non-dimensional relation between the sliding velocity of the tread particles in longitudinal direction  $v_x^S = v_x - r_D \Omega$  and the average transport velocity  $r_D |\Omega|$  form the longitudinal slip

$$s_x = \frac{-(v_x - r_D \Omega)}{r_D |\Omega|}. \quad (3.86)$$

The longitudinal force  $F_x$  is proportional to the wheel load  $F_z$  and the longitudinal slip  $s_x$  in this first approximation

$$F_x = k F_z s_x, \quad (3.87)$$

where the constant  $k$  summarizes the tire properties  $r_0$ ,  $s$ ,  $a$ ,  $c_x^t$  and  $c_R$ .

Equation (3.87) holds only as long as all particles stick to the track. At moderate slip values the particles at the end of the contact patch start sliding, and at high

### 3 Tire

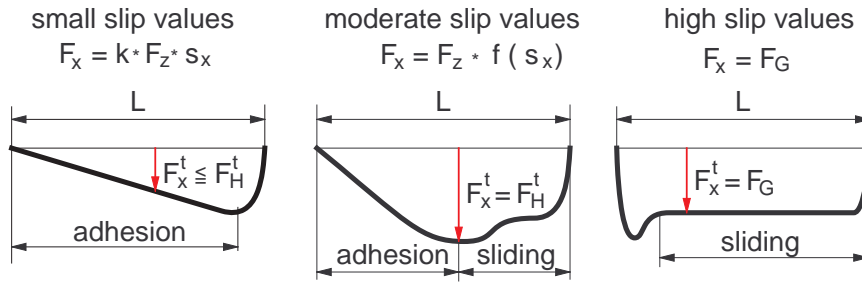


Figure 3.26: Longitudinal force distribution for different slip values

slip values only the parts at the beginning of the contact patch still stick to the road, Fig. 3.26. The resulting nonlinear function of the longitudinal force  $F_x$  versus the longitudinal slip  $s_x$  can be defined by the parameters initial inclination (driving stiffness)  $dF_x^0$ , location  $s_x^M$  and magnitude of the maximum  $F_x^M$ , start of full sliding  $s_x^S$  and the sliding force  $F_x^S$ , Fig. 3.27.

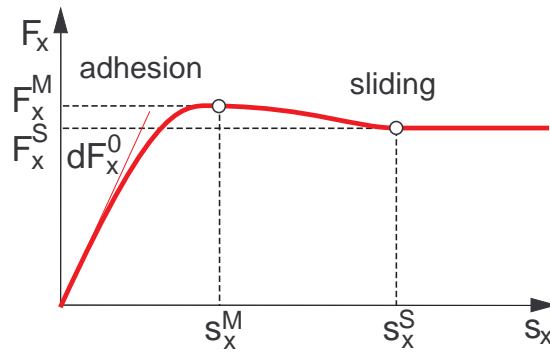


Figure 3.27: Typical longitudinal force characteristics

### 3.3.5 Lateral Slip, Lateral Force and Self Aligning Torque

Similar to the longitudinal slip  $s_x$ , given by Eq. (3.86), the lateral slip is given by

$$s_y = \frac{-v_y}{r_D |\Omega|}, \quad (3.88)$$

where the lateral component of the contact point velocity  $v_y$  follows from Eq. (3.50). As long as the tread particles stick to the road (small amounts of slip), an almost linear distribution of the forces along the length  $L$  of the contact patch appears. At moderate slip values the particles at the end of the contact patch start sliding, and at high slip values only the parts at the beginning of the contact patch stick to the road, Fig. 3.28. The nonlinear characteristics of the lateral force versus the lateral

### 3.3 Steady State Forces and Torques

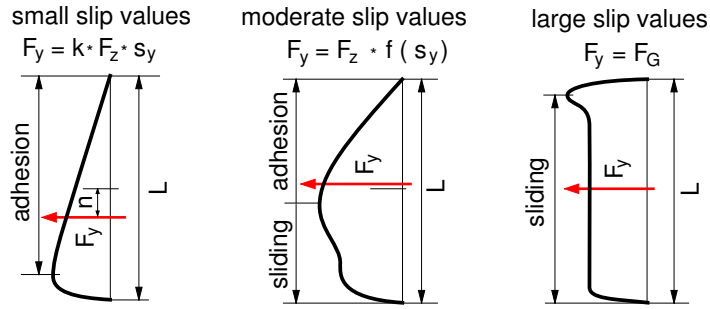


Figure 3.28: Lateral force distribution over contact patch

slip can be described by the initial inclination (cornering stiffness)  $dF_y^0$ , the location  $s_y^M$  and the magnitude  $F_y^M$  of the maximum, the beginning of full sliding  $s_y^S$ , and the magnitude  $F_y^S$  of the sliding force.

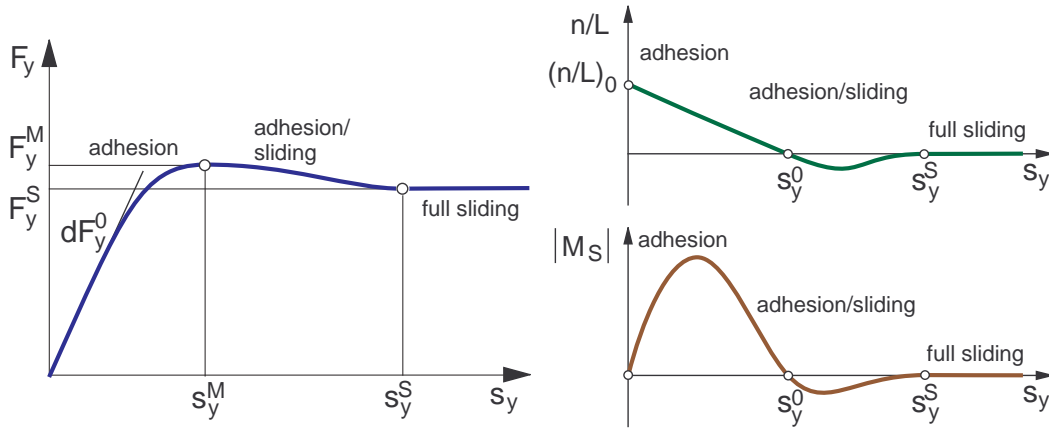


Figure 3.29: Typical plot of lateral force, tire offset and self aligning torque

The distribution of the lateral forces over the contact patch length also defines the point of application of the resulting lateral force. At small slip values this point lies behind the center of the contact patch (contact point P). With increasing slip values it moves forward, sometimes even before the center of the contact patch. At extreme slip values, when practically all particles are sliding, the resulting force is applied at the center of the contact patch. The resulting lateral force  $F_y$  with the dynamic tire offset or pneumatic trail  $n$  as a lever generates the self aligning torque

$$T_S = -n F_y . \quad (3.89)$$

The lateral force  $F_y$  as well as the dynamic tire offset are functions of the lateral slip  $s_y$ . Typical plots of these quantities are shown in Fig.3.29. Characteristic parameters of the lateral force graph are initial inclination (cornering stiffness)  $dF_y^0$ ,

### 3 Tire

location  $s_y^M$  and magnitude of the maximum  $F_y^M$ , begin of full sliding  $s_y^S$ , and the sliding force  $F_y^S$ .

The dynamic tire offset has been normalized by the length of the contact patch  $L$ . The initial value  $(n/L)_0$  as well as the slip values  $s_y^0$  and  $s_y^S$  sufficiently characterize the graph. The normalized dynamic tire offset starts at  $s_y = 0$  with an initial value

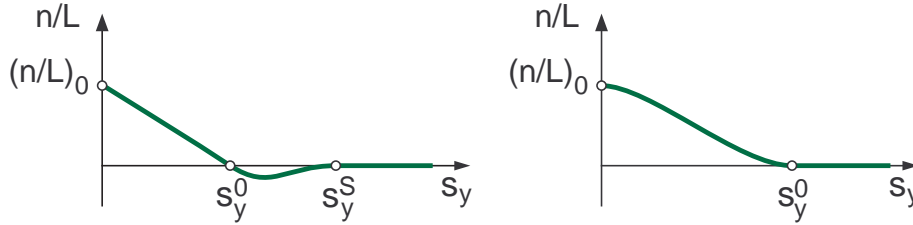


Figure 3.30: Normalized tire offset with and without overshoot

$(n/L)_0 > 0$  and, it tends to zero,  $n/L \rightarrow 0$  at large slip values,  $s_y \geq s_y^S$ . Sometimes the normalized dynamic tire offset overshoots to negative values before it reaches zero again. This behavior can be modeled by introducing the slip values  $s_y^0$  and  $s_y^S$  where the normalized dynamic tire offset overshoots and reaches zero again as additional model parameter, Fig. 3.30. In order to achieve a simple and smooth approximation of the normalized tire offset versus the lateral slip, a linear and a cubic function are overlaid in the first section  $s_y \leq s_y^0$

$$\frac{n}{L} = \left(\frac{n}{L}\right)_0 \begin{cases} [(1-w)(1-s) + w(1-(3-2s)s^2)] & |s_y| \leq s_y^0 \quad \text{and} \quad s = \frac{|s_y|}{s_y^0} \\ - (1-w) \frac{|s_y| - s_y^0}{s_y^0} \left( \frac{s_y^S - |s_y|}{s_y^S - s_y^0} \right)^2 & s_y^0 < |s_y| \leq s_y^S \\ 0 & |s_y| > s_y^S \end{cases} \quad (3.90)$$

where the factor  $w = s_y^0/s_y^S$  weights the linear and the cubic function according to the values of the parameter  $s_y^0$  and  $s_y^S$ . No overshoot will occur for  $s_y^0 = s_y^S$ . Here,  $w = 1$  and  $(1-w) = 0$  will produce a cubic transition from  $n/L = (n/L)_0$  to  $n/L = 0$  with vanishing inclinations at  $s_y = 0$  and  $s_y = s_y^0$ .

At least, the value of  $(n/L)_0$  can be estimated very well. At small values of lateral slip  $s_y \approx 0$  one gets at first approximation a triangular distribution of lateral forces over the contact patch length cf. Fig. 3.28. The working point of the resulting force (dynamic tire offset) is then given by

$$n_0 = n(F_z \rightarrow 0, s_y = 0) = \frac{1}{6} L. \quad (3.91)$$

Because the triangular force distribution will take a constant pressure in the contact patch for granted, the value  $n_0/L = \frac{1}{6} \approx 0.17$  can serve as a first approximation

only. In reality the pressure will drop to zero in the front and in the rear of the contact patch, Fig. 3.23. As low pressure means low friction forces, the triangular force distribution will be rounded to zero in the rear of the contact patch which will move the working point of the resulting force slightly to the front. If no measurements are available, the slip values  $s_y^0$  and  $s_y^S$  where the tire offset passes and finally approaches the  $x$ -axis have to be estimated. Usually the value for  $s_y^0$  is somewhat higher than the slip value  $s_y^M$  where the lateral force reaches its maximum.

### 3.3.6 Bore Torque

#### 3.3.6.1 Modeling Aspects

The angular velocity of the wheel consists of two components

$$\omega_{0W} = \omega_{0R}^* + \Omega e_{yR}. \quad (3.92)$$

The wheel rotation itself is represented by  $\Omega e_{yR}$ , whereas  $\omega_{0R}^*$  describes the motions of the knuckle without any parts into the direction of the wheel rotation axis. In particular during steering motions the angular velocity of the wheel has a component in direction of the track normal  $e_n$

$$\omega_n = e_n^T \omega_{0W} \neq 0 \quad (3.93)$$

which will cause a bore motion. If the wheel moves in longitudinal and lateral direction too then, a very complicated deflection profile of the tread particles in the contact patch will occur. However, by a simple approach the resulting bore torque can be approximated quite good by the parameter of the generalized tire force characteristics.

At first, the complex shape of a tire's contact patch is approximated by a circle, Fig. 3.31. By setting

$$R_P = \frac{1}{2} \left( \frac{L}{2} + \frac{B}{2} \right) = \frac{1}{4} (L + B) \quad (3.94)$$

the radius of the circle can be adjusted to the length  $L$  and the width  $B$  of the actual contact patch. During pure bore motions circumferential forces  $F$  are generated at each patch element  $dA$  at the radius  $r$ . The integration over the contact patch  $A$

$$T_B = \frac{1}{A} \int_A F r dA \quad (3.95)$$

will then produce the resulting bore torque.

#### 3.3.6.2 Maximum Torque

At large bore motions all particles in the contact patch are sliding. Then,  $F = F^S = \text{const.}$  will hold and Eq. (3.95) simplifies to

$$T_B^{max} = \frac{1}{A} F^S \int_A r dA. \quad (3.96)$$

### 3 Tire

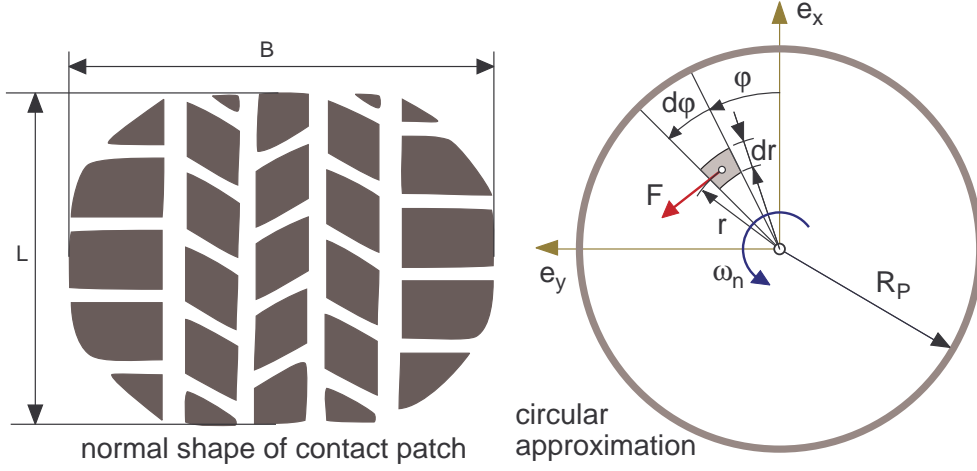


Figure 3.31: Bore torque approximation

With  $dA = r d\varphi dr$  and  $A = R_P^2 \pi$  one gets

$$T_B^{max} = \frac{1}{R_P^2 \pi} F^S \int_0^{R_P} \int_0^{2\pi} r r d\varphi dr = \frac{2}{R_P^2} F^S \int_0^{R_P} r^2 dr = \frac{2}{3} R_P F^S = R_B F^S, \quad (3.97)$$

where

$$R_B = \frac{2}{3} R_P \quad (3.98)$$

can be considered as the bore radius of the contact patch.

#### 3.3.6.3 Bore Slip

For small slip values the force transmitted in the patch element can be approximated by

$$F = F(s) \approx dF^0 s \quad (3.99)$$

where  $s$  denotes the slip of the patch element, and  $dF^0$  is the initial inclination of the generalized tire force characteristics. Similar to Eqs. (3.86) and (3.88) we define

$$s = \frac{-r \omega_n}{r_D |\Omega|} \quad (3.100)$$

where  $r \omega_n$  describes the sliding velocity in the patch element and the term  $r_D |\Omega|$  consisting of the dynamic tire radius  $r_D$  and the angular velocity of the wheel  $\Omega$  represents the average transport velocity of the tread particles. By setting  $r = R_B$  we can define a bore slip now

$$s_B = \frac{-R_B \omega_n}{r_D |\Omega|}. \quad (3.101)$$

### 3.3 Steady State Forces and Torques

Then, Eq. (3.103) simplifies to

$$s = \frac{r}{R_B} s_B . \quad (3.102)$$

Inserting Eqs. (3.99) and (3.102) into Eq. (3.95) results in

$$T_B = = \frac{1}{R_P^2 \pi} \int_0^{R_P} \int_0^{2\pi} dF^0 \frac{r}{R_B} s_B r r d\varphi dr . \quad (3.103)$$

As the bore slip  $s_B$  does not depend on  $r$  Eq. (3.103) simplifies to

$$T_B = \frac{2}{R_P^2} dF^0 \frac{s_B}{R_B} \int_0^{R_P} r^3 dr = \frac{2}{R_P^2} dF^0 \frac{s_B}{R_B} \frac{R_P^4}{4} = \frac{1}{2} R_P dF^0 \frac{R_P}{R_B} s_B . \quad (3.104)$$

With  $R_P = \frac{3}{2} R_B$  one finally gets

$$T_B = \frac{9}{8} R_B dF^0 s_B . \quad (3.105)$$

Via the initial inclination  $dF^0$  and the bore radius  $R_B$  the bore torque  $T_B$  automatically takes the actual tire properties into account.

To avoid numerical problems at a locked wheel, where  $\Omega = 0$  will hold, the modified bore slip

$$s_B = \frac{-R_B \omega_n}{r_D |\Omega| + v_N} \quad (3.106)$$

can be used for practical applications. Where a small fictitious positive velocity  $v_N > 0$  is added in the denominator.

#### 3.3.6.4 Model Realisation

With regard to the overall model assumptions Eq. (3.105) can be simplified to

$$T_B = \frac{9}{8} R_B dF^0 s_B \approx R_B dF^0 s_B . \quad (3.107)$$

But, it is limited by Eq. (3.97) for large bore motions. Hence, the simple, but nonlinear bore torque model finally is given by

$$T_B = R_B dF^0 s_B \quad \text{with} \quad |T_B| \leq R_B F^S , \quad (3.108)$$

where the bore radius  $R_B$  and the bore slip  $s_B$  are defined by Eqs. (3.98) and (3.101) and  $dF^0$  and  $F^S$  are the initial inclination and the sliding value of the generalized tire force characteristics.

This bore torque model is just a simple approach to Coulomb's dry friction, Fig. 3.32. It avoids the jump at  $s_B = 0$  but, it is not able to produce correct results at slow bore motions ( $s_B \approx 0$ ) which will occur at parking manoeuvres in particular. However, a straight forward extension to a dynamic bore torque model will generate realistic parking torques later on.

### 3 Tire

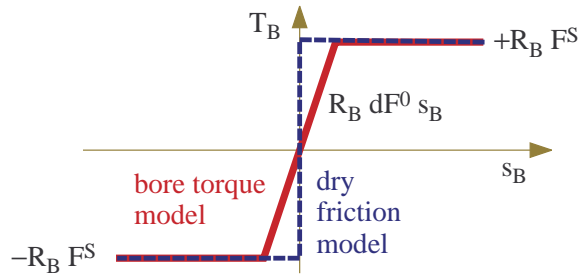


Figure 3.32: Simple nonlinear bore torque model

### 3.3.7 Different Influences

#### 3.3.7.1 Wheel Load

The resistance of a real tire against deformations has the effect that with increasing wheel load the distribution of pressure over the contact patch becomes more and more uneven. The tread particles are deflected just as they are transported through the contact patch. The pressure peak in the front of the contact patch cannot be used, for these tread particles are far away from the adhesion limit because of their small deflection. In the rear of the contact patch the pressure drop leads to a reduction of the maximally transmittable friction force. With rising imperfection of the pressure distribution over the contact patch, the ability to transmit forces of friction between tire and road lessens. In practice, this leads to a degressive influence of the wheel load on the characteristic curves of longitudinal and lateral forces. In order to respect this fact in a tire model, the characteristic data for two nominal wheel loads  $F_z^N$  and  $2 F_z^N$  are given in Table 3.4.

Table 3.4: Characteristic tire data with degressive wheel load influence

Longitudinal force $F_x$		Lateral force $F_y$	
$F_z = 4.0 \text{ kN}$	$F_z = 8.0 \text{ kN}$	$F_z = 4.0 \text{ kN}$	$F_z = 8.0 \text{ kN}$
$dF_x^0 = 120 \text{ kN}$	$dF_x^0 = 200 \text{ kN}$	$dF_y^0 = 55 \text{ kN}$	$dF_y^0 = 80 \text{ kN}$
$s_x^M = 0.110$	$s_x^M = 0.100$	$s_y^M = 0.200$	$s_y^M = 0.220$
$F_x^M = 4.40 \text{ kN}$	$F_x^M = 8.70 \text{ kN}$	$F_y^M = 4.20 \text{ kN}$	$F_y^M = 7.50 \text{ kN}$
$s_x^S = 0.500$	$s_x^S = 0.800$	$s_y^S = 0.800$	$s_y^S = 1.000$
$F_x^S = 4.25 \text{ kN}$	$F_x^S = 7.60 \text{ kN}$	$F_y^S = 4.15 \text{ kN}$	$F_y^S = 7.40 \text{ kN}$

### 3.3 Steady State Forces and Torques

From this data the initial inclinations  $dF_x^0$ ,  $dF_y^0$ , the maximal forces  $F_x^M$ ,  $F_y^M$  and the sliding forces  $F_x^S$ ,  $F_y^S$  for arbitrary wheel loads  $F_z$  are calculated by quadratic functions. For the maximum longitudinal force it reads as

$$F_x^M(F_z) = \frac{F_z}{F_z^N} \left[ 2 F_x^M(F_z^N) - \frac{1}{2} F_x^M(2F_z^N) - \left( F_x^M(F_z^N) - \frac{1}{2} F_x^M(2F_z^N) \right) \frac{F_z}{F_z^N} \right]. \quad (3.109)$$

The location of the maxima  $s_x^M$ ,  $s_y^M$ , and the slip values,  $s_x^S$ ,  $s_y^S$ , at which full sliding appears, are defined as linear functions of the wheel load  $F_z$ . For the location of the maximum longitudinal force this will result in

$$s_x^M(F_z) = s_x^M(F_z^N) + \left( s_x^M(2F_z^N) - s_x^M(F_z^N) \right) \left( \frac{F_z}{F_z^N} - 1 \right). \quad (3.110)$$

The TMeasy parameter in Tab. 3.4 generate the tire characteristics of a standard passenger car tire, Fig. 3.33. Typically the maximum longitudinal force is significantly larger than the maximum lateral force.

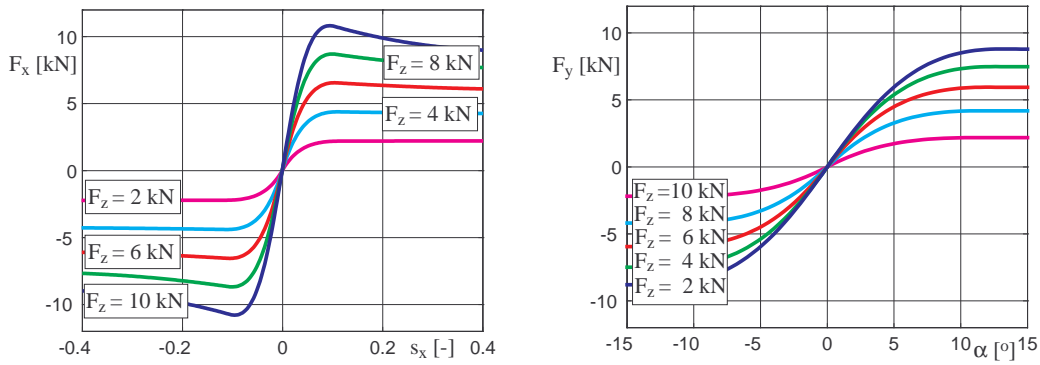


Figure 3.33: Tire characteristics at different wheel loads

According to Eq. (3.89) the self-aligning torque is modeled via the lateral force and the dynamic tire offset. The lateral force characteristics are defined in Tab. 3.4. The characteristic curve parameters describing the dynamic tire offset will be provided for the single and double pay load too. The resulting self-aligning torque is plotted in Fig. 3.34.

Similar to Eq. (3.110) the parameters for arbitrary wheel loads were calculated by linear inter- or extrapolation. The degressive influence of the wheel load on the self aligning torque can be seen here as well. With the parameters for the description of the tire offset it has been assumed that at the payload  $F_z = F_z^N$  the related tire offset reaches the value of  $(n/L)_0 = 0.167 \approx 1/6$  at  $s_y = 0$ . The slip value  $s_y^0$ , at which the tire offset passes the  $x$ -axis, has been estimated. Usually the value is somewhat higher than the position of the lateral force maximum. With increasing wheel load it will move to higher values. The values for  $s_y^S$  are estimated too.

### 3 Tire

Tire offset parameter	
$F_z = 4.0 \text{ kN}$	$F_z = 8.0 \text{ kN}$
$(n/L)_0 = 0.178$	$(n/L)_0 = 0.190$
$s_y^0 = 0.200$	$s_y^0 = 0.225$
$s_y^E = 0.350$	$s_y^E = 0.375$

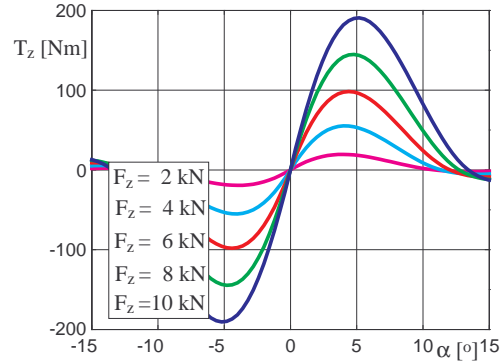


Figure 3.34: Self-aligning torque  $T_z$  at different wheel loads

#### 3.3.7.2 Friction

The tire characteristics are valid for one specific tire road combination only. Hence, different tire road combinations will demand for different sets of model parameter. A reduced or changed friction coefficient mainly influences the maximum force and the sliding force, whereas the initial inclination will remain unchanged. So, by setting

$$s^M \rightarrow \frac{\mu_L}{\mu_0} s^M, \quad F^M \rightarrow \frac{\mu_L}{\mu_0} F^M, \quad s^S \rightarrow \frac{\mu_L}{\mu_0} s^S, \quad F^S \rightarrow \frac{\mu_L}{\mu_0} F^S, \quad (3.111)$$

the essential tire model parameter which primarily depend on the friction coefficient  $\mu_0$  are adjusted to the new or a local friction coefficient  $\mu_L$ . The result of this simple approach is shown in Fig. 3.35.

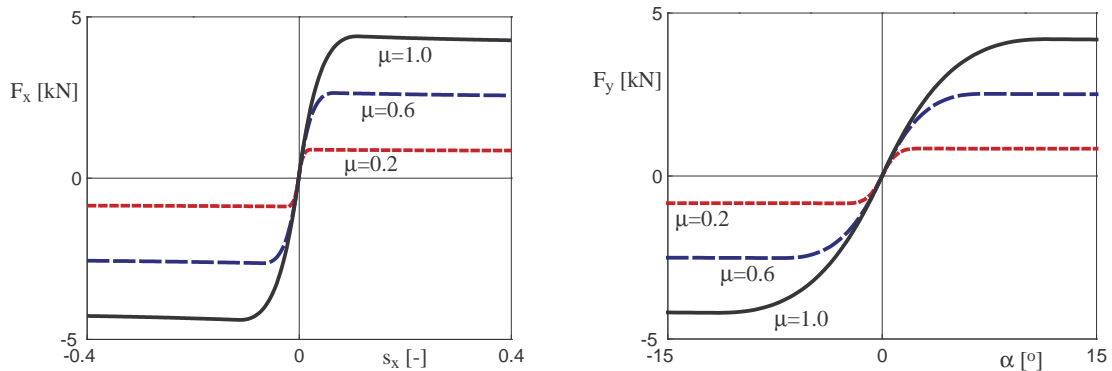


Figure 3.35: Force characteristics at different friction coefficients,  $\mu = \mu_L/\mu_0$

If the road model will not only provide the roughness information  $z = f_R(x, y)$  but also the local friction coefficient  $[z, \mu_L] = f_R(x, y)$  then, braking on  $\mu$ -split maneuvers can easily be simulated, [28].

### 3.3.7.3 Camber

At a cambered tire, Fig. 3.36, the angular velocity of the wheel  $\Omega$  has a component normal to the road

$$\Omega_n = \Omega \sin \gamma, \quad (3.112)$$

where  $\gamma$  denotes the camber angle. Now, the tread particles in the contact patch

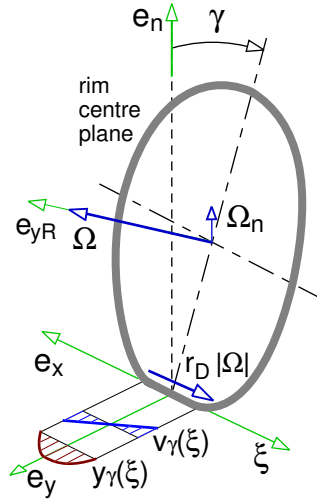


Figure 3.36: Velocity state of tread particles at cambered tire

have a lateral velocity which depends on their position  $\xi$  and is provided by

$$v_\gamma(\xi) = -\Omega_n \frac{L}{2} \frac{\xi}{L/2}, = -\Omega \sin \gamma \xi, \quad -L/2 \leq \xi \leq L/2. \quad (3.113)$$

At the contact point it vanishes whereas at the end of the contact patch it takes on the same value as at the beginning, however, pointing into the opposite direction. Assuming that the tread particles stick to the track, the deflection profile is defined by

$$\dot{y}_\gamma(\xi) = v_\gamma(\xi). \quad (3.114)$$

The time derivative can be transformed to a space derivative

$$\dot{y}_\gamma(\xi) = \frac{dy_\gamma(\xi)}{d\xi} \frac{d\xi}{dt} = \frac{dy_\gamma(\xi)}{d\xi} r_D |\Omega| \quad (3.115)$$

where  $r_D |\Omega|$  denotes the average transport velocity. Now, Eq. (3.114) can be written as

$$\frac{dy_\gamma(\xi)}{d\xi} r_D |\Omega| = -\Omega \sin \gamma \xi \quad \text{or} \quad \frac{dy_\gamma(\xi)}{d\xi} = -\frac{\Omega \sin \gamma}{r_D |\Omega|} \frac{L}{2} \frac{\xi}{L/2}, \quad (3.116)$$

### 3 Tire

where  $L/2$  was used to achieve dimensionless terms. Similar to the lateral slip  $s_y$  which is defined by Eq. (3.88) we can introduce a camber slip now

$$s_\gamma = \frac{-\Omega \sin \gamma}{r_D |\Omega|} \frac{L}{2}. \quad (3.117)$$

Then, Eq. (3.116) simplifies to

$$\frac{dy_\gamma(\xi)}{d\xi} = s_\gamma \frac{\xi}{L/2}. \quad (3.118)$$

The shape of the lateral displacement profile is obtained by integration

$$y_\gamma = s_\gamma \frac{1}{2} \frac{L}{2} \left( \frac{\xi}{L/2} \right)^2 + C. \quad (3.119)$$

The boundary condition  $y(\xi = \frac{1}{2}L) = 0$  can be used to determine the integration constant  $C$ . One gets

$$C = -s_\gamma \frac{1}{2} \frac{L}{2}. \quad (3.120)$$

Then, Eq. (3.119) reads as

$$y_\gamma(\xi) = -s_\gamma \frac{1}{2} \frac{L}{2} \left[ 1 - \left( \frac{\xi}{L/2} \right)^2 \right]. \quad (3.121)$$

The lateral displacements of the tread particles caused by a camber slip are compared now with the ones caused by pure lateral slip, Fig. 3.37. At a tire with pure

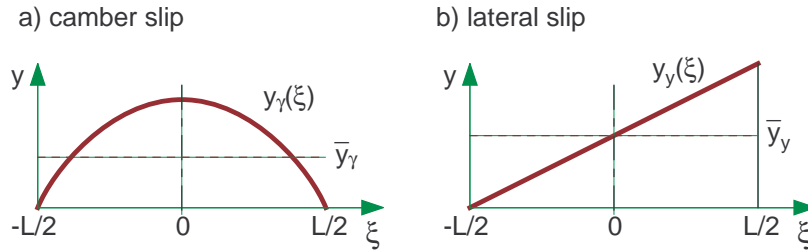


Figure 3.37: Displacement profiles of tread particles

lateral slip each tread particle in the contact patch possesses the same lateral velocity which results in  $dy_y/d\xi r_D |\Omega| = v_y$ , where according to Eq. (3.115) the time derivative  $\dot{y}_y$  was transformed to the space derivative  $dy_y/d\xi$ . Hence, the deflection profile is linear, and reads as  $y_y = v_y/(r_D |\Omega|) \xi = -s_y \xi$ , where the definition in Eq. (3.88) was used to introduce the lateral slip  $s_y$ . Then, the average deflection of the tread particles under pure lateral slip is given by

$$\bar{y}_y = -s_y \frac{L}{2}. \quad (3.122)$$

### 3.3 Steady State Forces and Torques

The average deflection of the tread particles under pure camber slip is obtained from

$$\bar{y}_\gamma = -s_\gamma \frac{1}{2} \frac{L}{2} \frac{1}{L} \int_{-L/2}^{L/2} \left[ 1 - \left( \frac{x}{L/2} \right)^2 \right] d\xi = -\frac{1}{3} s_\gamma \frac{L}{2}. \quad (3.123)$$

A comparison of Eq. (3.122) with Eq. (3.123) shows, that by using

$$s_y^\gamma = \frac{1}{3} s_\gamma \quad (3.124)$$

the lateral camber slip  $s_\gamma$  can be converted to an equivalent lateral slip  $s_y^\gamma$ .

In normal driving conditions, the camber angle and thus, the lateral camber slip are limited to small values,  $s_y^\gamma \ll 1$ . So, the lateral camber force can be modeled by

$$F_y^\gamma = \left. \frac{\partial dF_y}{\partial s_y} \right|_{s_y=0} s_y^\gamma, \quad (3.125)$$

where

$$|F_y^\gamma| \leq F^M \quad (3.126)$$

limits the camber force to the maximum tire force. By replacing the partial derivative of the lateral tire force at a vanishing lateral slip by the global derivative of the generalized tire force

$$\left. \frac{\partial dF_y}{\partial s_y} \right|_{s_y=0} \longrightarrow \frac{F}{s} = f(s) \quad (3.127)$$

the camber force will be automatically reduced when approaching the sliding area, Fig. 3.38.

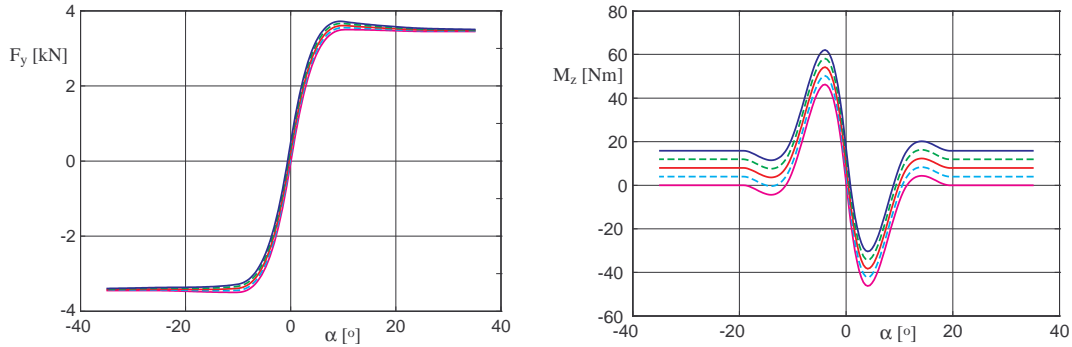


Figure 3.38: Camber influence on lateral force and torque:  $\gamma = 0, 2, 4, 6, 8^\circ$

The angular velocity  $\Omega_n$  defined in Eq. (3.112) generates a bore slip and hence a bore torque  $T_B$ . The tire torque around an axis normal to the local road plane is then generated by the self-aligning and the bore torque,  $T_z = T_S + T_B$ . The resulting

torque is plotted in Fig. 3.38. As the camber angle affects the pressure distribution in the contact patch and it changes the shape of the contact patch from rectangular to trapezoidal it is extremely difficult, if not impossible, to quantify the camber influence with the aid of such a simple model approach. But, it turns out that the results are very realistic. By introducing a load dependent weighting factor in Eq. (3.125) the camber force can be adjusted to measurements.

### 3.3.8 Combined Forces

#### 3.3.8.1 Generalized Slip

The longitudinal force as a function of the longitudinal slip  $F_x = F_x(s_x)$  and the lateral force depending on the lateral slip  $F_y = F_y(s_y)$  can be defined by their characteristic parameters initial inclination  $dF_x^0, dF_y^0$ , location  $s_x^M, s_y^M$  and magnitude of the maximum  $F_x^M, F_y^M$  as well as sliding limit  $s_x^S, s_y^S$  and sliding force  $F_x^S, F_y^S$ , Fig. 3.39. During general driving situations, e.g. acceleration or deceleration in curves, longi-

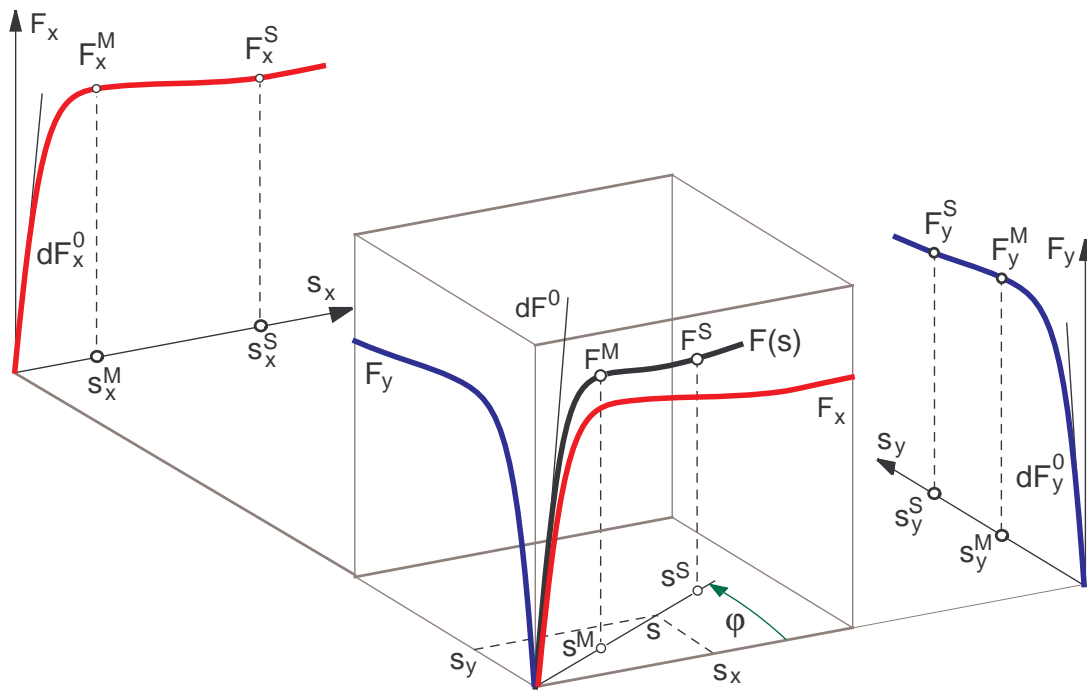


Figure 3.39: Generalized tire characteristics

tudinal  $s_x$  and lateral slip  $s_y$  appear simultaneously. The combination of the more or less differing longitudinal and lateral tire forces requires a normalization process, cf. [20], [14].

### 3.3 Steady State Forces and Torques

The longitudinal slip  $s_x$  and the lateral slip  $s_y$  can vectorially be added to a generalized slip

$$s = \sqrt{\left(\frac{s_x}{\hat{s}_x}\right)^2 + \left(\frac{s_y}{\hat{s}_y}\right)^2} = \sqrt{(s_x^N)^2 + (s_y^N)^2}, \quad (3.128)$$

where the slips were normalized,  $s_x \rightarrow s_x^N$  and  $s_y \rightarrow s_y^N$ , in order to achieve a nearly equally weighted contribution to the generalized slip. The normalizing factors

$$\hat{s}_x = \frac{s_x^M}{s_x^M + s_y^M} + \frac{F_x^M/dF_x^0}{F_x^M/dF_x^0 + F_y^M/dF_y^0} \quad (3.129)$$

and

$$\hat{s}_y = \frac{s_y^M}{s_x^M + s_y^M} + \frac{F_y^M/dF_y^0}{F_x^M/dF_x^0 + F_y^M/dF_y^0} \quad (3.130)$$

take characteristic properties of the longitudinal and lateral tire force characteristics into account. If the longitudinal and the lateral tire characteristics do not differ too much, the normalizing factors will be approximately equal to one.

If the wheel locks, the average transport velocity will vanish,  $r_D |\Omega| = 0$ . Hence, longitudinal, lateral, and generalized slip will tend to infinity,  $s \rightarrow \infty$ . To avoid this problem, the normalized slips  $s_x^N$  and  $s_y^N$  are modified to

$$s_x^N = \frac{s_x}{\hat{s}_x} = \frac{-(v_x - r_D \Omega)}{r_D |\Omega| \hat{s}_x} \Rightarrow s_x^N = \frac{-(v_x - r_D \Omega)}{r_D |\Omega| \hat{s}_x + v_N} \quad (3.131)$$

and

$$s_y^N = \frac{s_y}{\hat{s}_y} = \frac{-v_y}{r_D |\Omega| \hat{s}_y} \Rightarrow s_y^N = \frac{-v_y}{r_D |\Omega| \hat{s}_y + v_N}. \quad (3.132)$$

In normal driving situations, where  $r_D |\Omega| \gg v_N$  holds, the difference between the original slips and the modified slips are hardly noticeable. However, the fictitious velocity  $v_N > 0$  avoids the singularities at  $r_D |\Omega| = 0$  and will produce in this particular case a generalized slip which points exactly into the direction of the sliding velocity of a locked wheel.

Similar to the graphs of the longitudinal and lateral forces the graph  $F = F(s)$  of the generalized tire force can be defined by the characteristic parameters  $dF^0$ ,  $s^M$ ,  $F^M$ ,  $s^S$  and  $F^S$ . These parameters are calculated from the corresponding values of the longitudinal and lateral force characteristics

$$dF^0 = \sqrt{(dF_x^0 \hat{s}_x \cos \varphi)^2 + (dF_y^0 \hat{s}_y \sin \varphi)^2}, \quad (3.133)$$

$$s^M = \sqrt{\left(\frac{s_x^M}{\hat{s}_x} \cos \varphi\right)^2 + \left(\frac{s_y^M}{\hat{s}_y} \sin \varphi\right)^2}, \quad (3.134)$$

$$F^M = \sqrt{(F_x^M \cos \varphi)^2 + (F_y^M \sin \varphi)^2}, \quad (3.135)$$

### 3 Tire

$$s^S = \sqrt{\left(\frac{s_x^S}{\hat{s}_x} \cos \varphi\right)^2 + \left(\frac{s_y^S}{\hat{s}_y} \sin \varphi\right)^2}, \quad (3.136)$$

$$F^S = \sqrt{(F_x^S \cos \varphi)^2 + (F_y^S \sin \varphi)^2}, \quad (3.137)$$

where the slip normalization have also to be considered at the initial inclination. The angular functions

$$\cos \varphi = \frac{s_x^N}{s} \quad \text{and} \quad \sin \varphi = \frac{s_y^N}{s} \quad (3.138)$$

grant a smooth transition from the characteristic curve of longitudinal to the curve of lateral forces in the range of  $\varphi = 0$  to  $\varphi = 90^\circ$ . The longitudinal and the lateral forces follow then from the according projections in longitudinal

$$F_x = F \cos \varphi = F \frac{s_x^N}{s} = \frac{F}{s} s_x^N = f s_x^N \quad (3.139)$$

and lateral direction

$$F_y = F \sin \varphi = F \frac{s_y^N}{s} = \frac{F}{s} s_y^N = f s_y^N, \quad (3.140)$$

where  $f = F/s$  describes the global derivative of the generalized tire force characteristics.

#### 3.3.8.2 Suitable Approximation

The generalized tire force characteristics  $F = F(s)$  is now approximated in intervals by appropriate functions, Fig. 3.40. In the first interval  $0 \leq s \leq s^M$  the rational fraction

$$F(s) = \frac{dF^0 s}{1 + \frac{s}{s^M} \left( \frac{s}{s^M} + \frac{dF^0 s^M}{F^M} - 2 \right)} \quad (3.141)$$

is used which is defined by the initial inclination  $dF^0$  and the location  $s^M$  and the magnitude  $F^M$  of the maximum tire force. When fixing the parameter values, one just has to make sure that the condition  $dF^0 \geq 2 F^M/s^M$  is fulfilled, because otherwise the function will have a turning point in the interval of interest. It can be seen that the global derivative of the generalized tire force  $f = F/s$  is well defined at a vanishing slip and coincides in this particular case with the initial inclination of the generalized tire force characteristics  $f(s=0) = dF^0$ . In the interval  $s^M \leq s \leq s^S$  the generalized tire force characteristics is smoothly continued by two parabolas

$$F(s) = \begin{cases} F^M - a (s - s^M)^2, & s^M \leq s \leq s^*; \\ F^S + b (s^S - s)^2, & s^* \leq s \leq s^S, \end{cases} \quad (3.142)$$

### 3.3 Steady State Forces and Torques

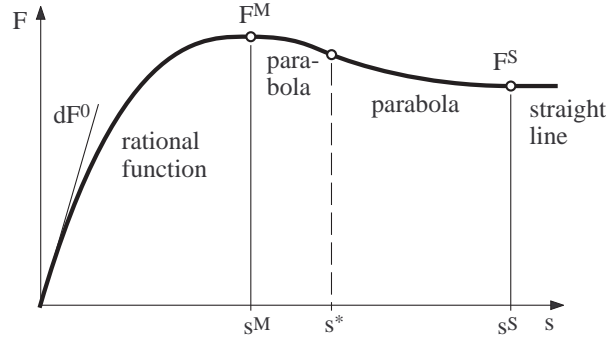


Figure 3.40: Approximation of generalized tire characteristics

until it finally reaches the sliding area  $s \geq s^S$ , where the generalized tire force is approximated by a straight line

$$F(s) = F^S. \quad (3.143)$$

The curve parameter  $a$ ,  $b$  and  $s^*$  defining the two parabolas are determined by the demands

$$\left. \frac{d^2 F}{ds^2} \right|_{s \rightarrow s^M} = \left. \frac{d^2 F}{ds^2} \right|_{s^M \leftarrow s}, \quad (3.144)$$

$$F(s \rightarrow s^*) = F(s^* \leftarrow s) \quad \text{and} \quad \left. \frac{dF}{ds} \right|_{s \rightarrow s^*} = \left. \frac{dF}{ds} \right|_{s^* \leftarrow s}. \quad (3.145)$$

To calculate the second derivative of the rational function at  $s = s^M$  the first derivative is needed at first. One gets

$$\frac{dF}{ds} = dF^0 \frac{1 + \frac{s}{s^M} \left( \frac{s}{s^M} + \frac{dF^0 s^M}{F^M} - 2 \right) - s \left( \frac{1}{s^M} \left( \frac{s}{s^M} + \frac{dF^0 s^M}{F^M} - 2 \right) + \frac{s}{s^M} \frac{1}{s^M} \right)}{\left( 1 + \frac{s}{s^M} \left( \frac{s}{s^M} + \frac{dF^0 s^M}{F^M} - 2 \right) \right)^2} \quad (3.146)$$

which can be simplified to

$$\frac{dF}{ds} = dF^0 \frac{1 - (s/s^M)^2}{D^2}, \quad (3.147)$$

where the denominator in Eq. (3.146) was abbreviated by  $D^2$ . A further derivative yields

$$\frac{d^2 F}{ds^2} = \frac{d}{ds} \frac{dF}{ds} = dF^0 \frac{D^2 (-2s/s^M 1/s^M) - (1 - (s/s^M)^2) 2D \frac{dD}{ds}}{D^4}. \quad (3.148)$$

At  $s = s^M$  the abbreviation  $D$  simplifies to

$$D(s=s^M) = D_M = 1 + \frac{s^M}{s^M} \left( \frac{s^M}{s^M} + \frac{dF^0 s^M}{F^M} - 2 \right) = \frac{dF^0 s^M}{F^M} \quad (3.149)$$

### 3 Tire

and Eq. (3.148) results in

$$\left. \frac{d^2 F}{ds^2} \right|_{s \rightarrow s^M} = dF^0 \frac{-2/s^M}{D_M^2} = -2 \frac{dF^0}{s^M} \left( \frac{F^M}{dF^0 s^M} \right)^2. \quad (3.150)$$

The second derivative of the first parabola defined in Eq. (3.142) simply yields the value  $2a$ . Hence, the parameter

$$a = -\frac{dF^0}{s^M} \left( \frac{F^M}{dF^0 s^M} \right)^2 \quad (3.151)$$

will grant a smooth transition from the rational function to the first parabola.

#### 3.3.8.3 Results

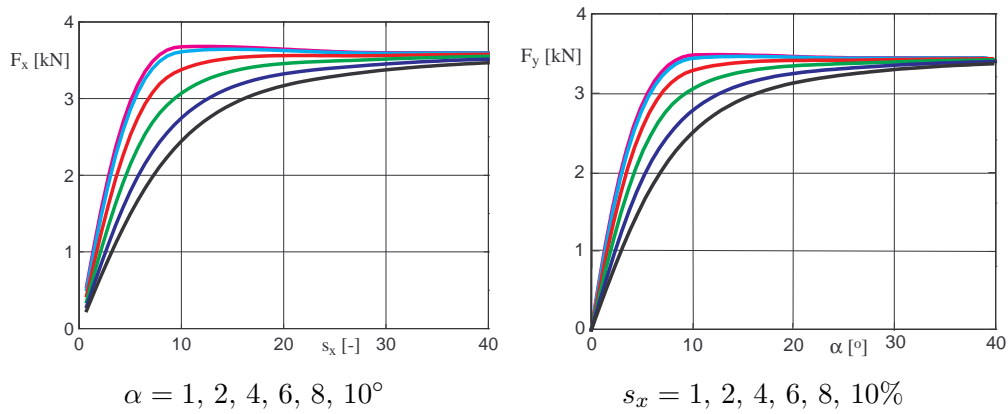


Figure 3.41: Two-dimensional tire characteristics,  $F_z = 3.5 \text{ kN}$

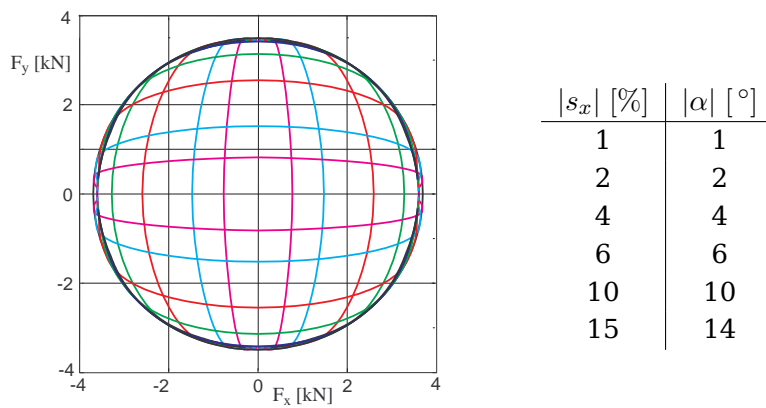


Figure 3.42: Combined forces,  $F_z = 3.5 \text{ kN}$

Within the TMeasy model approach the one-dimensional tire characteristics  $F_x = F_x(s_x)$  and  $F_y = F_y(s_y)$  are automatically converted to two-dimensional characteristics  $F_x = F_x(s_x, s_y)$  and  $F_y = F_y(s_x, s_y)$ , Fig. 3.41. The combined force characteristics in Fig. 3.42 demonstrates the friction limits of the tire. As usual, the relationship  $\tan \alpha = s_y$  was used to convert the lateral slip  $s_y$  into the slip angle  $\alpha$ .

## 3.4 First Order Tire Dynamics

### 3.4.1 Simple Dynamic Extension

Measurements show that the dynamic reaction of the tire forces and torques to disturbances can be approximated quite well by first order systems [12]. Then, the

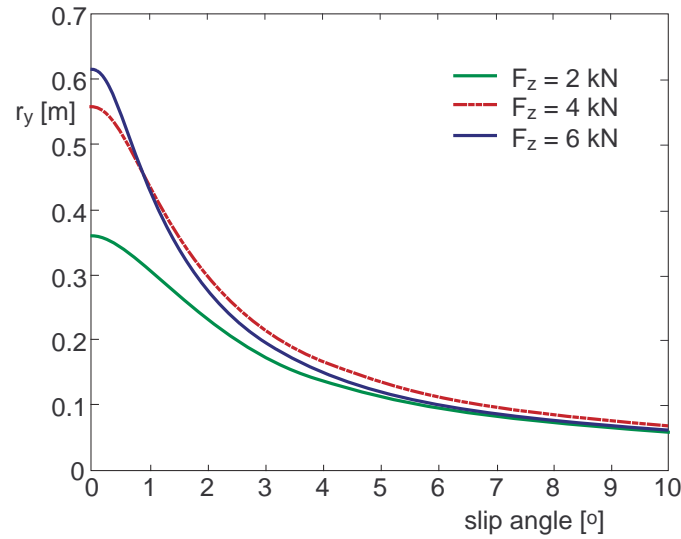


Figure 3.43: Measured lateral force relaxation length for a typical passenger car tire, [12]

dynamic tire forces  $F_x^D$ ,  $F_y^D$  and the dynamic tire torque  $T_z^D$  are given by first order differential equations

$$\tau_x \dot{F}_x^D + F_x^D = F_x^S \quad (3.152)$$

$$\tau_y \dot{F}_y^D + F_y^D = F_y^S \quad (3.153)$$

$$\tau_\psi \dot{T}_z^D + T_z^D = T_z^S \quad (3.154)$$

which are driven by the steady values  $F_x^S$ ,  $F_y^S$  and  $T_z^S$ . The time constants  $\tau_x$ ,  $\tau_y$ ,  $\tau_\psi$  can be derived from corresponding relaxation lengths  $r_x$ ,  $r_y$ ,  $r_\psi$ . Because the tread particles of a rolling tire move with the transport velocity  $r_D|\Omega|$  through the contact

### 3 Tire

patch,

$$\tau_i = \frac{r_i}{r_D |\Omega|} \quad i = x, y, \psi. \quad (3.155)$$

will hold. But, it turned out that these relaxation lengths are functions of the longitudinal and lateral slip  $s_x$ ,  $s_y$  and the wheel load  $F_z$ , Fig. 3.43. Therefore, constant relaxation lengths will approximate the real tire behavior in zero order approximation only. An appropriate model for the dynamic tire performance would be of great advantage because then, the cumbersome task of deriving the relaxation lengths from measurements can be avoided.

### 3.4.2 Enhanced Force Dynamics

#### 3.4.2.1 Compliance Model

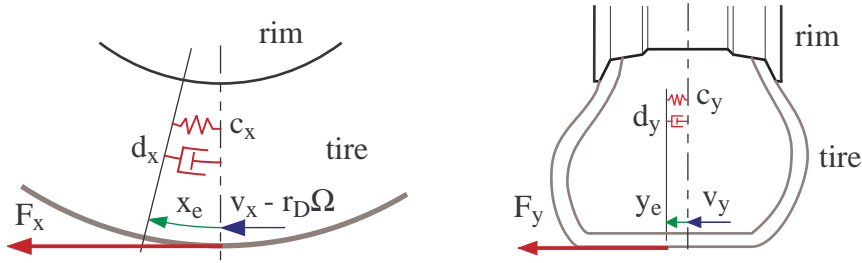


Figure 3.44: Tire deflection in longitudinal and lateral direction

The tire forces  $F_x$  and  $F_y$  acting in the contact patch deflect the tire in longitudinal and lateral direction, Fig. 3.44. In a first order approximation the dynamic tire forces in longitudinal and lateral direction follow from

$$\underbrace{F_x(v_x + \dot{x}_e)}_{F_x^D} \approx \underbrace{F_x(v_x)}_{F_x^S} + \frac{\partial F_x}{\partial v_x} \dot{x}_e, \quad (3.156)$$

$$\underbrace{F_y(v_y + \dot{y}_e)}_{F_y^D} \approx \underbrace{F_y(v_y)}_{F_y^S} + \frac{\partial F_y}{\partial v_y} \dot{y}_e, \quad (3.157)$$

where  $x_e$  and  $y_e$  name the longitudinal and the lateral tire deflection. In steady state the longitudinal tire forces  $F_x^S$  and  $F_y^S$  will be provided by Eqs. (3.139) and (3.140) as functions of the normalized slips  $s_x^N$  and  $s_y^N$ . Their derivatives with respect to the components of the contact point velocity are given by

$$\frac{\partial F_x^S}{\partial v_x} = \frac{\partial F_x^S}{\partial s_x^N} \frac{\partial s_x^N}{\partial v_x} = \frac{\partial F_x^S}{\partial s_x^N} \frac{-1}{r_D |\Omega| \hat{s}_x + v_N} \quad (3.158)$$

### 3.4 First Order Tire Dynamics

$$\frac{\partial F_y^S}{\partial v_y} = \frac{\partial F_y^S}{\partial s_y^N} \frac{\partial s_y^N}{\partial v_y} = \frac{\partial F_y^S}{\partial s_y^N} \frac{-1}{r_D |\Omega| \hat{s}_y + v_N} \quad (3.159)$$

where the definition of the normalized longitudinal slip in Eqs. (3.131) and (3.132) were used to generate the derivatives of the slips with respect to the components of the contact point velocity. Corresponding to the first order approximations in Eqs. (3.156) and (3.157) the partial derivatives of the steady state tire forces with respect to the normalized slips will be approximated by their global derivatives

$$\frac{\partial F_x^S}{\partial s_x^N} \approx \frac{F_x^S}{s_x^N} = \frac{f s_x^N}{s_x^N} = f, \quad (3.160)$$

$$\frac{\partial F_y^S}{\partial s_y^N} \approx \frac{F_y^S}{s_y^N} = \frac{f s_y^N}{s_y^N} = f, \quad (3.161)$$

Then, Eqs. (3.156) and (3.157) will read as

$$F_x^D \approx f s_x^N + f \frac{-1}{r_D |\Omega| \hat{s}_x + v_N} \dot{x}_e, \quad (3.162)$$

$$F_y^D \approx f s_y^N + f \frac{-1}{r_D |\Omega| \hat{s}_y + v_N} \dot{y}_e, \quad (3.163)$$

where according to Eqs. (3.139) and (3.140) the steady state tire forces  $F_x^S$  and  $F_y^S$  were replaced by the terms  $f s_x^N$  and  $f s_y^N$ . On the other hand, the dynamic tire forces can be derived from

$$F_x^D = c_x x_e + d_x \dot{x}_e, \quad (3.164)$$

$$F_y^D = c_y y_e + d_y \dot{y}_e, \quad (3.165)$$

where  $c_x$ ,  $c_y$  and  $d_x$ ,  $d_y$  denote stiffness and damping properties of the tire in longitudinal and lateral direction. Inserting the normalized longitudinal slips defined by Eqs. (3.131) and (3.132) into the Eqs. (3.162) and (3.163) and combining them with Eqs. (3.164) and (3.165) yields first order differential equations for the longitudinal and lateral tire deflection

$$\left( d_x + f \frac{1}{r_D |\Omega| \hat{s}_x + v_N} \right) \dot{x}_e = f \frac{-(v_x - r_D \Omega)}{r_D |\Omega| \hat{s}_x + v_N} - c_x x_e, \quad (3.166)$$

$$\left( d_y + f \frac{1}{r_D |\Omega| \hat{s}_y + v_N} \right) \dot{y}_e = f \frac{-v_y}{r_D |\Omega| \hat{s}_y + v_N} - c_y y_e. \quad (3.167)$$

Multiplying these differential equations with the modified transport velocities

$$v_{Tx}^* = r_D |\Omega| \hat{s}_x + v_N \quad \text{and} \quad v_{Ty}^* = r_D |\Omega| \hat{s}_y + v_N \quad (3.168)$$

finally results in

$$(v_{Tx}^* d_x + f) \dot{x}_e = -f (v_x - r_D \Omega) - v_{Tx}^* c_x x_e, \quad (3.169)$$

### 3 Tire

$$(v_{Ty}^* d_y + f) \dot{y}_e = -f v_y - v_{Ty}^* c_y y_e . \quad (3.170)$$

This first order dynamic tire force model is completely characterized by the generalized steady state tire characteristics  $f$ , and the stiffness  $c_x, c_y$  and damping  $d_x, d_y$  properties of the tire. Via the steady state tire characteristics the dynamics of the tire deflections and hence the dynamics of the tire forces automatically depends on the wheel load  $F_z$  and the longitudinal and lateral slip.

#### 3.4.2.2 Relaxation Lengths

According to (3.155) the relaxation length for the tire deflections and hence for the tire force is now given by

$$r_x = r_D |\Omega| \tau_x \quad \text{and} \quad r_y = r_D |\Omega| \tau_y , \quad (3.171)$$

where the time constants

$$\tau_x = \frac{v_{Tx}^* d_x + f}{v_{Tx}^* c_x} = \frac{d_x}{c_x} + \frac{f}{v_{Tx}^* c_x} \quad \text{and} \quad \tau_y = \frac{v_{Ty}^* d_y + f}{v_{Ty}^* c_y} = \frac{d_y}{c_y} + \frac{f}{v_{Ty}^* c_y} \quad (3.172)$$

can easily be derived from Eqs. (3.169) and (3.170).

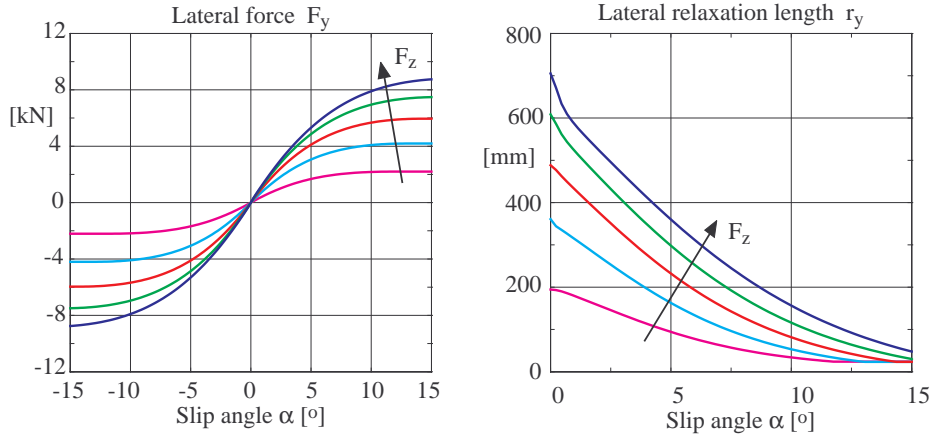


Figure 3.45: Lateral force characteristics and relaxation length, computed with  $c_y = 180\,000\text{N/m}$ ,  $d_y = 250\text{N/(m/s)}$ ,  $r_D|\Omega| = 60\text{km/h}$  at different wheel loads  $F_z = 1.75, 3.50, 5.25, 7.00, 8.75\text{ kN}$

This simple model approach needs steady state tire characteristics only. It leads to a relaxation length which is automatically adapted to the tire parameter, Fig. 3.45. The relaxation length  $r_y$  depends on the wheel load  $F_z$  and on the lateral slip  $s_y$  or the slip angle  $\alpha = \arctan s_y$  respectively. A comparison with Fig. 3.43 shows, that magnitude and the overall behavior of the lateral relaxation length are reproduced quite well. But, of course a perfect matching cannot be expected. However, by

introducing nonlinear characteristics for the longitudinal and lateral tire stiffness,  $c_x \rightarrow c_x(x_e)$  and  $c_y \rightarrow c_y(y_e)$  or an appropriate weighting function a better fitting to measured relaxation lengths would be possible.

### 3.4.3 Enhanced Torque Dynamics

#### 3.4.3.1 Self Aligning Torque

The self aligning torque is generated by the lateral force  $F_y$  and the caster offset  $c_o$ . By neglecting a possible dynamics of the caster offset the dynamic self aligning torque can be approximated by

$$T_S^D = -c_o F_y^D, \quad (3.173)$$

where  $c_o$  denotes the steady state tire offset and  $F_y^D$  names the dynamic tire force. In this approach the dynamics of the self aligning torque is controlled by the dynamics of the lateral tire force.

#### 3.4.3.2 Bore Torque

Following the calculation of the maximum bore torque the contact patch can be reduced to an equivalent contact ring, Fig. 3.46. During bore motions the wheel rim rotates with the angle  $\varphi_W$  around an axis normal to the contact patch. The position of the contact ring relative to the wheel is described by the twist angle  $\varphi$ .

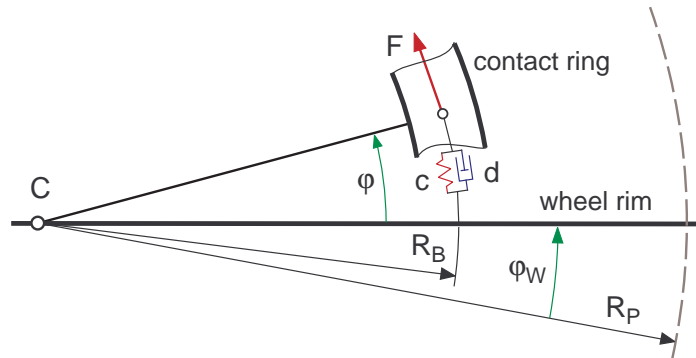


Figure 3.46: Simple bore torque model

The contact ring with a radius which is equal to the bore radius  $R_B$  is attached to the rim by a spring damper element. Hence, the force applied to the rim is given by

$$F_\varphi = c R_B \varphi + d R_B \dot{\varphi}, \quad (3.174)$$

where  $c, d$  represent the stiffness and damping properties of the tire in circumferential direction.

### 3 Tire

If the contact ring slides in circumferential direction the friction force transmitted between the ring and the road can be approximated by

$$F = F(s) \approx dF_0 s, \quad (3.175)$$

where  $dF_0$  is the initial inclination of the generalized tire force and, the circumferential slip is now given by

$$s = \frac{-R_B (\dot{\varphi}_W + \dot{\varphi})}{r_D |\Omega|}. \quad (3.176)$$

Neglecting the inertia of the contact ring, the torque balance

$$R_B \underbrace{(c R_B \varphi + d R_B \dot{\varphi})}_{F_\varphi} = R_B \underbrace{dF_0 \frac{-R_B (\dot{\varphi}_W + \dot{\varphi})}{r_D |\Omega|}}_F \quad (3.177)$$

must hold. Rearranging some terms in Eq. (3.177) results in a first order differential equation for the tire twist angle  $\varphi$

$$\left( \frac{dF_0 R_B^2}{r_D |\Omega|} + d_\varphi \right) \dot{\varphi} = - \frac{dF_0 R_B^2}{r_D |\Omega|} \dot{\varphi}_W - c_\varphi \varphi, \quad (3.178)$$

where the constants

$$c_\varphi = c R_B^2 \quad \text{and} \quad d_\varphi = d R_B^2 \quad (3.179)$$

were introduced to describe the torsional tire stiffness and damping properties. The dynamic bore torque is given by

$$T_B^D = c_\varphi \varphi + d_\varphi \dot{\varphi}. \quad (3.180)$$

The relaxation length

$$r_\psi = r_D |\Omega| \frac{d_\varphi}{c_\varphi} + \frac{1}{c_\varphi} R_B^2 dF_0 \quad (3.181)$$

characterizes the dynamics of the torsional tire deflection  $\varphi$  and hence, of the bore torque  $T_B^D$ . In this simple approach  $r_\psi$  depends only on the wheel load  $F_z$  but, this corresponds quite well with measurements, Fig.3.47 The term  $c_\varphi \varphi$  represents the steady state bore torque

$$T_B^{st} = c_\varphi \varphi. \quad (3.182)$$

It is limited by the maximum bore torque

$$|T_B^{st}| \leq T_B^{max}. \quad (3.183)$$

which according to Eq. (3.97) is defined by the bore radius  $R_B$  and the sliding force  $F^S$ .

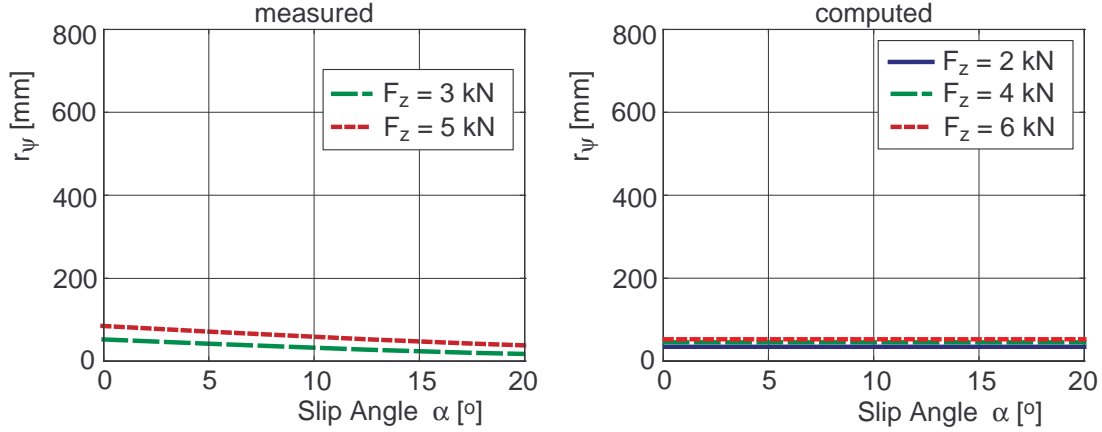


Figure 3.47: Measured [12] and computed bore torque relaxation length:

$$c_\varphi = 1200 \text{ Nm/rad}, d_\varphi = 1.2 \text{ Nm/(rad/s)}, r_D |\Omega| = 60 \text{ km/h}$$

### 3.4.3.3 Parking Torque

The dynamic bore torque model is not yet ready to describe steering motions at stand still where  $\Omega = 0$  will hold. Multiplying (3.178) with  $r_D |\Omega|$  and replacing the term  $c_\varphi \varphi$  by the steady state bore torque  $T_B^{st}$  results in

$$(dF_0 R_B^2 + r_D |\Omega| d_\varphi) \dot{\varphi} = -dF_0 R_B^2 \dot{\varphi}_W - r_D |\Omega| T_B^{st}. \quad (3.184)$$

Now, at stand still ( $\Omega = 0$ ) the simple differential equation

$$\dot{\varphi} = -\dot{\varphi}_W \quad (3.185)$$

remains which means that the torsional tire deflection  $\varphi$  is increased or decreased as long as steering motions  $\dot{\varphi}_W \neq 0$  are performed. But, the differential equation (3.185) is only valid as long as the resulting bore torque does not exceed the maximum value. To take this effect into account at first the steady state torque is limited

$$T_B^{st} = c_\varphi \varphi \quad \text{with} \quad |T_B^{st}| \leq T_B^{max}. \quad (3.186)$$

Then, adhesion is assumed which is described by

$$\dot{\varphi}_A = -\frac{dF_0 R_B^2 \dot{\varphi}_W + r_D |\Omega| T_B^{st}}{dF_0 R_B^2 + r_D |\Omega| d_\varphi}. \quad (3.187)$$

The resulting dynamic bore torque

$$T_B^D = c_\varphi \varphi + d_\varphi \dot{\varphi}_A \quad (3.188)$$

### 3 Tire

now allows to check for sliding which finally is done by

$$\dot{\varphi} = \begin{cases} \dot{\varphi}_A & \text{if } |T_B^D| < T_B^{max} \\ 0 & \text{if } |T_B^D| \geq T_B^{max} \end{cases} \quad (3.189)$$

This model approach provides a continuous transition from stand still,  $r_D |\Omega| = 0$ , to normal driving situations,  $r_D |\Omega| > 0$ .

For measuring the parking effort the tire is rotated at stand still with a low frequent sine input around an axis perpendicular to the contact patch. The simple dynamic torque model operates with parameter which are derived from steady state tire properties and generates here pure stick-slip cycles. Whereas the measurements show a soft transition from adhesion to sliding, Fig.3.48. In [12] a non-

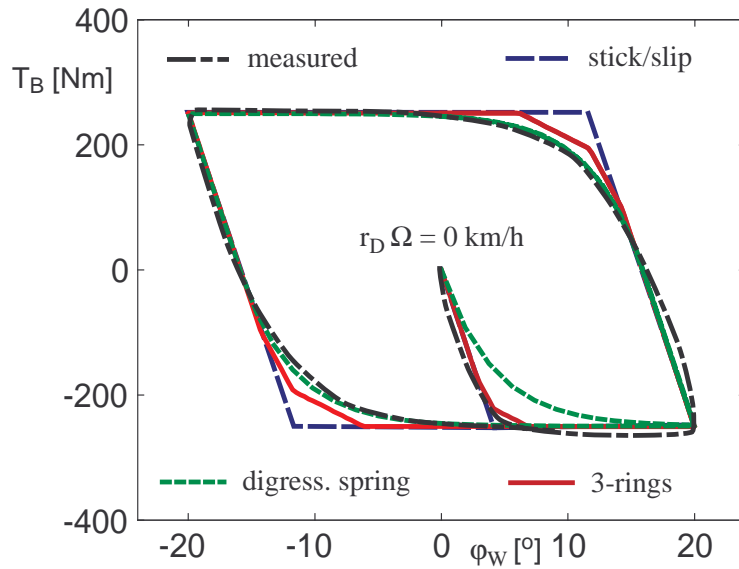


Figure 3.48: Measured [12] and computed parking torque at stand still

physical degressive torsional spring stiffness is used to round the edges of the steady state stick-slip cycle. But, the transient behavior of this approach is not convincing. An enhanced bore torque model, where three contact rings instead of one are used, results in a quite good conformity to the measurements.

As soon as the tire starts to roll,  $r_D |\Omega| > 0$  The different model approaches very soon produce identical results, Fig.3.49. Hence, there is no need for an enhanced bore torque model in normal driving situations.

### 3.4 First Order Tire Dynamics

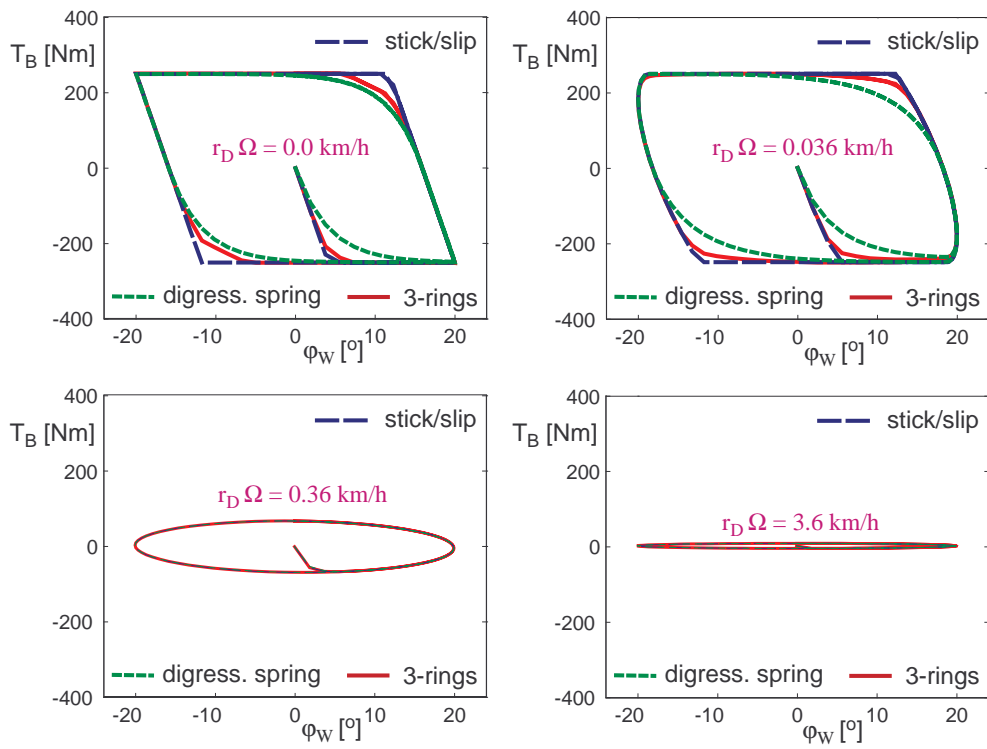


Figure 3.49: Parking torque at different driving velocities

## 4 Drive Train

### 4.1 Components

The drive train serves two functions: it transmits power from the engine to the drive wheels, and it varies the amount of torque. The main parts of a drive train for standard ground vehicles are engine, clutch, transmission, differentials, shafts, brakes and wheels, Fig.. 4.1. On heavy trucks planetary gears are imbedded into the wheels in order to reduce the amount of torque transmitted by the drive and half shafts. Most passenger cars have rear or front wheel drive. All wheel drive is often used on upper class cars and sport utility vehicles. Front wheel drive is very common on light trucks. Advanced drive trains make use of electronically controlled differentials in order to transfer the driving torque properly to the axles and wheels.

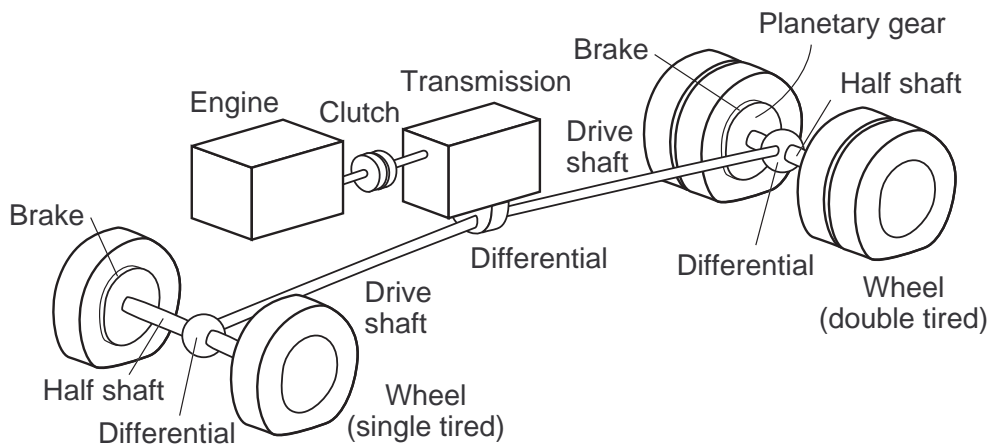


Figure 4.1: Drive train components

Different kinds of driving concepts can be found on heavy trucks. Here, the notation  $w \times d$  where  $w$  names the number of wheels in total and  $d$  the number of driven wheels is usually used to specify the driving concept. Hence,  $4 \times 4$  stands for all wheel drive on a truck with 2 axles, and  $8 \times 4$  names a truck with 4 axles (= 8 wheels) in total where 2 axles (= 4 wheels) are driven. Note, the number of tires and the number of wheels may be different because on solid axles usually on one wheel two tires (double tires) are mounted.

## 4.2 Wheel and Tire

### 4.2.1 Eigen-Dynamics

Besides the longitudinal tire force  $F_x$  which generates a torque around the wheel rotation axis via the static radius  $r_S$  and the rolling resistance torque  $T_y$  the rotation of a wheel is influenced by the driving torque  $T_S$  and the braking torque  $T_B$ , Fig.. 4.2. Then, the angular momentum around the wheel rotation axis results in

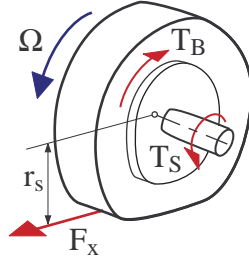


Figure 4.2: Wheel and tire

$$\Theta \dot{\Omega} = T_S - T_B - r_S F_x + T_y, \quad (4.1)$$

where  $\Theta$  and  $\Omega$  denote the inertia and the angular velocity of the wheel. Usually the rolling resistance of a tire is very small,  $|T_y| \ll |r_S F_x|$ . Hence, the dynamics of a wheel which is neither driven nor braked may be simplified to

$$\Theta \dot{\Omega} = -r_S F_x. \quad (4.2)$$

Within handling tire models the longitudinal tire force  $F_x$  is described as a function of the longitudinal slip  $s_x$ . For vanishing lateral slips the normalization factor  $\hat{s}_x$  in Eq. (3.131) can be set to one. Then, the longitudinal slip is given by

$$s_x = \frac{-(v_x - r_D \Omega)}{r_D |\Omega| + v_N} \quad (4.3)$$

where  $v_x$  denotes the longitudinal component of the contact point velocity and the fictitious but small velocity  $v_N > 0$  avoids numerical problems at  $\Omega = 0$ . Now, the angular velocity of the wheel is approximated by

$$\Omega = \frac{v_x}{r_D} + \Delta\Omega, \quad (4.4)$$

where  $\Delta\Omega \ll v_x/r_D$  describes small disturbances of the rolling condition  $r_D \Omega = v_x$ . Then, the longitudinal slip simplifies to

$$s_x = \frac{-(v_x - (v_x + r_D \Delta\Omega))}{|v_x + r_D \Delta\Omega| + v_N} \approx \frac{-r_D \Delta\Omega}{|v_x| + v_N}. \quad (4.5)$$

#### 4 Drive Train

Now, the longitudinal slip is small too,  $s_x \ll 1$  and the steady state longitudinal force characteristics can be approximated by

$$F_x \approx dF_0 s_x = dF_0 \frac{r_D \Delta\Omega}{|v_x| + v_N}, \quad (4.6)$$

where  $dF_0$  describes the initial inclination of the longitudinal tire characteristics  $F_x = F_x(s_x)$ . The equation of motion (4.2) simplifies to a linear differential equation

$$\Theta \Delta\dot{\Omega} = -r_S dF_0 \frac{r_D \Delta\Omega}{|v_x| + v_N}. \quad (4.7)$$

The dynamics of this simple wheel tire model is characterized by the eigenvalue

$$\lambda = -\frac{dF_0}{|v_x| + v_N} \frac{r_S^2}{\Theta}, \quad (4.8)$$

where  $r_S \approx r_D$  was assumed in addition. In drive away or braking to stand still maneuvers where  $v_x = 0$  will hold, the eigenvalues is proportional to  $1/v_N$ . This strong dependency on the fictitious velocity causes problems, because small values for  $v_N$  will result in a very stiff wheel dynamics and too large values for  $v_N$  may produce results with poor accuracy, [26].

However, a simple but effective extension to first order dynamic tire forces gets rid of the strong influence of the fictitious velocity  $v_N$  and produces good results in any driving situation, [25]. As shown in section 3.4 the dynamics of the longitudinal tire force may be approximated by

$$F_x^D = c_x x_e + d_x \dot{x}_e, \quad (4.9)$$

where  $c_x$  and  $d_x$  denote the stiffness and damping properties of the tire in longitudinal direction. The tire deflection  $x_e$  and its time derivative  $\dot{x}_e$  are defined by a first order differential equation

$$(v_{Tx}^* d_x + f) \dot{x}_e = -f (v_x - r_D \Omega) - v_{Tx}^* c_x x_e, \quad (4.10)$$

where the modified transport velocity is defined by

$$v_{Tx}^* = r_D |\Omega| \hat{s}_x + v_N. \quad (4.11)$$

The generalized tire force characteristics  $f$  can be approximated by the initial inclination  $dF_0$  for small longitudinal slips. In addition, the normalization factor  $\hat{s}_x$  can again set to one for vanishing lateral slips. Then, Eq. (4.10) simplifies to

$$((|v_x + r_D \Delta\Omega| + v_N) d_x + dF_0) \dot{x}_e = -dF_0 (-r_D \Delta\Omega) - (|v_x + r_D \Delta\Omega| + v_N) c_x x_e. \quad (4.12)$$

## 4.2 Wheel and Tire

where Eq. 4.4 was already inserted. Assuming small values for the tire displacement  $x_e$  and its time derivative  $\dot{x}_e$  Eq. (4.12) may be further simplified to

$$(|v| d_x + dF_0) \dot{x}_e = r_D dF_0 \Delta\Omega - |v| c_x x_e, \quad (4.13)$$

where the abbreviation  $v = v_x + v_N$  was used. Using the dynamic tire force  $F_x^D$  defined by Eq. (4.9) the angular momentum (4.2) reads as

$$\Theta \Delta\dot{\Omega} = -r_S (c_x x_e + d_x \dot{x}_e). \quad (4.14)$$

The time derivative of Eq. (4.13) combined with Eq. (4.14) results in a second order differential equation for the longitudinal tire deflection

$$(|v| d_x + dF_0) \ddot{x}_e = \frac{r_D dF_0}{\Theta} (-r_S c_x x_e - r_S d_x \dot{x}_e) - |v| c_x \dot{x}_e, \quad (4.15)$$

which can be written as

$$\underbrace{\left( \frac{|v| d_x}{dF_0} + 1 \right) \frac{\Theta}{r_S r_D}}_m \ddot{x}_e + \underbrace{\left( d_x + \frac{|v| c_x \Theta}{dF_0 r_S r_D} \right)}_d \dot{x}_e + c_x x_e = 0. \quad (4.16)$$

Hence, the wheel tire dynamics corresponds to a single mass oscillator where the eigenvalues are given by

$$\lambda_{1,2} = -\frac{d}{2m} \pm i \sqrt{\frac{c_x}{m} - \left( \frac{d}{2m} \right)^2}. \quad (4.17)$$

The results for different vehicle velocities are plotted in Fig. 4.3.

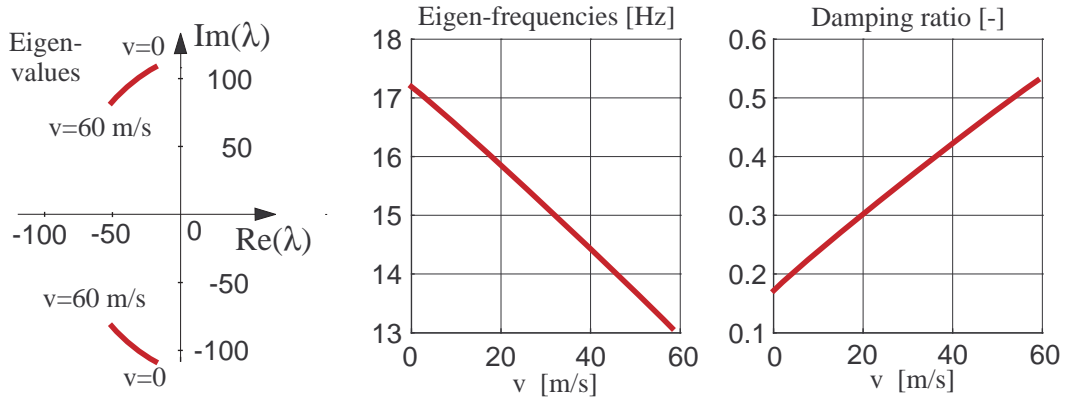


Figure 4.3: Wheel tire eigendynamics:  $\Theta = 1.2 \text{ km}^2$ ,  $r_S = r_D = 0.3 \text{ m}$ ,  $dF_0 = 100\,000 \text{ N/-}$ ,  $c_x = 160\,000 \text{ N/m}$ ,  $d_x = 500 \text{ N/(m/s)}$

## 4 Drive Train

The results are not sensitive to the fictitious velocity  $v_N$  as long as

$$\frac{v_N d_x}{dF_0} \ll 1 \quad \text{or} \quad v_N \ll \frac{dF_0}{d_x} \quad \text{and} \quad \frac{v_N c_x \Theta}{dF_0 r_S r_D} \ll d_x \quad \text{or} \quad v_N \ll \frac{d_x dF_0 r_S r_D}{c_x \Theta} \quad (4.18)$$

will be granted. For standard wheel tire data any value of  $v_N < 1 \text{ m/s}$  will be possible;  $v_N = 0.01 \text{ m/s}$  was chosen here.

### 4.2.2 Performance at Stand Still

At stand still the contact point velocities  $v_x, v_y$ , the angular velocity of the wheel  $\Omega$  and in consequence the generalized slip  $s$  will vanish. At stand still, where  $v_x = 0$ ,  $v_y = 0$  and  $\Omega = 0$  will hold, the differential equations (3.169) and (3.170) simplify to

$$\frac{v_N d_x + dF^0}{v_N c_x} \dot{x}_e = -x_e \quad \text{and} \quad \frac{v_N d_y + dF^0}{v_N c_y} \dot{y}_e = -y_e, \quad (4.19)$$

where  $f(s=0) = dF^0$  was factored in and according to Eq.(3.168) the modified transport velocities  $v_{Tx}^*$  and  $v_{Ty}^*$  are reduced to the fictitious velocity  $v_N$ . This means that existing tire deflections and in consequence the tire forces too will decay exponentially in time.

However, after transforming the differential equations for the tire deflections into the form of (3.169) and (3.170) the modified transport velocities may be restored to their original values. Replacing  $v_{Tx}^*$  by  $v_{Tx} = r_D |\Omega| \hat{s}_x$  and  $v_{Ty}^*$  by  $v_{Ty} = r_D |\Omega| \hat{s}_y$  Eqs. (3.169) and (3.170) will read as

$$(r_D |\Omega| \hat{s}_x d_x + f) \dot{x}_e = -f (v_x - r_D \Omega) - r_D |\Omega| \hat{s}_x c_x x_e, \quad (4.20)$$

$$(r_D |\Omega| \hat{s}_y d_y + f) \dot{y}_e = -f v_y - r_D |\Omega| \hat{s}_y c_y y_e. \quad (4.21)$$

At stand still the contact point velocity and angular velocity of the wheel will vanish,  $v_x = 0$ ,  $v_y = 0$  and  $\Omega = 0$ . Then, Eqs. (4.20) and (4.21) simply will result in  $\dot{x}_e = 0$  and  $\dot{y}_e$  which means that existing tire deflections and hence existing tire forces will be maintained now. On hard braking maneuvers the wheel will lock in an instant  $\Omega = 0$  while the vehicle is still moving  $v_x \neq 0$  and  $v_y \neq 0$ . In this case Eqs. (4.20) and (4.21) will result in

$$\dot{x}_e = -v_x \quad \text{and} \quad \dot{y}_e = -v_y \quad (4.22)$$

which means that the tire deflections are increased or decreased as long as the vehicle is still moving. But, Eq.(4.22) takes no longer into account that the tire forces are limited to a maximum values,  $\sqrt{F_x^2 + F_y^2} \leq F^M$ . In order to achieve this Eqs. (4.20) and (4.21) must be supplemented by appropriate if statements. Then, the dynamic tire model corresponds at stand still with a simple stick slip model [29].

The results of a driving and braking maneuver on a grade are shown in Fig. 4.4 for the simple vehicle model. The vehicle ( $m = 400 \text{ kg}$ ,  $\Theta = 0.8 \text{ kgm}^2$ ,  $r = 0.3 \text{ m}$ ) starts from

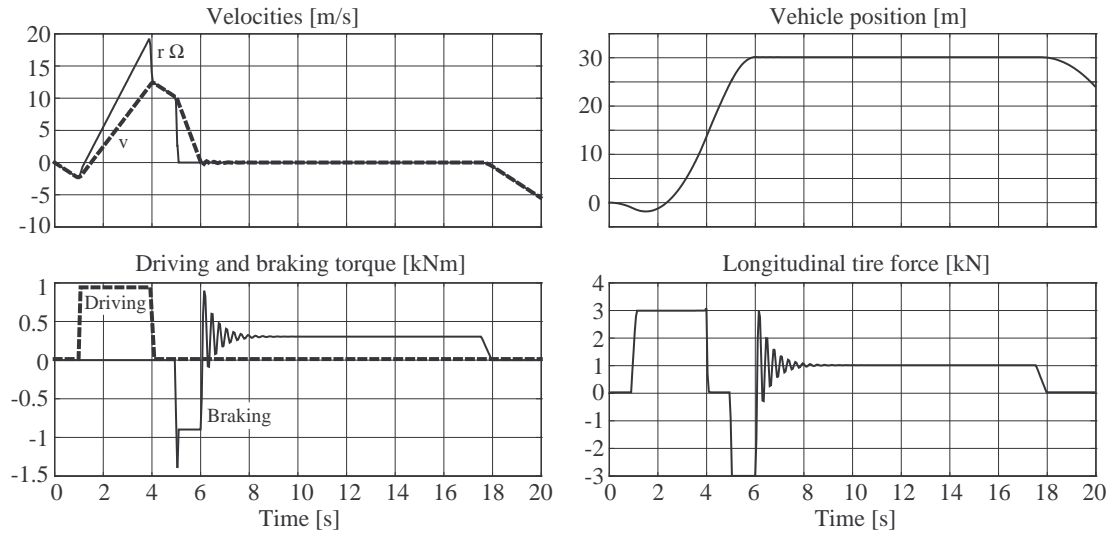


Figure 4.4: Driving and braking on a grade

stand still on a grade ( $\alpha = -15^\circ$ ). At first it rolls backwards,  $v = r\Omega$ , then, the vehicle is accelerated by a driving torque  $r\Omega > v$ . After a short period a braking torque is applied which causes the wheel to lock in an instant,  $r\Omega = 0$ . The maximum tire force is limited here to  $|F_x| < 3.1 \text{ kN}$ . When the vehicle comes to a stand still  $r\Omega = 0$ ,  $v = 0$  at  $t \approx 6 \text{ s}$  the braking torque model automatically changes the sign in order to prevent the vehicle from moving downhill again. As the brake is not released yet the vehicle oscillates some time in longitudinal direction. During this period where the wheel is locked the system vehicle and tire represent a damped oscillator. The stiffness and damping properties of the tire in longitudinal direction  $c_x = 180000 \text{ N/m}$  and  $d_x = 1500 \text{ N/(m/s)}$  together with the corresponding vehicle mass of  $m = 400 \text{ kg}$  result in a frequency of  $f = \sqrt{c/m - (d/(2m))^2}/(2\pi) = 3.4 \text{ Hz}$ . Inspecting the time history of the longitudinal force in Fig. 4.4 one counts approximately 7 cycles in the interval  $6 \text{ s} \leq t \leq 8 \text{ s}$  which yields  $f = 3.5 \text{ Hz}$ , and corresponds very well with the predicted result. Finally, the vehicle comes to a complete stand still,  $v = 0$ ,  $\Omega = 0$ . The tire force of  $F_x \approx 1 \text{ kN}$  which is needed to compensate the downhill force is perfectly maintained as long as the brake is applied. At  $t = 18 \text{ s}$  the brake is fully released and the vehicle starts to roll downhill again.

### 4.2.3 Driving and Braking Torques

Usually, the driving torque is transmitted by the half shaft. By modeling the torsional flexibility of the drive shaft by a linear spring damper model one gets

$$T_S = -c_S \Delta\varphi_S - d_S (\Omega - \omega_S) , \quad (4.23)$$

## 4 Drive Train

where  $\Omega$  and  $\omega_S$  denote the angular velocities of the wheel and of the drive shaft. The torsional stiffness and damping properties are described by  $c_S$  and  $d_S$ . Finally, the torsional angle of the half shaft is defined by the differential equation

$$\frac{d}{dt} (\Delta\varphi_S) = \Omega - \omega_S . \quad (4.24)$$

The braking torque applied to the wheel can be calculated via an enhanced dry friction model

$$T_B = T_B^{st} - d_N \omega \quad \text{with} \quad |T_B| \leq T_B^{mx} , \quad (4.25)$$

where  $T_B^{st}$  is the static part,  $d_N > 0$  is a constant,  $T_B^{mx}$  denotes the maximum braking torque and

$$\omega = \Omega - \omega_K \quad (4.26)$$

describes the relative angular velocity between the wheel and the knuckle. The

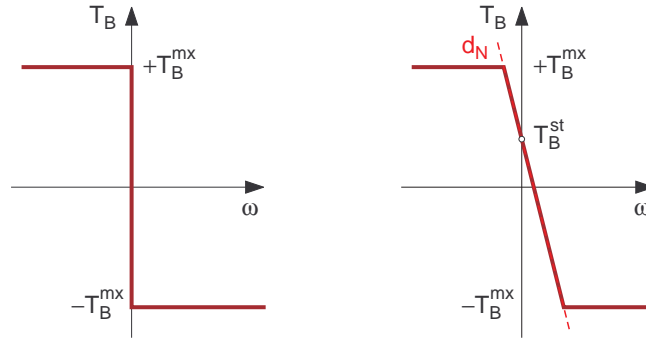


Figure 4.5: Coulomb Dry Friction Model and Enhanced Brake Torque Model

enhanced brake torque model avoids the jump at  $\omega = 0$ , Fig 4.5, but via the static part it still provides a locking torque,  $T_B(\omega = 0) = T_B^{st}$ .

## 4.3 Drive Shafts, Half Shafts and Differentials

### 4.3.1 Structure

The subsystem consisting of the drive shafts, the differentials and the half shafts interacts on one side with the engine and on the other side with the wheels, Fig. 4.6. Hence, the angular velocities of the wheels  $\omega_1, \dots, \omega_4$ , and the engine or respectively the transmission output angular velocity  $\omega_T$  serve as inputs for this subsystem. Engine, clutch, transmission, wheels and tires are described separately. Via the tire forces and torques the whole drive train is coupled with the steering system and the vehicle frame work.

Usually the drive shafts are modeled by massless torsional springs and the differentials by kinematic constraints [13].

### 4.3 Drive Shafts, Half Shafts and Differentials

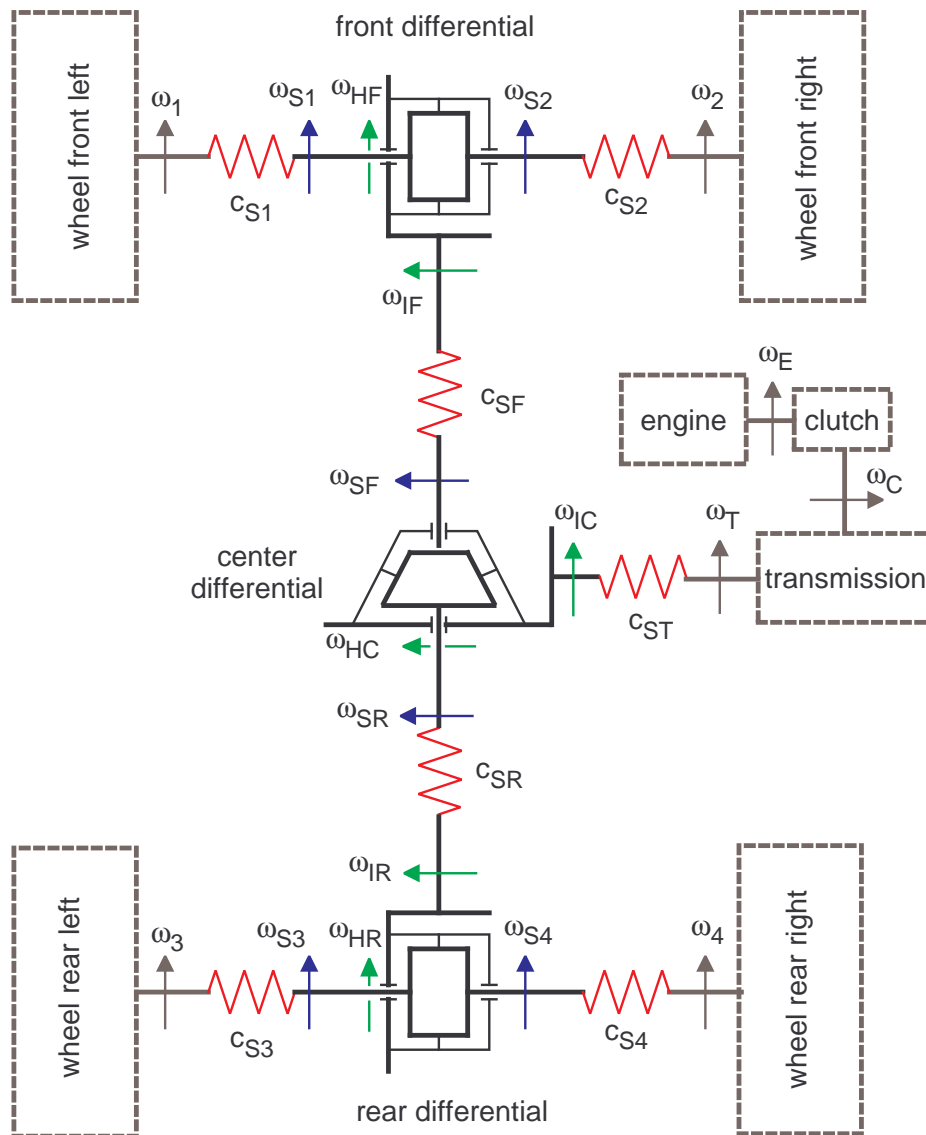


Figure 4.6: Drive Train Model

#### 4.3.2 Active Differentials

Today advanced drive trains include an electronically active center differential and an active yaw control rear differential unit. At present two systems are available, Fig. 4.7.

The active center differential (ACD) is an electronically controlled hydraulic multi-plate clutch which distributes torque between the front and rear to improve traction under acceleration out of a corner. It works in conjunction with active yaw control

## 4 Drive Train

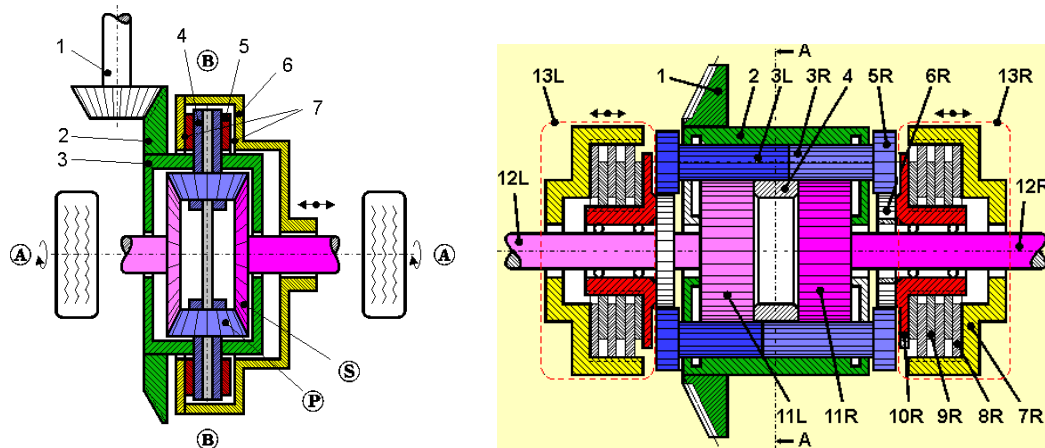


Figure 4.7: Active differentials with friction cage and multi-plate clutch

(AYC) which can actively split torque based on input from various sensors in the vehicle measuring longitudinal and lateral acceleration, steering, brakes and throttle position.

### 4.4 Transmission

The transmission or gearbox allows the gear ratio to be adjusted. This is necessary because combustion engines work best if they run in a limited rate of revolutions. By shifting the gears, which can be done manually or automatically, the engine is kept at its most efficient rate while allowing the vehicle to run at a large range of speed.

Operating the gear lever of a manual transmission brings a different train of gear wheels into play, Fig. 4.8. The different ratios of teeth on the gear wheels involved produce different speeds. If a gear is selected then the dog teeth lock the required upper gear wheel to the transmission shaft. Then, the transmission goes from the clutch shaft via the counter shaft and the lower gear wheels to the upper gear wheels and finally to the transmission shaft. Selecting reverse gear introduces the idler wheel which reverses the rotation of the transmission shaft. Usually the gear ratio is defined as

$$r_G = \frac{\omega_T}{\omega_C} \quad (4.27)$$

where the  $\omega_T$  and  $\omega_C$  denote the angular velocities of the transmission and the clutch shaft. Typical gear ratios are given in Tab. 4.1.

For a gear to be engaged the different speeds of the rotating parts need to be matched and locked together. The synchromesh uses friction to do this smoothly and quietly. Pushed by the selector fork, the collar slides along the transmission

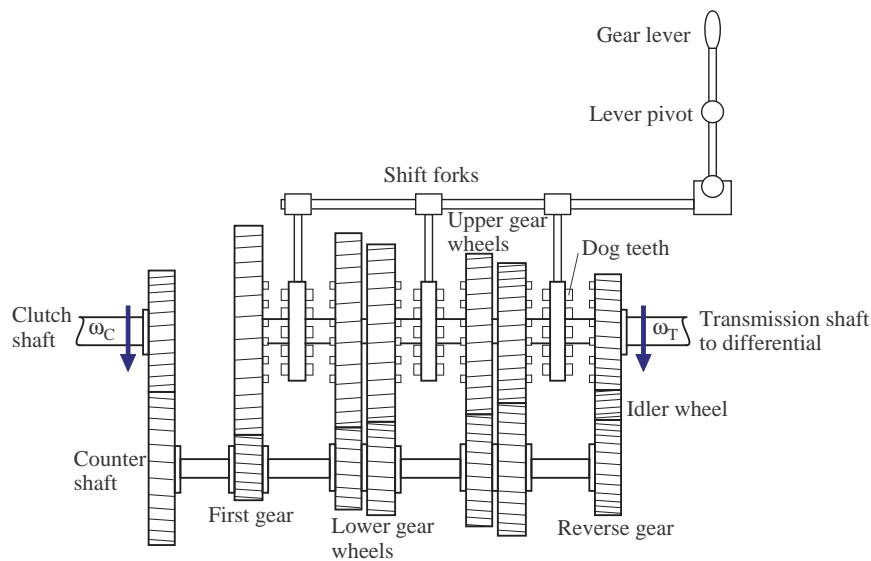


Figure 4.8: Manual transmission

Table 4.1: Typical gear ratios for a passenger car

gear	reverse	neutral	first	second	third	forth	fifth
ratio	-4.181	0	3.818	2.294	1.500	1.133	0.911

shaft, rotating with it. The collar fits over a cone on the upper gear wheel, making the wheel speed up or slow down until both are moving with the same speed. Then, the dog teeth are engaged, locking the upper gear wheel to the collar and hence, to the transmission shaft.

## 4.5 Clutch

The clutch makes use of friction to transmit the rotation of the engine crankshaft to the gearbox. When the clutch pedal is released the clutch spring forces the clutch plate and the flywheel, which is turned by the crankshaft, together, Fig. 4.9.

The maximum friction torque  $T_C^{mx}$  transmitted by the clutch depends on the position of the clutch pedal  $p_C$ , Fig. 4.10. Pressing the clutch pedal reduces the normal force between the clutch plate and the flywheel and hence, reduces the maximum friction torque.

## 4 Drive Train

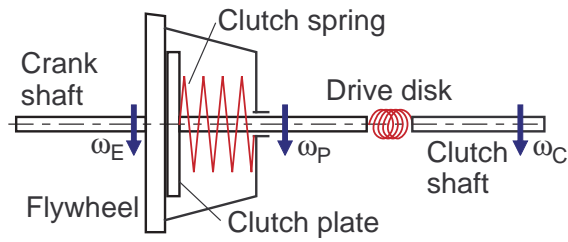


Figure 4.9: Clutch model without clutch pedal mechanism

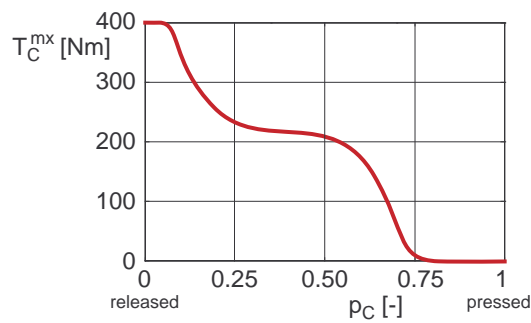


Figure 4.10: Example for the maximum friction torque transmitted by a clutch

## 4.6 Engine

### 4.6.1 Combustion engine

Combustion engines are very common on ground vehicles. In a first approximation the torque  $T_E$  of a combustion engine can be characterized as a function of its angular velocity  $\omega_E$  and the gas pedal  $p_G$ , Fig. 4.11.

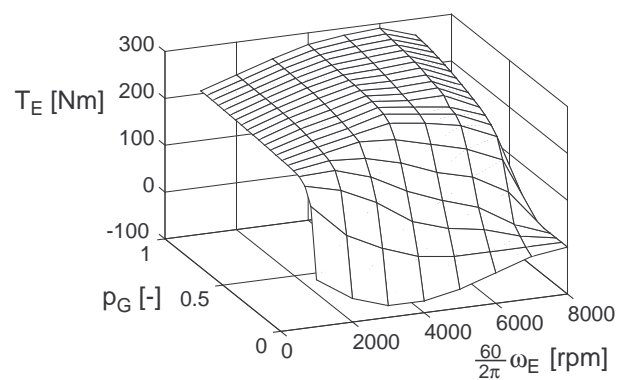


Figure 4.11: Example for a combustion engine torque:  $T_E = T_E(\omega_E, p_G)$

A sophisticated combustion engine model en-DYNA<sup>®</sup>, where the air flow, the fuel supply, the torque calculation, and the exhaust system is modeled in detail, will be provided by TESIS<sup>1</sup>.

#### 4.6.2 Hybrid drive

Electric cars create less pollution than gasoline-powered cars, but they need a large array of batteries in order to achieve a reasonable range of miles per charge. In addition recharging the batteries will take a long time. Hence, electric cars usually are restricted to specific operating conditions.

Nowadays hybrid driven cars have become very popular. At present many hybrid models are already available and most automobile manufacturers have announced plans to put their own versions on the market. The hybrid is a compromise. It attempts to significantly increase the mileage and reduce the emissions of a gasoline-powered car while overcoming the shortcomings of an electric car. The power sources can be combined in two different ways. In a series hybrid the combustion engine turns a generator, and the generator can either charge the batteries or power an electric motor that drives the transmission. Thus, the gasoline engine never directly powers the vehicle. A parallel hybrid has a fuel tank that supplies gasoline to the combustion engine and a set of batteries that supplies power to the electric motor. The batteries store energy recovered from braking or generated by the engine. Both the engine and the electric motor can turn the transmission at the same time. Hence, a significant increase of the drive torque is possible, Fig. 4.12.

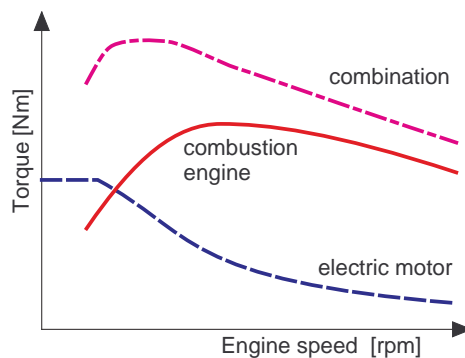


Figure 4.12: Hybride drive torque characteristics

Usually, the combustion engine on a conventional car will be sized for the peak power requirement. Whereas the hybrid car may use a much smaller engine, one that is sized closer to the average power requirement than to the peak power. Hence, fuel consumption and pollution may be reduced significantly.

<sup>1</sup>[www.thesis.de](http://www.thesis.de)

# 5 Suspension System

## 5.1 Purpose and Components

The automotive industry uses different kinds of wheel/axle suspension systems. Important criteria are costs, space requirements, kinematic properties, and compliance attributes.

The main purposes of a vehicle suspension system are

- carry the car and its weight,
- maintain correct wheel alignment,
- control the vehicle's direction of travel,
- keep the tires in contact with the road,
- reduce the effect of shock forces.

Vehicle suspension systems consist of

- guiding elements
  - control arms, links
  - struts
  - leaf springs
- force elements
  - coil spring, torsion bar, air spring, leaf spring
  - anti-roll bar, anti-sway bar or stabilizer
  - damper
  - bushings, hydro-mounts
- tires.

From the modeling point of view force elements may be separated into static and dynamic systems. Examples and modeling aspects are discussed in chapter 6. Tires are air springs that support the total weight of the vehicle. The air spring action of the tire is very important to the ride quality and safe handling of the vehicle. In addition, the tire must provide the forces and torque which keep the vehicle on track. The tire was discussed in detail in chapter 3.

## 5.2 Some Examples

### 5.2.1 Multi Purpose Systems

The double wishbone suspension, the McPherson suspension and the multi-link suspension are multi purpose wheel suspension systems, Fig. 5.1. They are used as steered front or non steered rear axle suspension systems. These suspension systems are also suitable for driven axles.

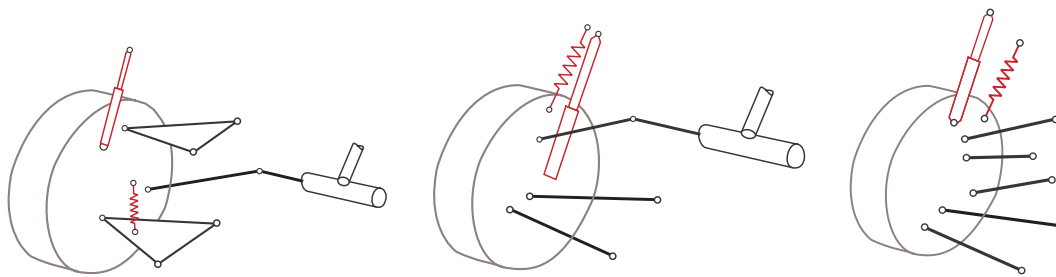


Figure 5.1: Double wishbone, McPherson and multi-link suspension

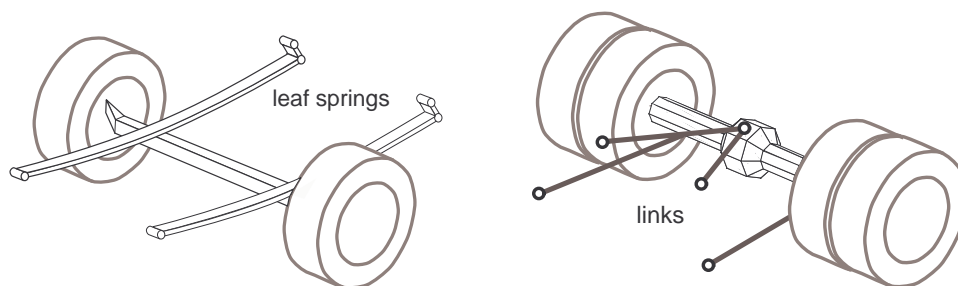


Figure 5.2: Solid axles guided by leaf springs and links

In a McPherson suspension the spring is mounted with an inclination to the strut axis. Thus, bending torques at the strut, which cause high friction forces, can be reduced. At pickups, trucks, and busses solid axles are used often. They are guided either by leaf springs or by rigid links, Fig. 5.2. Solid axles tend to tramp on rough roads. Leaf-spring-guided solid axle suspension systems are very robust. Dry friction between the leaves leads to locking effects in the suspension. Although the leaf springs provide axle guidance on some solid axle suspension systems, additional links in longitudinal and lateral direction are used. Thus, the typical wind-up effect on braking can be avoided. Solid axles suspended by air springs need at least four links for guidance. In addition to a good driving comfort air springs allow level control too.

### 5.2.2 Specific Systems

The semi-trailing arm, the short-long-arm axle (SLA), and the twist beam axle suspension are suitable only for non-steered axles, Fig. 5.3.

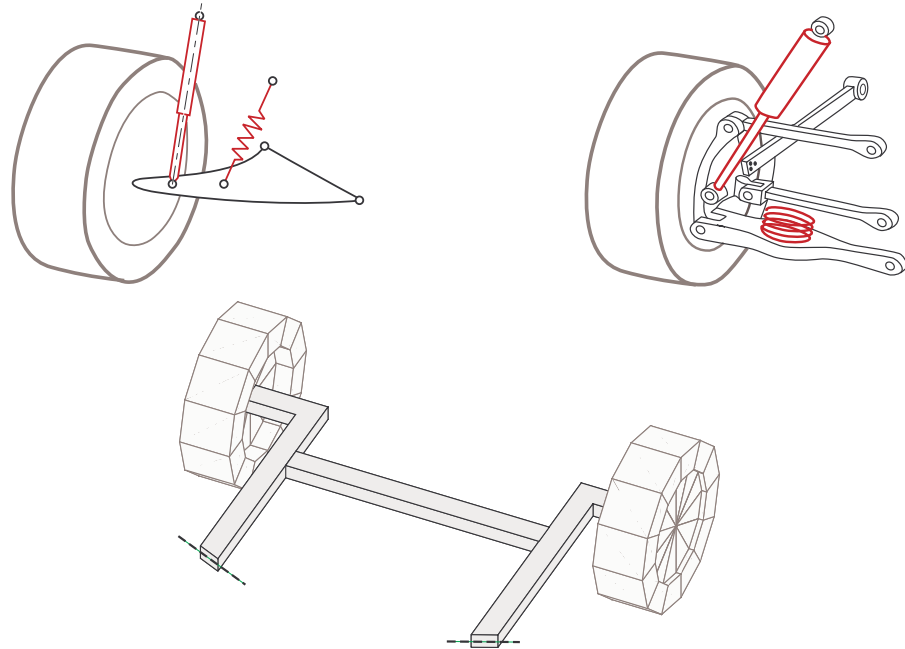


Figure 5.3: Specific wheel/axles suspension systems

The semi-trailing arm is a simple and cheap design which requires only few space. It is mostly used for driven rear axles. The short-long-arm axle design allows a nearly independent layout of longitudinal and lateral axle motions. It is similar to the central control arm axle suspension, where the trailing arm is completely rigid and hence, only two lateral links are needed. The twist beam axle suspension exhibits either a trailing arm or a semi-trailing arm characteristic. It is used for non driven rear axles only. The twist beam axle provides enough space for spare tire and fuel tank.

### 5.2.3 Toe-in, Toe-out

Wheel toe-in is an angle formed by the center line of the wheel and the longitudinal axis of the vehicle, looking at the vehicle from above, Figure 5.4. When the extensions of the wheel center lines tend to meet in front of the direction of travel of the vehicle, this is known as toe-in. If, however the lines tend to meet behind the direction of travel of the vehicle, this is known as toe-out. The amount of toe can be expressed in degrees as the angle  $\delta$  to which the wheels are out of parallel, or,

as the difference between the track widths as measured at the leading and trailing edges of the tires or wheels.

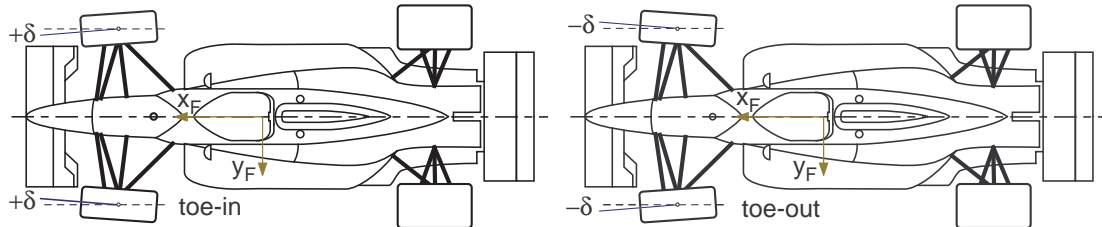


Figure 5.4: Toe-in and Toe-out

Toe settings affect three major areas of performance: tire wear, straight-line stability and corner entry handling characteristics. For minimum tire wear and power loss, the wheels on a given axle of a car should point directly ahead when the car is running in a straight line. Excessive toe-in or toe-out causes the tires to scrub, since they are always turned relative to the direction of travel. Toe-in improves the directional stability of a car and reduces the tendency of the wheels to shimmy.

#### 5.2.4 Wheel Camber

Wheel camber is the angle of the wheel relative to vertical, as viewed from the front or the rear of the car, Fig. 5.5.

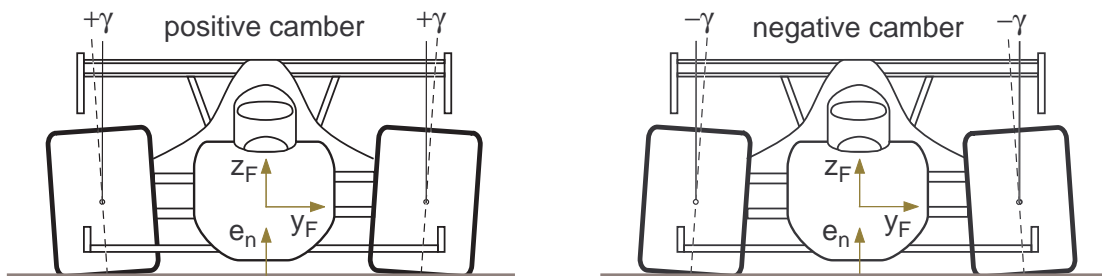


Figure 5.5: Positive camber angle

If the wheel leans away from the car, it has positive camber; if it leans in towards the chassis, it has negative camber. The wheel camber angle must not be mixed up with the tire camber angle which is defined as the angle between the wheel center plane and the local track normal  $e_n$ . Excessive camber angles cause a non symmetric tire wear. A tire can generate the maximum lateral force during cornering if it is operated with a slightly negative tire camber angle. As the chassis rolls in corner the suspension must be designed such that the wheels performs camber changes as the

## 5 Suspension System

suspension moves up and down. An ideal suspension will generate an increasingly negative wheel camber as the suspension deflects upward.

### 5.2.5 Design Position of Wheel Rotation Axis

The unit vector  $e_{yR}$  describes the wheel rotation axis. Its orientation with respect to the wheel carrier fixed reference frame can be defined by the angles  $\delta_0$  and  $\gamma_0$  or  $\delta_0$  and  $\gamma_0^*$ , Fig. 5.6.

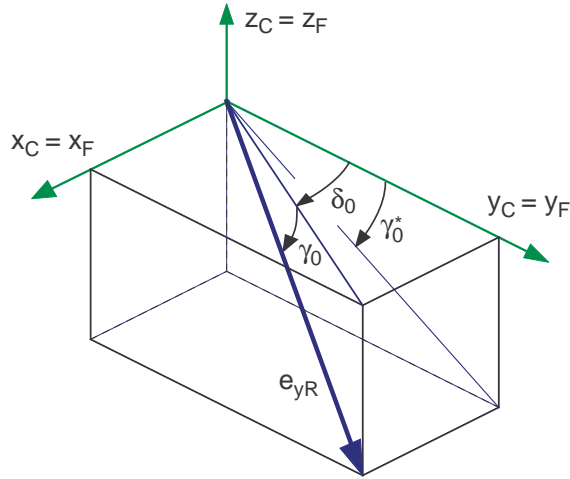


Figure 5.6: Design position of wheel rotation axis

In design position the corresponding axes of the frames  $C$  and  $F$  are parallel. Then, for the left wheel we get

$$e_{yR,F} = e_{yR,C} = \frac{1}{\sqrt{\tan^2 \delta_0 + 1 + \tan^2 \gamma_0^*}} \begin{bmatrix} \tan \delta_0 \\ 1 \\ -\tan \gamma_0^* \end{bmatrix} \quad (5.1)$$

or

$$e_{yR,F} = e_{yR,C} = \begin{bmatrix} \sin \delta_0 \cos \gamma_0 \\ \cos \delta_0 \cos \gamma_0 \\ -\sin \gamma_0 \end{bmatrix}, \quad (5.2)$$

where  $\delta_0$  is the angle between the  $y_F$ -axis and the projection line of the wheel rotation axis into the  $x_F$ - $y_F$ -plane, the angle  $\gamma_0^*$  describes the angle between the  $y_F$ -axis and the projection line of the wheel rotation axis into the  $y_F$ - $z_F$ -plane, whereas  $\gamma_0$  is the angle between the wheel rotation axis  $e_{yR}$  and its projection into the  $x_F$ - $y_F$ -plane. Kinematics and compliance test machines usually measure the angle  $\gamma_0^*$ . That is why, the automotive industry mostly uses this angle instead of  $\gamma_0$ .

On a flat and horizontal road where the track normal  $e_n$  points into the direction of the vertical axes  $z_C = z_F$  the angles  $\delta_0$  and  $\gamma_0$  correspond with the toe angle  $\delta$  and

the camber angle  $\gamma_0$ . To specify the difference between  $\gamma_0$  and  $\gamma_0^*$  the ratio between the third and second component of the unit vector  $e_{yR}$  is considered. The Equations 5.1 and 5.2 deliver

$$\frac{-\tan \gamma_0^*}{1} = \frac{-\sin \gamma_0}{\cos \delta_0 \cos \gamma_0} \quad \text{or} \quad \tan \gamma_0^* = \frac{\tan \gamma_0}{\cos \delta_0}. \quad (5.3)$$

Hence, for small angles  $\delta_0 \ll 1$  the difference between the angles  $\gamma_0$  and  $\gamma_0^*$  is hardly noticeable.

### 5.2.6 Steering Geometry

At steered front axes, the McPherson-damper strut axis, the double wishbone axis, and the multi-link wheel suspension or the enhanced double wishbone axis are mostly used in passenger cars, Figs. 5.7 and 5.8.

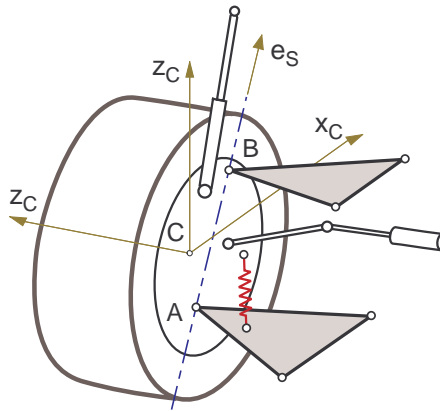


Figure 5.7: Double wishbone wheel suspension

The wheel body rotates around the kingpin line at steering motions. At the double wishbone axis the ball joints  $A$  and  $B$ , which determine the kingpin line, are both fixed to the wheel body. Whereas the ball joint  $A$  is still fixed to the wheel body at the standard McPherson wheel suspension, the top mount  $T$  is now fixed to the vehicle body. At a multi-link axle the kingpin line is no longer defined by real joints. Here, as well as with an enhanced McPherson wheel suspension, where the A-arm is resolved into two links, the momentary rotation axis serves as kingpin line. In general the momentary rotation axis is neither fixed to the wheel body nor to the chassis and, it will change its position at wheel travel and steering motions.

The unit vector  $e_s$  describes the direction of the kingpin line. Within the vehicle fixed reference frame  $F$  it can be fixed by two angles. The caster angle  $\nu$  denotes the angle between the  $z_F$ -axis and the projection line of  $e_s$  into the  $x_F$ -,  $z_F$ -plane. In a similar way the projection of  $e_s$  into the  $y_F$ -,  $z_F$ -plane results in the kingpin

## 5 Suspension System

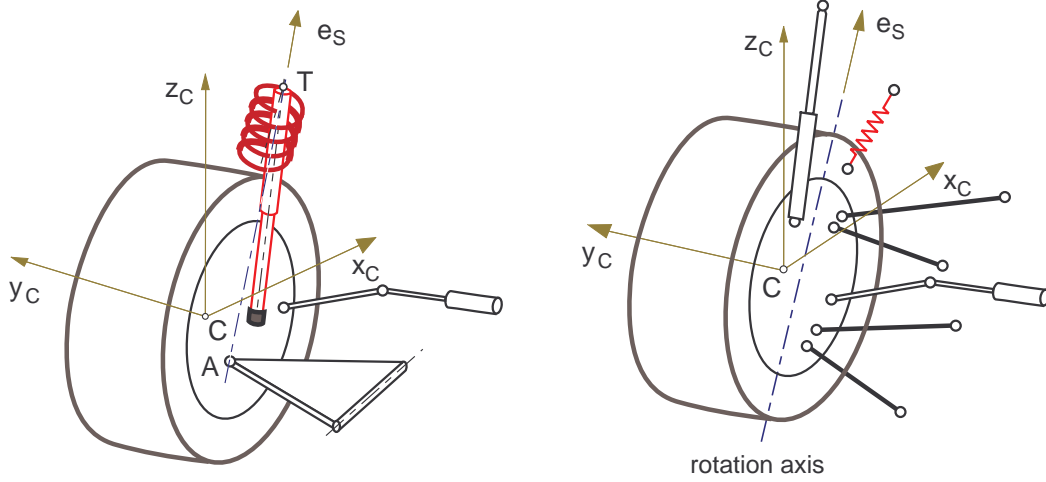


Figure 5.8: McPherson and multi-link wheel suspensions

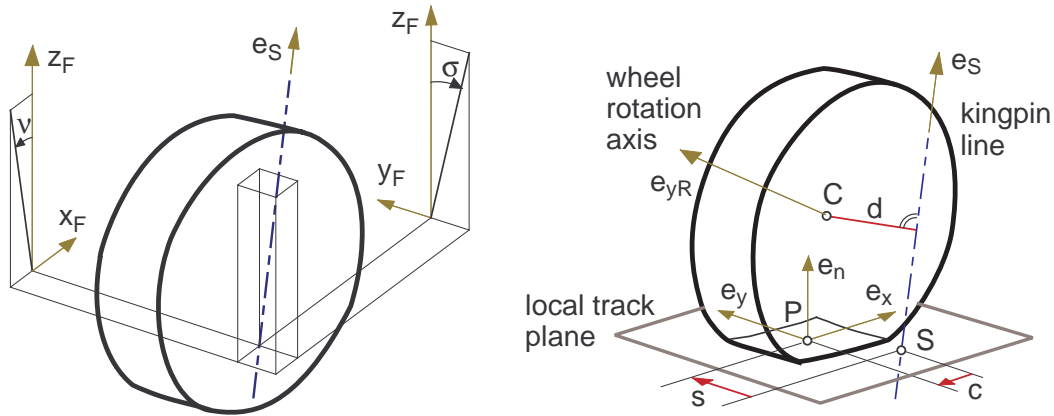


Figure 5.9: Kingpin inclination and caster and steering offset

inclination angle  $\sigma$ , Fig. 5.9. At many axles the kingpin and caster angle can no longer be determined directly. Here, the current rotation axis at steering motions, which can be taken from kinematic calculations will yield a virtual kingpin line. The current values of the caster angle  $\nu$  and the kingpin inclination angle  $\sigma$  can be calculated from the components of the unit vector  $e_s$  in the direction of the kingpin line, described in the vehicle fixed reference frame

$$\tan \nu = \frac{-e_{S,F}^{(1)}}{e_{S,F}^{(3)}} \quad \text{and} \quad \tan \sigma = \frac{-e_{S,F}^{(2)}}{e_{S,F}^{(3)}}, \quad (5.4)$$

where  $e_{S,F}^{(1)}$ ,  $e_{S,F}^{(2)}$ ,  $e_{S,F}^{(3)}$  are the components of the unit vector  $e_{S,F}$  expressed in the vehicle fixed reference frame  $F$ .

The contact point  $P$ , the local track normal  $e_n$  and the unit vectors  $e_x$  and  $e_y$  which point into the direction of the longitudinal and lateral tire force result from the contact geometry. The axle kinematics defines the kingpin axis. In general, the point  $S$  where an extension of the kingpin axis meets the road surface does not coincide with the contact point  $P$ , Fig. 5.9. As both points are located on the local track plane, for the left wheel the vector from  $S$  to  $P$  can be written as

$$r_{SP} = -c e_x + s e_y, \quad (5.5)$$

where  $s$  names the steering offset or scrub radius and  $c$  is the caster. Caster and steering offset will be positive, if  $S$  is located in front of and inwards of  $P$ . The kingpin offset  $d$  describes the distance between the wheel center  $C$  and the king pin axis. It is an important quantity in evaluating the overall steering behavior, [18].

## 5.3 Steering Systems

### 5.3.1 Components and Requirements

The steering system is a very important interface between driver and vehicle. Via the steering wheel the driver controls the vehicle and gets a feedback by the steering torque. The traditional steering system of high speed vehicles is a mechanical system consisting of the steering wheel, the steering shaft, the steering box and the steering linkage. Usually the steering torque produced by the driver is amplified by a hydraulic system. Modern steering systems use an overriding gear to amplify or change the steering wheel angle. Recently some companies have started investigations on 'steer by wire' techniques. In the future steer-by-wire systems will be used probably. Here an electronically controlled actuator is used to convert the rotation of the steering wheel into steer movements of the wheels. Steer-by-wire systems are based on mechanics, micro-controllers, electro-motors, power electronics and digital sensors. At present fail-safe systems with a mechanical backup system are under investigation. Modeling concepts for modern steering systems are discussed in [28].

The steering system must guarantee easy and safe steering of the vehicle. The entirety of the mechanical transmission devices must be able to cope with all loads and stresses occurring in operation.

In order to achieve a good maneuverability a maximum steering angle of approx.  $30^\circ$  must be provided at the front wheels of passenger cars. Depending on the wheel base, busses and trucks need maximum steering angles up to  $55^\circ$  at the front wheels.

### 5.3.2 Rack and Pinion Steering

Rack-and-pinion is the most common steering system of passenger cars, Fig. 5.10. The rack may be located either in front of or behind the axle. Firstly, the rotations

## 5 Suspension System

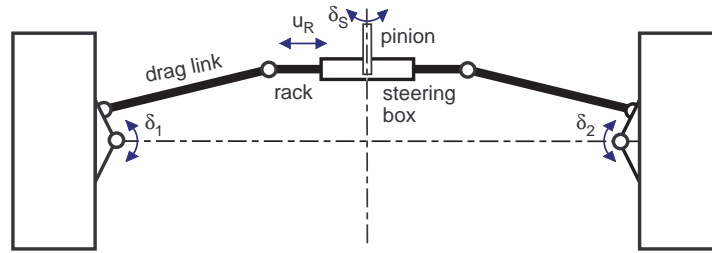


Figure 5.10: Rack and pinion steering

of the steering wheel  $\delta_S$  are transformed by the steering box to the rack travel  $u_R = u_R(\delta_S)$  and then via the drag links transmitted to the wheel rotations  $\delta_1 = \delta_1(u_R)$ ,  $\delta_2 = \delta_2(u_R)$ . Hence, the overall steering ratio depends on the ratio of the steering box and on the kinematics of the steering linkage.

### 5.3.3 Lever Arm Steering System

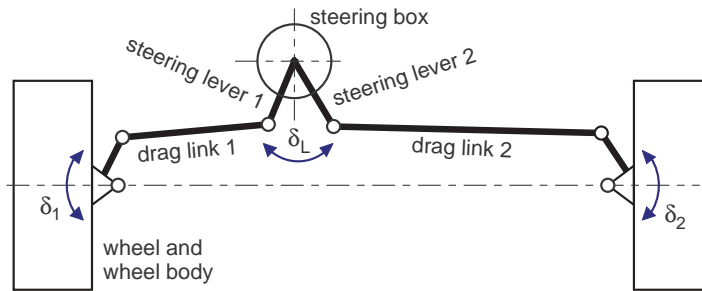


Figure 5.11: Lever arm steering system

Using a lever arm steering system Fig. 5.11, large steering angles at the wheels are possible. This steering system is used on trucks with large wheel bases and independent wheel suspension at the front axle. Here, the steering box can be placed outside of the axle center. At first, the rotations of the steering wheel  $\delta_S$  are transformed by the steering box to the rotation of the steer levers  $\delta_L = \delta_L(\delta_S)$ . The drag links transmit this rotation to the wheel  $\delta_1 = \delta_1(\delta_L)$ ,  $\delta_2 = \delta_2(\delta_L)$ . Hence, the overall steering ratio again depends on the ratio of the steering box and on the kinematics of the steering linkage.

### 5.3.4 Toe Bar Steering System

At solid axles the toe bar steering system is used, Fig. 5.12. The rotations of the steering wheel  $\delta_S$  are transformed by the steering box to the rotation of the steering

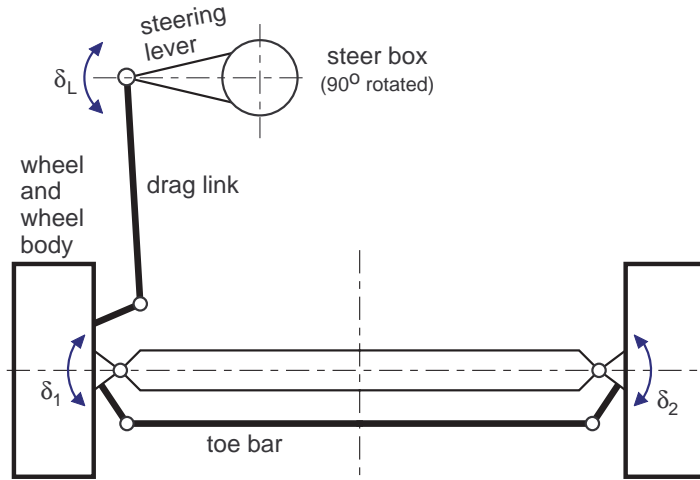


Figure 5.12: Toe bar steering system

lever arm  $\delta_L = \delta_L(\delta_S)$  and further on to the rotation of the left wheel,  $\delta_1 = \delta_1(\delta_L)$ . The toe bar transmits the rotation of the left wheel to the right wheel,  $\delta_2 = \delta_2(\delta_1)$ . The steering ratio is defined by the ratio of the steering box and the kinematics of the steering link. Here, the ratio  $\delta_2 = \delta_2(\delta_1)$  given by the kinematics of the toe bar can be changed separately.

### 5.3.5 Bus Steer System

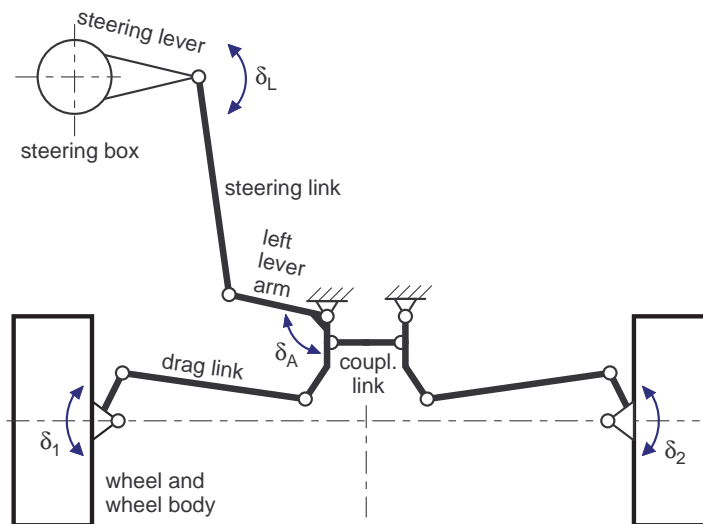


Figure 5.13: Typical bus steering system

## 5 Suspension System

In busses the driver sits more than  $2\text{ m}$  in front of the front axle. In addition, large steering angles at the front wheels are needed to achieve a good manoeuvrability. That is why, more sophisticated steering systems are needed, Fig. 5.13. The rotations of the steering wheel  $\delta_S$  are transformed by the steering box to the rotation of the steering lever arm  $\delta_L = \delta_L(\delta_S)$ . The left lever arm is moved via the steering link  $\delta_A = \delta_A(\delta_L)$ . This motion is transferred by a coupling link to the right lever arm. Finally, the left and right wheels are rotated via the drag links,  $\delta_1 = \delta_1(\delta_A)$  and  $\delta_2 = \delta_2(\delta_A)$ .

# 6 Force Elements

## 6.1 Standard Force Elements

### 6.1.1 Springs

Springs support the weight of the vehicle. In vehicle suspensions coil springs, air springs, torsion bars, and leaf springs are used, Fig. 6.1.

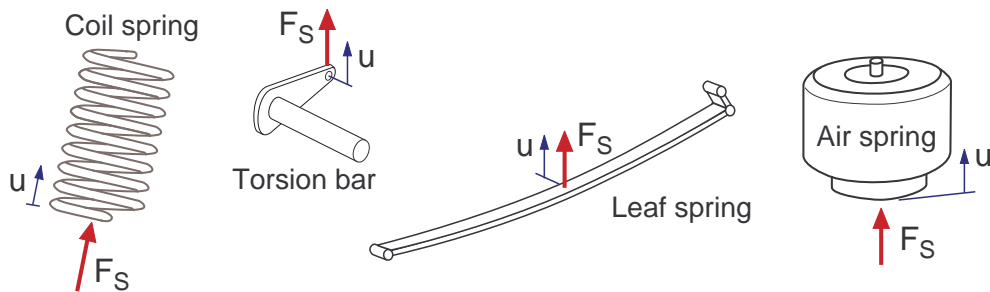


Figure 6.1: Vehicle suspension springs

Coil springs, torsion bars, and leaf springs absorb additional load by compressing. Thus, the ride height depends on the loading condition. Air springs are rubber cylinders filled with compressed air. They are becoming more popular on passenger cars, light trucks, and heavy trucks because here the correct vehicle ride height can be maintained regardless of the loading condition by adjusting the air pressure.

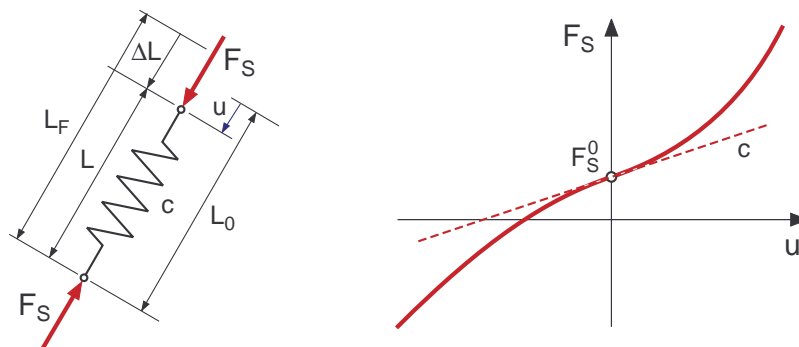


Figure 6.2: Linear coil spring and general spring characteristics

## 6 Force Elements

A linear coil spring may be characterized by its free length  $L_F$  and the spring stiffness  $c$ , Fig. 6.2. The force acting on the spring is then given by

$$F_S = c (L_F - L) , \quad (6.1)$$

where  $L$  denotes the actual length of the spring. Mounted in a vehicle suspension the spring has to support the corresponding chassis weight. Hence, the spring will be compressed to the configuration length  $L_0 < L_F$ . Now, Eq. (6.1) can be written as

$$F_S = c (L_F - (L_0 - u)) = c (L_F - L_0) + c u = F_S^0 + c u , \quad (6.2)$$

where  $F_S^0$  is the spring preload and  $u$  describes the spring displacement measured from the spring's configuration length.

In general the spring force  $F_S$  can be defined by a nonlinear function of the spring displacement  $u$

$$F_S = F_S(u) . \quad (6.3)$$

Now, arbitrary spring characteristics can be approximated by elementary functions, like polynomials, or by tables which are then inter- and extrapolated by linear functions or cubic splines.

The complex behavior of leaf springs and air springs can only be approximated by simple nonlinear spring characteristics,  $F_S = F_S(u)$ . For detailed investigations sophisticated, [30] or even dynamic spring models, [6] have to be used.

### 6.1.2 Anti-Roll Bar

The anti-roll or anti-sway bar or stabilizer is used to reduce the roll angle during cornering and to provide additional stability. Usually, it is simply a U-shaped metal rod connected to both of the lower control arms, Fig. 6.3. Thus, the two wheels of an axle are interconnected by a torsion bar spring. This affects each one-sided bouncing. The axle with the stronger stabilizer is rather inclined to breaking out, in order to reduce the roll angle.

When the suspension at one wheel moves up and on the other down the anti-roll bar generates a force acting in opposite direction at each wheel. In a good approximation this force is given by

$$F_{arb} = \pm c_{arb} (s_1 - s_2) , \quad (6.4)$$

where  $s_1, s_2$  denote the vertical suspension motion of the left and right wheel center, and  $c_{arb}^W$  in [N/m] names the stiffness of the anti-roll bar with respect to the vertical suspension motions of the wheel centers.

Assuming a simple U-shaped anti-roll bar the stiffness of the anti-roll bar is defined by the geometry and material properties. Vertical forces with the magnitude

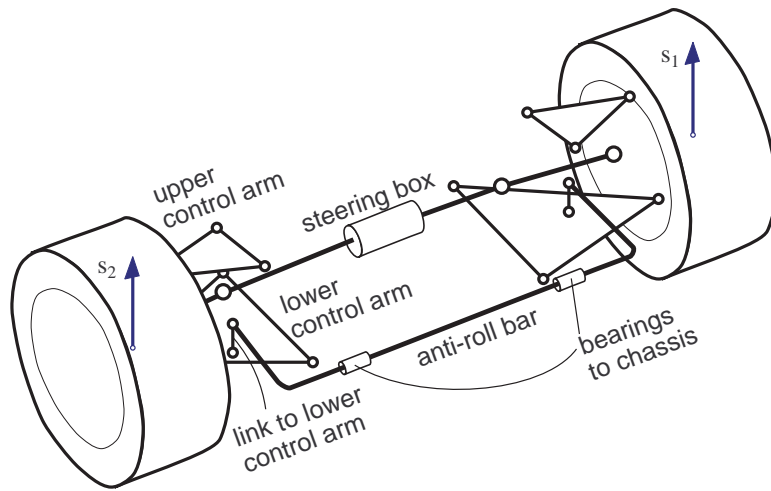


Figure 6.3: Axle with anti-roll bar attached to lower control arms

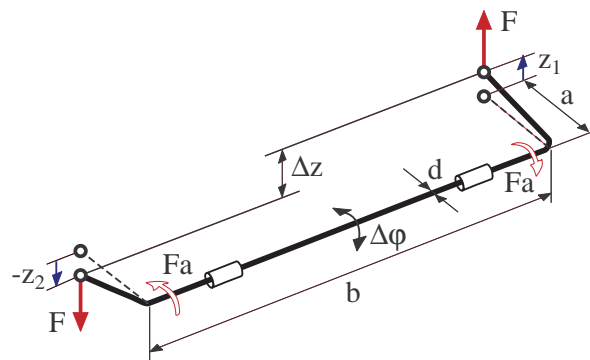


Figure 6.4: Anti-roll bar loaded by vertical forces

$F$  applied in opposite direction at both ends to the anti-roll bar, result in the vertical displacement  $\Delta z$  measured between both ends of the anti-roll bar, Fig. 6.4. The stiffness of the anti-roll bar itself is then defined by

$$c = \frac{F}{\Delta z} . \tag{6.5}$$

Neglecting all bending effects one gets

$$\Delta z = a \Delta\varphi = a \frac{F a b}{G \frac{\pi}{32} D^4} , \tag{6.6}$$

## 6 Force Elements

where  $G$  denotes the modulus of shear and the distances  $a$  and  $b$  are defined in Fig. 6.4. Hence, the stiffness of the anti-roll bar is given by

$$c = \frac{\pi}{32} \frac{G D^4}{a^2 b}. \quad (6.7)$$

Depending on the axle design the ends of the anti-roll bar are attached via links to the knuckle or, as shown in Fig. refFig:susp Axle with anti-roll bar, to the lower control arm. In both cases the displacement of the anti-roll bar end is given as a function of the vertical suspension motion of the wheel center. For small displacements one gets

$$z_1 = i_{arb} s_1 \quad \text{and} \quad z_2 = i_{arb} s_2, \quad (6.8)$$

where  $i_{arb}$  denotes the ratio of the vertical motions of the wheel centers  $s_1, s_2$  and the anti-roll bar ends  $z_1, z_2$ . Now, the stiffness of the anti-roll bar with respect to the vertical suspension motions of the wheel centers is given by

$$c_{arb} = i_{arb}^2 \frac{\pi}{32} \frac{G D^4}{a^2 b}. \quad (6.9)$$

The stiffness strongly depends (fourth power) on the diameter of the anti-roll bar.

For a typical passenger car the following data will hold:  $a = 230 \text{ mm}$ ,  $b = 725 \text{ mm}$ ,  $D = 20 \text{ mm}$  and  $i_{arb} = 2/3$ . The shear modulus of steel is given by  $G = 85\,000 \text{ N/mm}^2$ . Then, one gets

$$c_{arb} = \left(\frac{2}{3}\right)^2 \frac{\pi}{32} \frac{85\,000 \text{ N/mm}^2 (20 \text{ mm})^4}{(230 \text{ mm})^2 725 \text{ mm}} = 15.5 \text{ N/mm} = 15\,500 \text{ N/m}. \quad (6.10)$$

This simple calculation will produce the real stiffness not exactly, because bending effects and compliances in the anti-roll bar bearings will reduce the stiffness of the anti-roll bar.

### 6.1.3 Damper

Dampers are basically oil pumps, Fig. 6.5. As the suspension travels up and down, the hydraulic fluid is forced by a piston through tiny holes, called orifices. This slows down the suspension motion.

Today twin-tube and mono-tube dampers are used in vehicle suspension systems. Dynamic damper model, like the one in [1], compute the damper force via the fluid pressure applied to each side of the piston. The change in fluid pressures in the compression and rebound chambers are calculated by applying the conservation of mass.

In standard vehicle dynamics applications simple characteristics

$$F_D = F_D(v) \quad (6.11)$$

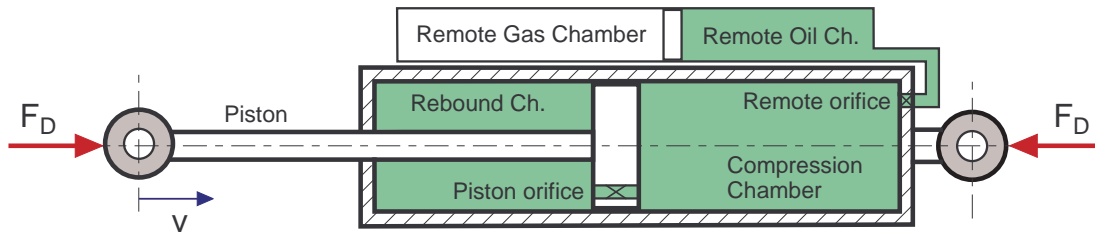


Figure 6.5: Principle of a mono-tube damper

are used to describe the damper force  $F_D$  as a function of the damper velocity  $v$ . To obtain this characteristics the damper is excited with a sinusoidal displacement signal  $u = u_0 \sin 2\pi ft$ . By varying the frequency in several steps from  $f = f_0$  to  $f = f_E$  different force displacement curves  $F_D = F_D(u)$  are obtained, Fig. 6.6. By taking the peak values of the damper force at the displacement  $u = u_0$  which corresponds with the velocity  $v = \pm 2\pi f u_0$  the characteristics  $F_D = F_D(v)$  is generated now. Here, the rebound cycle is associated with negative damper velocities.

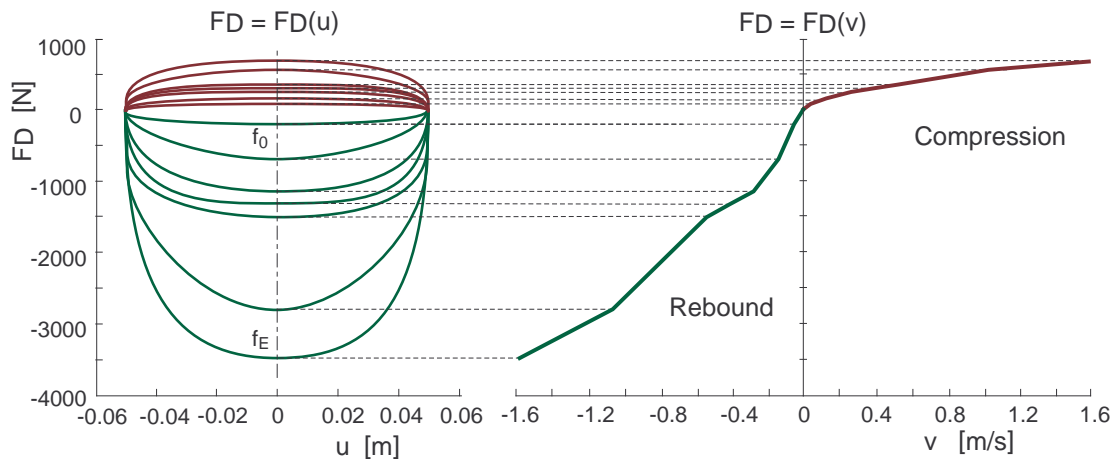


Figure 6.6: Damper characteristics generated from measurements, [12]

Typical passenger car or truck dampers will have more resistance during its rebound cycle than its compression cycle.

#### 6.1.4 Rubber Elements

Force elements made of natural rubber or urethane compounds are used in many locations on the vehicle suspension system, Fig. 6.7. Those elements require no lubrication, isolate minor vibration, reduce transmitted road shock, operate noise free, offer high load carrying capabilities, and are very durable.

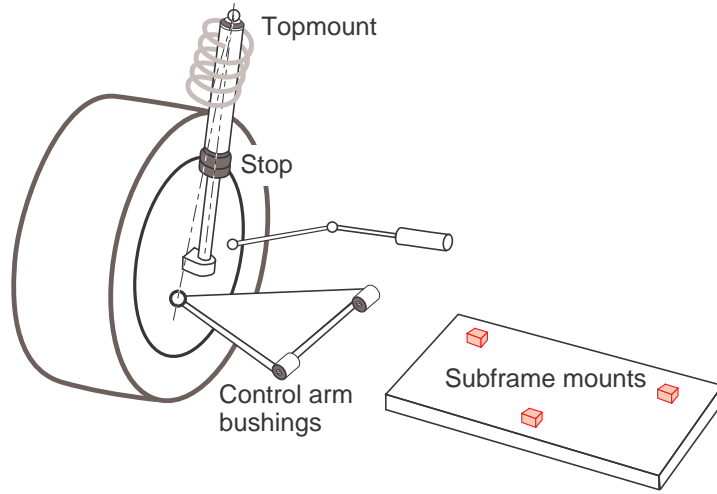


Figure 6.7: Rubber elements in vehicle suspension

During suspension travel, the control arm bushings provide a pivot point for the control arm. They also maintain the exact wheel alignment by fixing the lateral and vertical location of the control arm pivot points. During suspension travel the rubber portion of the bushing must twist to allow control arm motion. Thus, an additional resistance to suspension motion is generated.

Bump and rebound stops limit the suspension travel. The compliance of the topmount avoids the transfer of large shock forces to the chassis. The subframe mounts isolate the suspension system from the chassis and allow elasto-kinematic steering effects of the whole axle.

It turns out, that those elastic elements can hardly be described by simple spring and damper characteristics,  $F_S = F_S(u)$  and  $F_D = F_D(v)$ , because their stiffness and damping properties change with the frequency of the motion. Here, more sophisticated dynamic models are needed.

## 6.2 Dynamic Force Elements

### 6.2.1 Testing and Evaluating Procedures

The effect of dynamic force elements is usually evaluated in the frequency domain. For this, on test rigs or in simulation the force element is excited by sine waves

$$x_e(t) = A \sin(2\pi f t), \quad (6.12)$$

with different frequencies  $f_0 \leq f \leq f_E$  and amplitudes  $A_{min} \leq A \leq A_{max}$ . Starting at  $t = 0$ , the system will usually be in a steady state condition after several periods  $t \geq nT$ , where  $T = 1/f$  and  $n = 2, 3, \dots$  have to be chosen appropriately. Due to the

nonlinear system behavior the system response is periodic,  $F(t + T) = F(t)$ , where  $T = 1/f$ , yet not harmonic. That is why, the measured or calculated force  $F$  will be approximated within one period  $nT \leq t \leq (n + 1)T$ , by harmonic functions as good as possible

$$\underbrace{F(t)}_{\substack{\text{measured/} \\ \text{calculated}}} \approx \underbrace{\alpha \sin(2\pi f t) + \beta \cos(2\pi f t)}_{\text{first harmonic approximation}}. \quad (6.13)$$

The coefficients  $\alpha$  and  $\beta$  can be calculated from the demand for a minimal overall error

$$\frac{1}{2} \int_{nT}^{(n+1)T} \left( \alpha \sin(2\pi f t) + \beta \cos(2\pi f t) - F(t) \right)^2 dt \longrightarrow \text{Minimum}. \quad (6.14)$$

The differentiation of Eq. (6.14) with respect to  $\alpha$  and  $\beta$  yields two linear equations as necessary conditions

$$\begin{aligned} \int_{nT}^{(n+1)T} \left( \alpha \sin(2\pi f t) + \beta \cos(2\pi f t) - F(t) \right) \sin(2\pi f t) dt &= 0 \\ \int_{nT}^{(n+1)T} \left( \alpha \sin(2\pi f t) + \beta \cos(2\pi f t) - F(t) \right) \cos(2\pi f t) dt &= 0 \end{aligned} \quad (6.15)$$

with the solutions

$$\begin{aligned} \alpha &= \frac{\int F \sin dt \int \cos^2 dt - \int F \cos dt \int \sin \cos dt}{\int \sin^2 dt \int \cos^2 dt - 2 \int \sin \cos dt} \\ \beta &= \frac{\int F \cos dt \int \sin^2 dt - \int F \sin dt \int \sin \cos dt}{\int \sin^2 dt \int \cos^2 dt - 2 \int \sin \cos dt} \end{aligned}, \quad (6.16)$$

where the integral limits and arguments of sine and cosine no longer have been written. Because it is integrated exactly over one period  $nT \leq t \leq (n + 1)T$ , for the integrals in Eq. (6.16)

$$\int \sin \cos dt = 0; \quad \int \sin^2 dt = \frac{T}{2}; \quad \int \cos^2 dt = \frac{T}{2} \quad (6.17)$$

hold, and as solution

$$\alpha = \frac{2}{T} \int F \sin dt, \quad \beta = \frac{2}{T} \int F \cos dt \quad (6.18)$$

remains. However, these are exactly the first two coefficients of a Fourier approximation.

## 6 Force Elements

The first order harmonic approximation in Eq. (6.13) can now be written as

$$F(t) = \hat{F} \sin(2\pi f t + \Psi) \quad (6.19)$$

where amplitude  $\hat{F}$  and phase angle  $\Psi$  are given by

$$\hat{F} = \sqrt{\alpha^2 + \beta^2} \quad \text{and} \quad \tan \Psi = \frac{\beta}{\alpha}. \quad (6.20)$$

A simple force element consisting of a linear spring with the stiffness  $c$  and a linear damper with the constant  $d$  in parallel would respond with

$$F(t) = c x_e + d \dot{x}_e = c A \sin 2\pi f t + d 2\pi f A \cos 2\pi f t. \quad (6.21)$$

Here, amplitude and phase angle are given by

$$\hat{F} = A \sqrt{c^2 + (2\pi f d)^2} \quad \text{and} \quad \tan \Psi = \frac{d 2\pi f A}{c A} = 2\pi f \frac{d}{c}. \quad (6.22)$$

Hence, the response of a pure spring,  $c \neq 0$  and  $d = 0$  is characterized by  $\hat{F} = A c$  and  $\tan \Psi = 0$  or  $\Psi = 0$ , whereas a pure damper response with  $c = 0$  and  $d \neq 0$  results in  $\hat{F} = 2\pi f d A$  and  $\tan \Psi \rightarrow \infty$  or  $\Psi = 90^\circ$ . Hence, the phase angle  $\Psi$  which is also called the dissipation angle can be used to evaluate the damping properties of the force element. The dynamic stiffness, defined by

$$c_{dyn} = \frac{\hat{F}}{A} \quad (6.23)$$

is used to evaluate the stiffness of the element.

In practice the frequency response of a system is not determined punctually, but continuously. For this, the system is excited by a sweep-sine. In analogy to the simple sine-function

$$x_e(t) = A \sin(2\pi f t), \quad (6.24)$$

where the period  $T = 1/f$  appears as pre-factor at differentiation

$$\dot{x}_e(t) = A 2\pi f \cos(2\pi f t) = \frac{2\pi}{T} A \cos(2\pi f t). \quad (6.25)$$

A generalized sine-function can be constructed, now. Starting with

$$x_e(t) = A \sin(2\pi h(t)), \quad (6.26)$$

the time derivative results in

$$\dot{x}_e(t) = A 2\pi \dot{h}(t) \cos(2\pi h(t)). \quad (6.27)$$

In the following we demand that the function  $h(t)$  generates periods fading linearly in time, i.e:

$$\dot{h}(t) = \frac{1}{T(t)} = \frac{1}{p - qt}, \quad (6.28)$$

where  $p > 0$  and  $q > 0$  are constants yet to determine. Eq. (6.28) yields

$$h(t) = -\frac{1}{q} \ln(p - qt) + C. \quad (6.29)$$

The initial condition  $h(t = 0) = 0$  fixes the integration constant

$$C = \frac{1}{q} \ln p. \quad (6.30)$$

With Eqs. (6.30) and (6.29) Eq. (6.26) results in a sine-like function

$$x_e(t) = A \sin\left(\frac{2\pi}{q} \ln \frac{p}{p - qt}\right), \quad (6.31)$$

which is characterized by linear fading periods.

The important zero values for determining the period duration lie at

$$\frac{1}{q} \ln \frac{p}{p - qt_n} = 0, 1, 2, \quad \text{or} \quad \frac{p}{p - qt_n} = e^{nq}, \quad \text{mit } n = 0, 1, 2, \quad (6.32)$$

and

$$t_n = \frac{p}{q}(1 - e^{-nq}), \quad n = 0, 1, 2, \dots \quad (6.33)$$

The time difference between two zero values yields the period

$$\begin{aligned} T_n &= t_{n+1} - t_n = \frac{p}{q}(1 - e^{-(n+1)q} - 1 + e^{-nq}) \\ T_n &= \frac{p}{q} e^{-nq} (1 - e^{-q}) \end{aligned}, \quad n = 0, 1, 2, \dots \quad (6.34)$$

For the first ( $n = 0$ ) and last ( $n = N$ ) period one finds

$$\begin{aligned} T_0 &= \frac{p}{q} (1 - e^{-q}) \\ T_N &= \frac{p}{q} (1 - e^{-q}) e^{-Nq} = T_0 e^{-Nq} \end{aligned}. \quad (6.35)$$

With the frequency range to investigate, given by the initial  $f_0$  and final frequency  $f_E$ , the parameters  $q$  and the ratio  $q/p$  can be calculated from Eq. (6.35)

$$q = \frac{1}{N} \ln \frac{f_E}{f_0}, \quad \frac{q}{p} = f_0 \left\{ 1 - \left[ \frac{f_E}{f_0} \right]^{\frac{1}{N}} \right\}, \quad (6.36)$$

with  $N$  fixing the number of frequency intervals. The passing of the whole frequency range then takes the time

$$t_{N+1} = \frac{1 - e^{-(N+1)q}}{q/p}. \quad (6.37)$$

Hence, to test or simulate a force element in the frequency range from  $0.1 \text{ Hz}$  to  $f = 100 \text{ Hz}$  with  $N = 500$  intervals will only take  $728 \text{ s}$  or  $12 \text{ min}$ .

### 6.2.2 Simple Spring Damper Combination

Fig. 6.8 shows a simple dynamic force element where a linear spring with the stiffness  $c$  and a linear damper with the damping constant  $d$  are arranged in series. The displacements of the force element and the spring itself are described by  $u$  and  $s$ . Then, the forces acting in the spring and damper are given by

$$F_S = c s \quad \text{and} \quad F_D = d(\dot{u} - \dot{s}). \quad (6.38)$$

The force balance  $F_D = F_S$  results in a linear first order differential equation for the spring displacement  $s$

$$d(\dot{u} - \dot{s}) = c s \quad \text{or} \quad \frac{d}{c} \dot{s} = -s + \frac{d}{c} \dot{u}, \quad (6.39)$$

where the ratio between the damping coefficient  $d$  and the spring stiffness  $c$  acts as time constant,  $T = d/c$ . Hence, this force element will respond dynamically to any excitation.

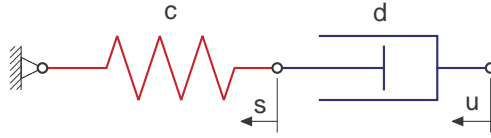


Figure 6.8: Spring and damper in series

The steady state response to a harmonic excitation

$$u(t) = u_0 \sin \Omega t \quad \text{respectively} \quad \dot{u} = u_0 \Omega \cos \Omega t \quad (6.40)$$

can be calculated easily. The steady state response will be of the same type as the excitation. Inserting

$$s_\infty(t) = u_0 (a \sin \Omega t + b \cos \Omega t) \quad (6.41)$$

into Eq. (6.39) results in

$$\frac{d}{c} \underbrace{u_0 (a \Omega \cos \Omega t - b \Omega \sin \Omega t)}_{\dot{s}_\infty} = - \underbrace{u_0 (a \sin \Omega t + b \cos \Omega t)}_{s_\infty} + \frac{d}{c} \underbrace{u_0 \Omega \cos \Omega t}_{\dot{u}}. \quad (6.42)$$

Collecting all sine and cosine terms we obtain two equations

$$- \frac{d}{c} u_0 b \Omega = -u_0 a \quad \text{and} \quad \frac{d}{c} u_0 a \Omega = -u_0 b + \frac{d}{c} u_0 \Omega \quad (6.43)$$

which can be solved for the two unknown parameter

$$a = \frac{\Omega^2}{\Omega^2 + (c/d)^2} \quad \text{and} \quad b = \frac{c}{d} \frac{\Omega}{\Omega^2 + (c/d)^2}. \quad (6.44)$$

Hence, the steady state force response reads as

$$F_S = c s_\infty = c u_0 \frac{\Omega}{\Omega^2 + (c/d)^2} \left( \Omega \sin \Omega t + \frac{c}{d} \cos \Omega t \right) \quad (6.45)$$

which can be transformed to

$$F_S = \hat{F}_S \sin(\Omega t + \Psi) \quad (6.46)$$

where the force magnitude  $\hat{F}_S$  and the phase angle  $\Psi$  are given by

$$\hat{F}_S = \frac{c u_0 \Omega}{\Omega^2 + (c/d)^2} \sqrt{\Omega^2 + (c/d)^2} = \frac{c u_0 \Omega}{\sqrt{\Omega^2 + (c/d)^2}} \quad \text{and} \quad \Psi = \arctan \frac{c/d}{\Omega}. \quad (6.47)$$

The dynamic stiffness  $c_{dyn} = \hat{F}_S/u_0$  and the phase angle  $\Psi$  are plotted in Fig. 6.9 for different damping values.

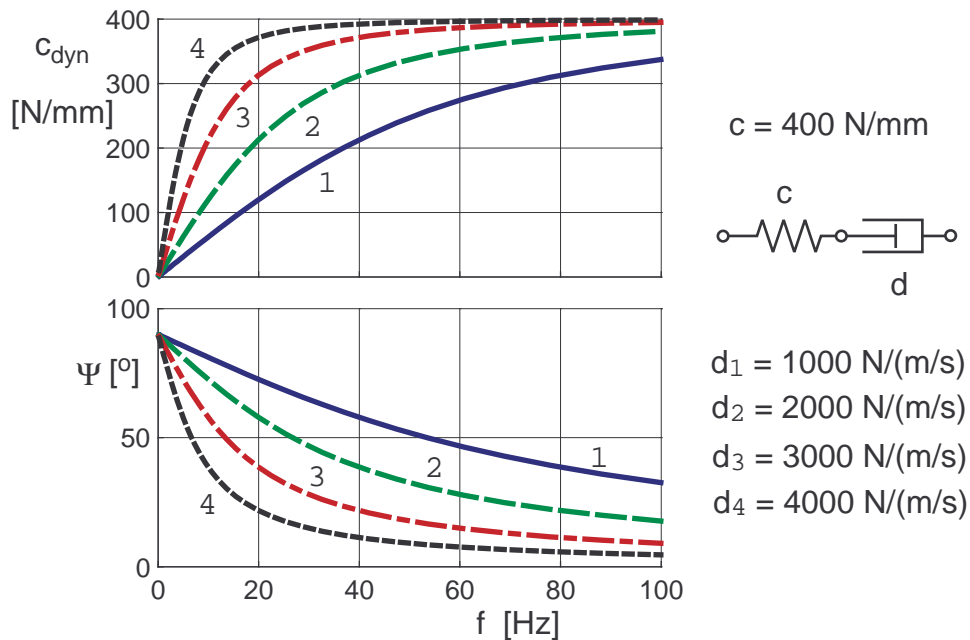


Figure 6.9: Frequency response of a spring damper combination

With increasing frequency the spring damper combination changes from a pure damper performance,  $c_{dyn} \rightarrow 0$  and  $\Psi \approx 90^\circ$  to a pure spring behavior,  $c_{dyn} \approx c$  and  $\Psi \rightarrow 0$ . The frequency range, where the element provides stiffness and damping is controlled by the value for the damping constant  $d$ .

### 6.2.3 General Dynamic Force Model

To approximate the complex dynamic behavior of bushings and elastic mounts different spring damper models can be combined. A general dynamic force model is

## 6 Force Elements

constructed by  $N$  parallel force elements, Fig. 6.10. The static load is carried by a single spring with the stiffness  $c_0$  or an arbitrary nonlinear force characteristics  $F_0 = F_0(u)$ .

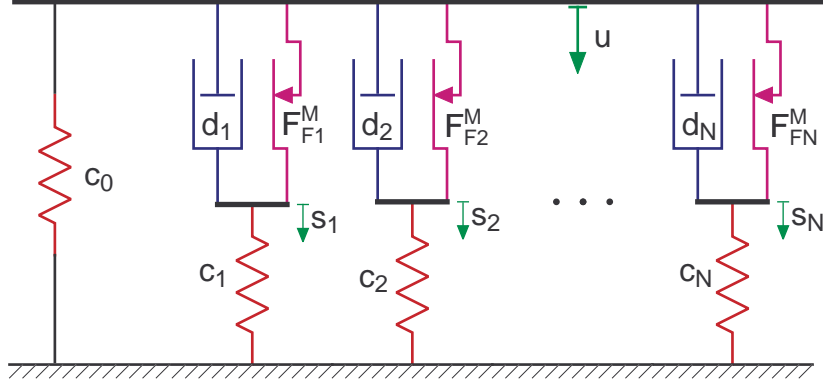


Figure 6.10: Dynamic force model

Within each force element the spring acts in serial to parallel combination of a damper and a dry friction element. Now, even hysteresis effects and the stress history of the force element can be taken into account.

The forces acting in the spring and damper of force element  $i$  are given by

$$F_{Si} = -c_i s_i \quad \text{and} \quad F_{Di} = d_i (\dot{s}_i - \dot{u}), \quad (6.48)$$

where  $u$  and  $s_i$  describe the overall element and the spring displacement.

As long as the absolute value of the spring force  $F_{Si}$  is lower than the maximum friction force  $F_{Fi}^M$  the damper friction combination will not move at all

$$\dot{u} - \dot{s}_i = 0 \quad \text{for} \quad |F_{Si}| \leq F_{Fi}^M. \quad (6.49)$$

In all other cases the force balance

$$F_{Si} = F_{Di} \pm F_{Fi}^M \quad (6.50)$$

holds. Using Eq. 6.48 the force balance results in

$$d_i (\dot{s}_i - \dot{u}) = F_{Si} \mp F_{Fi}^M \quad (6.51)$$

which can be combined with Eq. 6.49 to

$$d_i \dot{s}_i = \begin{cases} F_{Si} + F_{Fi}^M & F_{Si} < -F_{Fi}^M \\ d_i \dot{u} & \text{for} \quad -F_{Fi}^M \leq F_{Si} \leq +F_{Fi}^M \\ F_{Si} - F_{Fi}^M & +F_{Fi}^M < F_{Si} \end{cases} \quad (6.52)$$

where according to Eq. 6.48 the spring force is given by  $F_{Si} = -c_i s_i$ .

In extension to this linear approach nonlinear springs and dampers may be used. To derive all the parameters an extensive set of static and dynamic measurements is needed.

### 6.2.3.1 Hydro-Mount

For the elastic suspension of engines in vehicles very often specially developed hydro-mounts are used. The dynamic nonlinear behavior of these components guarantees a good acoustic decoupling but simultaneously provides sufficient damping.

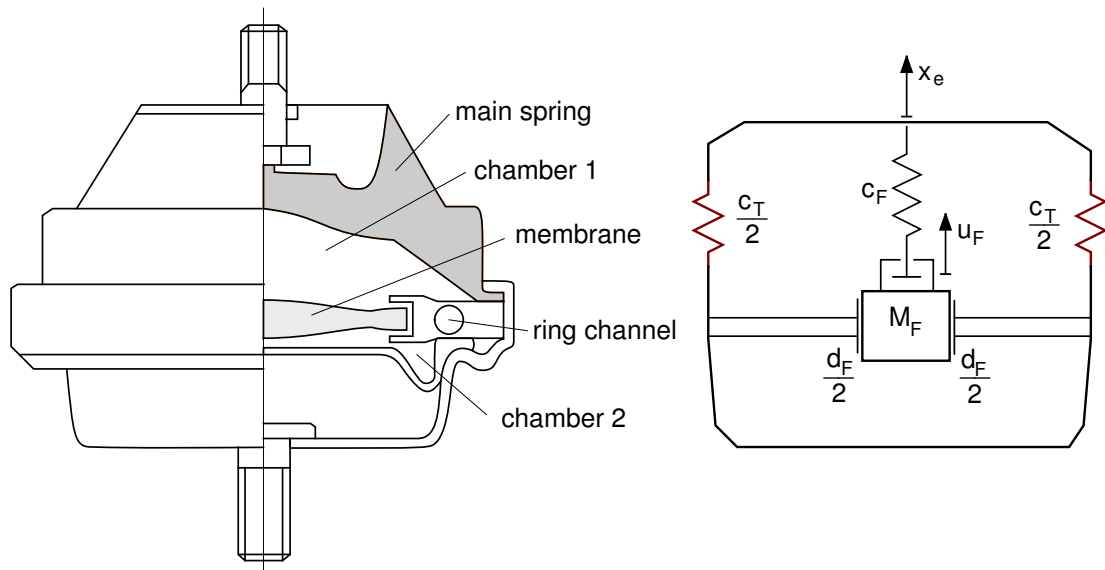


Figure 6.11: Hydro-mount

Fig. 6.11 shows the principle and mathematical model of a hydro-mount. At small deformations the change of volume in chamber 1 is compensated by displacements of the membrane. When the membrane reaches the stop, the liquid in chamber 1 is pressed through a ring channel into chamber 2. The ratio of the chamber cross section to the ring channel cross section is very large. Thus the fluid is moved through the ring channel at very high speed. This results in remarkable inertia and resistance forces (damping forces).

The force effect of a hydro-mount is combined from the elasticity of the main spring and the volume change in chamber 1.

With  $u_F$  labeling the displacement of the generalized fluid mass  $M_F$ ,

$$F_H = c_T x_e + F_F(x_e - u_F) \tag{6.53}$$

holds, where the force effect of the main spring has been approximated by a linear spring with the constant  $c_T$ .

## 6 Force Elements

With  $M_{FR}$  as the actual mass in the ring channel and the cross sections  $A_K$ ,  $A_R$  of chamber and ring channel the generalized fluid mass is given by

$$M_F = \left(\frac{A_K}{A_R}\right)^2 M_{FR}. \quad (6.54)$$

The fluid in chamber 1 is not being compressed, unless the membrane can evade no longer. With the fluid stiffness  $c_F$  and the membrane clearance  $s_F$ , one gets

$$F_F(x_e - u_F) = \begin{cases} c_F \left( (x_e - u_F) + s_F \right) & (x_e - u_F) < -s_F \\ 0 & \text{for } |x_e - u_f| \leq s_F \\ c_F \left( (x_e - u_F) - s_F \right) & (x_e - u_f) > +s_F \end{cases} \quad (6.55)$$

The hard transition from clearance  $F_F = 0$  and fluid compression resp. chamber deformation with  $F_F \neq 0$  is not realistic and leads to problems, even with the numeric solution. Therefore, the function (6.55) is smoothed by a parabola in the range  $|x_e - u_f| \leq 2 * s_F$ .

The motions of the fluid mass cause friction losses in the ring channel, which are as a first approximation proportional to the speed,

$$F_D = d_F \dot{u}_F. \quad (6.56)$$

Then, the equation of motion for the fluid mass reads as

$$M_F \ddot{u}_F = -F_F - F_D. \quad (6.57)$$

The membrane clearance makes Eq. (6.57) nonlinear and only solvable by numerical integration. The nonlinearity also affects the overall force in the hydro-mount, Eq. (6.53).

The dynamic stiffness and the dissipation angle of a hydro-mount are displayed in Fig. 6.12 versus the frequency. The simulation is based on the following system parameters

$m_F$	=	25 kg	generalized fluid mass
$c_T$	=	125 000 N/m	stiffness of main spring
$d_F$	=	750 N/(m/s)	damping constant
$c_F$	=	100 000 N/m	fluid stiffness
$s_F$	=	0.0002 mm	clearance in membrane bearing

By the nonlinear and dynamic behavior a very good compromise can be achieved between noise isolation and vibration damping.

## 6.2 Dynamic Force Elements

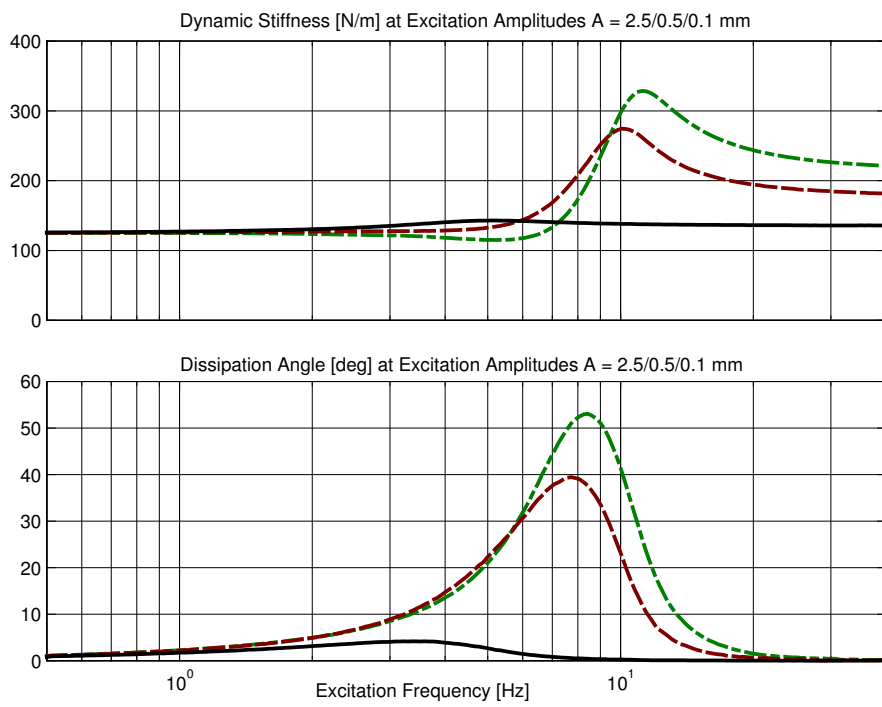


Figure 6.12: Dynamic Stiffness [N/mm] and Dissipation Angle [deg] for a Hydro-Mount

# 7 Vertical Dynamics

## 7.1 Goals

The aim of vertical dynamics is the tuning of body suspension and damping to guarantee good ride comfort, resp. a minimal stress of the load at sufficient safety. The stress of the load can be judged fairly well by maximal or integral values of the body accelerations.

The wheel load  $F_z$  is linked to the longitudinal  $F_x$  and lateral force  $F_y$  by the coefficient of friction. The degressive influence of  $F_z$  on  $F_x$  and  $F_y$  as well as non-stationary processes at the increase of  $F_x$  and  $F_y$  in the average lead to lower longitudinal and lateral forces at wheel load variations. Maximal driving safety can therefore be achieved with minimal variations of the wheel load. Small variations of the wheel load also reduce the stress on the track.

The comfort of a vehicle is subjectively judged by the driver. In literature, i.e. [16], different approaches of describing the human sense of vibrations by different metrics can be found. Transferred to vehicle vertical dynamics, the driver primarily registers the amplitudes and accelerations of the body vibrations. These values are thus used as objective criteria in practice.

## 7.2 Basic Tuning

### 7.2.1 From complex to simple models

For detailed investigations of ride comfort and ride safety sophisticated road and vehicle models are needed, [31]. The three-dimensional vehicle model, shown in Fig. 7.1, includes an elastically suspended engine, and dynamic seat models. The elasto-kinematics of the wheel suspension was described fully nonlinear. In addition, dynamic force elements for the damper elements and the hydro-mounts are used. Such sophisticated models not only provide simulation results which are in good conformity to measurements but also make it possible to investigate the vehicle dynamic attitude in an early design stage.

Much simpler models can be used, however, for basic studies on ride comfort and ride safety. A two-dimensional vehicle model, for instance, suits perfectly with a single track road model, Fig. 7.2. Neglecting longitudinal accelerations, the vehicle chassis only performs hub and pitch motions. Here, the chassis is considered as one rigid body. Then, mass and inertia properties can be represented by three point

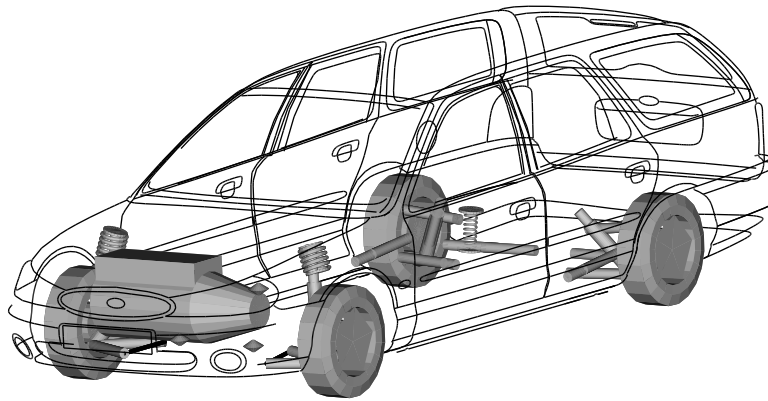


Figure 7.1: Full Vehicle Model

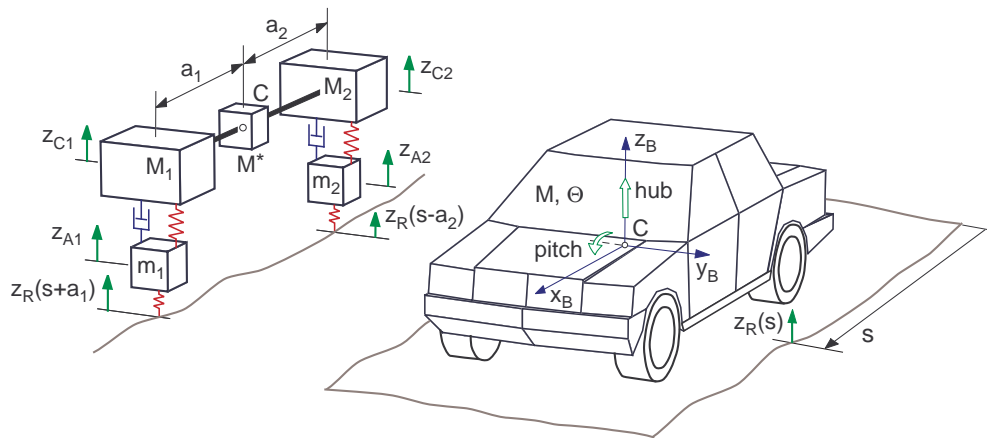


Figure 7.2: Vehicle Model for Basic Comfort and Safety Analysis

masses which are located in the chassis center of gravity and on top of the front and the rear axle. The lumped mass model has 4 degrees of freedom. The hub and pitch motion of the chassis are represented by the vertical motions of the chassis in the front  $z_{C1}$  and in the rear  $z_{C2}$ . The coordinates  $z_{A1}$  and  $z_{A2}$  describe the vertical motions of the front and rear axle. The function  $z_R(s)$  provides road irregularities in the space domain, where  $s$  denotes the distance covered by the vehicle and measured at the chassis center of gravity. Then, the irregularities at the front and rear axle are given by  $z_R(s + a_1)$  and  $z_R(s - a_2)$  respectively, where  $a_1$  and  $a_2$  locate the position of the chassis center of gravity  $C$ .

The point masses must add up to the chassis mass

$$M_1 + M^* + M_2 = M \tag{7.1}$$

## 7 Vertical Dynamics

and they have to provide the same inertia around an axis located in the chassis center  $C$  and pointing into the lateral direction

$$a_1^2 M_1 + a_2^2 M_2 = \Theta. \quad (7.2)$$

The correct location of the center of gravity is assured by

$$a_1 M_1 = a_2 M_2. \quad (7.3)$$

Now, Eqs. (7.2) and (7.3) yield the main masses

$$M_1 = \frac{\Theta}{a_1(a_1+a_2)} \quad \text{and} \quad M_2 = \frac{\Theta}{a_2(a_1+a_2)}, \quad (7.4)$$

and the coupling mass

$$M^* = M \left( 1 - \frac{\Theta}{M a_1 a_2} \right) \quad (7.5)$$

follows from Eq. (7.1).

If the mass and the inertia properties of a real vehicle happen to result in  $\Theta = M a_1 a_2$  then, the coupling mass vanishes  $M^* = 0$ , and the vehicle can be represented by two uncoupled two mass systems describing the vertical motion of the axle and the hub motion of the chassis mass on top of each axle.

Table 7.1: Mass and Inertia Properties of different Vehicles

vehicles		mid size car	full size car	sports utility vehicle	commercial vehicle	heavy truck
front axle mass		80	100	125	120	600
$m_1$ [kg]						
rear axle mass	$m_2$ [kg]	80	100	125	180	1100
center of gravity	$a_1$ [m]	1.10	1.40	1.45	1.90	2.90
	$a_2$ [m]	1.40	1.40	1.38	1.40	1.90
chassis mass	$M$ [kg]	1100	1400	1950	3200	14300
chassis inertia	$\Theta$ [kg m <sup>2</sup> ]	1500	2350	3750	5800	50000
lumped mass model	$M_1$	545	600	914	925	3592
	$M^*$	126	200	76	1020	5225
	$M_2$	429	600	960	1255	5483
	[kg]					

Depending on the actual mass and inertia properties the vertical dynamics of a vehicle can be investigated by two simple decoupled mass models describing the vibrations of the front and rear axle and the corresponding chassis masses. By using half of the chassis and half of the axle mass we finally end up in quarter car models.

The data in Table 7.1 show that for a wide range of passenger cars the coupling mass is smaller than the corresponding chassis masses,  $M^* < M_1$  and  $M^* < M_2$ . Here, the two mass model or the quarter car model represent a quite good approximation to the lumped mass model. For commercial vehicles and trucks, where the coupling mass has the same magnitude as the corresponding chassis masses, the quarter car model serves for basic studies only.

At most vehicles, c.f. Table 7.1, the axle mass is much smaller than the corresponding chassis mass,  $m_i \ll M_i$ ,  $i = 1, 2$ . Hence, for a first basic study axle and chassis motions can be investigated independently. The quarter car model is now further simplified to two single mass models, Fig. 7.3.

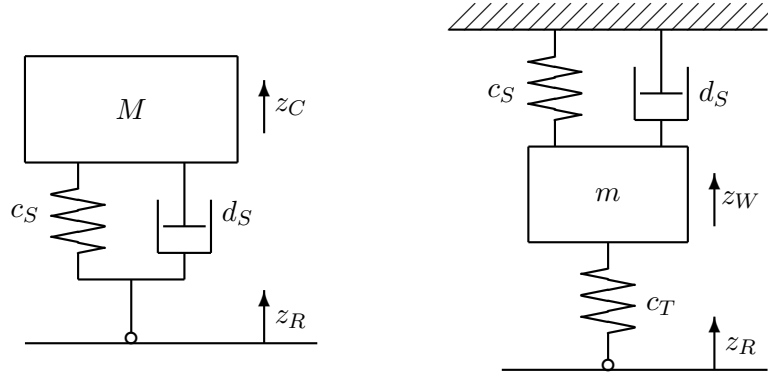


Figure 7.3: Simple Vertical Vehicle Models

The chassis model neglects the tire deflection and the inertia forces of the wheel. For the high frequent wheel motions the chassis can be considered as fixed to the inertia frame.

The equations of motion for the models read as

$$M \ddot{z}_C + d_S \dot{z}_C + c_S z_C = d_S \dot{z}_R + c_S z_R \quad (7.6)$$

and

$$m \ddot{z}_W + d_S \dot{z}_W + (c_S + c_T) z_W = c_T z_R, \quad (7.7)$$

where  $z_C$  and  $z_W$  label the vertical motions of the corresponding chassis mass and the wheel mass with respect to the steady state position. The constants  $c_S$ ,  $d_S$  describe the suspension stiffness and damping. The dynamic wheel load is calculated by

$$F_T^D = c_T (z_R - z_W) \quad (7.8)$$

## 7 Vertical Dynamics

where  $c_T$  is the vertical or radial stiffness of the tire and  $z_R$  denotes the road irregularities. In this simple approach the damping effects in the tire are not taken into account.

### 7.2.2 Natural Frequency and Damping Rate

At an ideally even track the right side of the equations of motion (7.6), (7.7) vanishes because of  $z_R=0$  and  $\dot{z}_R=0$ . The remaining homogeneous second order differential equations can be written in a more general form as

$$\ddot{z} + 2\zeta\omega_0\dot{z} + \omega_0^2 z = 0, \quad (7.9)$$

where  $\omega_0$  represents the undamped natural frequency, and  $\zeta$  is a dimensionless parameter called viscous damping ratio. For the chassis and the wheel model the new parameter are given by

$$\begin{aligned} \text{Chassis:} \quad z \rightarrow z_C, \quad \zeta \rightarrow \zeta_C &= \frac{d_S}{2\sqrt{c_S M}}, \quad \omega_0^2 \rightarrow \omega_{0C}^2 = \frac{c_S}{M}; \\ \text{Wheel:} \quad z \rightarrow z_W, \quad \zeta \rightarrow \zeta_W &= \frac{d_S}{2\sqrt{(c_S+c_T)m}}, \quad \omega_0^2 \rightarrow \omega_{0W}^2 = \frac{c_S+c_T}{m}. \end{aligned} \quad (7.10)$$

The solution of Eq. (7.9) is of the type

$$z(t) = z_0 e^{\lambda t}, \quad (7.11)$$

where  $z_0$  and  $\lambda$  are constants. Inserting Eq. (7.11) into Eq. (7.9) results in

$$(\lambda^2 + 2\zeta\omega_0\lambda + \omega_0^2) z_0 e^{\lambda t} = 0. \quad (7.12)$$

Non-trivial solutions  $z_0 \neq 0$  are possible, if

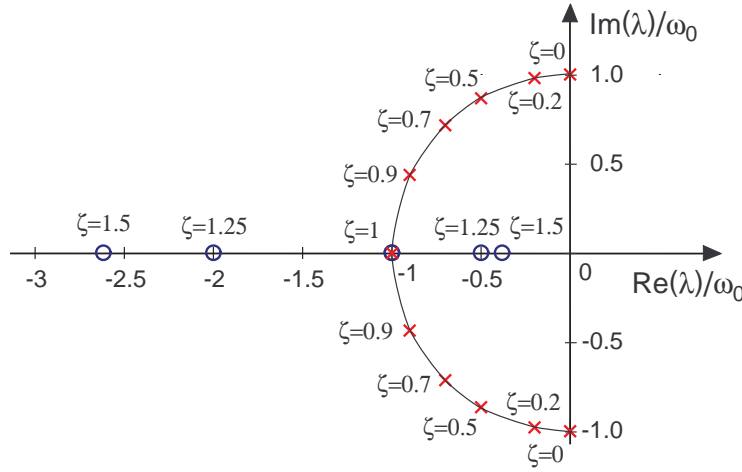
$$\lambda^2 + 2\zeta\omega_0\lambda + \omega_0^2 = 0 \quad (7.13)$$

will hold. The roots of the characteristic equation (7.13) depend on the value of  $\zeta$

$$\begin{aligned} \zeta < 1 : \quad \lambda_{1,2} &= -\zeta\omega_0 \pm i\omega_0\sqrt{1-\zeta^2}, \\ \zeta \geq 1 : \quad \lambda_{1,2} &= -\omega_0 \left( \zeta \mp \sqrt{\zeta^2-1} \right). \end{aligned} \quad (7.14)$$

Figure 7.4 shows the root locus of the eigenvalues for different values of the viscous damping rate  $\zeta$ .

For  $\zeta \geq 1$  the eigenvalues  $\lambda_{1,2}$  are both real and negative. Hence, Eq. (7.11) will produce a exponentially decaying solution. If  $\zeta < 1$  holds, the eigenvalues  $\lambda_{1,2}$  will

Figure 7.4: Eigenvalues  $\lambda_1$  and  $\lambda_2$  for different values of  $\zeta$ 

become complex, where  $\lambda_2$  is the complex conjugate of  $\lambda_1$ . Now, the solution can be written as

$$z(t) = A e^{-\zeta\omega_0 t} \sin\left(\omega_0 \sqrt{1-\zeta^2} t - \Psi\right), \quad (7.15)$$

where  $A$  and  $\Psi$  are constants which have to be adjusted to given initial conditions  $z(0) = z_0$  and  $\dot{z}(0) = \dot{z}_0$ . The real part  $Re(\lambda_{1,2}) = -\zeta\omega_0$  is negative and determines the decay of the solution. The imaginary  $Im(\lambda_{1,2}) = \omega_0 \sqrt{1-\zeta^2}$  part defines the actual frequency of the vibration. The actual frequency

$$\omega = \omega_0 \sqrt{1-\zeta^2} \quad (7.16)$$

tends to zero,  $\omega \rightarrow 0$ , if the viscous damping ratio will approach the value one,  $\zeta \rightarrow 1$ .

In a more general way the relative damping may be judged by the ratio

$$D_\lambda = \frac{-Re(\lambda_{1,2})}{|\lambda_{1,2}|}. \quad (7.17)$$

For complex eigenvalues which characterize vibrations

$$D_\lambda = \zeta \quad (7.18)$$

holds, because the absolute value of the complex eigenvalues is given by

$$|\lambda_{1,2}| = \sqrt{Re(\lambda_{1,2})^2 + Im(\lambda_{1,2})^2} = \sqrt{(-\zeta\omega_0)^2 + (\omega_0 \sqrt{1-\zeta^2})^2} = \omega_0, \quad (7.19)$$

and hence, Eq. (7.17) results in

$$D_\lambda = \frac{+\zeta\omega_0}{\omega_0} = \zeta. \quad (7.20)$$

For  $\zeta \geq 1$  the eigenvalues become real and negative. Then, Eq. (7.17) will always produce the relative damping value  $D_\lambda = 1$ . In this case the viscous damping rate  $\zeta$  is more sensitive.

### 7.2.3 Spring Rates

#### 7.2.3.1 Minimum Spring Rates

The suspension spring is loaded with the corresponding vehicle weight. At linear spring characteristics the steady state spring deflection is calculated from

$$u_0 = \frac{Mg}{c_S}. \quad (7.21)$$

At a conventional suspension without niveau regulation a load variation  $M \rightarrow M + \Delta M$  leads to changed spring deflections  $u_0 \rightarrow u_0 + \Delta u$ . In analogy to (7.21) the additional deflection follows from

$$\Delta u = \frac{\Delta M g}{c_S}. \quad (7.22)$$

If for the maximum load variation  $\Delta M$  the additional spring deflection is limited to  $\Delta u$  the suspension spring rate can be estimated by a lower bound

$$c_S \geq \frac{\Delta M g}{\Delta u}. \quad (7.23)$$

In the standard design of a passenger car the engine is located in the front and the trunk in the rear part of the vehicle. Hence, most of the load is supported by the rear axle suspension.

For an example we assume that 150 kg of the permissible load of 500 kg are going to the front axle. Then, each front wheel is loaded by  $\Delta M_F = 150 \text{ kg}/2 = 75 \text{ kg}$  and each rear wheel by  $\Delta M_R = (500 - 150) \text{ kg}/2 = 175 \text{ kg}$ .

The maximum wheel travel is limited,  $u \leq u_{max}$ . At standard passenger cars it is in the range of  $u_{max} \approx 0.08 \text{ m}$  to  $u_{max} \approx 0.10 \text{ m}$ . By setting  $\Delta u = u_{max}/2$  we demand that the spring deflection caused by the load should not exceed half of the maximum value. Then, according to Eq. (7.23) a lower bound of the spring rate at the front axle can be estimated by

$$c_S^{min} = (75 \text{ kg} * 9.81 \text{ m/s}^2)/(0.08/2) \text{ m} = 18400 \text{ N/m}. \quad (7.24)$$

The maximum load over one rear wheel was estimated here by  $\Delta M_R = 175 \text{ kg}$ . Assuming that the suspension travel at the rear axle is slightly larger,  $u_{max} \approx 0.10 \text{ m}$  the minimum spring rate at the rear axle can be estimated by

$$c_S^{min} = (175 \text{ kg} * 9.81 \text{ m/s}^2)/(0.10/2) \text{ m} = 34300 \text{ N/m}, \quad (7.25)$$

which is nearly two times the minimum value of the spring rate at the front axle. In order to reduce this difference we will choose a spring rate of  $c_S = 20000 \text{ N/m}$  at the front axle.

In Tab. 7.1 the lumped mass chassis model of a full size passenger car is described by  $M_1 = M_2 = 600 \text{ kg}$  and  $M^* = 200$ . To approximate the lumped mass model by

two decoupled two mass models we have to neglect the coupling mass or, in order to achieve the same chassis mass, to distribute  $M^*$  equally to the front and the rear. Then, the corresponding chassis mass of a quarter car model is given here by

$$M = (M_1 + M^*/2) / 2 = (600 \text{ kg} + 200/2 \text{ kg})/2 = 350 \text{ kg} . \quad (7.26)$$

According to Eq. 7.10 the undamped natural eigen frequency of the simple chassis model is then given by  $\omega_{0C}^2 = c_S/M$ . Hence, for a spring rate of  $c_S = 20000 \text{ N/m}$  the undamped natural frequency of the unloaded car amounts to

$$f_{0C} = \frac{1}{2\pi} \sqrt{\frac{20000 \text{ N/m}}{350 \text{ kg}}} = 1.2 \text{ Hz} , \quad (7.27)$$

which is a typical value for most of all passenger cars. Due to the small amount of load the undamped natural frequency for the loaded car does not change very much,

$$f_{0C} = \frac{1}{2\pi} \sqrt{\frac{20000 \text{ N/m}}{(350 + 75) \text{ kg}}} = 1.1 \text{ Hz} . \quad (7.28)$$

The corresponding chassis mass over the rear axle is given here by

$$M = (M_2 + M^*/2) / 2 = (600 \text{ kg} + 200/2 \text{ kg})/2 = 350 \text{ kg} . \quad (7.29)$$

Now the undamped natural frequencies for the unloaded

$$f_{0C}^0 = \frac{1}{2\pi} \sqrt{\frac{34300 \text{ N/m}}{350 \text{ kg}}} = 1.6 \text{ Hz} \quad (7.30)$$

and the loaded car

$$f_{0C}^L = \frac{1}{2\pi} \sqrt{\frac{34300 \text{ N/m}}{(350 + 175) \text{ kg}}} = 1.3 \text{ Hz} \quad (7.31)$$

are larger and differ more.

### 7.2.3.2 Nonlinear Springs

In order to reduce the spring rate at the rear axle and to avoid too large spring deflections when loaded nonlinear spring characteristics are used, Fig. 7.5. Adding soft bump stops the overall spring force in the compression mode  $u \geq 0$  can be modeled by the nonlinear function

$$F_S = F_S^0 + c_0 u \left( 1 + k \left( \frac{u}{\Delta u} \right)^2 \right) , \quad (7.32)$$

where  $F_S^0$  is the spring preload,  $c_S$  describes the spring rate at  $u = 0$ , and  $k > 0$  characterizes the intensity of the nonlinearity. The linear characteristic provides

## 7 Vertical Dynamics

at  $u = \Delta u$  the value  $F_S^{lin}(\Delta u) = F_S^0 + c_S \Delta u$ . To achieve the same value with the nonlinear spring

$$F_S^0 + c_0 \Delta u (1 + k) = F_S^0 + c_S \Delta u \quad \text{or} \quad c_0 (1 + k) = c_S \quad (7.33)$$

must hold, where  $c_S$  describes the spring rate of the corresponding linear characteristics. The local spring rate is determined by the derivative

$$\frac{dF_S}{du} = c_0 \left( 1 + 3k \left( \frac{u}{\Delta u} \right)^2 \right). \quad (7.34)$$

Hence, the spring rate for the loaded car at  $u = \Delta u$  is given by

$$c_L = c_0 (1 + 3k). \quad (7.35)$$

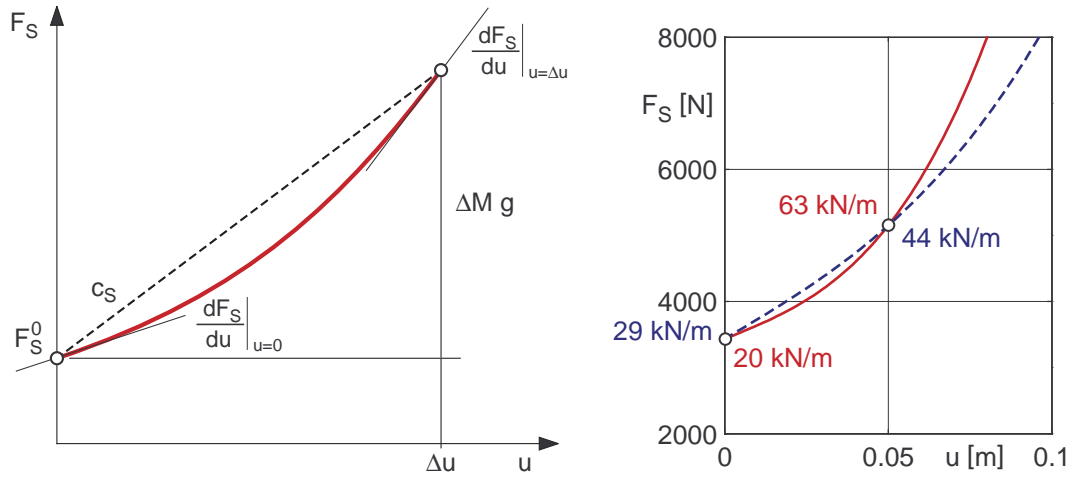


Figure 7.5: Principle and realizations of nonlinear spring characteristics

The intensity of the nonlinearity  $k$  can be fixed, for instance, by choosing an appropriate spring rate for the unloaded vehicle. With  $c_0 = 20000 \text{ N/m}$  the spring rates on the front and rear axle will be the same for the unloaded vehicle. With  $c_S = 34300 \text{ N/m}$  Eq. (7.33) yields

$$k = \frac{c_S}{c_0} - 1 = \frac{34300}{20000} - 1 = 0.715. \quad (7.36)$$

The solid line in Fig. 7.5 shows the resulting nonlinear spring characteristics which is characterized by the spring rates  $c_0 = 20000 \text{ N/m}$  and  $c_L = c_0 (1 + 3k) = 20000 * (1 + 3 * 0.715) = 62900 \text{ N/m}$  for the unloaded and the loaded vehicle. Again, the undamped natural frequencies

$$f_{0C}^0 = \frac{1}{2\pi} \sqrt{\frac{20000 \text{ N/m}}{350 \text{ kg}}} = 1.20 \text{ Hz} \quad \text{or} \quad f_{0C}^L = \frac{1}{2\pi} \sqrt{\frac{92000 \text{ N/m}}{(350+175) \text{ kg}}} = 1.74 \text{ Hz} \quad (7.37)$$

for the unloaded and the loaded vehicle differ quite a lot.

The unloaded and the loaded vehicle have the same undamped natural frequencies if

$$\frac{c_0}{M} = \frac{c_L}{M + \Delta M} \quad \text{or} \quad \frac{c_L}{c_0} = \frac{M + \Delta M}{M} \quad (7.38)$$

will hold. Combing this relationship with Eq. (7.35) one obtains

$$1 + 3k = \frac{M}{M + \Delta M} \quad \text{or} \quad k = \frac{1}{3} \left( \frac{M + \Delta M}{M} - 1 \right) = \frac{1}{3} \frac{\Delta M}{M}. \quad (7.39)$$

Hence, for the quarter car model with  $M = 350 \text{ kg}$  and  $\Delta M = 175$  the intensity of the nonlinear spring amounts to  $k = 1/3 * 175/350 = 0.1667$ . This value and  $c_S = 34300 \text{ N/m}$  will produce the dotted line in Fig. 7.5. The spring rates  $c_0 = c_S/(1+k) = 34300 \text{ N/m} / (1 + 0.1667) = 29400 \text{ N/m}$  for the unloaded and  $c_L = c_0(1 + 3k) = 29400 \text{ N/m} * (1 + 3 * 0.1667) = 44100 \text{ N/m}$  for the loaded vehicle follow from Eqs. (7.34) and (7.35). Now, the undamped natural frequency for the unloaded  $f_{0C}^0 = \sqrt{c_0/M} = 1.46 \text{ Hz}$  and the loaded vehicle  $f_{0C}^0 = \sqrt{c_L/(M + \Delta M)} = 1.46 \text{ Hz}$  are in deed the same.

## 7.2.4 Influence of Damping

To investigate the influence of the suspension damping to the chassis and wheel motion the simple vehicle models are exposed to initial disturbances. Fig. 7.6 shows the time response of the chassis  $z_C(t)$  and wheel displacement  $z_W(t)$  as well as the chassis acceleration  $\ddot{z}_C$  and the wheel load  $F_T = F_T^0 + F_T^D$  for different damping rates  $\zeta_C$  and  $\zeta_W$ . The dynamic wheel load follows from Eq. (7.8), and the static wheel load is given by  $F_T^0 = (M + m)g$ , where  $g$  labels the constant of gravity.

To achieve the same damping rates for the chassis and the wheel model different values for the damping parameter  $d_S$  were needed.

With increased damping the overshoot effect in the time history of the chassis displacement and the wheel load becomes smaller and smaller till it vanishes completely at  $\zeta_C = 1$  and  $\zeta_W = 1$ . The viscous damping rate  $\zeta = 1$

## 7.2.5 Optimal Damping

### 7.2.5.1 Avoiding Overshoots

If avoiding overshoot effects is the design goal then,  $\zeta = 1$  will be the optimal damping ratio. For  $\zeta = 1$  the eigenvalues of the single mass oscillator change from complex to real. Thus, producing a non oscillating solution without any sine and cosine terms.

According to Eq. (7.10)  $\zeta_C = 1$  and  $\zeta_W = 1$  results in the optimal damping parameter

$$d_S^{opt} \Big|_{Comfort}^{\zeta_C=1} = 2\sqrt{c_S M}, \quad \text{and} \quad d_S^{opt} \Big|_{Safety}^{\zeta_W=1} = 2\sqrt{(c_S + c_T)m}. \quad (7.40)$$

## 7 Vertical Dynamics

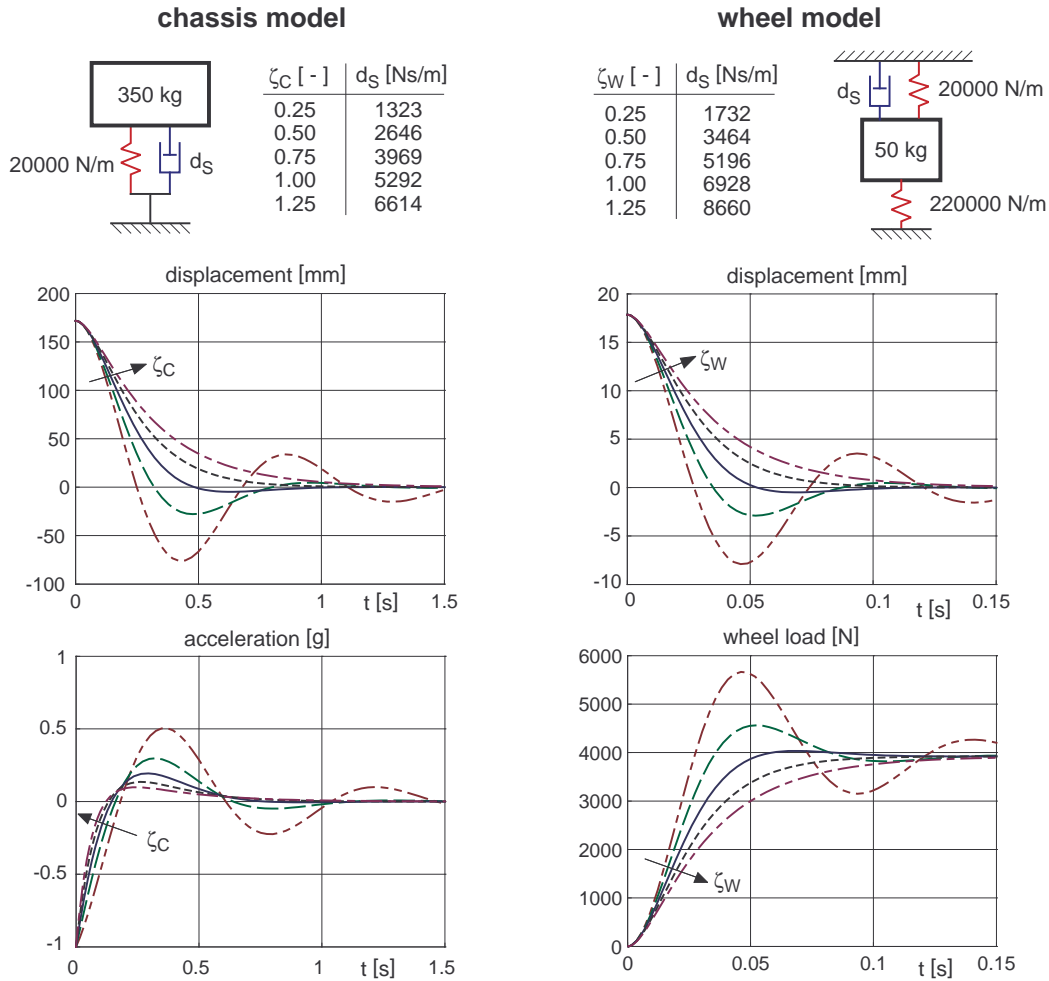


Figure 7.6: Time response of simple vehicle models to initial disturbances

So, the damping values

$$d_S^{opt} \Big|_{Comfort}^{\zeta_C=1} = 5292 \frac{N}{m/s} \quad \text{and} \quad d_S^{opt} \Big|_{Safety}^{\zeta_W=1} = 6928 \frac{N}{m/s} \quad (7.41)$$

will avoid an overshoot effect in the time history of the chassis displacement  $z_C(t)$  or in the in the time history of the wheel load  $F_T(t)$ . Usually, as it is here, the damping values for optimal comfort and optimal ride safety will be different. Hence, a simple linear damper can either avoid overshoots in the chassis motions or in the wheel loads.

The overshoot in the time history of the chassis accelerations  $\ddot{z}_C(t)$  will only vanish for  $\zeta_C \rightarrow \infty$  which surely is not a desirable configuration, because then, it takes a very long time till the initial chassis displacement has fully disappeared.

### 7.2.5.2 Disturbance Reaction Problem

Instead of avoiding overshoot effects we better demand that the time history of the system response will approach the steady state value as fast as possible. Fig. 7.7 shows the typical time response of a damped single-mass oscillator to the initial disturbance  $z(t=0) = z_0$  and  $\dot{z}(t=0) = 0$ .

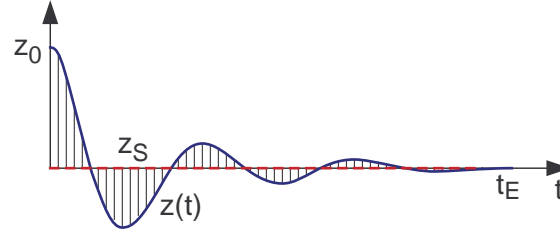


Figure 7.7: Evaluating a damped vibration

Counting the differences of the system response  $z(t)$  from the steady state value  $z_S = 0$  as errors allows to judge the attenuation. If the overall quadratic error becomes a minimum

$$\epsilon^2 = \int_{t=0}^{t=t_E} z(t)^2 dt \rightarrow Min, \quad (7.42)$$

the system approaches the steady state position as fast as possible. In theory  $t_E \rightarrow \infty$  holds, for practical applications a finite  $t_E$  have to be chosen appropriately.

To judge ride comfort and ride safety the hub motion of the chassis  $z_C$ , its acceleration  $\ddot{z}_C$  and the variations of the dynamic wheel load  $F_T^D$  can be used. In the absence of road irregularities  $z_R = 0$  the dynamic wheel load from Eq. (7.8) simplifies to  $F_T^D = -c_T z_W$ . Hence, the demands

$$\epsilon_C^2 = \int_{t=0}^{t=t_E} \left[ (g_1 \ddot{z}_C)^2 + (g_2 z_C)^2 \right] dt \rightarrow Min \quad (7.43)$$

and

$$\epsilon_S^2 = \int_{t=0}^{t=t_E} (-c_T z_W)^2 dt \rightarrow Min \quad (7.44)$$

will guarantee optimal ride comfort and optimal ride safety. By the factors  $g_1$  and  $g_2$  the acceleration and the hub motion can be weighted differently.

The equation of motion for the chassis model can be resolved for the acceleration

$$\ddot{z}_C = -(\omega_{0C}^2 z_C + 2\delta_C \dot{z}_C), \quad (7.45)$$

## 7 Vertical Dynamics

where, the system parameter  $M$ ,  $d_S$  and  $c_S$  were substituted by the damping rate  $\delta_C = \zeta_C \omega_{0C} = d_S/(2M)$  and by the undamped natural frequency  $\omega_{0C} = c_S/M$ . Then, the problem in Eq. (7.43) can be written as

$$\begin{aligned} \epsilon_C^2 &= \int_{t=0}^{t=t_E} \left[ g_1^2 (\omega_{0C}^2 z_C + 2\delta_C \dot{z}_C)^2 + g_2^2 z_C^2 \right] dt \\ &= \int_{t=0}^{t=t_E} \begin{bmatrix} z_C & \dot{z}_C \end{bmatrix} \begin{bmatrix} g_1^2 (\omega_{0C}^2)^2 + g_2^2 & g_1^2 \omega_{0C}^2 2\delta_C \\ g_1^2 \omega_{0C}^2 2\delta_C & g_1^2 (2\delta_C)^2 \end{bmatrix} \begin{bmatrix} z_C \\ \dot{z}_C \end{bmatrix} \rightarrow Min, \end{aligned} \quad (7.46)$$

where  $x_C^T = [z_C \ \dot{z}_C]$  is the state vector of the chassis model. In a similar way Eq. (7.44) can be transformed to

$$\epsilon_S^2 = \int_{t=0}^{t=t_E} c_T^2 z_W^2 dt = \int_{t=0}^{t=t_E} \begin{bmatrix} z_W & \dot{z}_W \end{bmatrix} \begin{bmatrix} c_T^2 & 0 \\ 0 & 0 \end{bmatrix} \begin{bmatrix} z_W \\ \dot{z}_W \end{bmatrix} \rightarrow Min, \quad (7.47)$$

where  $x_W^T = [z_W \ \dot{z}_W]$  denotes the state vector of the wheel model.

The problems given in Eqs. (7.46) and (7.47) are called disturbance-reaction problems, [5]. They can be written in a more general form

$$\int_{t=0}^{t=t_E} x^T(t) Q x(t) dt \rightarrow Min \quad (7.48)$$

where  $x(t)$  denotes the state vector and  $Q = Q^T$  is a symmetric weighting matrix. For single mass oscillators described by Eq. (7.9) the state equation reads as

$$\underbrace{\begin{bmatrix} \dot{z} \\ \ddot{z} \end{bmatrix}}_{\dot{x}} = \underbrace{\begin{bmatrix} 0 & 1 \\ -\omega_0^2 & -2\delta \end{bmatrix}}_A \underbrace{\begin{bmatrix} z \\ \dot{z} \end{bmatrix}}_x. \quad (7.49)$$

For  $t_E \rightarrow \infty$  the time response of the system exposed to the initial disturbance  $x(t=0) = x_0$  vanishes  $x(t \rightarrow \infty) = 0$ , and the integral in Eq.(7.48) can be solved by

$$\int_{t=0}^{t=t_E} x^T(t) Q x(t) dt = x_0^T R x_0, \quad (7.50)$$

where the symmetric matrix  $R = R^T$  is given by the Ljapunov equation

$$A^T R + R A + Q = 0. \quad (7.51)$$

For the single mass oscillator the Ljapunov equation

$$\begin{bmatrix} 0 & -\omega_0^2 \\ 1 & -2\delta \end{bmatrix} \begin{bmatrix} R_{11} & R_{12} \\ R_{12} & R_{22} \end{bmatrix} + \begin{bmatrix} R_{11} & R_{12} \\ R_{12} & R_{22} \end{bmatrix} \begin{bmatrix} 0 & 1 \\ -\omega_0^2 & -2\delta \end{bmatrix} + \begin{bmatrix} Q_{11} & Q_{12} \\ Q_{12} & Q_{22} \end{bmatrix} = 0. \quad (7.52)$$

results in 3 linear equations

$$\begin{aligned} -\omega_0^2 R_{12} - \omega_0^2 R_{12} + Q_{11} &= 0 \\ -\omega_0^2 R_{22} + R_{11} - 2\delta R_{12} + Q_{12} &= 0 \\ R_{12} - 2\delta R_{22} + R_{12} - 2\delta R_{22} + Q_{22} &= 0 \end{aligned} \quad (7.53)$$

which easily can be solved for the elements of  $R$

$$R_{11} = \left( \frac{\delta}{\omega_0^2} + \frac{1}{4\delta} \right) Q_{11} - Q_{12} + \frac{\omega_0^2}{4\delta} Q_{22}, \quad R_{12} = \frac{Q_{11}}{2\omega_0^2}, \quad R_{22} = \frac{Q_{11}}{4\delta\omega_0^2} + \frac{Q_{22}}{4\delta}. \quad (7.54)$$

For the initial disturbance  $x_0 = [z_0 \ 0]^T$  Eq. (7.50) finally results in

$$\int_{t=0}^{t=t_E} x^T(t) Q x(t) dt = z_0^2 R_{11} = z_0^2 \left[ \left( \frac{\delta}{\omega_0^2} + \frac{1}{4\delta} \right) Q_{11} - Q_{12} + \frac{\omega_0^2}{4\delta} Q_{22} \right]. \quad (7.55)$$

Now, the integral in Eq. (7.46) evaluating the ride comfort is solved by

$$\begin{aligned} \epsilon_C^2 &= z_{0C}^2 \left[ \left( \frac{\delta_C}{\omega_{0C}^2} + \frac{1}{4\delta_C} \right) (g_1^2 (\omega_{0C}^2)^2 + g_2^2) - g_1^2 \omega_{0C}^2 2\delta_C + \frac{\omega_{0C}^2}{4\delta_C} g_1^2 (2\delta_C)^2 \right] \\ &= z_{0C}^2 \omega_{0C}^2 \left[ \frac{\omega_{0C}}{4\zeta_C} \left( g_1^2 + \left( \frac{g_2}{\omega_{0C}^2} \right)^2 \right) + \left( \frac{g_2}{\omega_{0C}^2} \right)^2 \zeta_C \omega_{0C} \right]. \end{aligned} \quad (7.56)$$

where the abbreviation  $\delta_C$  was finally replaced by  $\zeta_C \omega_{0C}$ .

By setting  $g_1 = 1$  and  $g_2 = 0$  the time history of the chassis acceleration  $\ddot{z}_C$  is weighted only. Eq. (7.56) then simplifies to

$$\epsilon_C^2|_{\ddot{z}_C} = z_{0C}^2 \omega_{0C}^2 \frac{\omega_{0C}}{4\zeta_C} \quad (7.57)$$

which will become a minimum for  $\omega_{0C} \rightarrow 0$  or  $\zeta_C \rightarrow \infty$ . As mentioned before,  $\zeta_C \rightarrow \infty$  surely is not a desirable configuration. A low undamped natural frequency  $\omega_{0C} \rightarrow 0$  is achieved by a soft suspension spring  $c_S \rightarrow 0$  or a large chassis mass  $M \rightarrow \infty$ . However, a large chassis mass is uneconomic and the suspension stiffness is limited by the loading conditions. Hence, weighting the chassis accelerations only does not lead to a specific result for the system parameter.

The combination of  $g_1 = 0$  and  $g_2 = 1$  weights the time history of the chassis displacement only. Then, Eq. (7.56) results in

$$\epsilon_C^2|_{z_C} = \frac{z_{0C}^2}{\omega_{0C}} \left[ \frac{1}{4\zeta_C} + \zeta_C \right] \quad (7.58)$$

which will become a minimum for  $\omega_{0C} \rightarrow \infty$  or

$$\frac{d \epsilon_C^2|_{z_C}}{d \zeta_C} = \frac{z_{0C}^2}{\omega_{0C}} \left[ \frac{-1}{4\zeta_C^2} + 1 \right] = 0. \quad (7.59)$$

## 7 Vertical Dynamics

A high undamped natural frequency  $\omega_{0C} \rightarrow \infty$  contradicts the demand for rapidly vanishing accelerations. The viscous damping ratio  $\zeta_C = \frac{1}{2}$  solves Eq. (7.59) and minimizes the merit function in Eq. (7.58). But again, this value does not correspond with  $\zeta_C \rightarrow \infty$  which minimizes the merit function in Eq. (7.57).

Hence, practical results can be achieved only if the chassis displacements and the chassis accelerations will be evaluated simultaneously. To do so, appropriate weighting factors have to be chosen. In the equation of motion for the chassis (7.6) the terms  $M \ddot{z}_C$  and  $c_S z_C$  are added. Hence,  $g_1 = M$  and  $g_2 = c_S$  or

$$g_1 = 1 \quad \text{and} \quad g_2 = \frac{c_S}{M} = \omega_{0C}^2 \quad (7.60)$$

provide system-fitted weighting factors. Now, Eq. (7.56) reads as

$$\epsilon_C^2 = z_{0C}^2 \omega_{0C}^2 \left[ \frac{\omega_{0C}}{2\zeta_C} + \zeta_C \omega_{0C} \right]. \quad (7.61)$$

Again, a good ride comfort will be achieved by  $\omega_{0C} \rightarrow 0$ . For finite undamped natural frequencies Eq. (7.61) becomes a minimum, if the viscous damping rate  $\zeta_C$  will satisfy

$$\frac{d \epsilon_C^2}{d \zeta_C} \Big|_{z_C} = z_{0C}^2 \omega_{0C}^2 \left[ \frac{-\omega_{0C}}{2\zeta_C^2} + \omega_{0C} \right] = 0. \quad (7.62)$$

Hence, a viscous damping rate of

$$\zeta_C = \frac{1}{2} \sqrt{2} \quad (7.63)$$

or a damping parameter of

$$d_S^{opt} \Big|_{\zeta_C = \frac{1}{2} \sqrt{2}} \Big|_{Comfort} = \sqrt{2 c_S M}, \quad (7.64)$$

will provide optimal comfort by minimizing the merit function in Eq. (7.61).

For the passenger car with  $M = 350 \text{ kg}$  and  $c_S = 20000 \text{ N/m}$  the optimal damping parameter will amount to

$$d_S^{opt} \Big|_{\zeta_C = \frac{1}{2} \sqrt{2}} \Big|_{Comfort} = 3742 \frac{\text{N}}{\text{m/s}} \quad (7.65)$$

which is 70% of the value needed to avoid overshoot effects in the chassis displacements.

The integral in Eq. (7.47) evaluating the ride safety is solved by

$$\epsilon_S^2 = \frac{z_{0W}^2}{\omega_{0W}} \left( \zeta_W + \frac{1}{4\zeta_W} \right) c_T^2 \quad (7.66)$$

where the model parameter  $m$ ,  $c_S$ ,  $d_S$  and  $c_T$  where replaced by the undamped natural frequency  $\omega_{0W}^2 = (c_S + c_T)/m$  and by the damping ratio  $\delta_W = \zeta_W \omega_{0W} = d_S/(2m)$ .

### 7.3 Sky Hook Damper

A soft tire  $c_T \rightarrow 0$  make the safety criteria Eq. (7.66) small  $\epsilon_S^2 \rightarrow 0$  and thus, reduces the dynamic wheel load variations. However, the tire spring stiffness can not be reduced to arbitrary low values, because this would cause too large tire deformations. Small wheel masses  $m \rightarrow 0$  and/or a hard body suspension  $c_S \rightarrow \infty$  will increase  $\omega_{0W}$  and thus, reduce the safety criteria Eq. (7.66). The use of light metal rims improves, because of wheel weight reduction, the ride safety of a car. Hard body suspensions contradict a good driving comfort.

With fixed values for  $c_T$  and  $\omega_{0W}$  the merit function in Eq. (7.66) will become a minimum if

$$\frac{\partial \epsilon_S^2}{\partial \zeta_W} = \frac{z_{0W}^2}{\omega_{0W}} \left( 1 + \frac{-1}{4\zeta_W^2} \right) c_T^2 = 0 \quad (7.67)$$

will hold. Hence, a viscous damping rate of

$$\zeta_W = \frac{1}{2} \quad (7.68)$$

or the damping parameter

$$d_S^{opt} \Big|_{Safety} = \sqrt{(c_S + c_T) m} \quad (7.69)$$

will guarantee optimal ride safety by minimizing the merit function in Eq. (7.66).

For the passenger car with  $M = 350 \text{ kg}$  and  $c_S = 20\,000 \text{ N/m}$  the optimal damping parameter will now amount to

$$d_S^{opt} \Big|_{Safety}^{\zeta_W = \frac{1}{2}} = 3464 \frac{N}{m/s} \quad (7.70)$$

which is 50% of the value needed to avoid overshoot effects in the wheel loads.

## 7.3 Sky Hook Damper

### 7.3.1 Modeling Aspects

In standard vehicle suspension systems the damper is mounted between the wheel and the body. Hence, the damper affects body and wheel/axle motions simultaneously.

To take this situation into account the simple quarter car models of section 7.2.1 must be combined to a more enhanced model, Fig. 7.8a.

Assuming a linear characteristics the suspension damper force is given by

$$F_D = d_S (\dot{z}_W - \dot{z}_C) , \quad (7.71)$$

where  $d_S$  denotes the damping constant, and  $\dot{z}_C$ ,  $\dot{z}_W$  are the time derivatives of the absolute vertical body and wheel displacements.

## 7 Vertical Dynamics

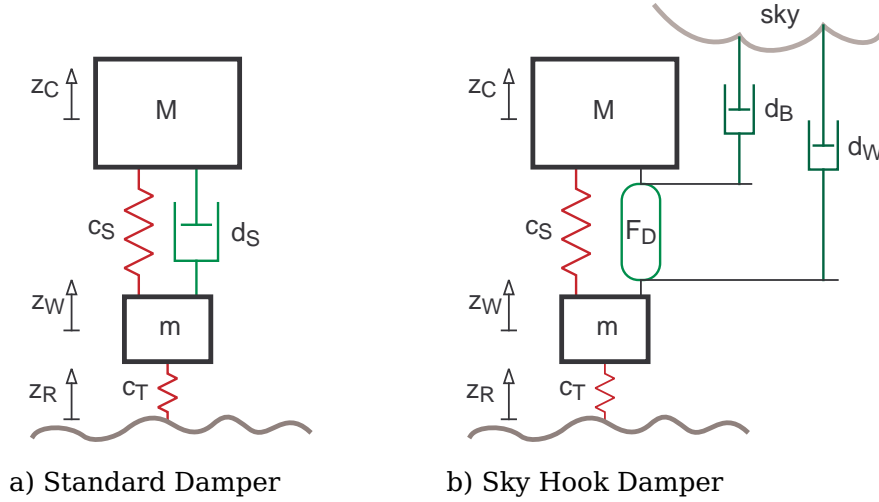


Figure 7.8: Quarter Car Model with Standard and Sky Hook Damper

The sky hook damping concept starts with two independent dampers for the body and the wheel/axle mass, Fig. 7.8b. A practical realization in form of a controllable damper will then provide the damping force

$$F_D = d_W \dot{z}_W - d_C \dot{z}_C, \quad (7.72)$$

where instead of the single damping constant  $d_S$  now two design parameter  $d_W$  and  $d_C$  are available.

The equations of motion for the quarter car model are given by

$$\begin{aligned} M \ddot{z}_C &= F_S + F_D - M g, \\ m \ddot{z}_W &= F_T - F_S - F_D - m g, \end{aligned} \quad (7.73)$$

where  $M$ ,  $m$  are the sprung and unsprung mass,  $z_C$ ,  $z_W$  denote their vertical displacements, and  $g$  is the constant of gravity.

The suspension spring force is modeled by

$$F_S = F_S^0 + c_S (z_W - z_C), \quad (7.74)$$

where  $F_S^0 = m_C g$  is the spring preload, and  $c_S$  the spring stiffness.

Finally, the vertical tire force is given by

$$F_T = F_T^0 + c_T (z_R - z_W), \quad (7.75)$$

where  $F_T^0 = (M + m) g$  is the tire preload,  $c_S$  the vertical tire stiffness, and  $z_R$  describes the road roughness. The condition  $F_T \geq 0$  takes the tire lift off into account.

### 7.3.2 Eigenfrequencies and Damping Ratios

Using the force definitions in Eqs. (7.72), (7.74) and (7.75) the equations of motion in Eq. (7.73) can be transformed to the state equation

$$\underbrace{\begin{bmatrix} \dot{z}_C \\ \dot{z}_W \\ \ddot{z}_C \\ \ddot{z}_W \end{bmatrix}}_{\dot{x}} = \underbrace{\begin{bmatrix} 0 & 0 & 1 & 0 \\ 0 & 0 & 0 & 1 \\ -\frac{c_S}{M} & \frac{c_S}{M} & -\frac{d_C}{M} & \frac{d_W}{M} \\ \frac{c_S}{m} & -\frac{c_S+c_T}{m} & \frac{d_C}{m} & -\frac{d_W}{m} \end{bmatrix}}_A \underbrace{\begin{bmatrix} z_C \\ z_W \\ \dot{z}_C \\ \dot{z}_W \end{bmatrix}}_x + \underbrace{\begin{bmatrix} 0 \\ 0 \\ 0 \\ \frac{c_T}{m} \end{bmatrix}}_B \underbrace{\begin{bmatrix} z_R \end{bmatrix}}_u, \quad (7.76)$$

where the weight forces  $Mg, mg$  were compensated by the preloads  $F_S^0, F_T^0$ , the term  $Bu$  describes the excitation,  $x$  denotes the state vector, and  $A$  is the state matrix. In this linear approach the tire lift off is no longer taken into consideration.

The eigenvalues  $\lambda$  of the state matrix  $A$  will characterize the eigen dynamics of the quarter car model. In case of complex eigenvalues the damped natural eigenfrequencies are given by the imaginary parts,  $\omega = Im(\lambda)$ , and according to Eq. (7.17)  $\zeta = D_\lambda = -Re(\lambda)/|\lambda|$  evaluates the damping ratio.

By setting  $d_C = d_S$  and  $d_W = d_S$  Eq. (7.76) represents a quarter car model with the standard damper described by Eq. (7.71). Fig. 7.9 shows the eigenfrequencies  $f = \omega/(2\pi)$  and the damping ratios  $\zeta = D_\lambda$  for different values of the damping parameter  $d_S$ .

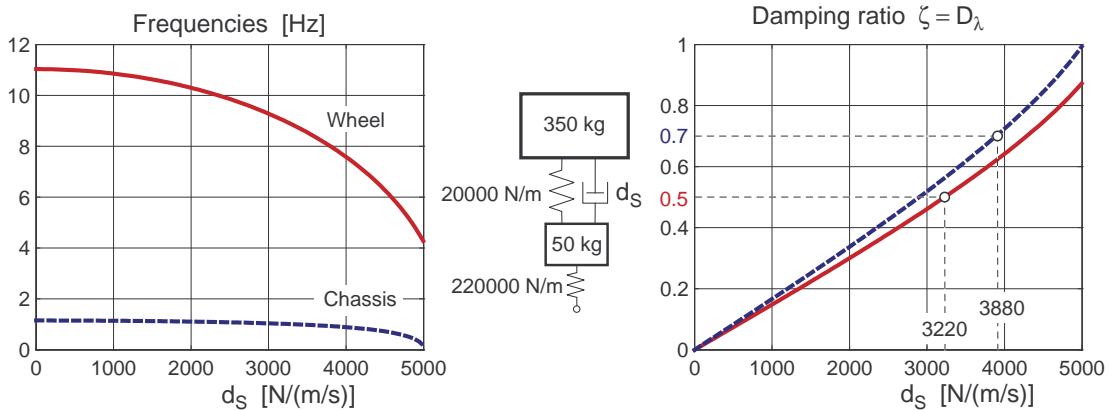


Figure 7.9: Quarter car model with standard damper

Optimal ride comfort with a damping ratio of  $\zeta_C = \frac{1}{2}\sqrt{2} \approx 0.7$  for the chassis motion could be achieved with the damping parameter  $d_S = 3880 N/(m/s)$ , and the damping parameter  $d_S = 3220 N/(m/s)$  would provide for the wheel motion a damping ratio of  $\zeta_W = 0.5$  which correspond to minimal wheel load variations. This damping parameter are very close to the values  $3742 N/(m/s)$  and  $3464 N/(m/s)$

## 7 Vertical Dynamics

which very calculated in Eqs. (7.65) and (7.70) with the single mass models. Hence, the very simple single mass models can be used for a first damper layout. Usually, as it is here, optimal ride comfort and optimal ride safety cannot achieved both by a standard linear damper.

The sky-hook damper, modeled by Eq. (7.72), provides with  $d_W$  and  $d_S$  two design parameter. Their influence to the eigenfrequencies  $f$  and the damping ratios  $\zeta$  is shown in Fig. 7.10.

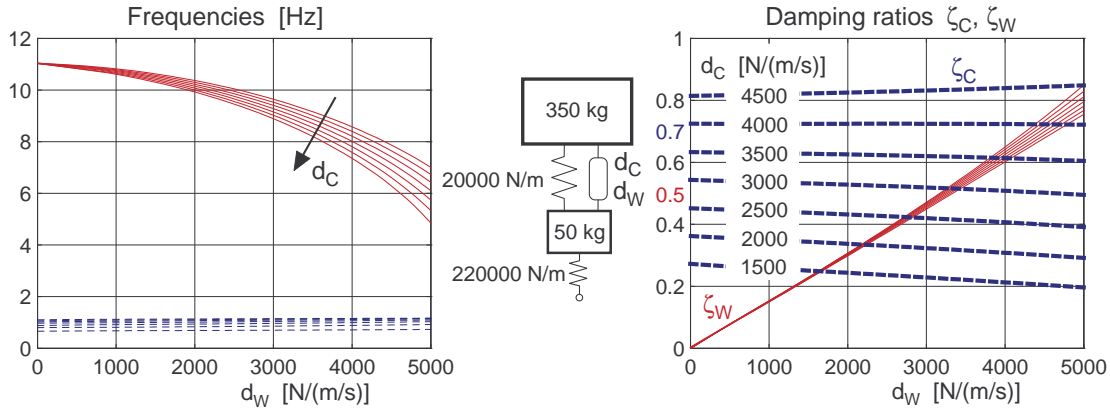


Figure 7.10: Quarter car model with sky-hook damper

The the sky-hook damping parameter  $d_C$ ,  $d_W$  have a nearly independent influence on the damping ratios. The chassis damping ratio  $\zeta_C$  mainly depends on  $d_C$ , and the wheel damping ratio  $\zeta_W$  mainly depends on  $d_W$ . Hence, the damping of the chassis and the wheel motion can be adjusted to nearly each design goal. Here, a sky-hook damper with  $d_C = 3900 \text{ N/(m/s)}$  and  $d_W = 3200 \text{ N/(m/s)}$  would generate the damping ratios  $d_C = 0.7$  and  $d_W = 0.5$  hence, combining ride comfort and ride safety within one damper layout.

### 7.3.3 Technical Realization

By modifying the damper law in Eq. (7.72) to

$$F_D = d_W \dot{z}_W - d_C \dot{z}_C + = \underbrace{\frac{d_W \dot{z}_W - d_C \dot{z}_C}{\dot{z}_W - \dot{z}_C}}_{d_S^*} (\dot{z}_W - \dot{z}_C) = d_S^* (\dot{z}_W - \dot{z}_C) \quad (7.77)$$

the sky-hook damper can be realized by a standard damper in the form of Eq. (7.71). The new damping parameter  $d_S^*$  now nonlinearly depends on the absolute vertical velocities of the chassis and the wheel  $d_S^* = d_S^*(\dot{z}_C, \dot{z}_W)$ . As, a standard damper operates in a dissipative mode only the damping parameter will be restricted to positive values,  $d_S^* > 0$ . Hence, the passive realization of a sky-hook damper will only

match with some properties of the ideal damper law in Eq. (7.72). But, compared with the standard damper it still can provide a better ride comfort combined with an increased ride safety.

## 7.4 Nonlinear Force Elements

### 7.4.1 Quarter Car Model

The principal influence of nonlinear characteristics on driving comfort and safety can already be studied on a quarter car model Fig. 7.11.

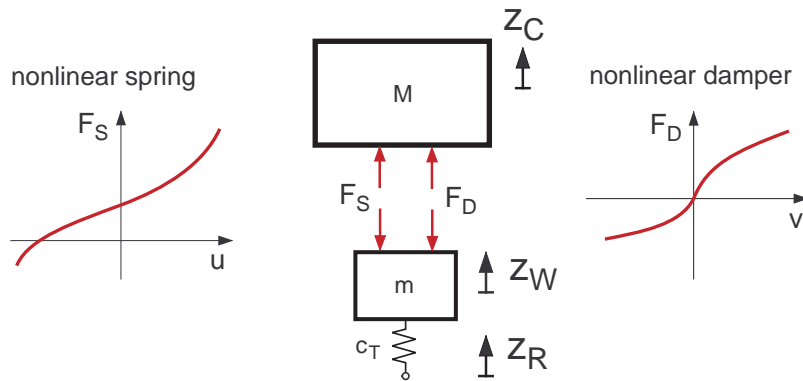


Figure 7.11: Quarter car model with nonlinear spring and damper characteristics

The equations of motion read as

$$\begin{aligned} M \ddot{z}_C &= F_S + F_D - M g \\ m \ddot{z}_W &= F_T - F_S - F_D - m g, \end{aligned} \quad (7.78)$$

where  $g = 9.81 \text{ m/s}^2$  labels the constant of gravity,  $M$ ,  $m$  are the masses of the chassis and the wheel,  $F_S$ ,  $F_D$ ,  $F_T$  describe the spring, the damper, and the vertical tire force, and the vertical displacements of the chassis  $z_C$  and the wheel  $z_W$  are measured from the equilibrium position.

In extension to Eq. (7.32) the spring characteristics is modeled by

$$F_S = F_S^0 + \begin{cases} c_0 u \left( 1 + k_r \left( \frac{u}{\Delta u_r} \right)^2 \right) & u < 0 \\ c_0 u \left( 1 + k_c \left( \frac{u}{\Delta u_c} \right)^2 \right) & u \geq 0 \end{cases} \quad (7.79)$$

## 7 Vertical Dynamics

where  $F_S^0 = M g$  is the spring preload, and

$$u = z_W - z_C \quad (7.80)$$

describes the spring travel. Here,  $u < 0$  marks tension (rebound), and  $u \geq 0$  compression. Two sets of  $k_r, u_r$  and  $k_c, u_c$  define the spring nonlinearity during rebound and compression. For  $k_r = 0$  and  $k_c = 0$  a linear spring characteristics is obtained.

A degressive damper characteristics can be modeled by

$$F_D(v) = \begin{cases} \frac{d_0 v}{1 - p_r v} & v < 0, \\ \frac{d_0 v}{1 + p_c v} & v \geq 0, \end{cases} \quad (7.81)$$

where  $d_0$  denotes the damping constant at  $v = 0$ , and the damper velocity is defined by

$$v = \dot{z}_W - \dot{z}_C. \quad (7.82)$$

The sign convention of the damper velocity was chosen consistent to the spring travel. Hence, rebound is characterized by  $v < 0$  and compression by  $v \geq 0$ . The parameter  $p_r$  and  $p_c$  make it possible to model the damper nonlinearity differently in the rebound and compression mode. A linear damper characteristics is obtained with  $p_r = 0$  and  $p_c = 0$ .

The nonlinear spring design in Section 7.2.3 holds for the compression mode. Hence, using the same data we obtain:  $c_0 = 29\,400 \text{ N/m}$ ,  $u_c = \Delta u = u_{max}/2 = 0.10/2 = 0.05$  and  $k_c = k = 0.1667$ . By setting  $u_r = u_c$  and  $k_r = 0$  a simple linear spring is used in the rebound mode, Fig. 7.12a.

According to Section 7.2.5 damping coefficients optimizing the ride comfort and the ride safety can be calculated from

Eqs. (7.64) and (7.69). For  $c_S = 34\,300 \text{ N/m}$  which is the equivalent linear spring rate,  $M = 350 \text{ kg}$ ,  $m = 50 \text{ kg}$  and  $c_T = 220\,000 \text{ N/m}$  we obtain

$$\begin{aligned} (d_S)_{opt}^C &= \sqrt{2 c_S M} = \sqrt{2 \cdot 34\,300 \cdot 350} = 4900 \text{ N/(m/s)}, \\ (d_S)_{opt}^S &= \sqrt{(c_S + c_T) m} = \sqrt{(18\,000 + 220\,000) \cdot 50} = 3570 \text{ N/(m/s)}. \end{aligned} \quad (7.83)$$

The mean value  $d_0 = 4200 \text{ N/(m/s)}$  may serve as compromise. With  $p_r = 0.4 \text{ (m/s)}^{-1}$  and  $p_c = 1.2 \text{ (m/s)}^{-1}$  the nonlinearity becomes more intensive in compression than rebound, Fig. 7.12b.

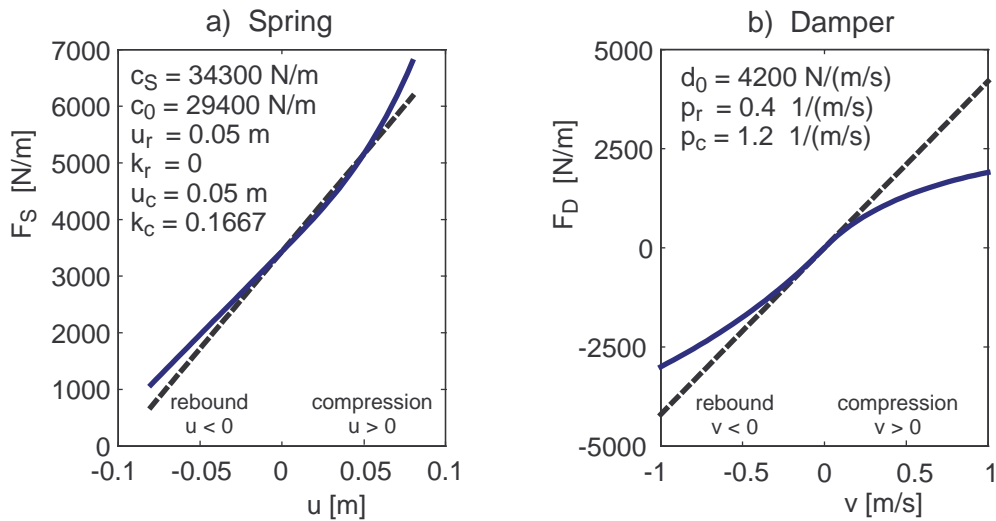
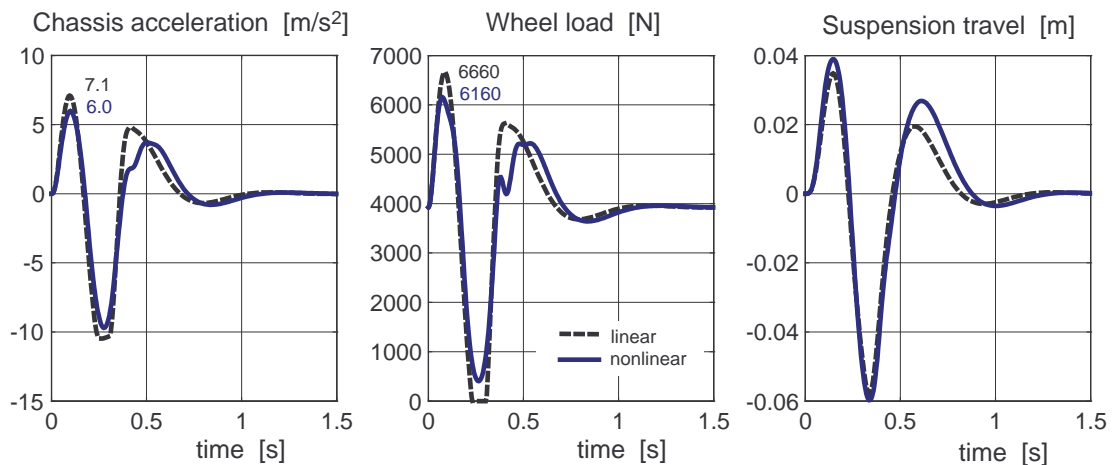


Figure 7.12: Spring and damper characteristics: - - - linear, — nonlinear

Figure 7.13: Quarter car model driving with  $v = 20 \text{ km/h}$  over a single obstacle

### 7.4.2 Results

The quarter car model is driven with constant velocity over a single obstacle. Here, a cosine shaped bump with a height of  $H = 0.08 \text{ m}$  and a length of  $L = 2.0 \text{ m}$  was used. The results are plotted in Fig. 7.13.

Compared to the linear model the nonlinear spring and damper characteristics result in significantly reduced peak values for the chassis acceleration ( $6.0 \text{ m/s}^2$  instead of  $7.1 \text{ m/s}^2$ ) and for the wheel load ( $6160 \text{ N}$  instead of  $6660 \text{ N}$ ). Even the tire lift off at  $t \approx 0.25 \text{ s}$  can be avoided. While crossing the bump large damper velocities

## 7 Vertical Dynamics

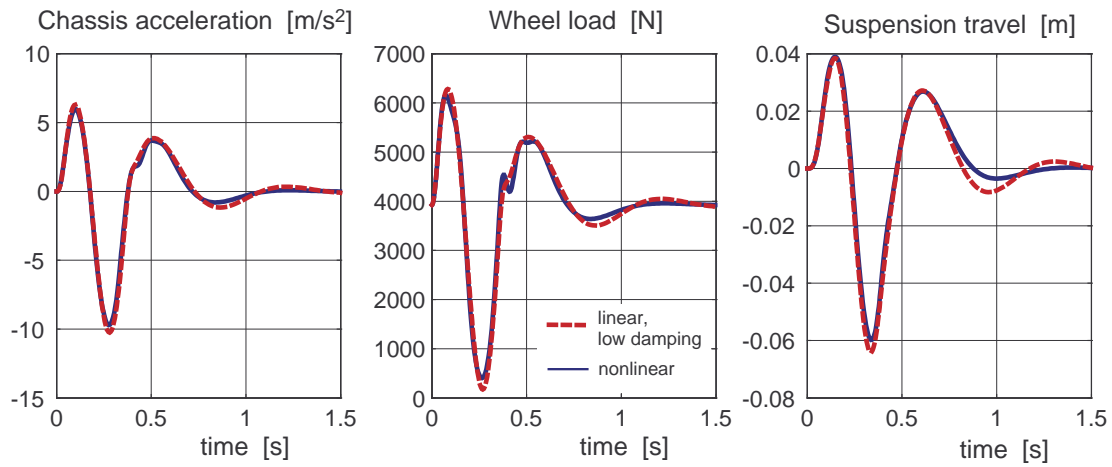


Figure 7.14: Results for low damping compared to nonlinear model

occur. Here, the degressive damper characteristics provides less damping compared to the linear damper which increases the suspension travel.

A linear damper with a lower damping coefficient,  $d_0 = 3000 \text{ N/m}$  for instance, also reduces the peaks in the chassis acceleration and in the wheel load, but then the attenuation of the disturbances will take more time. Fig. 7.14. Which surely is not optimal.

## 8 Longitudinal Dynamics

### 8.1 Dynamic Wheel Loads

#### 8.1.1 Simple Vehicle Model

The vehicle is considered as one rigid body which moves along an ideally even and horizontal road. At each axle the forces in the wheel contact points are combined in one normal and one longitudinal force.

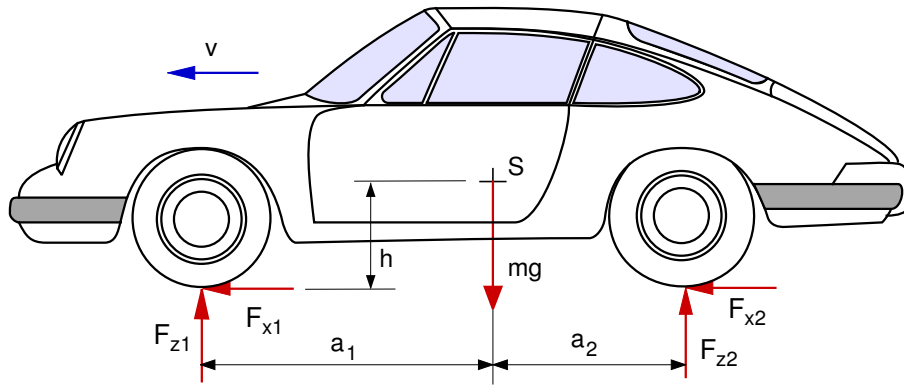


Figure 8.1: Simple vehicle model

If aerodynamic forces (drag, positive and negative lift) are neglected at first, the equations of motions in the  $x$ -,  $z$ -plane will read as

$$m \dot{v} = F_{x1} + F_{x2} , \quad (8.1)$$

$$0 = F_{z1} + F_{z2} - m g , \quad (8.2)$$

$$0 = F_{z1} a_1 - F_{z2} a_2 + (F_{x1} + F_{x2}) h , \quad (8.3)$$

where  $\dot{v}$  indicates the vehicle's acceleration,  $m$  is the mass of the vehicle,  $a_1 + a_2$  is the wheel base, and  $h$  is the height of the center of gravity.

These are only three equations for the four unknown forces  $F_{x1}$ ,  $F_{x2}$ ,  $F_{z1}$ ,  $F_{z2}$ . But, if we insert Eq. (8.1) in Eq. (8.3), we can eliminate two unknowns at a stroke

$$0 = F_{z1} a_1 - F_{z2} a_2 + m \dot{v} h . \quad (8.4)$$

## 8 Longitudinal Dynamics

The equations Eqs. (8.2) and (8.4) can be resolved for the axle loads now

$$F_{z1} = m g \frac{a_2}{a_1 + a_2} - \frac{h}{a_1 + a_2} m \dot{v}, \quad (8.5)$$

$$F_{z2} = m g \frac{a_1}{a_1 + a_2} + \frac{h}{a_1 + a_2} m \dot{v}. \quad (8.6)$$

The static parts

$$F_{z1}^{st} = m g \frac{a_2}{a_1 + a_2}, \quad F_{z2}^{st} = m g \frac{a_1}{a_1 + a_2} \quad (8.7)$$

describe the weight distribution according to the horizontal position of the center of gravity. The height of the center of gravity only influences the dynamic part of the axle loads,

$$F_{z1}^{dyn} = -m g \frac{h}{a_1 + a_2} \frac{\dot{v}}{g}, \quad F_{z2}^{dyn} = +m g \frac{h}{a_1 + a_2} \frac{\dot{v}}{g}. \quad (8.8)$$

When accelerating  $\dot{v} > 0$ , the front axle is relieved as the rear is when decelerating  $\dot{v} < 0$ .

### 8.1.2 Influence of Grade

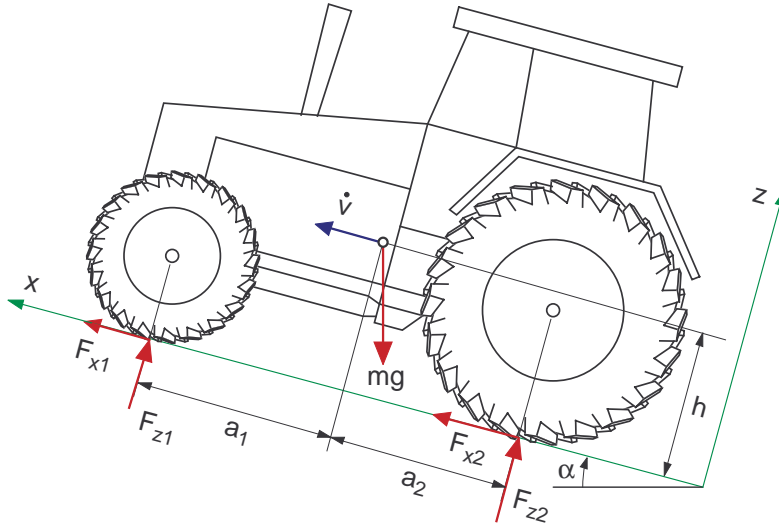


Figure 8.2: Vehicle on grade

For a vehicle on a grade, Fig.8.2, the equations of motion Eq. (8.1) to Eq. (8.3) can easily be extended to

$$\begin{aligned} m \dot{v} &= F_{x1} + F_{x2} - m g \sin \alpha, \\ 0 &= F_{z1} + F_{z2} - m g \cos \alpha, \\ 0 &= F_{z1} a_1 - F_{z2} a_2 + (F_{x1} + F_{x2}) h, \end{aligned} \quad (8.9)$$

where  $\alpha$  denotes the grade angle. Now, the axle loads are given by

$$F_{z1} = m g \cos \alpha \frac{a_2 - h \tan \alpha}{a_1 + a_2} - \frac{h}{a_1 + a_2} m \dot{v}, \quad (8.10)$$

$$F_{z2} = m g \cos \alpha \frac{a_1 + h \tan \alpha}{a_1 + a_2} + \frac{h}{a_1 + a_2} m \dot{v}, \quad (8.11)$$

where the dynamic parts remain unchanged, whereas now the static parts also depend on the grade angle and the height of the center of gravity.

### 8.1.3 Aerodynamic Forces

The shape of most vehicles or specific wings mounted at the vehicle produce aerodynamic forces and torques. The effect of these aerodynamic forces and torques can be represented by a resistant force applied at the center of gravity and "down forces" acting at the front and rear axle, Fig. 8.3. If we assume a positive driving

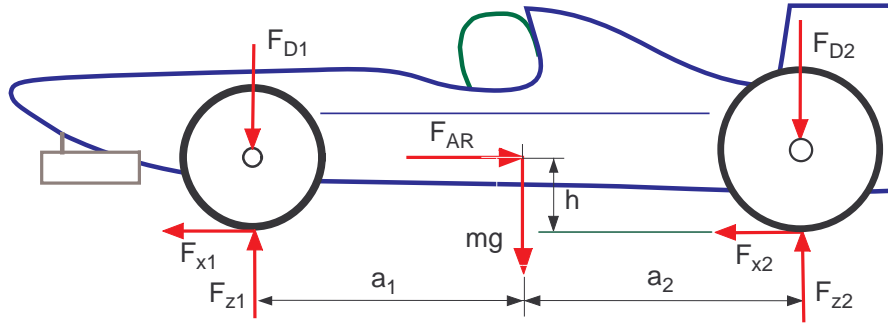


Figure 8.3: Vehicle with aerodynamic forces

speed,  $v > 0$ , the equations of motion will read as

$$\begin{aligned} m \dot{v} &= F_{x1} + F_{x2} - F_{AR}, \\ 0 &= F_{z1} - F_{D1} + F_{z2} - F_{D2} - m g, \\ 0 &= (F_{z1} - F_{D1}) a_1 - (F_{z2} - F_{D2}) a_2 + (F_{x1} + F_{x2}) h, \end{aligned} \quad (8.12)$$

where  $F_{AR}$  and  $F_{D1}$ ,  $F_{D2}$  describe the air resistance and the down forces. For the dynamic axle loads we get

$$F_{z1} = F_{D1} + m g \frac{a_2}{a_1 + a_2} - \frac{h}{a_1 + a_2} (m \dot{v} + F_{AR}), \quad (8.13)$$

$$F_{z2} = F_{D2} + m g \frac{a_1}{a_1 + a_2} + \frac{h}{a_1 + a_2} (m \dot{v} + F_{AR}). \quad (8.14)$$

The down forces  $F_{D1}$ ,  $F_{D2}$  increase the static axle loads, and the air resistance  $F_{AR}$  generates an additional dynamic term.

## 8.2 Maximum Acceleration

### 8.2.1 Tilting Limits

Ordinary automotive vehicles can only apply pressure forces to the road. If we take the demands  $F_{z1} \geq 0$  and  $F_{z2} \geq 0$  into account, Eqs. (8.10) and (8.11) will result in

$$\frac{\dot{v}}{g} \leq \frac{a_2}{h} \cos \alpha - \sin \alpha \quad \text{and} \quad \frac{\dot{v}}{g} \geq -\frac{a_1}{h} \cos \alpha - \sin \alpha. \quad (8.15)$$

These two conditions can be combined in one

$$-\frac{a_1}{h} \cos \alpha \leq \frac{\dot{v}}{g} + \sin \alpha \leq \frac{a_2}{h} \cos \alpha. \quad (8.16)$$

Hence, the maximum achievable accelerations ( $\dot{v} > 0$ ) and decelerations ( $\dot{v} < 0$ ) are limited by the grade angle  $\alpha$  and the position  $a_1, a_2, h$  of the center of gravity. For  $\dot{v} \rightarrow 0$  the tilting condition Eq. (8.16) results in

$$-\frac{a_1}{h} \leq \tan \alpha \leq \frac{a_2}{h} \quad (8.17)$$

which describes the climbing and downhill capacity of a vehicle.

The presence of aerodynamic forces complicates the tilting condition. Aerodynamic forces become important only at high speeds. Here, the vehicle acceleration is normally limited by the engine power.

### 8.2.2 Friction Limits

The maximum acceleration is also restricted by the friction conditions

$$|F_{x1}| \leq \mu F_{z1} \quad \text{and} \quad |F_{x2}| \leq \mu F_{z2} \quad (8.18)$$

where the same friction coefficient  $\mu$  has been assumed at front and rear axle. In the limit case

$$F_{x1} = \pm \mu F_{z1} \quad \text{and} \quad F_{x2} = \pm \mu F_{z2} \quad (8.19)$$

the linear momentum in Eq. (8.9) can be written as

$$m \dot{v}_{max} = \pm \mu (F_{z1} + F_{z2}) - m g \sin \alpha. \quad (8.20)$$

Using Eqs. (8.10) and (8.11) one obtains

$$\left(\frac{\dot{v}}{g}\right)_{max} = \pm \mu \cos \alpha - \sin \alpha. \quad (8.21)$$

That means climbing ( $\dot{v} > 0, \alpha > 0$ ) or downhill stopping ( $\dot{v} < 0, \alpha < 0$ ) requires at least a friction coefficient  $\mu \geq \tan |\alpha|$ .

According to the vehicle dimensions and the friction values the maximal acceleration or deceleration is restricted either by Eq. (8.16) or by Eq. (8.21).

If we take aerodynamic forces into account, the maximum acceleration and deceleration on a horizontal road will be limited by

$$-\mu \left( 1 + \frac{F_{D1}}{mg} + \frac{F_{D2}}{mg} \right) - \frac{F_{AR}}{mg} \leq \frac{\dot{v}}{g} \leq \mu \left( 1 + \frac{F_{D1}}{mg} + \frac{F_{D2}}{mg} \right) - \frac{F_{AR}}{mg}. \quad (8.22)$$

In particular the aerodynamic forces enhance the braking performance of the vehicle.

## 8.3 Driving and Braking

### 8.3.1 Single Axle Drive

With the rear axle driven in limit situations,  $F_{x1}=0$  and  $F_{x2}=\mu F_{z2}$  hold. Then, using Eq. (8.6) the linear momentum Eq. (8.1) results in

$$m \dot{v}_{RWD} = \mu m g \left[ \frac{a_1}{a_1 + a_2} + \frac{h}{a_1 + a_2} \frac{\dot{v}_{RWD}}{g} \right], \quad (8.23)$$

where the subscript  $RWD$  indicates the rear wheel drive. Hence, the maximum acceleration for a rear wheel driven vehicle is given by

$$\frac{\dot{v}_{RWD}}{g} = \frac{\mu}{1 - \mu \frac{h}{a_1 + a_2}} \frac{a_1}{a_1 + a_2}. \quad (8.24)$$

By setting  $F_{x1}=\mu F_{z1}$  and  $F_{x2}=0$ , the maximum acceleration for a front wheel driven vehicle can be calculated in a similar way. One gets

$$\frac{\dot{v}_{FWD}}{g} = \frac{\mu}{1 + \mu \frac{h}{a_1 + a_2}} \frac{a_2}{a_1 + a_2}, \quad (8.25)$$

where the subscript  $FWD$  denotes front wheel drive. Depending on the parameter  $\mu$ ,  $a_1$ ,  $a_2$  and  $h$  the accelerations may be limited by the tilting condition  $\frac{\dot{v}}{g} \leq \frac{a_2}{h}$ .

The maximum accelerations of a single axle driven vehicle are plotted in Fig. 8.4. For rear wheel driven passenger cars, the parameter  $a_2/(a_1+a_2)$  which describes the static axle load distribution is in the range of  $0.4 \leq a_2/(a_1+a_2) \leq 0.5$ . For  $\mu = 1$  and  $h = 0.55$  this results in maximum accelerations in between  $0.77 \geq \dot{v}/g \geq 0.64$ . Front wheel driven passenger cars usually cover the range  $0.55 \leq a_2/(a_1+a_2) \leq 0.60$  which produces accelerations in the range of  $0.45 \leq \dot{v}/g \leq 0.49$ . Hence, rear wheel driven vehicles can accelerate much faster than front wheel driven vehicles.

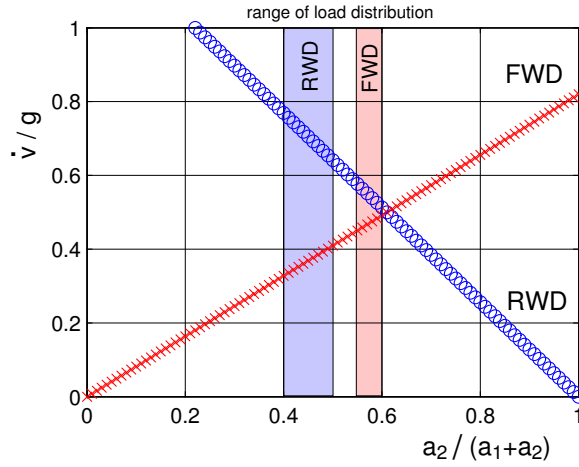


Figure 8.4: Single axle driven passenger car:  $\mu = 1$ ,  $h = 0.55 \text{ m}$ ,  $a_1 + a_2 = 2.5 \text{ m}$

### 8.3.2 Braking at Single Axle

If only the front axle is braked, in the limit case  $F_{x1} = -\mu F_{z1}$  and  $F_{x2} = 0$  will hold. With Eq. (8.5) one gets from Eq. (8.1)

$$m \dot{v}_{FWB} = -\mu m g \left[ \frac{a_2}{a_1 + a_2} - \frac{h}{a_1 + a_2} \frac{\dot{v}_{FWB}}{g} \right], \quad (8.26)$$

where the subscript  $FWB$  indicates front wheel braking. Then, the maximum deceleration is given by

$$\frac{\dot{v}_{FWB}}{g} = - \frac{\mu}{1 - \mu \frac{h}{a_1 + a_2}} \frac{a_2}{a_1 + a_2}. \quad (8.27)$$

If only the rear axle is braked ( $F_{x1} = 0$ ,  $F_{x2} = -\mu F_{z2}$ ), one will obtain the maximum deceleration

$$\frac{\dot{v}_{RWB}}{g} = - \frac{\mu}{1 + \mu \frac{h}{a_1 + a_2}} \frac{a_1}{a_1 + a_2}, \quad (8.28)$$

where the subscript  $RWB$  denotes a braked rear axle. Depending on the parameters  $\mu$ ,  $a_1$ ,  $a_2$ , and  $h$ , the decelerations may be limited by the tilting condition  $\frac{\dot{v}}{g} \geq -\frac{a_1}{h}$ .

The maximum decelerations of a single axle braked vehicle are plotted in Fig. 8.5. For passenger cars the load distribution parameter  $a_2/(a_1 + a_2)$  usually covers the range of 0.4 to 0.6. If only the front axle is braked, decelerations from  $\dot{v}/g = -0.51$  to  $\dot{v}/g = -0.77$  will be achieved. This is a quite large value compared to the deceleration range of a braked rear axle which is in the range of  $\dot{v}/g = -0.49$  to  $\dot{v}/g = -0.33$ . Therefore, the braking system at the front axle has a redundant design.

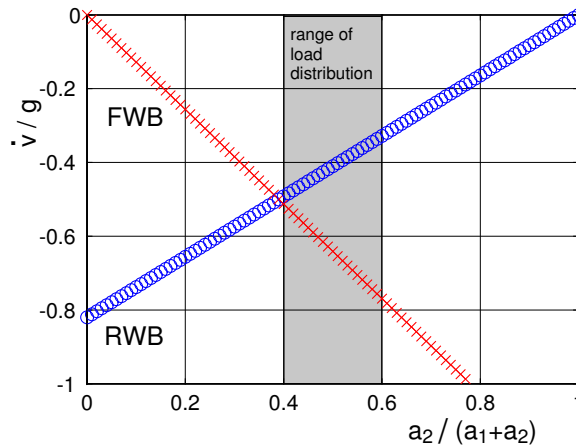


Figure 8.5: Single axle braked passenger car:  $\mu = 1$ ,  $h = 0.55 \text{ m}$ ,  $a_1 + a_2 = 2.5 \text{ m}$

### 8.3.3 Braking Stability

On a locked wheel the tire friction force points into the opposite direction of sliding velocity. Hence, no lateral guidance is provided. That is why a braked vehicle with locked front wheels will remain stable whereas a braked vehicle with locked rear wheels will become unstable.

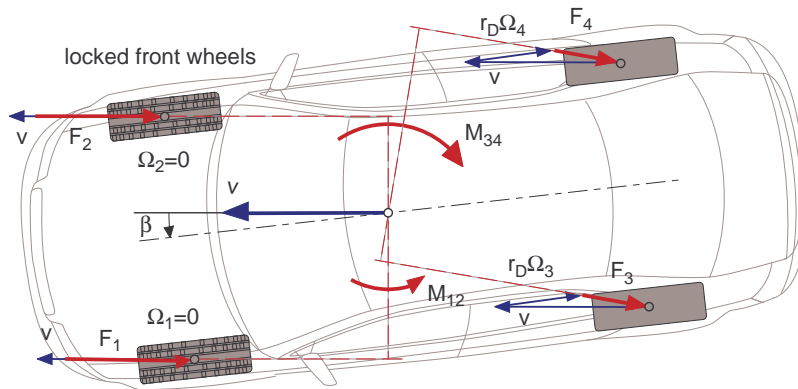


Figure 8.6: Locked front wheels

A small yaw disturbance of the vehicle will cause slip angles at the wheels. If the front wheels are locked and the rear wheels are still rotating, lateral forces can be generated at this axle which will produce a stabilizing torque, Fig. 8.6. However, a de-stabilizing torque will be generated, if the rear wheels are locked and the front wheels are still rotating, Fig. 8.7.

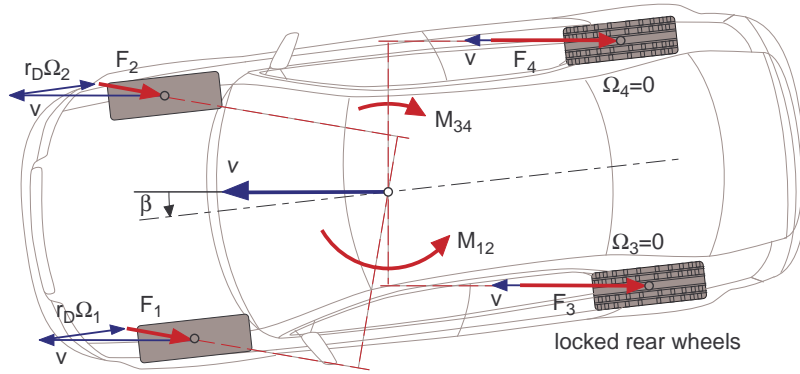


Figure 8.7: Locked rear wheels

### 8.3.4 Optimal Distribution of Drive and Brake Forces

The sum of the longitudinal forces accelerates or decelerates the vehicle. In dimensionless style Eq. (8.1) reads as

$$\frac{\dot{v}}{g} = \frac{F_{x1}}{mg} + \frac{F_{x2}}{mg}. \quad (8.29)$$

A certain acceleration or deceleration can only be achieved by different combinations of the longitudinal forces  $F_{x1}$  and  $F_{x2}$ . According to Eq. (8.19) the longitudinal forces are limited by wheel load and friction.

The optimal combination of  $F_{x1}$  and  $F_{x2}$  will be achieved, when front and rear axle have the same skid resistance.

$$F_{x1} = \pm \nu \mu F_{z1} \quad \text{and} \quad F_{x2} = \pm \nu \mu F_{z2}. \quad (8.30)$$

With Eq. (8.5) and Eq. (8.6) one obtains

$$\frac{F_{x1}}{mg} = \pm \nu \mu \left( \frac{a_2}{h} - \frac{\dot{v}}{g} \right) \frac{h}{a_1 + a_2} \quad (8.31)$$

and

$$\frac{F_{x2}}{mg} = \pm \nu \mu \left( \frac{a_1}{h} + \frac{\dot{v}}{g} \right) \frac{h}{a_1 + a_2}. \quad (8.32)$$

With Eq. (8.31) and Eq. (8.32) one gets from Eq. (8.29)

$$\frac{\dot{v}}{g} = \pm \nu \mu, \quad (8.33)$$

where it has been assumed that  $F_{x1}$  and  $F_{x2}$  have the same sign. Finally, if Eq. (8.33) is inserted in Eqs. (8.31) and (8.32) one will obtain

$$\frac{F_{x1}}{mg} = \frac{\dot{v}}{g} \left( \frac{a_2}{h} - \frac{\dot{v}}{g} \right) \frac{h}{a_1 + a_2} \quad (8.34)$$



### 8.3.5 Different Distributions of Brake Forces

Practical applications aim at approximating the optimal distribution of brake forces by constant distribution, limitation, or reduction of brake forces as good as possible. Fig. 8.9.

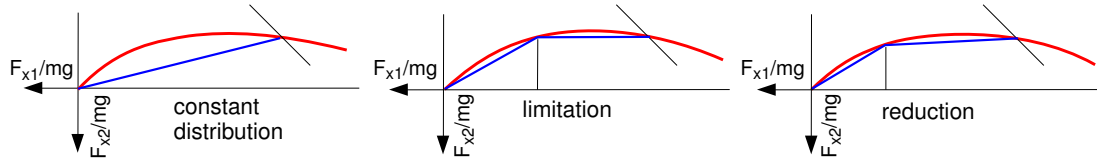


Figure 8.9: Different Distributions of Brake Forces

When braking, the stability of a vehicle depends on the potential of generating a lateral force at the rear axle. Thus, a greater skid (locking) resistance is realized at the rear axle than at the front axle. Therefore, the brake force distributions are all below the optimal curve in the physically relevant area. This restricts the achievable deceleration, specially at low friction values.

Because the optimal curve depends on the center of gravity of the vehicle an additional safety margin has to be installed when designing real brake force distributions. The distribution of brake forces is often fitted to the axle loads. There, the influence of the height of the center of gravity, which may also vary much on trucks, is not taken into account and has to be compensated by a safety margin from the optimal curve. Only the control of brake pressure in anti-lock-systems provides an optimal distribution of brake forces independently from loading conditions.

### 8.3.6 Anti-Lock-System

On hard braking maneuvers large longitudinal slip values occur. Then, the stability and/or steerability is no longer given because nearly no lateral forces can be generated. By controlling the brake torque or brake pressure respectively, the longitudinal slip can be restricted to values that allow considerable lateral forces.

Here, the angular wheel acceleration  $\dot{\Omega}$  is used as a control variable. Angular accelerations of the wheel are derived from the measured angular speeds of the wheel by differentiation. The rolling condition is fulfilled with a longitudinal slip of  $s_L = 0$ . Then

$$r_D \dot{\Omega} = \ddot{x} \tag{8.39}$$

holds, where  $r_D$  labels the dynamic tire radius and  $\ddot{x}$  names the longitudinal acceleration of the vehicle. According to Eq. (8.21), the maximum acceleration/deceleration of a vehicle depends on the friction coefficient,  $|\ddot{x}| = \mu g$ . For a given friction coeffi-

cient  $\mu$  a simple control law can be realized for each wheel

$$|\dot{\Omega}| \leq \frac{1}{r_D} |\ddot{x}|. \tag{8.40}$$

Because no reliable possibility to determine the local friction coefficient between tire and road has been found until today, useful information can only be gained from Eq. (8.40) at optimal conditions on dry road. Therefore, the longitudinal slip is used as a second control variable.

In order to calculate longitudinal slips, a reference speed is estimated from all measured wheel speeds which is used for the calculation of slip at all wheels, then. This method is too imprecise at low speeds. Therefore, no control is applied below a limit velocity. Problems also arise when all wheels lock simultaneously for example which may happen on icy roads.

The control of the brake torque is done via the brake pressure which can be *increased, held, or decreased* by a three-way valve. To prevent vibrations, the decrement is usually made slower than the increment.

To prevent a strong yaw reaction, the *select low* principle is often used with  $\mu$ -split braking at the rear axle. Here, the break pressure at both wheels is controlled by the wheel running on lower friction. Thus, at least the brake forces at the rear axle cause no yaw torque. However, the maximum achievable deceleration is reduced by this.

### 8.3.7 Braking on $\mu$ -Split

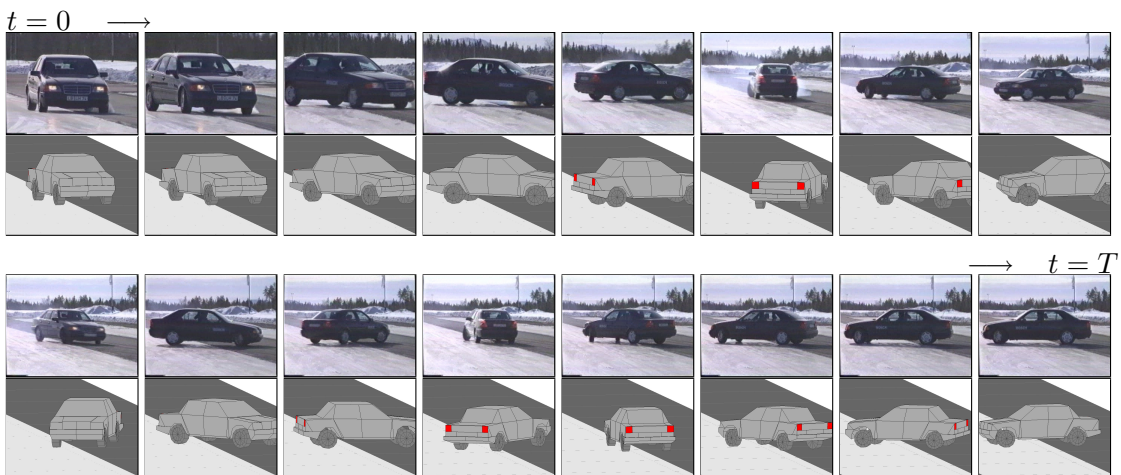


Figure 8.10: Braking on  $\mu$ -split: Field Test / ve-DYNA-Simulation [27]

A vehicle without an anti-lock system braked on a  $\mu$ -split surface shows a strong yaw reaction which causes the vehicle to spin around the vertical axis. In Fig. 8.10

screen shots of a commercial trailer to the EPS-system from the company Robert Bosch GmbH are compared with the results of a ve-DYNA-simulation. Despite of different vehicles and estimated friction coefficients for the dry ( $\mu = 1$ ) and the icy part ( $\mu = 0.05$ ) of the test track the simulation results are in good conformity to the field test. Whereas the reproducibility of field tests is not always given a computer simulation can be repeated exactly with the same environmental conditions.

## 8.4 Drive and Brake Pitch

### 8.4.1 Vehicle Model

The vehicle model in Fig. 8.11 consists of five rigid bodies. The body has three de-

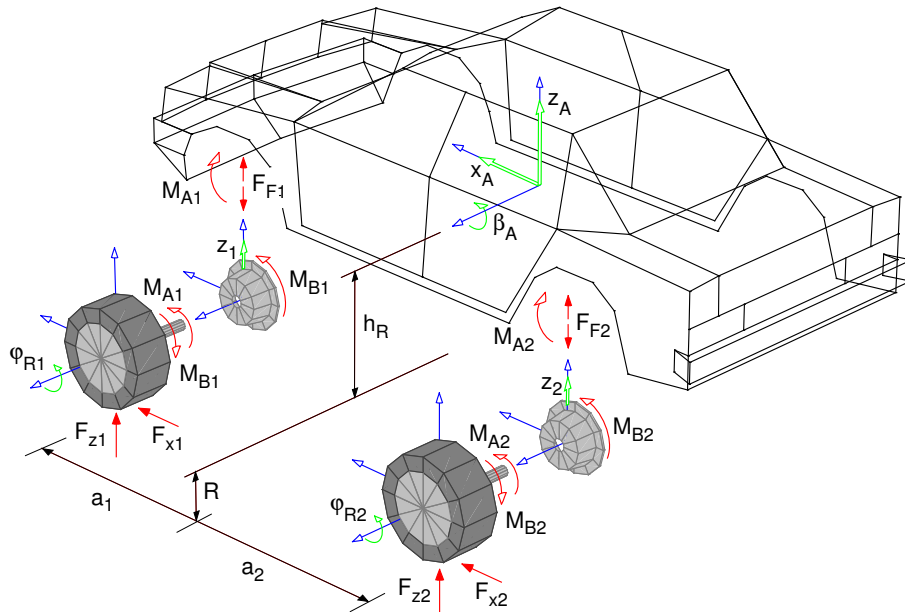


Figure 8.11: Planar Vehicle Model

grees of freedom: Longitudinal motion  $x_A$ , vertical motion  $z_A$  and pitch  $\beta_A$ . The coordinates  $z_1$  and  $z_2$  represent the vertical motions of wheel and axle bodies relative to the body. Finally, the rotation angles  $\varphi_{R1}$  and  $\varphi_{R2}$  describe the wheel rotations relative to the wheel bodies. The longitudinal and rotational motions of the wheel bodies relative to the body can be described via suspension kinematics as functions of the vertical wheel motion

$$x_1 = x_1(z_1), \quad \beta_1 = \beta_1(z_1) \quad \text{and} \quad x_2 = x_2(z_2), \quad \beta_2 = \beta_2(z_2). \quad (8.41)$$

The forces between wheel body and vehicle body are labeled  $F_{F1}$  and  $F_{F2}$ . At the wheels drive torques  $M_{A1}$ ,  $M_{A2}$  and brake torques  $M_{B1}$ ,  $M_{B2}$ , longitudinal forces

$F_{x1}$ ,  $F_{x2}$  and the wheel loads  $F_{z1}$ ,  $F_{z2}$  apply. The brake torques are directly supported by the wheel bodies, whereas the drive torques are transmitted by the drive shafts to the vehicle body. The forces and torques that apply to the single bodies are listed in the last column of the tables 8.1 and 8.2.

The velocity of the vehicle body and its angular velocity are given by

$$v_{0A,0} = \begin{bmatrix} \dot{x}_A \\ 0 \\ 0 \end{bmatrix} + \begin{bmatrix} 0 \\ 0 \\ \dot{z}_A \end{bmatrix}; \quad \omega_{0A,0} = \begin{bmatrix} 0 \\ \dot{\beta}_A \\ 0 \end{bmatrix}. \quad (8.42)$$

At small rotational motions of the body one gets for the velocities of the wheel bodies and wheels

$$v_{0RK_1,0} = v_{0R_1,0} = \begin{bmatrix} \dot{x}_A \\ 0 \\ 0 \end{bmatrix} + \begin{bmatrix} 0 \\ 0 \\ \dot{z}_A \end{bmatrix} + \begin{bmatrix} -h_R \dot{\beta}_A \\ 0 \\ -a_1 \dot{\beta}_A \end{bmatrix} + \begin{bmatrix} \frac{\partial x_1}{\partial z_1} \dot{z}_1 \\ 0 \\ \dot{z}_1 \end{bmatrix}; \quad (8.43)$$

$$v_{0RK_2,0} = v_{0R_2,0} = \begin{bmatrix} \dot{x}_A \\ 0 \\ 0 \end{bmatrix} + \begin{bmatrix} 0 \\ 0 \\ \dot{z}_A \end{bmatrix} + \begin{bmatrix} -h_R \dot{\beta}_A \\ 0 \\ +a_2 \dot{\beta}_A \end{bmatrix} + \begin{bmatrix} \frac{\partial x_2}{\partial z_2} \dot{z}_2 \\ 0 \\ \dot{z}_2 \end{bmatrix}. \quad (8.44)$$

The angular velocities of the wheel bodies and wheels are obtained from

$$\omega_{0RK_1,0} = \begin{bmatrix} 0 \\ \dot{\beta}_A \\ 0 \end{bmatrix} + \begin{bmatrix} 0 \\ \dot{\beta}_1 \\ 0 \end{bmatrix} \quad \text{and} \quad \omega_{0R_1,0} = \begin{bmatrix} 0 \\ \dot{\beta}_A \\ 0 \end{bmatrix} + \begin{bmatrix} 0 \\ \dot{\beta}_1 \\ 0 \end{bmatrix} + \begin{bmatrix} 0 \\ \dot{\varphi}_{R1} \\ 0 \end{bmatrix} \quad (8.45)$$

as well as

$$\omega_{0RK_2,0} = \begin{bmatrix} 0 \\ \dot{\beta}_A \\ 0 \end{bmatrix} + \begin{bmatrix} 0 \\ \dot{\beta}_2 \\ 0 \end{bmatrix} \quad \text{and} \quad \omega_{0R_2,0} = \begin{bmatrix} 0 \\ \dot{\beta}_A \\ 0 \end{bmatrix} + \begin{bmatrix} 0 \\ \dot{\beta}_2 \\ 0 \end{bmatrix} + \begin{bmatrix} 0 \\ \dot{\varphi}_{R2} \\ 0 \end{bmatrix} \quad (8.46)$$

Introducing a vector of generalized velocities

$$z = [\dot{x}_A \quad \dot{z}_A \quad \dot{\beta}_A \quad \dot{\beta}_1 \quad \dot{\varphi}_{R1} \quad \dot{\beta}_2 \quad \dot{\varphi}_{R2}]^T, \quad (8.47)$$

the velocities and angular velocities given by Eqs. (8.42), (8.43), (8.44), (8.45), and (8.46) can be written as

$$v_{0i} = \sum_{j=1}^7 \frac{\partial v_{0i}}{\partial z_j} z_j \quad \text{and} \quad \omega_{0i} = \sum_{j=1}^7 \frac{\partial \omega_{0i}}{\partial z_j} z_j \quad (8.48)$$

## 8 Longitudinal Dynamics

bodies	partial velocities $\partial v_{0i}/\partial z_j$							applied forces
	$\dot{x}_A$	$\dot{z}_A$	$\dot{\beta}_A$	$\dot{z}_1$	$\dot{\varphi}_{R1}$	$\dot{z}_2$	$\dot{\varphi}_{R2}$	$F_i^e$
chassis $m_A$	1	0	0	0	0	0	0	0
	0	0	0	0	0	0	0	0
	0	1	0	0	0	0	0	$F_{F1} + F_{F2} - m_A g$
wheel body front $m_{RK1}$	1	0	$-h_R$	$\frac{\partial x_1}{\partial z_1}$	0	0	0	0
	0	0	0	0	0	0	0	0
	0	1	$-a_1$	1	0	0	0	$-F_{F1} - m_{RK1} g$
wheel front $m_{R1}$	1	0	$-h_R$	$\frac{\partial x_1}{\partial z_1}$	0	0	0	$F_{x1}$
	0	0	0	0	0	0	0	0
	0	1	$-a_1$	1	0	0	0	$F_{z1} - m_{R1} g$
wheel body rear $m_{RK2}$	1	0	$-h_R$	0	0	$\frac{\partial x_2}{\partial z_2}$	0	0
	0	0	0	0	0	0	0	0
	0	1	$a_2$	0	0	1	0	$-F_{F2} - m_{RK2} g$
wheel rear $m_{R2}$	1	0	$-h_R$	0	0	$\frac{\partial x_2}{\partial z_2}$	0	$F_{x2}$
	0	0	0	0	0	0	0	0
	0	1	$a_2$	0	0	1	0	$F_{z2} - m_{R2} g$

Table 8.1: Partial velocities and applied forces

bodies	partial angular velocities $\partial \omega_{0i}/\partial z_j$							applied torques
	$\dot{x}_A$	$\dot{z}_A$	$\dot{\beta}_A$	$\dot{z}_1$	$\dot{\varphi}_{R1}$	$\dot{z}_2$	$\dot{\varphi}_{R2}$	$M_i^e$
chassis $\Theta_A$	0	0	0	0	0	0	0	0
	0	0	1	0	0	0	0	$-M_{A1} - M_{A2} - a_1 F_{F1} + a_2 F_{F2}$
	0	0	0	0	0	0	0	0
wheel body front $\Theta_{RK1}$	0	0	0	0	0	0	0	0
	0	0	1	$\frac{\partial \beta_1}{\partial z_1}$	0	0	0	$M_{B1}$
	0	0	0	0	0	0	0	0
wheel front $\Theta_{R1}$	0	0	0	0	0	0	0	0
	0	0	1	$\frac{\partial \beta_1}{\partial z_1}$	1	0	0	$M_{A1} - M_{B1} - R F_{x1}$
	0	0	0	0	0	0	0	0
wheel body rear $\Theta_{RK2}$	0	0	0	0	0	0	0	0
	0	0	1	0	0	$\frac{\partial \beta_2}{\partial z_2}$	0	$M_{B2}$
	0	0	0	0	0	0	0	0
wheel rear $\Theta_{R2}$	0	0	0	0	0	0	0	0
	0	0	1	0	0	$\frac{\partial \beta_2}{\partial z_2}$	1	$M_{A2} - M_{B2} - R F_{x2}$
	0	0	0	0	0	0	0	0

Table 8.2: Partial angular velocities and applied torques

### 8.4.2 Equations of Motion

The partial velocities  $\frac{\partial v_{0i}}{\partial z_j}$  and partial angular velocities  $\frac{\partial \omega_{0i}}{\partial z_j}$  for the five bodies  $i = 1(1)5$  and for the seven generalized speeds  $j = 1(1)7$  are arranged in the tables 8.1 and 8.2.

With the aid of the partial velocities and partial angular velocities the elements of the mass matrix  $M$  and the components of the vector of generalized forces and torques  $Q$  can be calculated.

$$M(i, j) = \sum_{k=1}^5 \left( \frac{\partial v_{0k}}{\partial z_i} \right)^T m_k \frac{\partial v_{0k}}{\partial z_j} + \sum_{k=1}^5 \left( \frac{\partial \omega_{0k}}{\partial z_i} \right)^T \Theta_k \frac{\partial \omega_{0k}}{\partial z_j}; \quad i, j = 1(1)7; \quad (8.49)$$

$$Q(i) = \sum_{k=1}^5 \left( \frac{\partial v_{0k}}{\partial z_i} \right)^T F_k^e + \sum_{k=1}^5 \left( \frac{\partial \omega_{0k}}{\partial z_i} \right)^T M_k^e; \quad i = 1(1)7. \quad (8.50)$$

Then, the equations of motion for the planar vehicle model are given by

$$M \dot{z} = Q. \quad (8.51)$$

### 8.4.3 Equilibrium

With the abbreviations

$$m_1 = m_{RK1} + m_{R1}; \quad m_2 = m_{RK2} + m_{R2}; \quad m_G = m_A + m_1 + m_2 \quad \text{and} \quad h = h_R + R \quad (8.52)$$

The components of the vector of generalized forces and torques read as

$$\begin{aligned} Q(1) &= F_{x1} + F_{x2}; \\ Q(2) &= F_{z1} + F_{z2} - m_G g; \end{aligned} \quad (8.53)$$

$$Q(3) = -a_1 F_{z1} + a_2 F_{z2} - h(F_{x1} + F_{x2}) + a_1 m_1 g - a_2 m_2 g;$$

$$Q(4) = F_{z1} - F_{F1} + \frac{\partial x_1}{\partial z_1} F_{x1} - m_1 g + \frac{\partial \beta_1}{\partial z_1} (M_{A1} - R F_{x1}); \quad (8.54)$$

$$Q(5) = M_{A1} - M_{B1} - R F_{x1};$$

$$Q(6) = F_{z2} - F_{F2} + \frac{\partial x_2}{\partial z_2} F_{x2} - m_2 g + \frac{\partial \beta_2}{\partial z_2} (M_{A2} - R F_{x2}); \quad (8.55)$$

$$Q(7) = M_{A2} - M_{B2} - R F_{x2}.$$

Without drive and brake forces

$$M_{A1} = 0; \quad M_{A2} = 0; \quad M_{B1} = 0; \quad M_{B2} = 0 \quad (8.56)$$

from Eqs. (8.53), (8.54) and (8.55) one gets the steady state longitudinal forces, the spring preloads, and the wheel loads

$$\begin{aligned} F_{x1}^0 &= 0; & F_{x2}^0 &= 0; \\ F_{F1}^0 &= \frac{a_2}{a_1+a_2} m_A g; & F_{F2}^0 &= \frac{a_1}{a_1+a_2} m_A g; \\ F_{z1}^0 &= m_1 g + \frac{a_2}{a_1+a_2} m_A g; & F_{z2}^0 &= m_2 g + \frac{a_1}{a_1+a_2} m_A g. \end{aligned} \quad (8.57)$$

### 8.4.4 Driving and Braking

Assuming that on accelerating or decelerating the vehicle the wheels neither slip nor lock,

$$R \dot{\varphi}_{R1} = \dot{x}_A - h_R \dot{\beta}_A + \frac{\partial x_1}{\partial z_1} \dot{z}_1 \quad \text{and} \quad R \dot{\varphi}_{R2} = \dot{x}_A - h_R \dot{\beta}_A + \frac{\partial x_2}{\partial z_2} \dot{z}_2 \quad (8.58)$$

hold. In steady state the pitch motion of the body and the vertical motion of the wheels reach constant values

$$\beta_A = \beta_A^{st} = \text{const.}, \quad z_1 = z_1^{st} = \text{const.}, \quad z_2 = z_2^{st} = \text{const.} \quad (8.59)$$

and Eq. (8.58) simplifies to

$$R \dot{\varphi}_{R1} = \dot{x}_A; \quad R \dot{\varphi}_{R2} = \dot{x}_A. \quad (8.60)$$

With Eqs. (8.59), (8.60) and (8.52) the equation of motion (8.51) results in

$$\begin{aligned} m_G \ddot{x}_A &= F_{x1}^a + F_{x2}^a; \\ 0 &= F_{z1}^a + F_{z2}^a; \\ -h_R(m_1 + m_2) \ddot{x}_A + \Theta_{R1} \frac{\ddot{x}_A}{R} + \Theta_{R2} \frac{\ddot{x}_A}{R} &= -a_1 F_{z1}^a + a_2 F_{z2}^a - (h_R + R)(F_{x1}^a + F_{x2}^a); \end{aligned} \quad (8.61)$$

$$\begin{aligned} \frac{\partial x_1}{\partial z_1} m_1 \ddot{x}_A + \frac{\partial \beta_1}{\partial z_1} \Theta_{R1} \frac{\ddot{x}_A}{R} &= F_{z1}^a - F_{F1}^a + \frac{\partial x_1}{\partial z_1} F_{x1}^a + \frac{\partial \beta_1}{\partial z_1} (M_{A1} - R F_{x1}^a); \\ \Theta_{R1} \frac{\ddot{x}_A}{R} &= M_{A1} - M_{B1} - R F_{x1}^a; \end{aligned} \quad (8.62)$$

$$\begin{aligned} \frac{\partial x_2}{\partial z_2} m_2 \ddot{x}_A + \frac{\partial \beta_2}{\partial z_2} \Theta_{R2} \frac{\ddot{x}_A}{R} &= F_{z2}^a - F_{F2}^a + \frac{\partial x_2}{\partial z_2} F_{x2}^a + \frac{\partial \beta_2}{\partial z_2} (M_{A2} - R F_{x2}^a); \\ \Theta_{R2} \frac{\ddot{x}_A}{R} &= M_{A2} - M_{B2} - R F_{x2}^a; \end{aligned} \quad (8.63)$$

where the steady state spring forces, longitudinal forces, and wheel loads have been separated into initial and acceleration-dependent terms

$$F_{xi}^{st} = F_{xi}^0 + F_{xi}^a; \quad F_{zi}^{st} = F_{zi}^0 + F_{zi}^a; \quad F_{Fi}^{st} = F_{Fi}^0 + F_{Fi}^a; \quad i=1,2. \quad (8.64)$$

With given torques of drive and brake the vehicle acceleration  $\ddot{x}_A$ , the wheel forces  $F_{x1}^a, F_{x2}^a, F_{z1}^a, F_{z2}^a$  and the spring forces  $F_{F1}^a, F_{F2}^a$  can be calculated from Eqs. (8.61), (8.62) and (8.63).

Via the spring characteristics which have been assumed as linear the acceleration-dependent forces also cause a vertical displacement and pitch motion of the body besides the vertical motions of the wheels,

$$\begin{aligned} F_{F1}^a &= c_{A1} z_1^a, & F_{F2}^a &= c_{A2} z_2^a, \\ F_{z1}^a &= -c_{R1} (z_A^a - a_1 \beta_A^a + z_1^a), & F_{z2}^a &= -c_{R2} (z_A^a + a_2 \beta_A^a + z_2^a). \end{aligned} \quad (8.65)$$

Especially the pitch of the vehicle  $\beta_A^a \neq 0$ , caused by drive or brake will be felt as annoying, if too distinct.

By an axle kinematics with 'anti dive' and/or 'anti squat' properties, the drive and/or brake pitch angle can be reduced by rotating the wheel body and moving the wheel center in longitudinal direction during the suspension travel.

#### 8.4.5 Anti Dive and Anti Squat

The pitch of the vehicle caused by drive or brake will be felt as annoying, if too distinct. By an axle kinematics with 'anti dive' and/or 'anti squat' properties, the drive and/or brake pitch angle can be reduced by rotating the wheel body and moving the wheel center in longitudinal direction during the suspension travel.

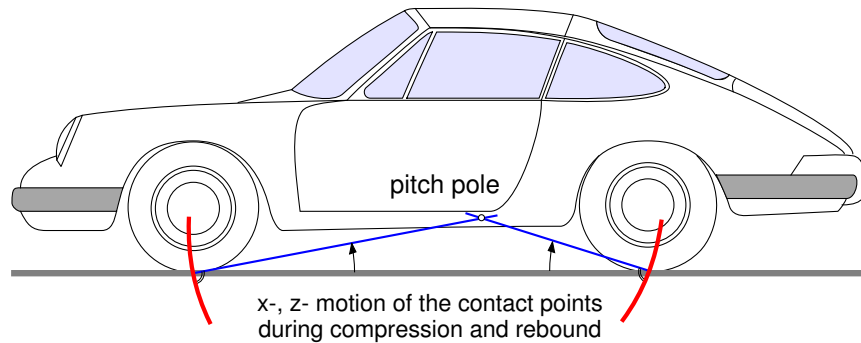


Figure 8.12: Brake Pitch Pole

For real suspension systems the brake pitch pole can be calculated from the motions of the wheel contact points in the  $x$ -,  $z$ -plane, Fig. 8.12. Increasing the pitch pole height above the track level means a decrease in the brake pitch angle. However, the pitch pole is not set above the height of the center of gravity in practice, because the front of the vehicle would rise at braking then.

# 9 Lateral Dynamics

## 9.1 Kinematic Approach

### 9.1.1 Kinematic Tire Model

When a vehicle drives through a curve at low lateral acceleration, small lateral forces will be needed for course holding. Then, hardly lateral slip occurs at the wheels. In the ideal case at vanishing lateral slip the wheels only move in circumferential direction. The velocity component of the contact point in the lateral direction of the tire vanishes then

$$v_y = e_y^T v_{0P} = 0. \quad (9.1)$$

This constraint equation can be used as "kinematic tire model" for course calculation of vehicles moving in the low lateral acceleration range.

### 9.1.2 Ackermann Geometry

Within the validity limits of the kinematic tire model the necessary steering angle of the front wheels can be constructed via the given momentary pivot pole  $M$ , Fig. 9.1.

At slowly moving vehicles the lay out of the steering linkage is usually done according to the Ackermann geometry. Then, the following relations apply

$$\tan \delta_1 = \frac{a}{R} \quad \text{and} \quad \tan \delta_2 = \frac{a}{R+s}, \quad (9.2)$$

where  $s$  labels the track width and  $a$  denotes the wheel base. Eliminating the curve radius  $R$ , we get

$$\tan \delta_2 = \frac{a}{\frac{a}{\tan \delta_1} + s} \quad \text{or} \quad \tan \delta_2 = \frac{a \tan \delta_1}{a + s \tan \delta_1}. \quad (9.3)$$

The deviations  $\Delta \delta_2 = \delta_2^a - \delta_2^A$  of the actual steering angle  $\delta_2^a$  from the Ackermann steering angle  $\delta_2^A$ , which follows from Eq. (9.3), are used, especially on commercial vehicles, to judge the quality of a steering system.

At a rotation around the momentary pole  $M$ , the direction of the velocity is fixed for every point of the vehicle. The angle  $\beta$  between the velocity vector  $v$  and the longitudinal axis of the vehicle is called side slip angle. The side slip angle at point  $P$  is given by

$$\tan \beta_P = \frac{x}{R} \quad \text{or} \quad \tan \beta_P = \frac{x}{a} \tan \delta_1, \quad (9.4)$$

where  $x$  defines the distance of  $P$  to the inner rear wheel.

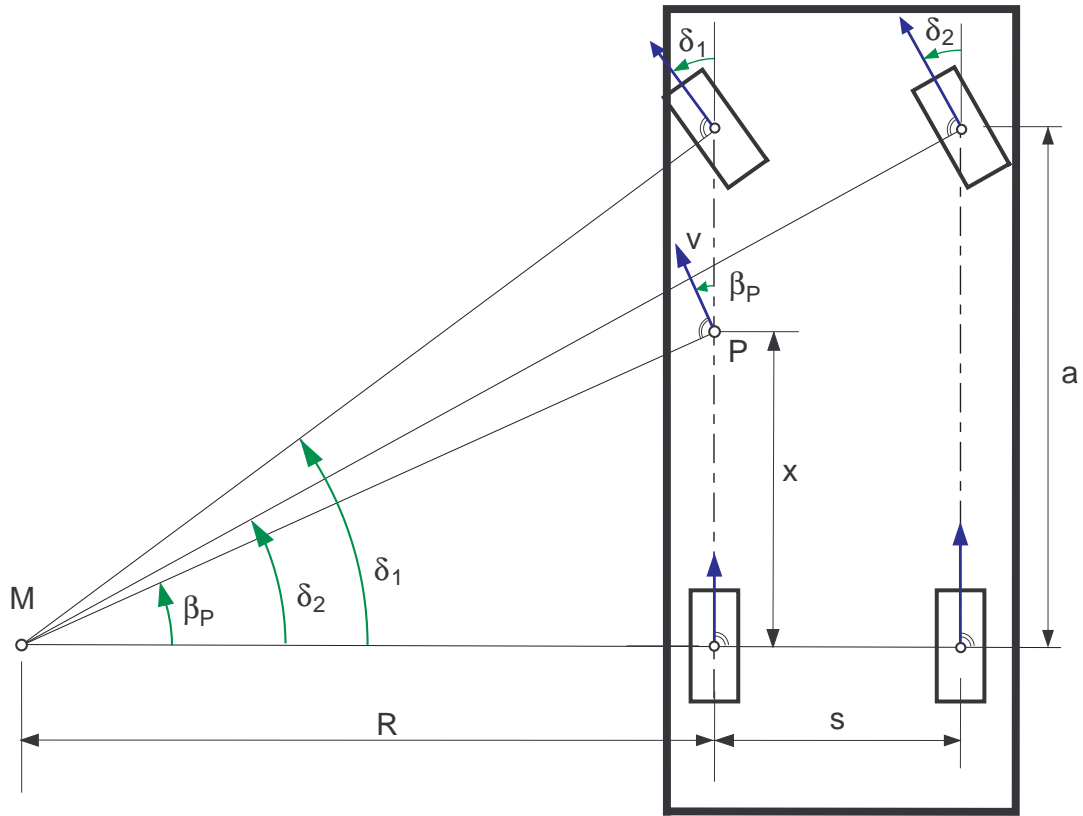


Figure 9.1: Ackermann steering geometry at a two-axled vehicle

### 9.1.3 Space Requirement

The Ackermann approach can also be used to calculate the space requirement of a vehicle during cornering, Fig. 9.2. If the front wheels of a two-axled vehicle are steered according to the Ackermann geometry, the outer point of the vehicle front will run on the maximum radius  $R_{max}$ , whereas a point on the inner side of the vehicle at the location of the rear axle will run on the minimum radius  $R_{min}$ . Hence, it holds

$$R_{max}^2 = (R_{min} + b)^2 + (a + f)^2, \quad (9.5)$$

where  $a$ ,  $b$  are the wheel base and the width of the vehicle, and  $f$  specifies the distance from the front of the vehicle to the front axle. Then, the space requirement  $\Delta R = R_{max} - R_{min}$  can be specified as a function of the cornering radius  $R_{min}$  for a given vehicle dimension

$$\Delta R = R_{max} - R_{min} = \sqrt{(R_{min} + b)^2 + (a + f)^2} - R_{min}. \quad (9.6)$$

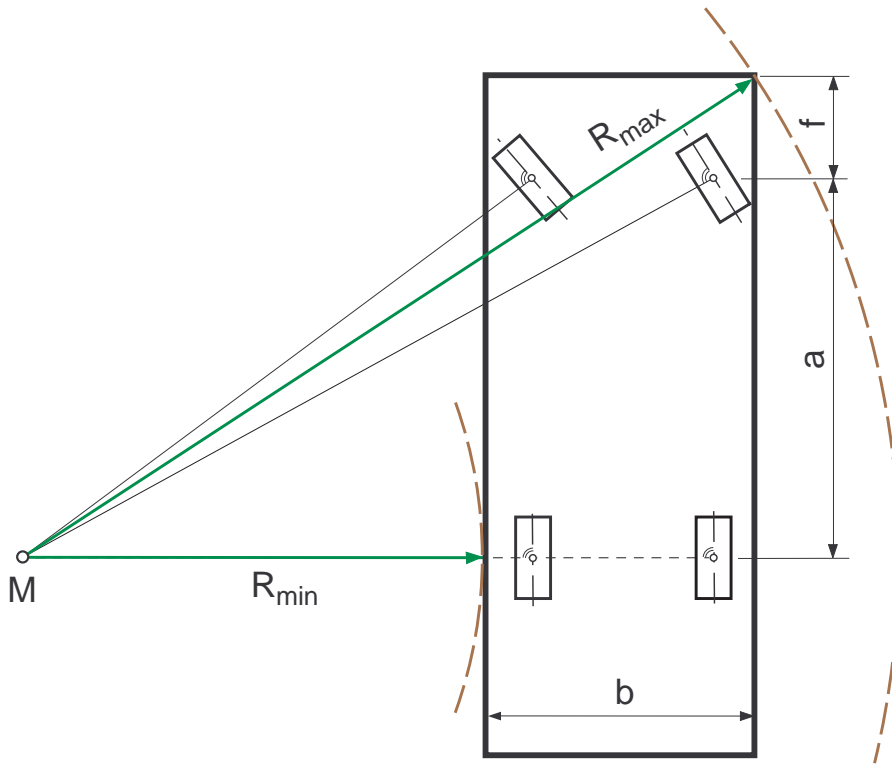


Figure 9.2: Space requirement

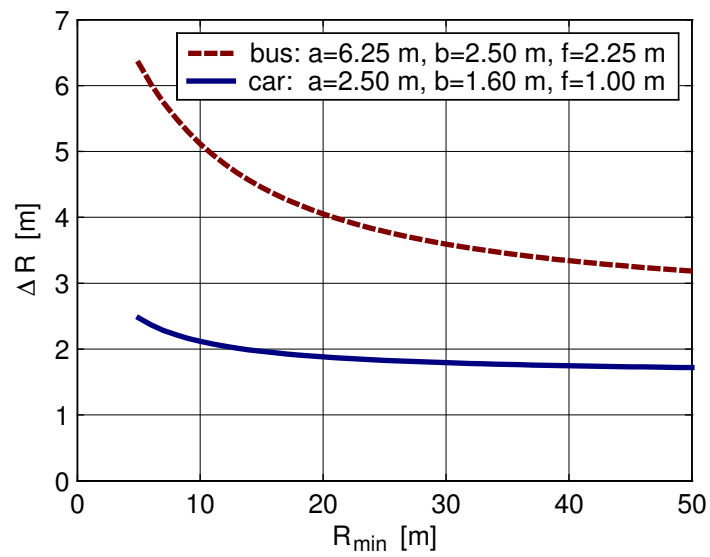


Figure 9.3: Space requirement of a typical passenger car and bus

The space requirement  $\Delta R$  of a typical passenger car and a bus is plotted in Fig. 9.3 versus the minimum cornering radius. In narrow curves  $R_{min} = 5.0 m$ , a bus requires a space of 2.5 times the width, whereas a passenger car needs only 1.5 times the width.

## 9.1.4 Vehicle Model with Trailer

### 9.1.4.1 Kinematics

Fig. 9.4 shows a simple lateral dynamics model for a two-axled vehicle with a single-axled trailer. Vehicle and trailer move on a horizontal track. The position and the orientation of the vehicle relative to the track fixed frame  $x_0, y_0, z_0$  is defined by the position vector to the rear axle center

$$r_{02,0} = \begin{bmatrix} x \\ y \\ R \end{bmatrix} \quad (9.7)$$

and the rotation matrix

$$A_{02} = \begin{bmatrix} \cos \gamma & -\sin \gamma & 0 \\ \sin \gamma & \cos \gamma & 0 \\ 0 & 0 & 1 \end{bmatrix}. \quad (9.8)$$

Here, the tire radius  $R$  is considered to be constant, and  $x, y$  as well as the yaw angle  $\gamma$  are generalized coordinates.

The position vector

$$r_{01,0} = r_{02,0} + A_{02} r_{21,2} \quad \text{with} \quad r_{21,2} = \begin{bmatrix} a \\ 0 \\ 0 \end{bmatrix} \quad (9.9)$$

and the rotation matrix

$$A_{01} = A_{02} A_{21} \quad \text{with} \quad A_{21} = \begin{bmatrix} \cos \delta & -\sin \delta & 0 \\ \sin \delta & \cos \delta & 0 \\ 0 & 0 & 1 \end{bmatrix} \quad (9.10)$$

describe the position and the orientation of the front axle, where  $a = const$  labels the wheel base and  $\delta$  the steering angle.

The position vector

$$r_{03,0} = r_{02,0} + A_{02} (r_{2K,2} + A_{23} r_{K3,3}) \quad (9.11)$$

with

$$r_{2K,2} = \begin{bmatrix} -b \\ 0 \\ 0 \end{bmatrix} \quad \text{and} \quad r_{K3,2} = \begin{bmatrix} -c \\ 0 \\ 0 \end{bmatrix} \quad (9.12)$$

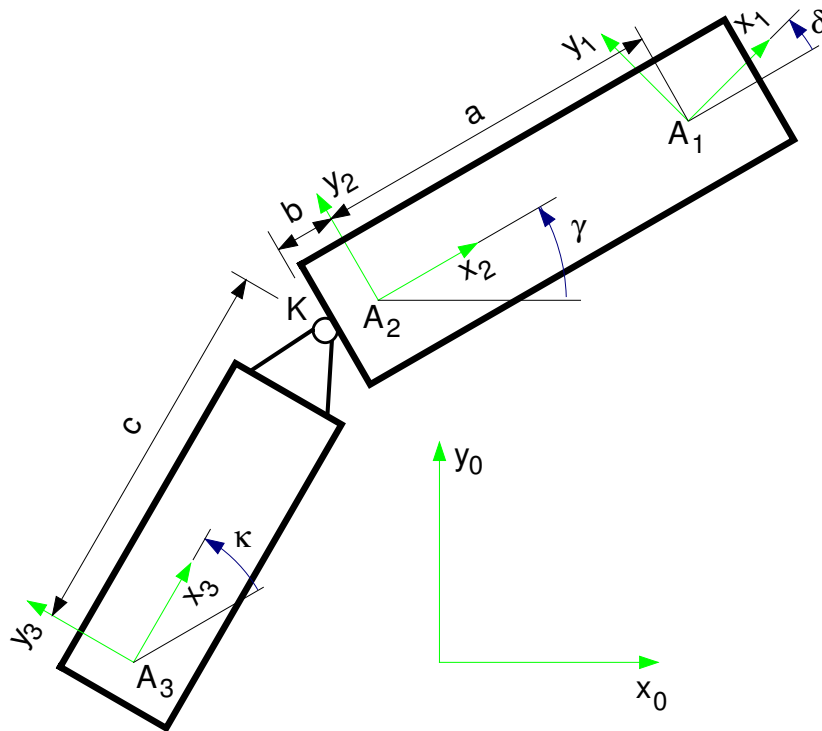


Figure 9.4: Kinematic model with trailer

and the rotation matrix

$$A_{03} = A_{02} A_{23} \quad \text{with} \quad A_{23} = \begin{bmatrix} \cos \kappa & -\sin \kappa & 0 \\ \sin \kappa & \cos \kappa & 0 \\ 0 & 0 & 1 \end{bmatrix} \quad (9.13)$$

define the position and the orientation of the trailer axis, with  $\kappa$  labeling the bend angle between vehicle and trailer, and  $b$ ,  $c$  marking the distances from the rear axle 2 to the coupling point  $K$  and from the coupling point  $K$  to the trailer axis 3.

#### 9.1.4.2 Vehicle Motion

According to the kinematic tire model, cf. section 9.1.1, the velocity at the rear axle can only have a component in the longitudinal direction of the tire which here corresponds with the longitudinal direction of the vehicle

$$v_{02,2} = \begin{bmatrix} v_{x2} \\ 0 \\ 0 \end{bmatrix}. \quad (9.14)$$

The time derivative of Eq. (9.7) results in

$$v_{02,0} = \dot{r}_{02,0} = \begin{bmatrix} \dot{x} \\ \dot{y} \\ 0 \end{bmatrix}. \quad (9.15)$$

The transformation of Eq. (9.14) into the system 0

$$v_{02,0} = A_{02} v_{02,2} = A_{02} \begin{bmatrix} v_{x2} \\ 0 \\ 0 \end{bmatrix} = \begin{bmatrix} \cos \gamma v_{x2} \\ \sin \gamma v_{x2} \\ 0 \end{bmatrix} \quad (9.16)$$

compared to Eq. (9.15) results in two first order differential equations for the position coordinates  $x$  and  $y$

$$\dot{x} = v_{x2} \cos \gamma, \quad (9.17)$$

$$\dot{y} = v_{x2} \sin \gamma. \quad (9.18)$$

The velocity at the front axle follows from Eq. (9.9)

$$v_{01,0} = \dot{r}_{01,0} = \dot{r}_{02,0} + \omega_{02,0} \times A_{02} r_{21,2}. \quad (9.19)$$

Transformed into the vehicle fixed system  $x_2, y_2, z_2$  we obtain

$$v_{01,2} = \underbrace{\begin{bmatrix} v_{x2} \\ 0 \\ 0 \end{bmatrix}}_{v_{02,2}} + \underbrace{\begin{bmatrix} 0 \\ 0 \\ \dot{\gamma} \end{bmatrix}}_{\omega_{02,2}} \times \underbrace{\begin{bmatrix} a \\ 0 \\ 0 \end{bmatrix}}_{r_{21,2}} = \begin{bmatrix} v_{x2} \\ a \dot{\gamma} \\ 0 \end{bmatrix}. \quad (9.20)$$

The unit vectors

$$e_{x1,2} = \begin{bmatrix} \cos \delta \\ \sin \delta \\ 0 \end{bmatrix} \quad \text{and} \quad e_{y1,2} = \begin{bmatrix} -\sin \delta \\ \cos \delta \\ 0 \end{bmatrix} \quad (9.21)$$

define the longitudinal and lateral direction at the front axle. According to Eq. (9.1) the velocity component lateral to the wheel must vanish,

$$e_{y1,2}^T v_{01,2} = -\sin \delta v_{x2} + \cos \delta a \dot{\gamma} = 0. \quad (9.22)$$

Whereas in longitudinal direction the velocity

$$e_{x1,2}^T v_{01,2} = \cos \delta v_{x2} + \sin \delta a \dot{\gamma} = v_{x1} \quad (9.23)$$

remains. From Eq. (9.22) a first order differential equation follows for the yaw angle

$$\dot{\gamma} = \frac{v_{x2}}{a} \tan \delta. \quad (9.24)$$

The momentary position  $x = x(t)$ ,  $y = y(t)$  and the orientation  $\gamma = \gamma(t)$  of the vehicle is defined by three differential equations (9.17), (9.18) and (9.24) which are driven by the vehicle velocity  $v_{x2}$  and the steering angle  $\delta$ .

### 9.1.4.3 Entering a Curve

In analogy to Eq. (9.2) the steering angle  $\delta$  can be related to the current track radius  $R$  or with  $k = 1/R$  to the current track curvature

$$\tan \delta = \frac{a}{R} = a \frac{1}{R} = a k. \quad (9.25)$$

Then, the differential equation for the yaw angle reads as

$$\dot{\gamma} = v_{x2} k. \quad (9.26)$$

With the curvature gradient

$$k = k(t) = k_C \frac{t}{T}, \quad (9.27)$$

the entering of a curve is described as a continuous transition from a straight line with the curvature  $k = 0$  into a circle with the curvature  $k = k_C$ .

The yaw angle of the vehicle can be calculated by simple integration now

$$\gamma(t) = \frac{v_{x2} k_C}{T} \frac{t^2}{2}, \quad (9.28)$$

where at time  $t = 0$  a vanishing yaw angle,  $\gamma(t = 0) = 0$ , has been assumed. Then, the position of the vehicle follows with Eq. (9.28) from the differential equations Eqs. (9.17) and (9.18)

$$x = v_{x2} \int_{t=0}^{t=T} \cos\left(\frac{v_{x2} k_C}{T} \frac{t^2}{2}\right) dt, \quad y = v_{x2} \int_{t=0}^{t=T} \sin\left(\frac{v_{x2} k_C}{T} \frac{t^2}{2}\right) dt. \quad (9.29)$$

At constant vehicle speed,  $v_{x2} = \text{const.}$ , Eq. (9.29) is the parameterized form of a clothoid. From Eq. (9.25) the necessary steering angle can be calculated, too. If only small steering angles are necessary for driving through the curve, the tan-function can be approximated by its argument, and

$$\delta = \delta(t) \approx a k = a k_C \frac{t}{T} \quad (9.30)$$

holds, i.e. the driving through a clothoid is manageable by a continuous steer motion.

### 9.1.4.4 Trailer Motions

The velocity of the trailer axis can be obtained by differentiation of the position vector Eq. (9.11)

$$v_{03,0} = \dot{r}_{03,0} = \dot{r}_{02,0} + \omega_{02,0} \times A_{02} r_{23,2} + A_{02} \dot{r}_{23,2}. \quad (9.31)$$

## 9.1 Kinematic Approach

The velocity  $\dot{r}_{02,0} = v_{02,0}$  and the angular velocity  $\omega_{02,0}$  of the vehicle are defined in Eqs. (9.16) and (9.20). The position vector from the rear axle to the axle of the trailer is given by

$$r_{23,2} = r_{2K,2} + A_{23} r_{K3,3} = \begin{bmatrix} -b - c \cos \kappa \\ -c \sin \kappa \\ 0 \end{bmatrix}, \quad (9.32)$$

where  $r_{2K,2}$  and  $r_{K3,3}$  are defined in Eq. (9.12). The time derivative of Eq. (9.32) results in

$$\dot{r}_{23,2} = \underbrace{\begin{bmatrix} 0 \\ 0 \\ \dot{\kappa} \end{bmatrix}}_{\omega_{23,2}} \times \underbrace{\begin{bmatrix} -c \cos \kappa \\ -c \sin \kappa \\ 0 \end{bmatrix}}_{A_{23} r_{K3,3}} = \begin{bmatrix} c \sin \kappa \dot{\kappa} \\ -c \cos \kappa \dot{\kappa} \\ 0 \end{bmatrix}. \quad (9.33)$$

Eq. (9.31) is transformed into the vehicle fixed frame  $x_2, y_2, z_2$  now

$$v_{03,2} = \underbrace{\begin{bmatrix} v_{x2} \\ 0 \\ 0 \end{bmatrix}}_{v_{02,2}} + \underbrace{\begin{bmatrix} 0 \\ 0 \\ \dot{\gamma} \end{bmatrix}}_{\omega_{02,2}} \times \underbrace{\begin{bmatrix} -b - c \cos \kappa \\ -c \sin \kappa \\ 0 \end{bmatrix}}_{r_{23,2}} + \underbrace{\begin{bmatrix} c \sin \kappa \dot{\kappa} \\ -c \cos \kappa \dot{\kappa} \\ 0 \end{bmatrix}}_{\dot{r}_{23,2}} = \begin{bmatrix} v_{x2} + c \sin \kappa (\dot{\kappa} + \dot{\gamma}) \\ -b \dot{\gamma} - c \cos \kappa (\dot{\kappa} + \dot{\gamma}) \\ 0 \end{bmatrix}. \quad (9.34)$$

The longitudinal and lateral direction at the trailer axle are defined by the unit vectors

$$e_{x3,2} = \begin{bmatrix} \cos \kappa \\ \sin \kappa \\ 0 \end{bmatrix} \quad \text{and} \quad e_{y3,2} = \begin{bmatrix} -\sin \kappa \\ \cos \kappa \\ 0 \end{bmatrix}. \quad (9.35)$$

At the trailer axis the lateral velocity must also vanish

$$e_{y3,2}^T v_{03,2} = -\sin \kappa (v_{x2} + c \sin \kappa (\dot{\kappa} + \dot{\gamma})) + \cos \kappa (-b \dot{\gamma} - c \cos \kappa (\dot{\kappa} + \dot{\gamma})) = 0, \quad (9.36)$$

whereas in longitudinal direction the velocity

$$e_{x3,2}^T v_{03,2} = \cos \kappa (v_{x2} + c \sin \kappa (\dot{\kappa} + \dot{\gamma})) + \sin \kappa (-b \dot{\gamma} - c \cos \kappa (\dot{\kappa} + \dot{\gamma})) = v_{x3} \quad (9.37)$$

remains. If Eq. (9.24) is inserted into Eq. (9.36) now, one will get a first order differential equation for the bend angle

$$\dot{\kappa} = -\frac{v_{x2}}{a} \left( \frac{a}{c} \sin \kappa + \left( \frac{b}{c} \cos \kappa + 1 \right) \tan \delta \right). \quad (9.38)$$

The differential equations Eqs. (9.17), (9.18) and (9.24) describe the position and the orientation of the vehicle within the  $x_0, y_0$  plane. The position of the trailer relative to the vehicle follows from Eq. (9.38).

### 9.1.4.5 Course Calculations

For a given set of vehicle parameters  $a, b, c$ , and predefined time functions of the vehicle velocity,  $v_{x2} = v_{x2}(t)$  and the steering angle,  $\delta = \delta(t)$ , the course of vehicle and trailer can be calculated by numerical integration of the differential equations Eqs. (9.17), (9.18), (9.24) and (9.38). If the steering angle is slowly increased at constant driving speed, the vehicle drives a figure which will be similar to a clothoide, Fig. 9.5.

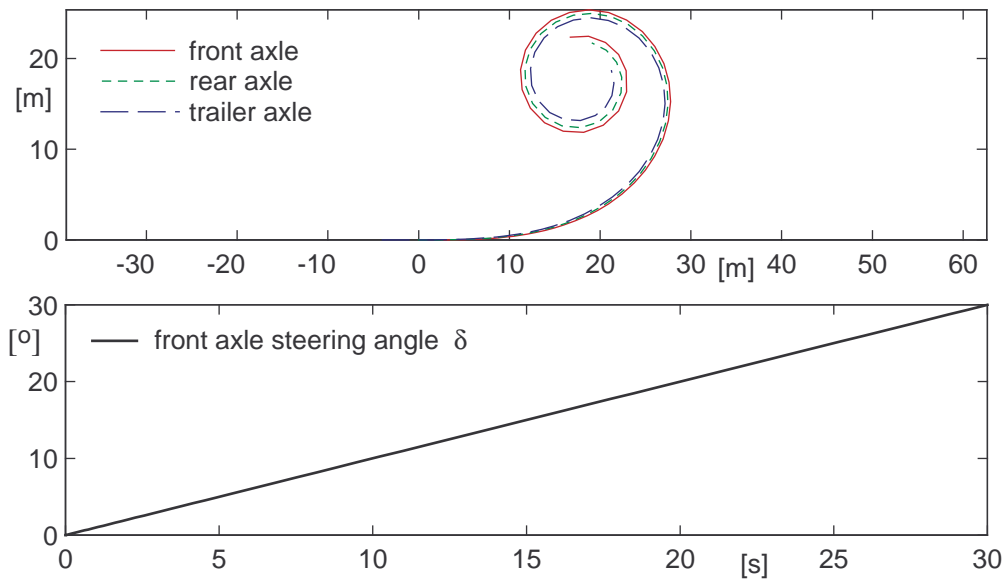


Figure 9.5: Entering a curve

## 9.2 Steady State Cornering

### 9.2.1 Cornering Resistance

In a body fixed reference frame  $B$ , Fig. 9.6, the velocity state of the vehicle can be described by

$$v_{0C,B} = \begin{bmatrix} v \cos \beta \\ v \sin \beta \\ 0 \end{bmatrix} \quad \text{and} \quad \omega_{0F,B} = \begin{bmatrix} 0 \\ 0 \\ \omega \end{bmatrix}, \quad (9.39)$$

where  $\beta$  denotes the side slip angle of the vehicle measured at the center of gravity. The angular velocity of a vehicle cornering with constant velocity  $v$  on an flat horizontal road is given by

$$\omega = \frac{v}{R}, \quad (9.40)$$

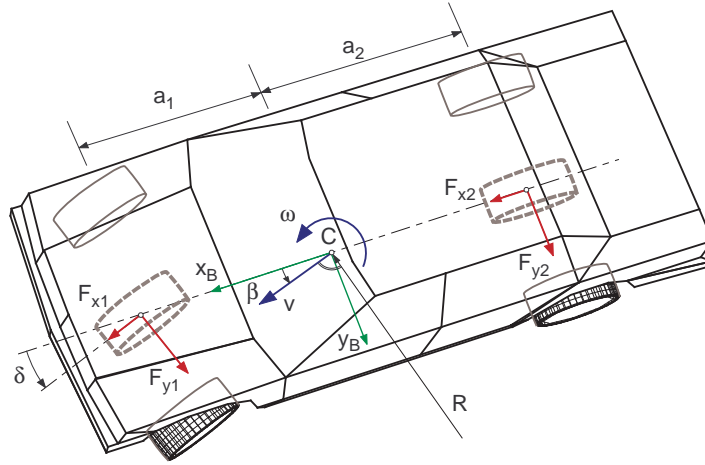


Figure 9.6: Cornering resistance

where  $R$  denotes the radius of curvature.

In the body fixed reference frame, linear and angular momentum result in

$$m \left( -\frac{v^2}{R} \sin \beta \right) = F_{x1} \cos \delta - F_{y1} \sin \delta + F_{x2}, \quad (9.41)$$

$$m \left( \frac{v^2}{R} \cos \beta \right) = F_{x1} \sin \delta + F_{y1} \cos \delta + F_{y2}, \quad (9.42)$$

$$0 = a_1 (F_{x1} \sin \delta + F_{y1} \cos \delta) - a_2 F_{y2}, \quad (9.43)$$

where  $m$  denotes the mass of the vehicle,  $F_{x1}$ ,  $F_{x2}$ ,  $F_{y1}$ ,  $F_{y2}$  are the resulting forces in longitudinal and vertical direction applied at the front and rear axle, and  $\delta$  specifies the average steer angle at the front axle.

The engine torque is distributed by the center differential to the front and rear axle. Then, in steady state condition we obtain

$$F_{x1} = k F_D \quad \text{and} \quad F_{x2} = (1 - k) F_D, \quad (9.44)$$

where  $F_D$  is the driving force and by  $k$  different driving conditions can be modeled:

$k = 0$	rear wheel drive	$F_{x1} = 0, F_{x2} = F_D$
$0 < k < 1$	all wheel drive	$\frac{F_{x1}}{F_{x2}} = \frac{k}{1 - k}$
$k = 1$	front wheel drive	$F_{x1} = F_D, F_{x2} = 0$

## 9 Lateral Dynamics

If we insert Eq. (9.44) into Eq. (9.41) we will get

$$\begin{aligned} \left( k \cos \delta + (1-k) \right) F_D - \sin \delta F_{y1} &= -\frac{mv^2}{R} \sin \beta, \\ k \sin \delta F_D + \cos \delta F_{y1} + F_{y2} &= \frac{mv^2}{R} \cos \beta, \\ a_1 k \sin \delta F_D + a_1 \cos \delta F_{y1} - a_2 F_{y2} &= 0. \end{aligned} \quad (9.45)$$

These equations can be resolved for the driving force

$$F_D = \frac{\frac{a_2}{a_1 + a_2} \cos \beta \sin \delta - \sin \beta \cos \delta}{k + (1-k) \cos \delta} \frac{mv^2}{R}. \quad (9.46)$$

The driving force will vanish, if

$$\frac{a_2}{a_1 + a_2} \cos \beta \sin \delta = \sin \beta \cos \delta \quad \text{or} \quad \frac{a_2}{a_1 + a_2} \tan \delta = \tan \beta \quad (9.47)$$

holds. This fully corresponds with the Ackermann geometry. But, the Ackermann geometry applies only for small lateral accelerations. In real driving situations, the side slip angle of a vehicle at the center of gravity is always smaller than the Ackermann side slip angle. Then, due to  $\tan \beta < \frac{a_2}{a_1 + a_2} \tan \delta$  a driving force  $F_D > 0$  is needed to overcome the "cornering resistance" of the vehicle.

### 9.2.2 Overturning Limit

The overturning hazard of a vehicle is primarily determined by the track width and the height of the center of gravity. With trucks however, also the tire deflection and the body roll have to be respected., Fig. 9.7.

The balance of torques at the height of the track plane applied at the already inclined vehicle results in

$$(F_{zL} - F_{zR}) \frac{s}{2} = m a_y (h_1 + h_2) + m g [(h_1 + h_2) \alpha_1 + h_2 \alpha_2], \quad (9.48)$$

where  $a_y$  describes the lateral acceleration,  $m$  is the sprung mass, and small roll angles of the axle and the body were assumed,  $\alpha_1 \ll 1$ ,  $\alpha_2 \ll 1$ . On a left-hand tilt, the right tire raises

$$F_{zR}^T = 0, \quad (9.49)$$

whereas the left tire carries the complete vehicle weight

$$F_{zL}^T = m g. \quad (9.50)$$

Using Eqs. (9.49) and (9.50) one gets from Eq. (9.48)

$$\frac{a_y^T}{g} = \frac{\frac{s}{2}}{h_1 + h_2} - \alpha_1^T - \frac{h_2}{h_1 + h_2} \alpha_2^T. \quad (9.51)$$

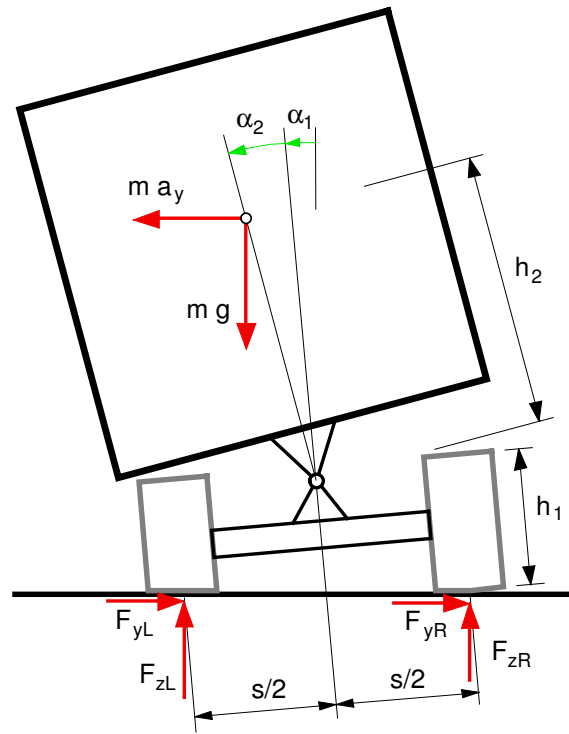


Figure 9.7: Overturning hazard on trucks

The vehicle will turn over, when the lateral acceleration  $a_y$  rises above the limit  $a_y^T$ . Roll of axle and body reduce the overturning limit. The angles  $\alpha_1^T$  and  $\alpha_2^T$  can be calculated from the tire stiffness  $c_R$  and the roll stiffness of the axle suspension.

If the vehicle drives straight ahead, the weight of the vehicle will be equally distributed to both sides

$$F_{zR}^{stat} = F_{zL}^{stat} = \frac{1}{2} m g . \quad (9.52)$$

With

$$F_{zL}^T = F_{zL}^{stat} + \Delta F_z \quad (9.53)$$

and Eqs. (9.50), (9.52), one obtains for the increase of the wheel load at the overturning limit

$$\Delta F_z = \frac{1}{2} m g . \quad (9.54)$$

Then, the resulting tire deflection follows from

$$\Delta F_z = c_R \Delta r , \quad (9.55)$$

where  $c_R$  is the radial tire stiffness.

## 9 Lateral Dynamics

Because the right tire simultaneously rebounds with the same amount, for the roll angle of the axle

$$2 \Delta r = s \alpha_1^T \quad \text{or} \quad \alpha_1^T = \frac{2 \Delta r}{s} = \frac{m g}{s c_R} \quad (9.56)$$

holds. In analogy to Eq. (9.48) the balance of torques at the body applied at the roll center of the body yields

$$c_W * \alpha_2 = m a_y h_2 + m g h_2 (\alpha_1 + \alpha_2), \quad (9.57)$$

where  $c_W$  names the roll stiffness of the body suspension. In particular, at the overturning limit  $a_y = a_y^T$

$$\alpha_2^T = \frac{a_y^T}{g} \frac{m g h_2}{c_W - m g h_2} + \frac{m g h_2}{c_W - m g h_2} \alpha_1^T \quad (9.58)$$

applies. Not allowing the vehicle to overturn already at  $a_y^T = 0$  demands a minimum of roll stiffness  $c_W > c_W^{min} = m g h_2$ . With Eqs. (9.56) and (9.58) the overturning condition Eq. (9.51) reads as

$$(h_1 + h_2) \frac{a_y^T}{g} = \frac{s}{2} - (h_1 + h_2) \frac{1}{c_R^*} - h_2 \frac{a_y^T}{g} \frac{1}{c_W^* - 1} - h_2 \frac{1}{c_W^* - 1} \frac{1}{c_R^*}, \quad (9.59)$$

where, for abbreviation purposes, the dimensionless stiffnesses

$$c_R^* = \frac{c_R}{m g} \quad \text{and} \quad c_W^* = \frac{c_W}{m g h_2} \quad (9.60)$$

have been used. Resolved for the normalized lateral acceleration

$$\frac{a_y^T}{g} = \frac{\frac{s}{2}}{h_1 + h_2 + \frac{h_2}{c_W^* - 1}} - \frac{1}{c_R^*} \quad (9.61)$$

remains.

At heavy trucks, a twin tire axle may be loaded with  $m = 13\,000 \text{ kg}$ . The radial stiffness of one tire is  $c_R = 800\,000 \text{ N/m}$ , and the track width can be set to  $s = 2 \text{ m}$ . The values  $h_1 = 0.8 \text{ m}$  and  $h_2 = 1.0 \text{ m}$  hold at maximal load. These values produce the results shown in Fig. 9.8. Even with a rigid body suspension  $c_W^* \rightarrow \infty$ , the vehicle turns over at a lateral acceleration of  $a_y \approx 0.5 g$ . Then, the roll angle of the vehicle solely results from the tire deflection. At a normalized roll stiffness of  $c_W^* = 5$ , the overturning limit lies at  $a_y \approx 0.45 g$  and so reaches already 90% of the maximum. The vehicle will turn over at a roll angle of  $\alpha = \alpha_1 + \alpha_2 \approx 10^\circ$  then.

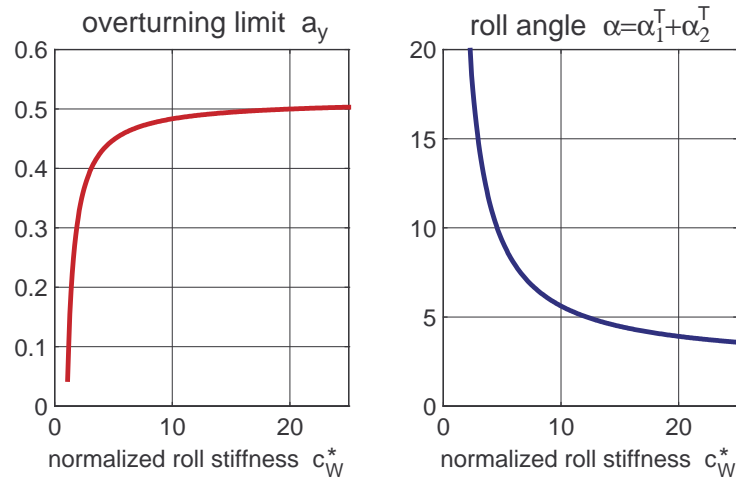


Figure 9.8: Tilting limit for a typical truck at steady state cornering

### 9.2.3 Roll Support and Camber Compensation

When a vehicle drives through a curve with the lateral acceleration  $a_y$ , centrifugal forces will be applied to the single masses. At the simple roll model in Fig. 9.9, these are the forces  $m_A a_y$  and  $m_R a_y$ , where  $m_A$  names the body mass and  $m_R$  the wheel mass. Through the centrifugal force  $m_A a_y$  applied to the body at the center of gravity, a torque is generated, which rolls the body with the angle  $\alpha_A$  and leads to an opposite deflection of the tires  $z_1 = -z_2$ .

At steady state cornering, the vehicle forces are balanced. With the principle of virtual work

$$\delta W = 0, \quad (9.62)$$

the equilibrium position can be calculated. At the simple vehicle model in Fig. 9.9 the suspension forces  $F_{F1}, F_{F2}$  and tire forces  $F_{y1}, F_{z1}, F_{y2}, F_{z2}$ , are approximated by linear spring elements with the constants  $c_A$  and  $c_Q, c_R$ . The work  $W$  of these forces can be calculated directly or using  $W = -V$  via the potential  $V$ . At small deflections with linearized kinematics one gets

$$\begin{aligned} W = & -m_A a_y y_A \\ & -m_R a_y (y_A + h_R \alpha_A + y_1) - m_R a_y (y_A + h_R \alpha_A + y_2) \\ & -\frac{1}{2} c_A z_1^2 - \frac{1}{2} c_A z_2^2 \\ & -\frac{1}{2} c_S (z_1 - z_2)^2 \\ & -\frac{1}{2} c_Q (y_A + h_0 \alpha_A + y_1 + r_0 \alpha_1)^2 - \frac{1}{2} c_Q (y_A + h_0 \alpha_A + y_2 + r_0 \alpha_2)^2 \\ & -\frac{1}{2} c_R (z_A + \frac{b}{2} \alpha_A + z_1)^2 - \frac{1}{2} c_R (z_A - \frac{b}{2} \alpha_A + z_2)^2, \end{aligned} \quad (9.63)$$

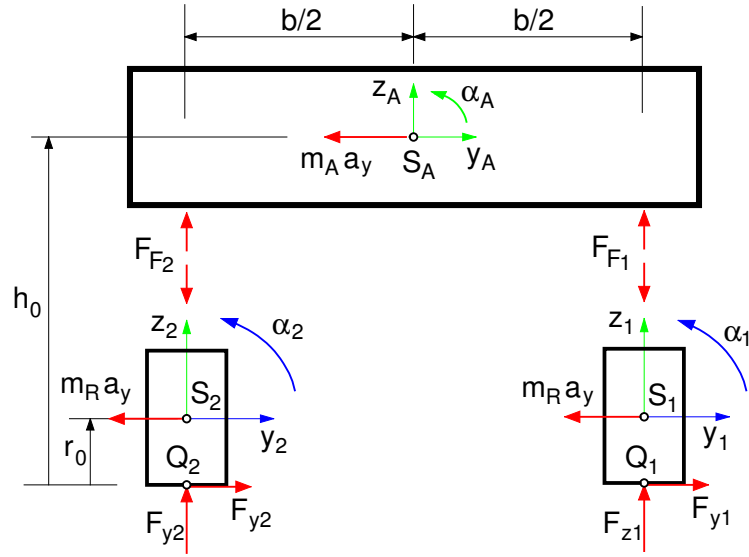


Figure 9.9: Simple vehicle roll model

where the abbreviation  $h_R = h_0 - r_0$  has been used, and  $c_S$  describes the spring constant of the anti roll bar, converted to the vertical displacement of the wheel centers.

The kinematics of the wheel suspension are symmetrical. With the linear approaches

$$y_1 = y_1(z_1) \approx \frac{\partial y}{\partial z} z_1, \quad \alpha_1 = \alpha_1(z_1) \approx \frac{\partial \alpha}{\partial z} z_1 \quad (9.64)$$

and

$$y_2 = y_2(z_2) \approx -\frac{\partial y}{\partial z} z_2, \quad \alpha_2 = \alpha_2(z_2) \approx -\frac{\partial \alpha}{\partial z} z_2 \quad (9.65)$$

the work  $W$  can be described as a function of the position vector

$$y = [y_A, z_A, \alpha_A, z_1, z_2]^T. \quad (9.66)$$

Due to

$$W = W(y) \quad (9.67)$$

the principle of virtual work Eq. (9.62) leads to

$$\delta W = \frac{\partial W}{\partial y} \delta y = 0. \quad (9.68)$$

Because of  $\delta y \neq 0$ , a system of linear equations in the form of

$$K y = b \quad (9.69)$$

results from Eq. (9.68). The matrix  $K$  and the vector  $b$  are given by

$$K = \begin{bmatrix} 2c_Q & 0 & 2c_Q h_0 & \frac{\partial y^Q}{\partial z} c_Q & -\frac{\partial y^Q}{\partial z} c_Q \\ 0 & 2c_R & 0 & c_R & c_R \\ 2c_Q h_0 & 0 & c_\alpha & \frac{b}{2} c_R + h_0 \frac{\partial y^Q}{\partial z} c_Q & -\frac{b}{2} c_R - h_0 \frac{\partial y^Q}{\partial z} c_Q \\ \frac{\partial y^Q}{\partial z} c_Q & c_R & \frac{b}{2} c_R + h_0 \frac{\partial y^Q}{\partial z} c_Q & c_A^* + c_S + c_R & -c_S \\ -\frac{\partial y^Q}{\partial z} c_Q & c_R & -\frac{b}{2} c_R - h_0 \frac{\partial y^Q}{\partial z} c_Q & -c_S & c_A^* + c_S + c_R \end{bmatrix} \quad (9.70)$$

and

$$b = - \begin{bmatrix} m_A + 2m_R \\ 0 \\ (m_1 + m_2) h_R \\ m_R \frac{\partial y}{\partial z} \\ -m_R \frac{\partial y}{\partial z} \end{bmatrix} a_y. \quad (9.71)$$

The following abbreviations have been used:

$$\frac{\partial y^Q}{\partial z} = \frac{\partial y}{\partial z} + r_0 \frac{\partial \alpha}{\partial z}, \quad c_A^* = c_A + c_Q \left( \frac{\partial y}{\partial z} \right)^2, \quad c_\alpha = 2c_Q h_0^2 + 2c_R \left( \frac{b}{2} \right)^2. \quad (9.72)$$

The system of linear equations Eq. (9.69) can be solved numerically, e.g. with MATLAB. Thus, the influence of axle suspension and axle kinematics on the roll behavior of the vehicle can be investigated.

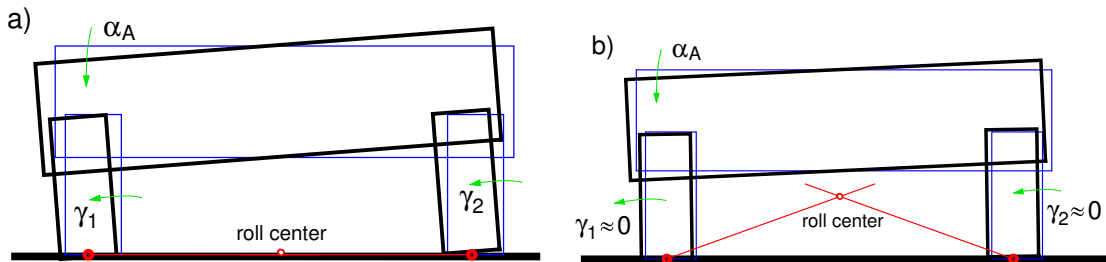


Figure 9.10: Roll behavior at cornering: a) without and b) with camber compensation

If the wheels only move vertically to the body at jounce and rebound, at fast cornering the wheels will be no longer perpendicular to the track Fig. 9.10 a. The camber angles  $\gamma_1 > 0$  and  $\gamma_2 > 0$  result in an unfavorable pressure distribution in the contact area, which leads to a reduction of the maximally transmittable lateral

## 9 Lateral Dynamics

forces. Thus, at more sportive vehicles axle kinematics are employed, where the wheels are rotated around the longitudinal axis at jounce and rebound,  $\alpha_1 = \alpha_1(z_1)$  and  $\alpha_2 = \alpha_2(z_2)$ . Hereby, a "camber compensation" can be achieved with  $\gamma_1 \approx 0$  and  $\gamma_2 \approx 0$ . Fig. 9.10 b. By the rotation of the wheels around the longitudinal axis on jounce and rebound, the wheel contact points are moved outwards, i.e against the lateral force. By this, a "roll support" is achieved that reduces the body roll.

### 9.2.4 Roll Center and Roll Axis

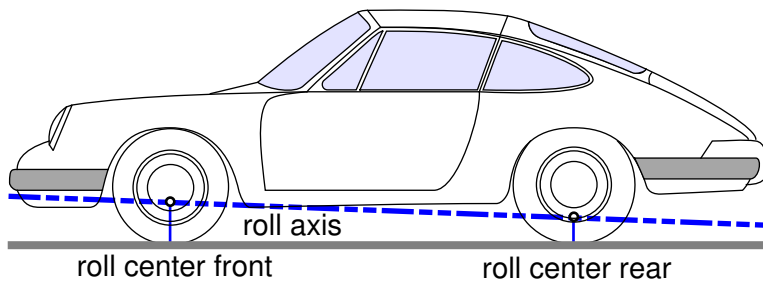


Figure 9.11: Roll axis

The "roll center" can be constructed from the lateral motion of the wheel contact points  $Q_1$  and  $Q_2$ , Fig. 9.10. The line through the roll center at the front and rear axle is called "roll axis", Fig. 9.11.

### 9.2.5 Wheel Loads

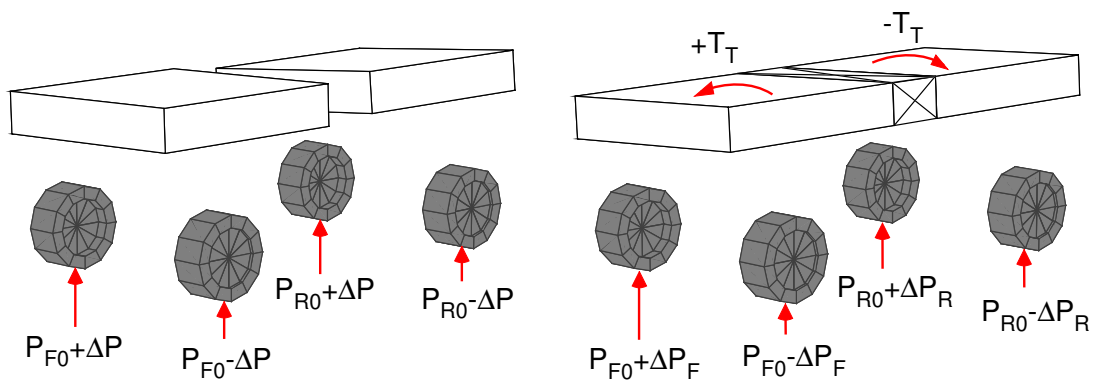


Figure 9.12: Wheel loads for a flexible and a rigid chassis

The roll angle of a vehicle during cornering depends on the roll stiffness of the axle and on the position of the roll center. Different axle layouts at the front and

rear axle may result in different roll angles of the front and rear part of the chassis, Fig. 9.12.

On most passenger cars the chassis is rather stiff. Hence, front and rear part of the chassis are forced by an internal torque to an overall chassis roll angle. This torque affects the wheel loads and generates different wheel load differences at the front and rear axle. Due to the degressive influence of the wheel load to longitudinal and lateral tire forces the steering tendency of a vehicle can be affected.

### 9.3 Simple Handling Model

#### 9.3.1 Modeling Concept

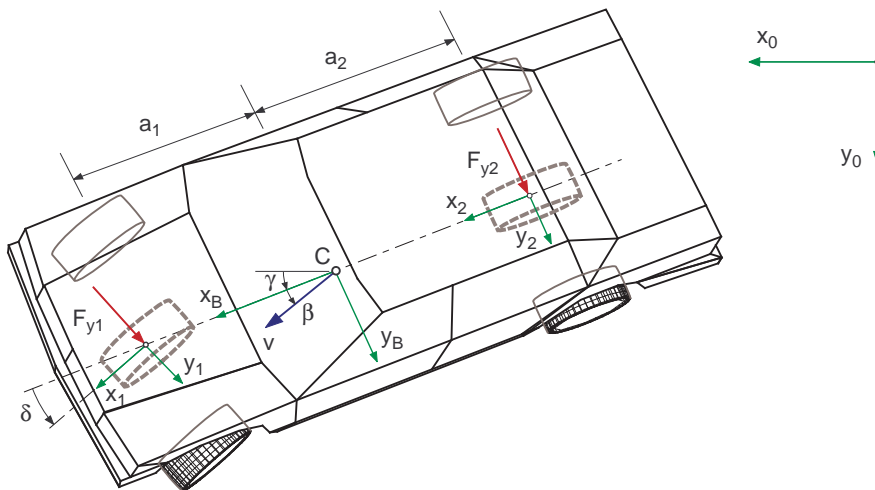


Figure 9.13: Simple handling model

The main vehicle motions take place in a horizontal plane defined by the earth-fixed frame 0, Fig. 9.13. The tire forces at the wheels of one axle are combined to one resulting force. Tire torques, rolling resistance, and aerodynamic forces and torques, applied at the vehicle, are not taken into consideration.

#### 9.3.2 Kinematics

The vehicle velocity at the center of gravity can be expressed easily in the body fixed frame  $x_B, y_B, z_B$

$$v_{C,B} = \begin{bmatrix} v \cos \beta \\ v \sin \beta \\ 0 \end{bmatrix}, \quad (9.73)$$

where  $\beta$  denotes the side slip angle, and  $v$  is the magnitude of the velocity.

## 9 Lateral Dynamics

The velocity vectors and the unit vectors in longitudinal and lateral direction of the axles are needed for the computation of the lateral slips. One gets

$$e_{x1,B} = \begin{bmatrix} \cos \delta \\ \sin \delta \\ 0 \end{bmatrix}, \quad e_{y1,B} = \begin{bmatrix} -\sin \delta \\ \cos \delta \\ 0 \end{bmatrix}, \quad v_{01,B} = \begin{bmatrix} v \cos \beta \\ v \sin \beta + a_1 \dot{\gamma} \\ 0 \end{bmatrix} \quad (9.74)$$

and

$$e_{x2,B} = \begin{bmatrix} 1 \\ 0 \\ 0 \end{bmatrix}, \quad e_{y2,B} = \begin{bmatrix} 0 \\ 1 \\ 0 \end{bmatrix}, \quad v_{02,B} = \begin{bmatrix} v \cos \beta \\ v \sin \beta - a_2 \dot{\gamma} \\ 0 \end{bmatrix}, \quad (9.75)$$

where  $a_1$  and  $a_2$  are the distances from the center of gravity to the front and rear axle, and  $\dot{\gamma}$  denotes the yaw angular velocity of the vehicle.

### 9.3.3 Tire Forces

Unlike with the kinematic tire model, now small lateral motions in the contact points are permitted. At small lateral slips, the lateral force can be approximated by a linear approach

$$F_y = c_S s_y, \quad (9.76)$$

where  $c_S$  is a constant depending on the wheel load  $F_z$ , and the lateral slip  $s_y$  is defined by Eq. (3.88). Because the vehicle is neither accelerated nor decelerated, the rolling condition is fulfilled at each wheel

$$r_D \Omega = e_x^T v_{0P}. \quad (9.77)$$

Here,  $r_D$  is the dynamic tire radius,  $v_{0P}$  the contact point velocity, and  $e_x$  the unit vector in longitudinal direction. With the lateral tire velocity

$$v_y = e_y^T v_{0P} \quad (9.78)$$

and the rolling condition Eq. (9.77), the lateral slip can be calculated from

$$s_y = \frac{-e_y^T v_{0P}}{|e_x^T v_{0P}|}, \quad (9.79)$$

with  $e_y$  labeling the unit vector in the lateral direction of the tire. So, the lateral forces are given by

$$F_{y1} = c_{S1} s_{y1}; F_{y2} = c_{S2} s_{y2}. \quad (9.80)$$

### 9.3.4 Lateral Slips

With Eq. (9.75), the lateral slip at the front axle follows from Eq. (9.79):

$$s_{y1} = \frac{+\sin \delta (v \cos \beta) - \cos \delta (v \sin \beta + a_1 \dot{\gamma})}{|\cos \delta (v \cos \beta) + \sin \delta (v \sin \beta + a_1 \dot{\gamma})|}. \quad (9.81)$$

The lateral slip at the rear axle is given by

$$s_{y2} = -\frac{v \sin \beta - a_2 \dot{\gamma}}{|v \cos \beta|}. \quad (9.82)$$

The yaw velocity of the vehicle  $\dot{\gamma}$ , the side slip angle  $\beta$  and the steering angle  $\delta$  are considered to be small

$$|a_1 \dot{\gamma}| \ll |v|; \quad |a_2 \dot{\gamma}| \ll |v| \quad (9.83)$$

$$|\beta| \ll 1 \quad \text{and} \quad |\delta| \ll 1. \quad (9.84)$$

Because the side slip angle always labels the smaller angle between the velocity vector and the vehicle longitudinal axis, instead of  $v \sin \beta \approx v \beta$  the approximation

$$v \sin \beta \approx |v| \beta \quad (9.85)$$

has to be used. Now, Eqs. (9.81) and (9.82) result in

$$s_{y1} = -\beta - \frac{a_1}{|v|} \dot{\gamma} + \frac{v}{|v|} \delta \quad (9.86)$$

and

$$s_{y2} = -\beta + \frac{a_2}{|v|} \dot{\gamma}, \quad (9.87)$$

where the consequences of Eqs. (9.83), (9.84), and (9.85) were already taken into consideration.

### 9.3.5 Equations of Motion

The velocities, angular velocities, and the accelerations are needed to derive the equations of motion, For small side slip angles  $\beta \ll 1$ , Eq. (9.73) can be approximated by

$$v_{C,B} = \begin{bmatrix} v \\ |v| \beta \\ 0 \end{bmatrix}. \quad (9.88)$$

The angular velocity is given by

$$\omega_{0F,B} = \begin{bmatrix} 0 \\ 0 \\ \dot{\gamma} \end{bmatrix}. \quad (9.89)$$

## 9 Lateral Dynamics

If the vehicle accelerations are also expressed in the vehicle fixed frame  $x_F, y_F, z_F$ , one will find at constant vehicle speed  $v = const$  and with neglecting small higher-order terms

$$a_{C,B} = \omega_{0F,B} \times v_{C,B} + \dot{v}_{C,B} = \begin{bmatrix} 0 \\ v \dot{\gamma} + |v| \dot{\beta} \\ 0 \end{bmatrix}. \quad (9.90)$$

The angular acceleration is given by

$$\dot{\omega}_{0F,B} = \begin{bmatrix} 0 \\ 0 \\ \dot{\omega} \end{bmatrix}, \quad (9.91)$$

where the substitution

$$\dot{\gamma} = \omega \quad (9.92)$$

was used. The linear momentum in the lateral direction of the vehicle reads as

$$m(v\omega + |v|\dot{\beta}) = F_{y1} + F_{y2}, \quad (9.93)$$

where, due to the small steering angle, the term  $F_{y1} \cos \delta$  has been approximated by  $F_{y1}$ , and  $m$  describes the vehicle mass. With Eq. (9.92) the angular momentum yields

$$\Theta \dot{\omega} = a_1 F_{y1} - a_2 F_{y2}, \quad (9.94)$$

where  $\Theta$  names the inertia of vehicle around the vertical axis. With the linear description of the lateral forces Eq. (9.80) and the lateral slips Eqs. (9.86), (9.87), one gets from Eqs. (9.93) and (9.94) two coupled, but linear first order differential equations

$$\dot{\beta} = \frac{c_{S1}}{m|v|} \left( -\beta - \frac{a_1}{|v|} \omega + \frac{v}{|v|} \delta \right) + \frac{c_{S2}}{m|v|} \left( -\beta + \frac{a_2}{|v|} \omega \right) - \frac{v}{|v|} \omega \quad (9.95)$$

$$\dot{\omega} = \frac{a_1 c_{S1}}{\Theta} \left( -\beta - \frac{a_1}{|v|} \omega + \frac{v}{|v|} \delta \right) - \frac{a_2 c_{S2}}{\Theta} \left( -\beta + \frac{a_2}{|v|} \omega \right), \quad (9.96)$$

which can be written in the form of a state equation

$$\underbrace{\begin{bmatrix} \dot{\beta} \\ \dot{\omega} \end{bmatrix}}_{\dot{x}} = \underbrace{\begin{bmatrix} -\frac{c_{S1} + c_{S2}}{m|v|} & \frac{a_2 c_{S2} - a_1 c_{S1}}{m|v||v|} - \frac{v}{|v|} \\ \frac{a_2 c_{S2} - a_1 c_{S1}}{\Theta} & -\frac{a_1^2 c_{S1} + a_2^2 c_{S2}}{\Theta|v|} \end{bmatrix}}_A \underbrace{\begin{bmatrix} \beta \\ \omega \end{bmatrix}}_x + \underbrace{\begin{bmatrix} \frac{v}{|v|} \frac{c_{S1}}{m|v|} \\ \frac{v}{|v|} \frac{a_1 c_{S1}}{\Theta} \end{bmatrix}}_B \underbrace{\begin{bmatrix} \delta \end{bmatrix}}_u. \quad (9.97)$$

If a system can be at least approximatively described by a linear state equation, stability, steady state solutions, transient response, and optimal controlling can be calculated with classic methods of system dynamics.

### 9.3.6 Stability

#### 9.3.6.1 Eigenvalues

The homogeneous state equation

$$\dot{x} = Ax \quad (9.98)$$

describes the eigen-dynamics. If the approach

$$x_h(t) = x_0 e^{\lambda t} \quad (9.99)$$

is inserted into Eq. (9.98), the homogeneous equation will remain

$$(\lambda E - A) x_0 = 0. \quad (9.100)$$

One gets non-trivial solutions  $x_0 \neq 0$  for

$$\det|\lambda E - A| = 0. \quad (9.101)$$

The eigenvalues  $\lambda$  provide information concerning the stability of the system.

#### 9.3.6.2 Low Speed Approximation

The state matrix

$$A_{v \rightarrow 0} = \begin{bmatrix} -\frac{c_{S1} + c_{S2}}{m|v|} & \frac{a_2 c_{S2} - a_1 c_{S1}}{m|v||v|} - \frac{v}{|v|} \\ 0 & -\frac{a_1^2 c_{S1} + a_2^2 c_{S2}}{\Theta|v|} \end{bmatrix} \quad (9.102)$$

approximates the eigen-dynamics of vehicles at low speeds,  $v \rightarrow 0$ . The matrix in Eq. (9.102) has the eigenvalues

$$\lambda_{1_{v \rightarrow 0}} = -\frac{c_{S1} + c_{S2}}{m|v|} \quad \text{and} \quad \lambda_{2_{v \rightarrow 0}} = -\frac{a_1^2 c_{S1} + a_2^2 c_{S2}}{\Theta|v|}. \quad (9.103)$$

The eigenvalues are real and always negative independent from the driving direction. Thus, vehicles possess an asymptotically stable driving behavior at low speed!

#### 9.3.6.3 High Speed Approximation

At high driving velocities,  $v \rightarrow \infty$ , the state matrix can be approximated by

$$A_{v \rightarrow \infty} = \begin{bmatrix} 0 & -\frac{v}{|v|} \\ \frac{a_2 c_{S2} - a_1 c_{S1}}{\Theta} & 0 \end{bmatrix}. \quad (9.104)$$

## 9 Lateral Dynamics

Using Eq. (9.104) one receives from Eq. (9.101) the relation

$$\lambda_{v \rightarrow \infty}^2 + \frac{v}{|v|} \frac{a_2 c_{S2} - a_1 c_{S1}}{\Theta} = 0 \quad (9.105)$$

with the solutions

$$\lambda_{1,2v \rightarrow \infty} = \pm \sqrt{-\frac{v}{|v|} \frac{a_2 c_{S2} - a_1 c_{S1}}{\Theta}} . \quad (9.106)$$

When driving forward with  $v > 0$ , the root argument will be positive, if

$$a_2 c_{S2} - a_1 c_{S1} < 0 \quad (9.107)$$

holds. Then however, one eigenvalue is positive, and the system is unstable. Two zero-eigenvalues  $\lambda_1 = 0$  and  $\lambda_2 = 0$  are obtained for

$$a_1 c_{S1} = a_2 c_{S2} . \quad (9.108)$$

The driving behavior is indifferent then. Slight parameter variations, however, can lead to an unstable behavior. With

$$a_2 c_{S2} - a_1 c_{S1} > 0 \quad \text{or} \quad a_1 c_{S1} < a_2 c_{S2} \quad (9.109)$$

and  $v > 0$  the root argument in Eq. (9.106) becomes negative. Then, the eigenvalues are imaginary, and disturbances lead to undamped vibrations. To avoid instability, high-speed vehicles have to satisfy the condition Eq. (9.109). The root argument in Eq. (9.106) changes at backward driving its sign. Hence, a vehicle showing stable driving behavior at forward driving becomes unstable at fast backward driving!

### 9.3.6.4 Critical Speed

The condition for non-trivial solutions (9.101) results here in a quadratic equation for the eigenvalues  $\lambda$

$$\det |\lambda E - A| = \lambda^2 + k_1 \lambda + k_2 = 0 \quad (9.110)$$

which is solved by

$$\lambda_{1,2} = -\frac{k_1}{2} \pm \sqrt{\left(\frac{k_1}{2}\right)^2 - k_2} . \quad (9.111)$$

Hence, asymptotically stable solutions demand for

$$k_1 > 0 \quad \text{and} \quad k_2 > 0 \quad (9.112)$$

which corresponds with the stability criteria of Stodola and Hurwitz [17].

According to Eq. (9.97) the coefficients in Eq. (9.110) can be derived from the vehicle data

$$k_1 = \frac{c_{S1} + c_{S2}}{m |v|} + \frac{a_1^2 c_{S1} + a_2^2 c_{S2}}{\Theta |v|} , \quad (9.113)$$

$$\begin{aligned}
 k_2 &= \frac{c_{S1} + c_{S2}}{m|v|} \frac{a_1^2 c_{S1} + a_2^2 c_{S2}}{\Theta|v|} - \frac{(a_2 c_{S2} - a_1 c_{S1})^2}{\Theta m|v||v|} + \frac{v}{|v|} \frac{a_2 c_{S2} - a_1 c_{S1}}{\Theta} \\
 &= \frac{c_{S1} c_{S2} (a_1 + a_2)^2}{m \Theta v^2} \left( 1 + \frac{v}{|v|} \frac{a_2 c_{S2} - a_1 c_{S1}}{c_{S1} c_{S2} (a_1 + a_2)^2} m v^2 \right).
 \end{aligned} \tag{9.114}$$

The coefficient  $k_1$  is always positive, whereas  $k_2 > 0$  is fulfilled only if

$$1 + \frac{v}{|v|} \frac{a_2 c_{S2} - a_1 c_{S1}}{c_{S1} c_{S2} (a_1 + a_2)^2} m v^2 > 0 \tag{9.115}$$

will hold. Hence, a vehicle designed stable for arbitrary velocities in forward direction becomes unstable, when it drives too fast backwards. Because,  $k_2 > 0$  for  $a_2 c_{S2} - a_1 c_{S1} > 0$  and  $v < 0$  demands for  $v > -v_C^-$ , where according to Eq. (9.115) the critical backwards velocity is given by

$$v_C^- = \sqrt{\frac{c_{S1} c_{S2} (a_1 + a_2)^2}{m (a_2 c_{S2} - a_1 c_{S1})}}. \tag{9.116}$$

On the other hand, vehicle layouts with  $a_2 c_{S2} - a_1 c_{S1} < 0$  or are only stable while driving forward as long as  $v < v_C^+$  will hold. Here, Eq. (9.115) yields the critical forward velocity of

$$v_C^+ = \sqrt{\frac{c_{S1} c_{S2} (a_1 + a_2)^2}{m (a_1 c_{S1} - a_2 c_{S2})}}. \tag{9.117}$$

Most vehicles are designed stable for fast forward drive. Then, the backwards velocity must be limited in order to avoid stability problems. That is why, fast driving vehicles have four or more gears for forward drive but, only one or two reverse gears.

### 9.3.7 Steady State Solution

#### 9.3.7.1 Steering Tendency

At a given steering angle  $\delta = \delta_0$ , a stable system reaches steady state after a certain time. Then, the vehicle will drive on a circle with the radius  $R_{st}$  which is determined by

$$\omega_{st} = \frac{v}{R_{st}} \tag{9.118}$$

where  $v$  is the velocity of the vehicle and  $\omega_{st}$  denotes its steady state angular velocity.

With  $x_{st} = const.$  or  $\dot{x}_{st} = 0$ , the state equation Eq. (9.97) is reduced to a system of linear equations

$$A x_{st} = -B u. \tag{9.119}$$

Using Eq. (9.118) the state vector can be described in steady state by

$$x_{st} = \begin{bmatrix} \beta_{st} \\ v/R_{st} \end{bmatrix}, \tag{9.120}$$

## 9 Lateral Dynamics

where  $\beta_{st}$  denotes the steady state side slip angle. With  $u = [\delta_0]$ , and the elements of the state matrix  $A$  and the vector  $B$  which are defined in Eq. (9.97) the system of linear equations (9.119) yields

$$(c_{S1} + c_{S2}) \beta_{st} + (m v |v| + a_1 c_{S1} - a_2 c_{S2}) \frac{v}{|v|} \frac{1}{R_{st}} = \frac{v}{|v|} c_{S1} \delta_0, \quad (9.121)$$

$$(a_1 c_{S1} - a_2 c_{S2}) \beta_{st} + (a_1^2 c_{S1} + a_2^2 c_{S2}) \frac{v}{|v|} \frac{1}{R_{st}} = \frac{v}{|v|} a_1 c_{S1} \delta_0, \quad (9.122)$$

where the first equation has been multiplied by  $-m |v|$  and the second with  $-\Theta$ . Eliminating the steady state side slip angle  $\beta_{st}$  leads to

$$\begin{aligned} [mv|v|(a_1 c_{S1} - a_2 c_{S2}) + (a_1 c_{S1} - a_2 c_{S2})^2 - (c_{S1} + c_{S2})(a_1^2 c_{S1} + a_2^2 c_{S2})] \frac{v}{|v|} \frac{1}{R_{st}} = \\ [a_1 c_{S1} - a_2 c_{S2} - a_1(c_{S1} + c_{S2})] \frac{v}{|v|} c_{S1} \delta_0, \end{aligned} \quad (9.123)$$

which can be simplified to

$$[mv|v|(a_1 c_{S1} - a_2 c_{S2}) - c_{S1} c_{S2} (a_1 + a_2)^2] \frac{v}{|v|} \frac{1}{R_{st}} = -\frac{v}{|v|} c_{S1} c_{S2} (a_1 + a_2) \delta_0. \quad (9.124)$$

Hence, driving the vehicle at a certain radius requires a steering angle of

$$\delta_0 = \frac{a_1 + a_2}{R_{st}} + m \frac{v|v|}{R_{st}} \frac{a_2 c_{S2} - a_1 c_{S1}}{c_{S1} c_{S2} (a_1 + a_2)}. \quad (9.125)$$

The first term is the Ackermann steering angle which follows from Eq. (9.2) with the wheel base  $a = a_1 + a_2$  and the approximation for small steering angles  $\tan \delta_0 \approx \delta_0$ . The Ackermann-steering angle provides a good approximation for slowly moving vehicles, because the second expression in Eq. (9.125) becomes very small at  $v \rightarrow 0$ . Depending on the value of  $a_2 c_{S2} - a_1 c_{S1}$  and the driving direction, forward  $v > 0$  or backward  $v < 0$ , the necessary steering angle differs from the Ackermann-steering angle at higher speeds. The difference is proportional to the lateral acceleration

$$a_y = \frac{v|v|}{R_{st}} = \pm \frac{v^2}{R_{st}}. \quad (9.126)$$

Hence, Eq. (9.125) can be written as

$$\delta_0 = \delta_A + k \frac{v^2}{R_{st}}, \quad (9.127)$$

where  $\delta_A = \frac{a_1 + a_2}{R_{st}}$  is the Ackermann steering angle, and  $k$  summarizes the relevant vehicle parameter. In a diagram where the steering angle  $\delta_0$  is plotted versus the lateral acceleration  $a_y = v^2/R_{st}$  Eq. (9.127) represents a straight line, Fig. 9.14.

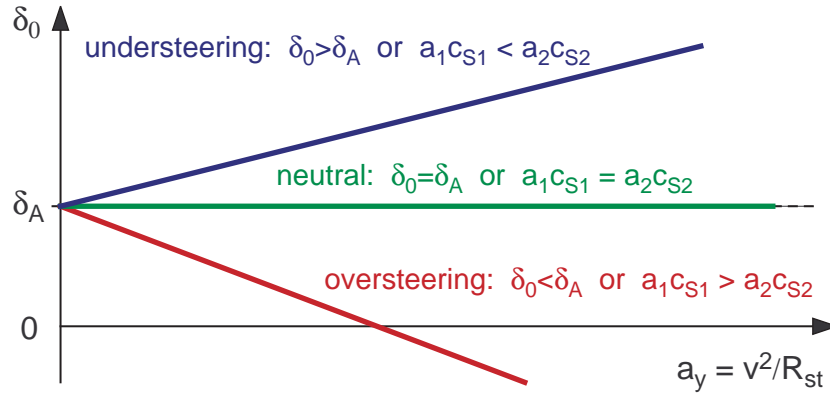


Figure 9.14: Steering angle versus lateral acceleration

On forward drive,  $v > 0$ , the inclination of the line is given by

$$k = \frac{m (a_2 c_{S2} - a_1 c_{S1})}{c_{S1} c_{S2} (a_1 + a_2)} \tag{9.128}$$

At steady state cornering the amount of the steering angle  $\delta_0 \cong \delta_A$  and hence, the steering tendency depends at increasing velocity on the stability condition  $a_2 c_{S2} - a_1 c_{S1} \cong 0$ . The various steering tendencies are also arranged in Tab. 9.1.

Table 9.1: Steering tendencies of a vehicle at forward driving

• understeering	$\delta_0 > \delta_0^A$	or	$a_1 c_{S1} < a_2 c_{S2}$	or	$a_1 c_{S1} / a_2 c_{S2} < 1$
• neutral	$\delta_0 = \delta_0^A$	or	$a_1 c_{S1} = a_2 c_{S2}$	or	$a_1 c_{S1} / a_2 c_{S2} = 1$
• oversteering	$\delta_0 < \delta_0^A$	or	$a_1 c_{S1} > a_2 c_{S2}$	or	$a_1 c_{S1} / a_2 c_{S2} > 1$

### 9.3.7.2 Side Slip Angle

Equations (9.121) and (9.122) can also be resolved for the steady state side slip angle. One gets

$$\beta_{st} = \frac{v}{|v|} \frac{a_2 - m v |v| \frac{a_1}{c_{S2} (a_1 + a_2)}}{a_1 + a_2 + m v |v| \frac{a_2 c_{S2} - a_1 c_{S1}}{c_{S1} c_{S2} (a_1 + a_2)}} \delta_0, \tag{9.129}$$

## 9 Lateral Dynamics

The steady state side slip angle starts with the kinematic value

$$\beta_{st}^{v \rightarrow 0} = \frac{v}{|v|} \frac{a_2}{a_1 + a_2} \delta_0. \quad (9.130)$$

On forward drive  $v > 0$  it decreases with increasing speed till the side slip angle changes the sign at

$$v_{\beta_{st}=0} = \sqrt{\frac{a_2 c_{S2} (a_1 + a_2)}{a_1 m}}. \quad (9.131)$$

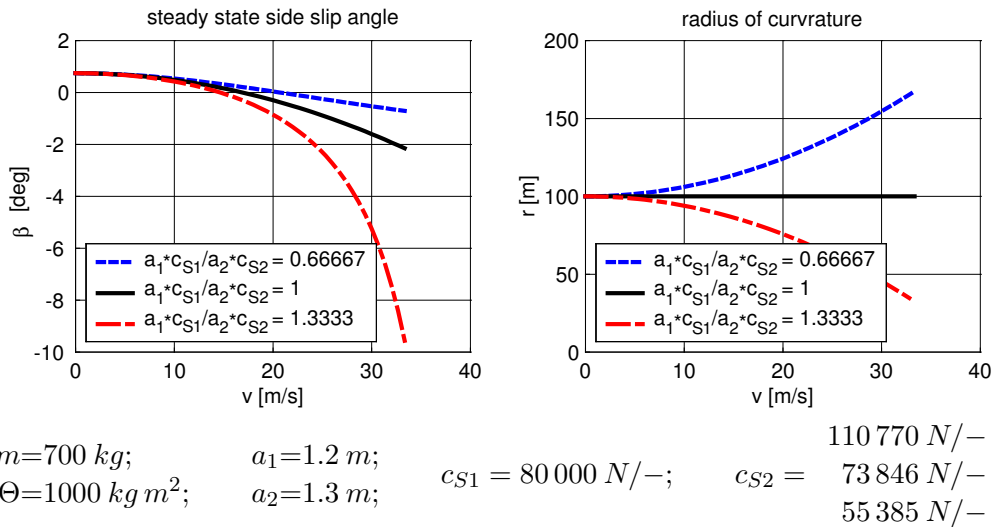


Figure 9.15: Side slip angle at steady state cornering

In Fig. 9.15 the side slip angle  $\beta$ , and the driven curve radius  $R$  are plotted versus the driving speed  $v$ . The steering angle has been set to  $\delta_0 = 1.4321^\circ$ , in order to let the vehicle drive a circle with the radius  $R_0 = 100 \text{ m}$  at  $v \rightarrow 0$ . The actually driven circle radius  $r = R_{st}(\delta_0)$  has been calculated from Eq. (9.125).

Some concepts for an additional steering of the rear axle were trying to keep the side slip angle of the vehicle, measured at the center of the vehicle to zero by an appropriate steering or controlling. Due to numerous problems, production stage could not yet be reached.

### 9.3.7.3 Slip Angles

With the conditions for a steady state solution  $\dot{\beta}_{st} = 0$ ,  $\dot{\omega}_{st} = 0$  and Eq. (9.118), the equations of motion Eq. (9.93) and Eq. (9.94) can be resolved for the lateral forces

$$\begin{aligned} F_{y1st} &= \frac{a_2}{a_1 + a_2} m \frac{v^2}{R_{st}}, & \text{or} & & \frac{a_1}{a_2} &= \frac{F_{y2st}}{F_{y1st}}. \\ F_{y2st} &= \frac{a_1}{a_1 + a_2} m \frac{v^2}{R_{st}} \end{aligned} \quad (9.132)$$

With the linear tire model in Eq. (9.76) one gets in addition

$$F_{y1}^{st} = c_{S1} s_{y1}^{st} \quad \text{and} \quad F_{y2}^{st} = c_{S2} s_{y2}^{st}, \quad (9.133)$$

where  $s_{yA1}^{st}$  and  $s_{yA2}^{st}$  label the steady state lateral slips at the front and rear axle. Now, from Eqs. (9.132) and (9.133) it follows

$$\frac{a_1}{a_2} = \frac{F_{y2}^{st}}{F_{y1}^{st}} = \frac{c_{S2} s_{y2}^{st}}{c_{S1} s_{y1}^{st}} \quad \text{or} \quad \frac{a_1 c_{S1}}{a_2 c_{S2}} = \frac{s_{y2}^{st}}{s_{y1}^{st}}. \quad (9.134)$$

That means, at a vehicle with a tendency to understeer ( $a_1 c_{S1} < a_2 c_{S2}$ ) during steady state cornering the slip angles at the front axle are larger than the slip angles at the rear axle,  $s_{y1}^{st} > s_{y2}^{st}$ . So, the steering tendency can also be determined from the slip angle at the axles.

### 9.3.8 Influence of Wheel Load on Cornering Stiffness

With identical tires at the front and rear axle, given a linear influence of wheel load on the raise of the lateral force over the lateral slip,

$$c_{S1}^{lin} = c_S F_{z1} \quad \text{and} \quad c_{S2}^{lin} = c_S F_{z2}. \quad (9.135)$$

holds. The weight of the vehicle  $G = mg$  is distributed over the axles according to the position of the center of gravity

$$F_{z1} = \frac{a_2}{a_1 + a_2} G \quad \text{and} \quad F_{z2} = \frac{a_1}{a_1 + a_2} G \quad (9.136)$$

With Eq. (9.135) and Eq. (9.136) one obtains

$$a_1 c_{S1}^{lin} = a_1 c_S \frac{a_2}{a_1 + a_2} G \quad (9.137)$$

and

$$a_2 c_{S2}^{lin} = a_2 c_S \frac{a_1}{a_1 + a_2} G. \quad (9.138)$$

## 9 Lateral Dynamics

Thus, a vehicle with identical tires would be steering neutrally at a linear influence of the wheel load on the cornering stiffness, because of

$$a_1 c_{S1}^{lin} = a_2 c_{S2}^{lin} \quad (9.139)$$

The lateral force is applied behind the center of the contact patch at the caster offset distance. Hence, the lever arms of the lateral forces change to  $a_1 \rightarrow a_1 - \frac{v}{|v|} n_{L1}$  and  $a_2 \rightarrow a_2 + \frac{v}{|v|} n_{L1}$ , which will stabilize the vehicle, independently from the driving direction.

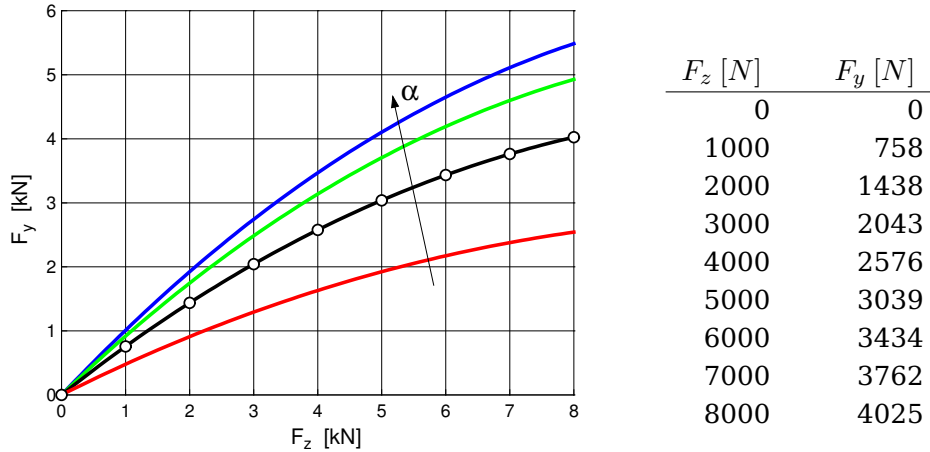


Figure 9.16: Lateral force  $F_y$  over wheel load  $F_z$  at different slip angles

At a real tire, a degressive influence of the wheel load on the tire forces is observed, Fig. 9.16. According to Eq. (9.94) the rotation of the vehicle is stable, if the torque from the lateral forces  $F_{y1}$  and  $F_{y2}$  is aligning, i.e.

$$a_1 F_{y1} - a_2 F_{y2} < 0 \quad (9.140)$$

holds. At a vehicle with the wheel base  $a = 2.45 \text{ m}$  the axle loads  $F_{z1} = 4000 \text{ N}$  and  $F_{z2} = 3000 \text{ N}$  yield the position of the center of gravity  $a_1 = 1.05 \text{ m}$  and  $a_2 = 1.40 \text{ m}$ . At equal slip on front and rear axle one gets from the table in 9.16  $F_{y1} = 2576 \text{ N}$  and  $F_{y2} = 2043 \text{ N}$ . With this, the condition in Eq. (9.140) yields  $1.05 * 2576 - 1.45 * 2043 = -257.55$ . The value is significantly negative and thus stabilizing.

Vehicles with  $a_1 < a_2$  have a stable, i.e. understeering driving behavior. If the axle load at the rear axle is larger than at the front axle ( $a_1 > a_2$ ), generally a stable driving behavior can only be achieved with different tires.

At increasing lateral acceleration the vehicle is more and more supported by the outer wheels. The wheel load differences can differ at a sufficiently rigid vehicle body, because of different kinematics (roll support) or different roll stiffness. Due to the degressive influence of wheel load, the lateral force at an axle decreases

with increasing wheel load difference. If the wheel load is split more strongly at the front axle than at the rear axle, the lateral force potential at the front axle will decrease more than at the rear axle and the vehicle will become more stable with an increasing lateral force, i.e. more understeering.

## 9.4 Mechatronic Systems

### 9.4.1 Electronic Stability Control (ESC)

Electronic Stability Control (ESC) is the generic term for systems designed to improve a vehicle's handling, particularly at the limits where the driver might lose control of the vehicle. Robert Bosch GmbH were the first to deploy an ESC system, called Electronic Stability Program that was used by Mercedes-Benz.

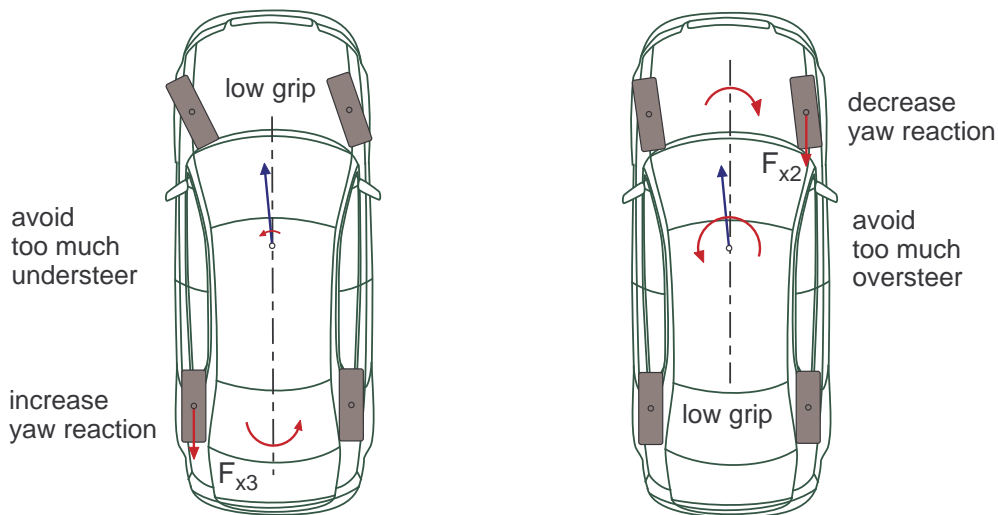


Figure 9.17: ESP braking concepts

ESC compares the driver's intended direction in steering and braking inputs, to the vehicle's response, via lateral acceleration, rotation (yaw) and individual wheel speeds. ESC then brakes individual front or rear wheels and/or reduces excess engine power as needed to help correct understeer or oversteer, Fig. 9.17.

ESC also integrates all-speed traction control, which senses drive-wheel slip under acceleration and individually brakes the slipping wheel or wheels, and/or reduces excess engine power, until control is regained. ESC combines anti-lock brakes, traction control and yaw control.

### 9.4.2 Steer-by-Wire

Modern steer-by-wire systems can improve the handling properties of vehicles [34]. Usually an electronically controlled actuator is used to convert the rotation of the steering wheel into steer movements of the wheels. Steer-by-wire systems are based on mechanics, micro-controllers, electro-motors, power electronics and digital sensors. At present fail-safe systems with a mechanical backup system are under investigation.

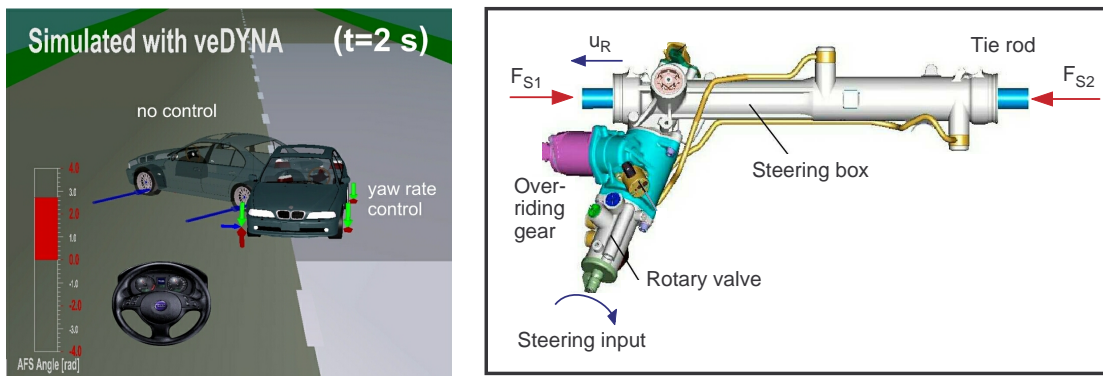


Figure 9.18: Braking on  $\mu$ -split with a standard and an active steering system

The potential of a modern active steering system can be demonstrated by the maneuver braking on a  $\mu$ -split [28]. The coefficient of friction at the left side of the vehicle is supposed to be 10% of the normal friction value at the right side. The vehicle speeds to  $v = 130 \text{ km/h}$  and then the driver applies full brake pressure and fixes the steering wheel like he would do at first in a panic reaction. During the whole maneuver the anti-lock brake system was disabled. The different brake forces at the left and right tires make the car spin around the vertical axis. The different reactions of the vehicle and the layout of the steering system are shown in Fig. 9.18. Only skilled drivers may be able to stabilize the car by counter steering. The success of the counter steering depends on the reactions in the very first seconds. A controller, who takes appropriate actions at the steering angle, can assist the drivers task.

# 10 Driving Behavior of Single Vehicles

## 10.1 Standard Driving Maneuvers

### 10.1.1 Steady State Cornering

The steering tendency of a real vehicle is determined by the driving maneuver called steady state cornering. The maneuver is performed quasi-static. The driver tries to keep the vehicle on a circle with the given radius  $R$ . He slowly increases the driving speed  $v$  and, with this also the lateral acceleration due  $a_y = \frac{v^2}{R}$  until reaching the limit. Typical results are displayed in Fig. 10.1.

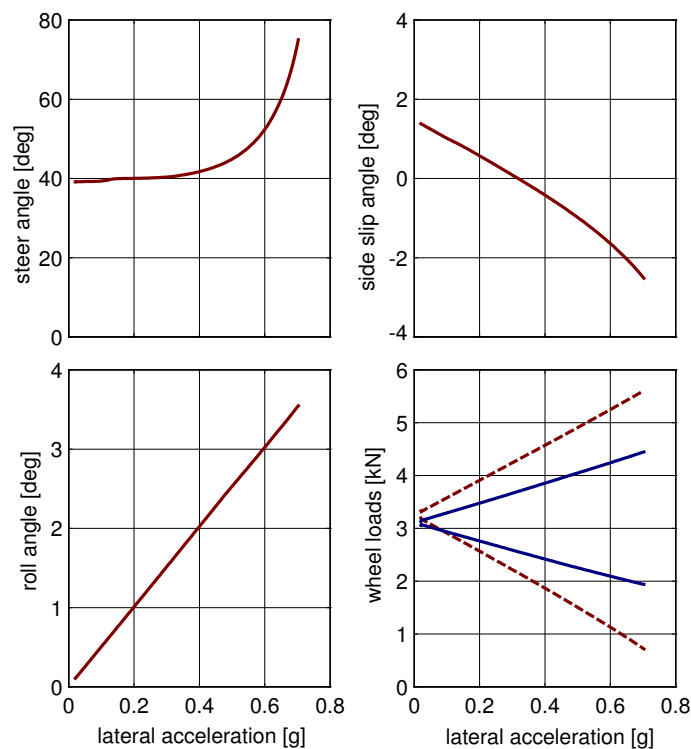


Figure 10.1: Steady state cornering: rear-wheel-driven car on  $R = 100 \text{ m}$

In forward drive the vehicle is understeering and thus stable for any velocity. The inclination in the diagram steering angle versus lateral velocity decides about the steering tendency and stability behavior.

## 10 Driving Behavior of Single Vehicles

The nonlinear influence of the wheel load on the tire performance is here used to design a vehicle that is weakly stable, but sensitive to steer input in the lower range of lateral acceleration, and is very stable but less sensitive to steer input in limit conditions.

With the increase of the lateral acceleration the roll angle becomes larger. The overturning torque is intercepted by according wheel load differences between the outer and inner wheels. With a sufficiently rigid frame the use of an anti roll bar at the front axle allows to increase the wheel load difference there and to decrease it at the rear axle accordingly.

Thus, the degressive influence of the wheel load on the tire properties, cornering stiffness and maximum possible lateral force, is stressed more strongly at the front axle, and the vehicle becomes more under-steering and stable at increasing lateral acceleration, until it drifts out of the curve over the front axle in the limit situation.

Problems occur at front driven vehicles, because due to the demand for traction, the front axle cannot be relieved at will.

Having a sufficiently large test site, the steady state cornering maneuver can also be carried out at constant speed. There, the steering wheel is slowly turned until the vehicle reaches the limit range. That way also weakly motorized vehicles can be tested at high lateral accelerations.

### 10.1.2 Step Steer Input

The dynamic response of a vehicle is often tested with a step steer input. Methods for the calculation and evaluation of an ideal response, as used in system theory or control technics, can not be used with a real car, for a step input at the steering wheel is not possible in practice. A real steering angle gradient is displayed in Fig. 10.2.

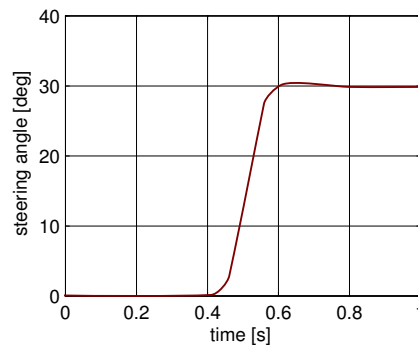


Figure 10.2: Step Steer Input

Not the angle at the steering wheel is the decisive factor for the driving behavior, but the steering angle at the wheels, which can differ from the steering wheel angle

because of elasticities, friction influences, and a servo-support. At very fast steering movements, also the dynamics of the tire forces plays an important role.

In practice, a step steer input is usually only used to judge vehicles subjectively. Exceeds in yaw velocity, roll angle, and especially sideslip angle are felt as annoying.

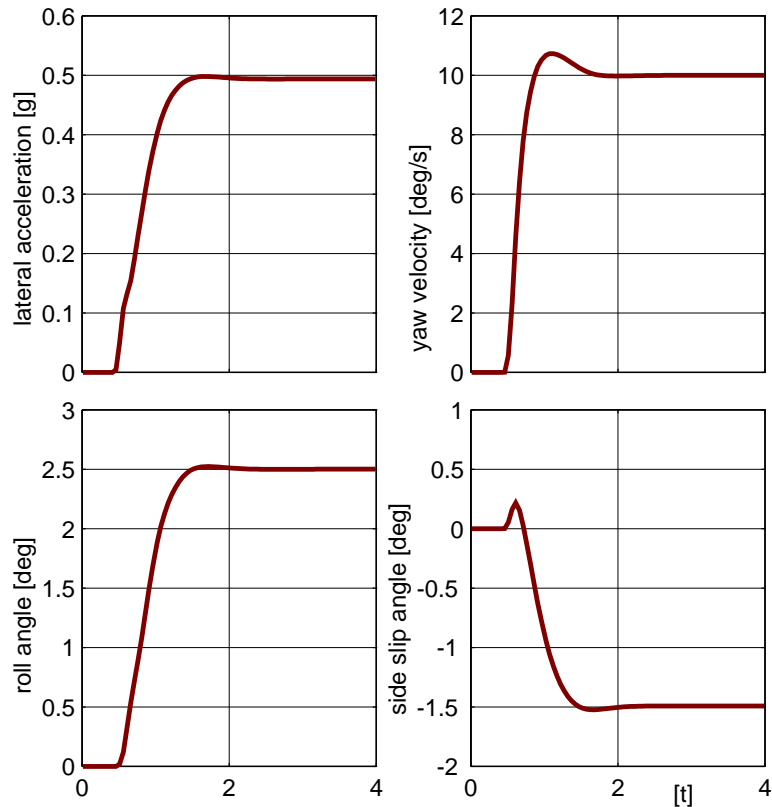


Figure 10.3: Step Steer: Passenger Car at  $v = 100 \text{ km/h}$

The vehicle under consideration behaves dynamically very well, Fig. 10.3. Almost no overshoots occur in the time history of the roll angle and the lateral acceleration. However, small overshoots can be noticed at yaw the velocity and the sideslip angle.

### 10.1.3 Driving Straight Ahead

#### 10.1.3.1 Random Road Profile

The irregularities of a track are of stochastic nature. Fig. 10.4 shows a country road profile in different scalings. To limit the effort of the stochastic description of a track, one usually employs simplifying models. Instead of a fully two-dimensional

## 10 Driving Behavior of Single Vehicles

description either two parallel tracks are evaluated

$$z = z(x, y) \rightarrow z_1 = z_1(s_1), \quad \text{and} \quad z_2 = z_2(s_2) \quad (10.1)$$

or one uses an isotropic track. The statistic properties are direction-independent at an isotropic track. Then, a two-dimensional track can be approximated by a single random process

$$z = z(x, y) \rightarrow z = z(s); \quad (10.2)$$

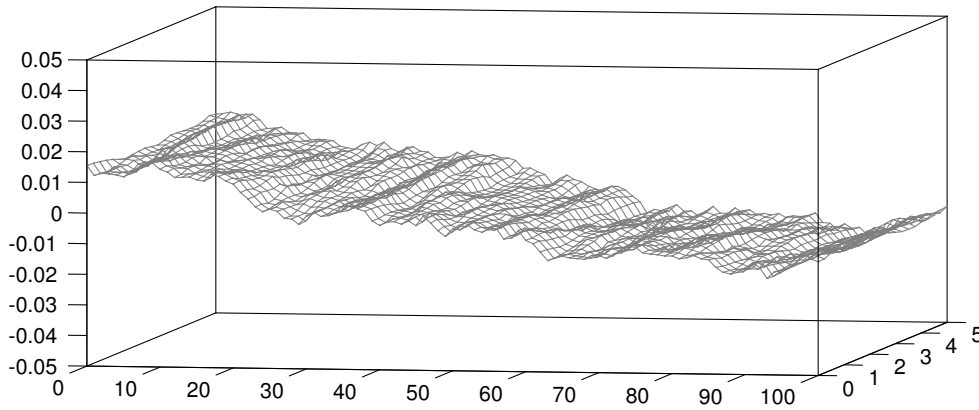


Figure 10.4: Track Irregularities

A normally distributed, stationary and ergodic random process  $z = z(s)$  is completely characterized by the first two expectation values, the mean value

$$m_z = \lim_{s \rightarrow \infty} \frac{1}{2s} \int_{-s}^s z(s) ds \quad (10.3)$$

and the correlation function

$$R_{zz}(\delta) = \lim_{s \rightarrow \infty} \frac{1}{2s} \int_{-s}^s z(s) z(s - \delta) ds. \quad (10.4)$$

A vanishing mean value  $m_z = 0$  can always be achieved by an appropriate coordinate transformation. The correlation function is symmetric,

$$R_{zz}(\delta) = R_{zz}(-\delta), \quad (10.5)$$

and

$$R_{zz}(0) = \lim_{s \rightarrow \infty} \frac{1}{2s} \int_{-s}^s (z(s))^2 ds \quad (10.6)$$

describes the variance of  $z_s$ .

Stochastic track irregularities are mostly described by power spectral densities (abbreviated by psd). Correlating function and the one-sided power spectral density are linked by the Fourier-transformation

$$R_{zz}(\delta) = \int_0^{\infty} S_{zz}(\Omega) \cos(\Omega\delta) d\Omega \quad (10.7)$$

where  $\Omega$  denotes the space circular frequency. With Eq. (10.7) follows from Eq. (10.6)

$$R_{zz}(0) = \int_0^{\infty} S_{zz}(\Omega) d\Omega . \quad (10.8)$$

Thus, the psd gives information, how the variance is compiled from the single frequency shares.

The power spectral densities of real tracks can be approximated by the relation

$$S_{zz}(\Omega) = S_0 \left[ \frac{\Omega}{\Omega_0} \right]^{-w} , \quad (10.9)$$

where the reference frequency is fixed to  $\Omega_0 = 1 \text{ m}^{-1}$ . The reference psd  $S_0 = S_{zz}(\Omega_0)$  acts as a measurement for unevenness and the waviness  $w$  indicates, whether the track has notable irregularities in the short or long wave spectrum. At real tracks, the reference-psd  $S_0$  lies within the range from  $1 * 10^{-6} \text{ m}^3$  to  $100 * 10^{-6} \text{ m}^3$  and the waviness can be approximated by  $w = 2$ .

### 10.1.3.2 Steering Activity

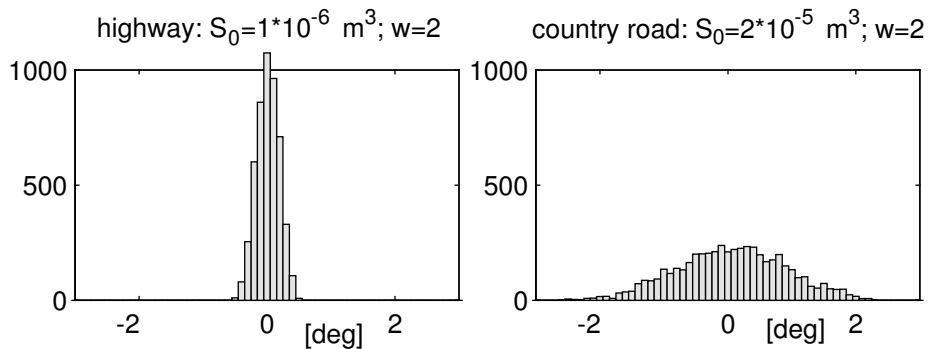


Figure 10.5: Steering activity on different roads

A straightforward drive upon an uneven track makes continuous steering corrections necessary. The histograms of the steering angle at a driving speed of

## 10 Driving Behavior of Single Vehicles

$v = 90 \text{ km/h}$  are displayed in Fig. 10.5. The track quality is reflected in the amount of steering actions. The steering activity is often used to judge a vehicle in practice.

### 10.2 Coach with different Loading Conditions

#### 10.2.1 Data

The difference between empty and laden is sometimes very large at trucks and coaches. In the table 10.1 all relevant data of a travel coach in fully laden and empty condition are listed. The coach has a wheel base of  $a = 6.25 \text{ m}$ . The front axle with

Table 10.1: Data for a laden and empty coach

vehicle	mass [kg]	center of gravity [m]	inertias [ $\text{kg m}^2$ ]		
empty	12 500	-3.800   0.000   1.500	12 500	0	0
			0	155 000	0
			0	0	155 000
fully laden	18 000	-3.860   0.000   1.600	15 400	0	250
			0	200 550	0
			250	0	202 160

the track width  $s_v = 2.046 \text{ m}$  has a double wishbone single wheel suspension. The twin-tire rear axle with the track widths  $s_h^o = 2.152 \text{ m}$  and  $s_h^i = 1.492 \text{ m}$  is guided by two longitudinal links and an a-arm. The air-springs are fitted to load variations via a niveau-control.

#### 10.2.2 Roll Steering

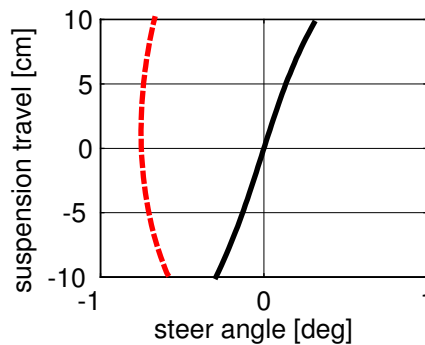


Figure 10.6: Roll steer: - - front, — rear

Whilst the kinematics at the front axle hardly causes steering movements at roll motions, the kinematics at the rear axle is tuned in a way to cause a notable roll steering effect, Fig. 10.6.

### 10.2.3 Steady State Cornering

Fig. 10.7 shows the results of a steady state cornering on a 100 m-Radius. The fully occupied vehicle is slightly more understeering than the empty one. The higher wheel loads cause greater tire aligning torques and increase the degressive wheel load influence on the increase of the lateral forces. Additionally roll steering at the rear axle occurs.

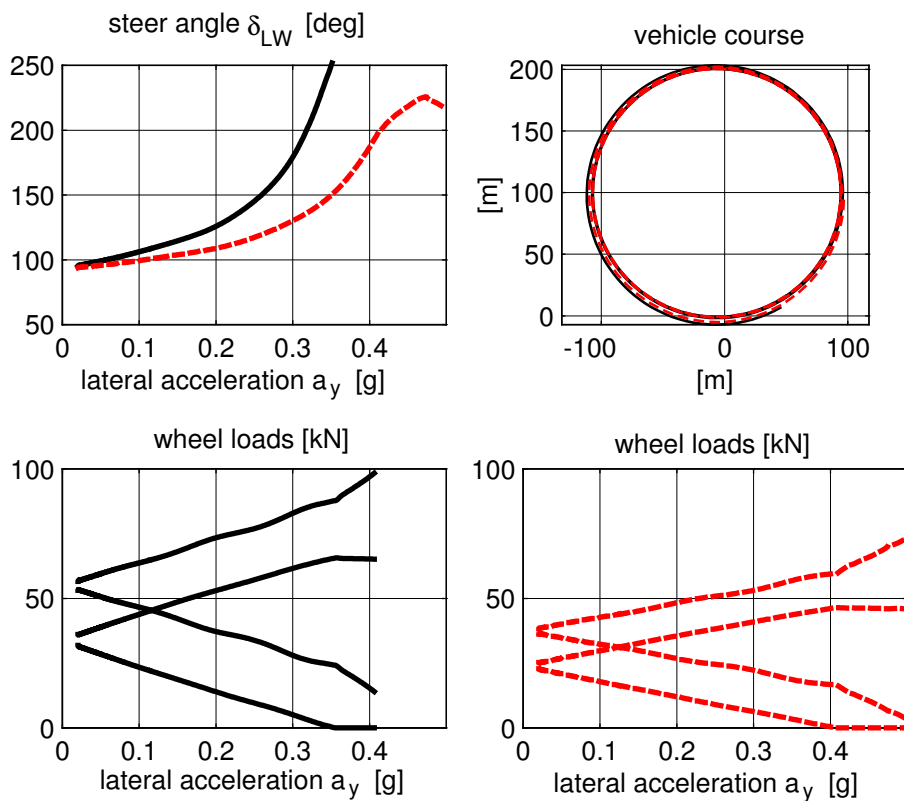


Figure 10.7: Steady State Cornering: Coach - - empty, — fully occupied

Both vehicles can not be kept on the given radius in the limit range. Due to the high position of the center of gravity the maximal lateral acceleration is limited by the overturning hazard. At the empty vehicle, the inner front wheel lift off at a lateral acceleration of  $a_y \approx 0.4 g$ . If the vehicle is fully occupied, this effect will occur already at  $a_y \approx 0.35 g$ .

### 10.2.4 Step Steer Input

The results of a step steer input at the driving speed of  $v = 80 \text{ km/h}$  can be seen in Fig. 10.8. To achieve comparable acceleration values in steady state condition, the

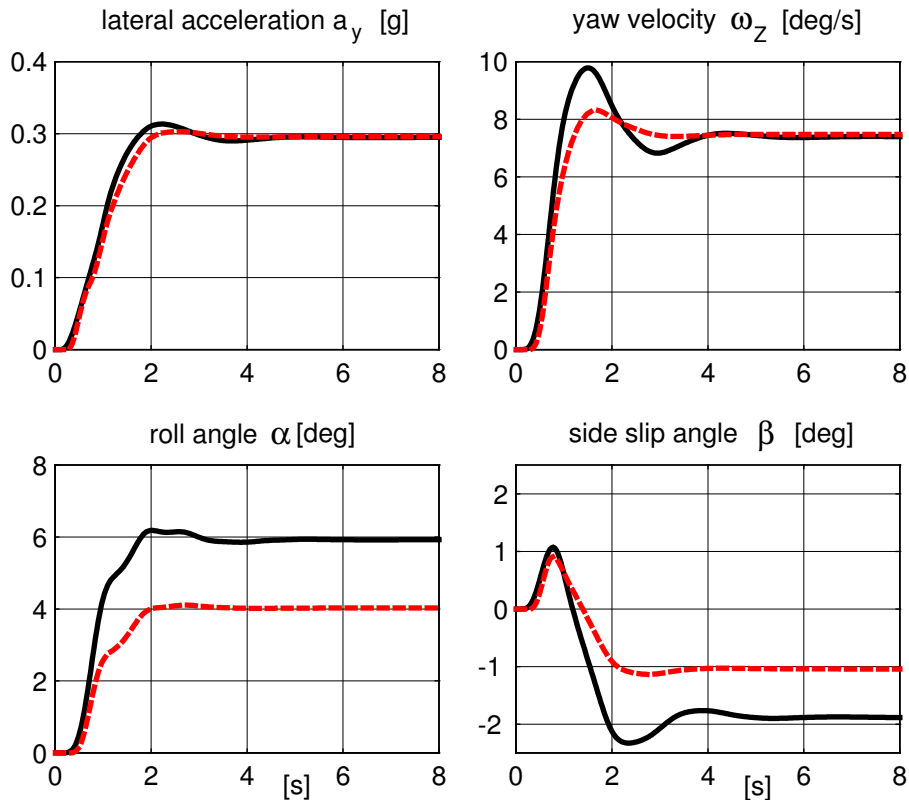


Figure 10.8: Step steer input: - - coach empty, — coach fully occupied

step steer input was done at the empty vehicle with  $\delta = 90^\circ$  and at the fully occupied one with  $\delta = 135^\circ$ . The steady state roll angle is 50% larger at the fully occupied bus than at the empty one. By the niveau-control, the air spring stiffness increases with the load. Because the damper effect remains unchanged, the fully laden vehicle is not damped as well as the empty one. This results in larger overshoots in the time histories of the lateral acceleration, the yaw angular velocity, and the sideslip angle.

### 10.3 Different Rear Axle Concepts for a Passenger Car

A medium-sized passenger car is equipped in standard design with a semi-trailing rear axle. By accordingly changed data this axle can easily be transformed into a trailing arm or a single wishbone axis. According to the roll support, the semi-trailing axle realized in serial production represents a compromise between the

### 10.3 Different Rear Axle Concepts for a Passenger Car

trailing arm and the single wishbone, Fig. 10.9. The influences on the driving behavior at steady state cornering on a 100 m radius are shown in Fig. 10.10.

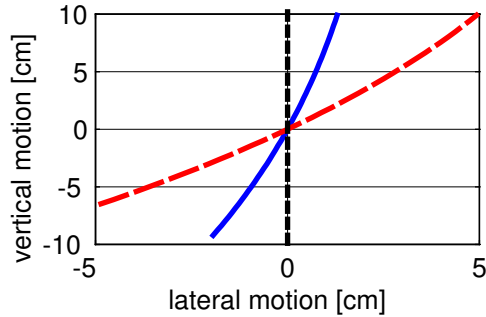


Figure 10.9: Rear axle: — semi-trailing arm, - - single wishbone, ··· trailing arm

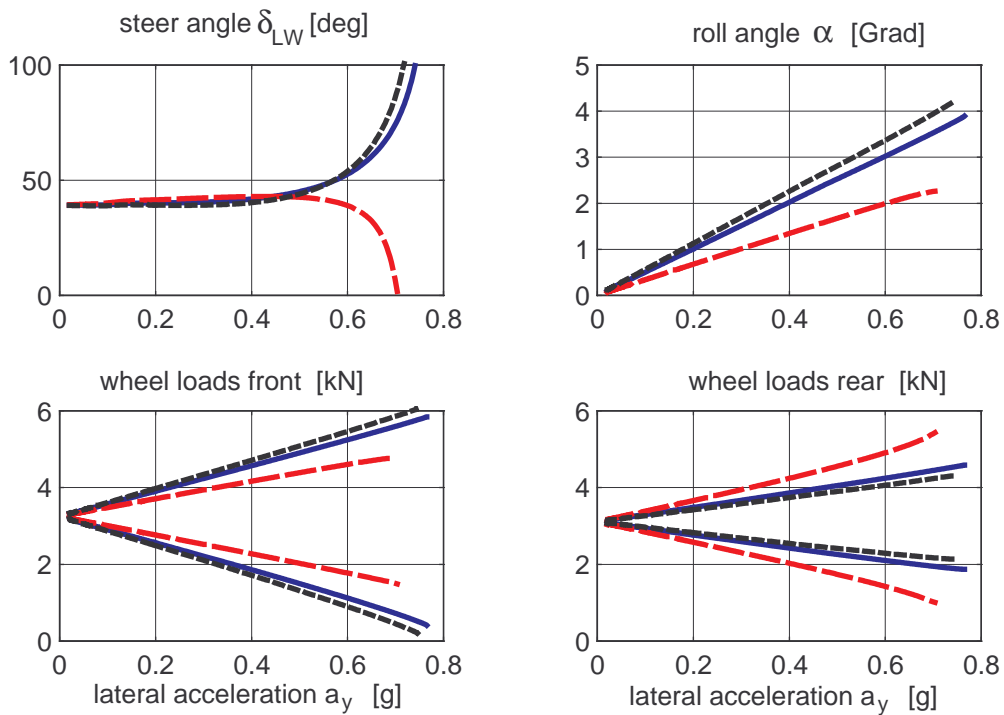


Figure 10.10: Steady state cornering, — semi-trailing arm, - - single wishbone, ··· trailing arm

Substituting the semi-trailing arm at the standard car by a single wishbone, one gets, without adaption of the other system parameters a vehicle oversteering in the limit range. Compared to the semi-trailing arm the single wishbone causes a

## *10 Driving Behavior of Single Vehicles*

notably higher roll support. This increases the wheel load difference at the rear axle, Fig. 10.10. Because the wheel load difference is simultaneously reduced at the front axle, the understeering tendency is reduced. In the limit range, this even leads to an oversteering behavior. The vehicle with a trailing arm rear axle is, compared to the serial car, more understeering. The lack of roll support at the rear axle also causes a larger roll angle.

# Bibliography

- [1] D. Bestle and M. Beffinger. Design of progressive automotive shock absorbers. In *Proc. of Multibody Dynamics*, Madrid, 2005.
- [2] H. Braun. *Untersuchung von Fahrbahnunebenheiten und Anwendung der Ergebnisse*. PhD thesis, TU Braunschweig, 1969.
- [3] T. Butz, M. Ehmann, and T.-M. Wolter. A realistic road model for real-time vehicle dynamics simulation. *Society of Automotive Engineers*, SAE Paper 2004-01-1068, 2004.
- [4] C. J. Dodds and J. D. Robson. The description of road surface roughness. *Journal of Sound and Vibration*, 31(2):175–183, 1973.
- [5] P. Dorato, C. Abdallah, and V. Cerone. *Linear-Quadratic Control. An Introduction*. Prentice-Hall, Englewood Cliffs, New Jersey, 1995.
- [6] M. Eichler, A. Lion, U. Sonnack, and R. Schuller. Dynamik von Luftfedersystemen mit Zusatzvolumen: Modellbildung, Fahrzeugsimulationen und Potenzial. Bericht 1791, VDI, 2003.
- [7] M. Gipser. Ftire, a new fast tire model for ride comfort simulations. In *International ADAMS User Conference*, Berlin, 1999.
- [8] W. Hirschberg, G. Rill, and H. Weinfurter. User-appropriate tyre-modeling for vehicle dynamics in standard and limit situations. *Vehicle System Dynamics*, 38(2):103–125, 2002.
- [9] W. Hirschberg, H. Weinfurter, and Ch. Jung. Ermittlung der Potenziale zur LKW-Stabilisierung durch Fahrdynamiksimulation. In *Berechnung und Simulation im Fahrzeugbau*. VDI, 14.-15. Sept. 2000.
- [10] M. Irmscher and M. Ehmann. Driver classification using ve-dyna advanced driver. *SAE International*, 01-0451, 2004.
- [11] ISO 8608. Mechanical vibration - road surface profiles - reporting of measured data. *International Standard (ISO)*, 1995.
- [12] P. van der Jagt. *The Road to Virtual Vehicle Prototyping; new CAE-models for accelerated vehicle dynamics development*. ISBN 90-386-2552-9 NUGI 834, Tech. Univ. Eindhoven, 2000.

## Bibliography

- [13] U. Kiencke and L. Nielsen. *Automotive Control Systems*. Springer, 2000.
- [14] W. Kortüm and P. Lugner. *Systemdynamik und Regelung von Fahrzeugen*. Springer, 1993.
- [15] P. Lugner, H. Pacejka, and M. Plöchl. Recent advances in tyre models and testing procedures. *Vehicle System Dynamics*, 43(67):413–436, 2005.
- [16] M. Mitschke and H. Wallentowitz. *Dynamik der Kraftfahrzeuge*, 4. Auflage. Springer, 2004.
- [17] P.C. Müller and W.O. *Lineare Schwingungen*. Akad. Verlagsgesellschaft, Wiesbaden, 1976.
- [18] U. Neureder. *Untersuchungen zur Übertragung von Radlastschwankungen auf die Lenkung von Pkw mit Federbein Vorderachse und Zahnstangenlenkung*, volume 12 of *Fortschritt-Berichte VDI*. VDI Verlag, D"usseldorf, 2002.
- [19] Ch. Oertel and A. Fandre. Ride comfort simulations an steps towards life time calculations; RMOD-K and ADAMS. In *International ADAMS User Conference*, Berlin, 1999.
- [20] H.B. Pacejka and E. Bakker. The magic formula tyre model. In *1st Int. Colloquium on Tyre Models for Vehicle Dynamic Analysis*, Lisse, 1993. Swets&Zeitlinger.
- [21] K. Popp and W. Schiehlen. *Fahrzeugdynamik*. Teubner, Stuttgart, 1993.
- [22] A. Riepl, W. Reinalter, and G. Fruhmann. Rough road simulation with tire model RMOD-K and FTire. In *Proc. of the 18th IAVSD Symposium on the Dynamics of vehicles on Roads and on Tracks*. Kanagawa, Japan, London, 2003. Taylor & Francis.
- [23] G. Rill. The influence of correlated random road excitation processes on vehicle vibration. In K. Hedrik, editor, *The Dynamics of Vehicles on Road and on Tracks*, Lisse, 1984. Swets-Zeitlinger.
- [24] G. Rill. Demands on vehicle modeling. In R.J. Anderson, editor, *The Dynamics of Vehicles on Road and on Tracks*, Lisse, 1990. Swets-Zeitlinger.
- [25] G. Rill. First order tire dynamics. In *Proc. of the III European Conference on Computational Mechanics Solids, Structures and Coupled Problems in Engineering*, Lisbon, Portugal, 2006.
- [26] G. Rill. Wheel dynamics. In *Proc. of the XII International Symposium on Dynamic Problems of Mechanics (DINAME 2007)*, 2007.

- [27] G. Rill and C. Chucholowski. A modeling technique for fast computer simulations of configurable vehicle systems. In *Proc. of the 21st International Congress of Theoretical and Applied Mechanics (ICTAM)*, Warsaw, Poland, 2004.
- [28] G. Rill and C. Chucholowski. Modeling concepts for modern steering systems. In *ECCOMAS Multibody Dynamics*, Madrid, Spanien, 2005.
- [29] G. Rill and C. Chucholowski. Real time simulation of large vehicle systems. In *ECCOMAS Multibody Dynamics*, Milano, Italy, 2007.
- [30] G. Rill, N. Kessing, O. Lange, and J. Meier. Leaf spring modeling for real time applications. In *The Dynamics of Vehicles on Road and on Tracks - Extensive Summaries, IAVSD 03*, 2003.
- [31] Th. Seibert and G. Rill. Fahrkomfortberechnungen unter einbeziehung der motorschwingungen. In *Berechnung und Simulation im Fahrzeugbau, VDI-Bericht 1411*, Düsseldorf, 1998. VDI.
- [32] M. Vögel, O. von Stryk, R. Bulirsch, T.-M. Wolter, and C. Chucholowski. An optimal control approach to real-time vehicle guidance. In W. Jäger and H.-J. Krebs, editors, *Mathematics – Key Technology for the Future*, pages 84–102, Berlin, Heidelberg, 2003. Springer.
- [33] M. Weigel, P. Lugner, and M. Plöchl. A driver model for a truck-semitrailer combination. *Vehicle System Dynamics Supplement*, 41:321–331, 2004.
- [34] H. Weinfurter, W. Hirschberg, and E. Hipp. Entwicklung einer Störgrößenkompensation für Nutzfahrzeuge mittels Steer-by-Wire durch Simulation. In *Berechnung und Simulation im Fahrzeugbau, VDI-Berichte 1846*, pages 923–941, Düsseldorf, 2004. VDI.

# Index

- $\mu$ -split, 139
- Ackermann geometry, 146
- Ackermann steering angle, 146, 170
- Active center differential, 75
- Active yaw control, 76
- Aerodynamic forces, 131
- Air resistance, 131
- Air spring, 91, 92
- All wheel drive, 155
- Anti dive, 145
- Anti roll bar, 160
- Anti squat, 145
- Anti-Lock-System, 138
- Anti-roll bar, 92
- Auto-correlation, 10
- Axle kinematics, 145
  - Double wishbone, 85
  - McPherson, 85
  - Multi-link, 85
- Axle Load, 130
- Axle suspension
  - Solid axle, 81
  - Twist beam, 82
- Bend angle, 150, 153
- Bore torque, 18, 45
- Brake pitch angle, 145
- Brake pitch pole, 145
- Braking torque, 74
- Camber angle, 83
- Camber compensation, 162
- Camber influence, 51
- Camber slip, 52
- Caster, 87
- Caster angle, 85
- Climbing capacity, 132
- Coil spring, 91
- Combustion engine, 78
- Comfort, 106
- Contact forces, 18
- Contact patch, 17
- Contact point, 24, 25
- Contact point velocity, 33
- Contact torques, 18
- Cornering resistance, 156
- Cornering stiffness, 43, 44
- Critical velocity, 169
- Damping rate, 110
- Deviation, 9
- Differential, 74
- Disturbance-reaction problems, 118
- Down forces, 131
- Downhill capacity, 132
- Drag link, 88
- Drive pitch angle, 145
- Drive shaft, 74
- Drive train, 68
- Driver, 1, 3
- Driver model, 3
- Driving safety, 106
- Driving torque, 73
- Dynamic axle load, 130
- Dynamic force elements, 96
- Dynamic tire forces, 59
- Dynamic tire offset, 43, 44
- Effective value, 9

## *Index*

- Eigenvalues, 167
- Environment, 3
- ESC, 175
- ESP, 175
  
- First harmonic oscillation, 96
- Fourier-approximation, 97
- Frequency domain, 96
- Friction, 132
- Friction coefficient, 50
- Front wheel drive, 133, 155
  
- Generalized fluid mass, 104
- Grade, 130
  
- Half shaft, 74
- Hybrid drive, 79
- Hydro-mount, 103
  
- Kinematic tire model, 146
- Kingpin, 85
- Kingpin angle, 86
- Kingpin offset, 87
  
- Lateral acceleration, 158, 170
- Lateral force, 18, 164
- Lateral force characteristics, 43
- Lateral force distribution, 42
- Lateral slip, 42, 164, 165
- Leaf spring, 91, 92
- Ljapunov equation, 118
- Load, 3
- Local track plane, 27
- Longitudinal force, 18, 40, 41
- Longitudinal force characteristics, 42
- Longitudinal force distribution, 41
- Longitudinal slip, 41
  
- Maximum acceleration, 132, 133
- Maximum deceleration, 132, 134
- Mean value, 9
  
- Natural frequency, 110
- Normal force, 18
  
- Optimal brake force distribution, 136
- Optimal chassis damping, 116
- Optimal damping, 115, 121
- Optimal drive force distribution, 136
- Optimal wheel damping, 116
- Overriding gear, 87
- Oversteer, 171
- Overturning, 156
  
- Parallel track model, 7
- Parallel tracks, 180
- Pivot pole, 146
- Pneumatic trail, 43
- Power spectral density, 181
  
- Quarter car model, 121, 125
  
- Rack, 87
- Random road profile, 179
- Rear wheel drive, 133, 155
- Reference frames
  - Ground fixed, 4
  - Inertial, 5
  - Vehicle fixed, 4
- Relative damping rate, 111
- Relaxation length, 59
- Ride comfort, 117
- Ride safety, 117
- Road, 24
- Roll axis, 162
- Roll center, 162
- Roll steer, 183
- Roll stiffness, 158
- Roll support, 162
- Rolling condition, 164
- Rolling resistance, 18, 38
- Rolling resistance coefficient, 39
  
- Safety, 106
- Scrub radius, 87
- Self aligning torque, 18, 43
- Side slip angle, 146, 171
- Sky hook damper, 121

- Space requirement, 147
- Spring rate, 112
- Stability, 167
- Stabilizer, 92
- State equation, 166
- State matrix, 123
- State vector, 123
- Steady state cornering, 154, 177, 183
- Steer-by-wire, 87, 176
- Steering activity, 181
- Steering angle, 152
- Steering box, 88
- Steering lever, 88
- Steering offset, 87
- Steering system
  - Lever arm, 88
  - Rack and pinion, 87
  - Toe bar steering system, 88
- Steering tendency, 163, 171
- Step steer input, 178, 184
- Suspension model, 106
- Suspension spring rate, 112
- Synchromesh, 76
- System response, 96
  
- Tilting, 132
- Tilting torque, 18
- Tipping torque, 37
- Tire
  - Lift off, 122
  - Linear Model, 164
- Tire camber, 25
- Tire characteristics, 23
- Tire composites, 17
- Tire damping
  - radial, 37
- Tire deflection, 28
- Tire deformation, 33
- Tire development, 16
- Tire model, 23, 173
- Tire radius
  - dynamic, 34, 35
  - loaded, 25, 34
  - static, 25, 34, 35
  - unloaded, 34
- Tire stiffness
  - radial, 36, 158
- TMeasy, 23
- Toe angle, 82
- Toe-in, 82
- Toe-out, 82
- Torsion bar, 91
- Track, 24
- Track curvature, 152
- Track normal, 5, 25, 27
- Track radius, 152
- Track width, 146, 158
- Trailer, 149, 153
- Transport velocity, 35
- Tread deflection, 40
- Tread particles, 40
  
- Understeer, 171
  
- Variance, 9
- Vehicle, 2
- Vehicle comfort, 106
- Vehicle dynamics, 1
- Vehicle model, 106, 125, 129, 140, 149, 159, 163
- Vertical dynamics, 106
- Virtual work, 159
  
- Waviness, 181
- Wheel base, 146
- Wheel camber, 83
- Wheel load, 18, 36
- Wheel load influence, 48
- Wheel rotation axis, 5
- Wheel suspension
  - Central control arm, 82
  - Double wishbone, 81
  - McPherson, 81
  - Multi-Link, 81
  - Semi-trailing arm, 82, 184

*Index*

Single wishbone, 184

SLA, 82

Trailing arm, 184

Yaw angle, 149, 152

Yaw Velocity, 164